

# Mathematical Modelling of Fungal Interactions

M. Javed A. Choudhury

Division of Mathematics and Statistics

University of South Wales



A submission presented in partial fulfilment of the requirements  
of the University of South Wales/ Prifysgol De Cymru  
for the degree of Doctor of Philosophy.

November, 2019

## Abstract

Fungi are central components of almost all ecosystems through their role as decomposers and symbiotic agents while also having significant impacts on many aspects of human livelihood. In these settings, fungal interactions, either with other fungi or in response to their local environment, are common but their study *in vivo* is complicated due to the multitude of processes involved. Thus, *in vitro* experiments are performed where fungi is grown on Petri dishes in a laboratory. However, even in these carefully controlled settings, experimental studies are complicated due to the scales involved: while a Petri dish is measured in centimetres, some species of fungi in the terrestrial environment can span kilometres while the underlying unit of growth is measured in microns. The mathematical models described and constructed in this thesis naturally link these different growth scales and includes the interactions experienced by growing fungi, thus complementing experimental approaches.

A set of previously published coupled partial differential equations describing the growth of a fungus are investigated and new solutions obtained. A number of these new solutions involve the application of a decomposition method resulting in semi-analytical formulations that agree with numerical integration, particularly concerning the growth rates of the fungus at both small and large times.

These models are adapted to focus on interactions between competing fungi and their response to domains containing toxic material. These new models, also sets of partial differential equations, are investigated using a combination of analytical, semi-analytical and numerical methods. For the first time in the literature, a mathematical model is constructed that includes a mechanism allowing fungi to obtain iron, a heavy metal essential for growth, through the production, release and reacquisition of siderophores which are molecules that bind and transport iron.

The results constructed in this thesis are of great significance and relevance to all instances involving the application of fungal interactions. In particular, nutrient availability influences fungal interactions and thus careful manipulation of this resource can improve the outcome of biotechnological applications involving fungi.

# Acknowledgments

I would like to express my sincere gratitude and appreciation to my respected supervisors, Dr. Graeme P. Boswell and Dr. Philip M. J. Trevelyan, without whose continuous support and guidance, the completion of this thesis would not have been possible. Graeme has spent a great deal of his time with my drafts and helped me mould them into coherent shape. From the day I became an undergraduate student at the University of Glamorgan, he has inspired and taught me the powerful tools of applied mathematics and introduced me to the wonderful field of mathematical biology. I thank him wholeheartedly for his critical insights, sense of perspective, saintly patience and his continuous encouragement. Grateful acknowledgment is also made to Philip for his extreme kindness, generosity, enthusiastic encouragement and support. His immense knowledge and meticulous feedback helped me profusely throughout my research and writing of this thesis. I cannot imagine having better mentors than them. Also, managing to get me through a PhD must be among their most impressive achievements to date.

I would like to extend my gratitude to the mathematics department at the University of South Wales, for their precious support and encouragement through the years.

I thank my fellow comrades Liam Harris and Daniel Williams for the stimulating discussions and for the fun we have had over the years. Also to all those who have been there from the beginning of my journey and those I have lost along the way, I would like to say thank you for everything.

I would like to thank my family: my parents (Tipu S. Choudhury and Salima A. Choudhury), to my brother (Jelani Choudhury) and my sisters (Raki and Ruhi Choudhury) for supporting me physically and spiritually throughout my life.

Finally, I am immensely grateful to Allah for enriching my life with countless blessings and filling my life with tranquility, love and happiness.

# Contents

|          |   |           |
|----------|---|-----------|
| <b>1</b> | <b>Introduction</b>   | <b>1</b>  |
| 1.1      | Biology and uses of fungi . . . . .                                   | 1         |
| 1.1.1    | Fungal morphology and fungal interactions . . . . .                   | 5         |
| 1.2      | Historical modelling approaches . . . . .                             | 8         |
| 1.3      | Summary . . . . .   | 14        |
| <b>2</b> | <b>The Basis for Mathematical Modelling of Filamentous Fungi</b>      | <b>16</b> |
| 2.1      | Mathematical modelling fundamentals . . . . .                         | 16        |
| 2.2      | Edelstein's modelling approach . . . . .                              | 16        |
| 2.2.1    | Formulation of $d(\rho)$ and $\sigma(n, \rho)$ . . . . .              | 17        |
| 2.2.2    | Non-dimensionalisation of model equations . . . . .                   | 20        |
| 2.3      | Specific phenotype of fungi . . . . .                                 | 21        |
| 2.3.1    | Phenotype FHD . . . . .   | 22        |
| 2.3.1.1  | Particular travelling wave solution for FHD . . . . .                 | 23        |
| 2.3.2    | Phenotype FXD . . . . .   | 24        |
| 2.3.2.1  | A particular travelling wave solution for FXD . . . . .               | 25        |
| 2.3.3    | Phenotype YWD . . . . .   | 26        |
| 2.3.3.1  | General analytical solution . . . . .                                 | 27        |
| 2.3.4    | Phenotype YHD . . . . .   | 29        |
| 2.4      | Phase space analysis . . . . .  | 30        |
| 2.4.1    | Travelling wave solutions . . . . .                                   | 30        |
| 2.4.2    | Phase plane analysis . . . . .  | 31        |
| 2.5      | Summary . . . . .   | 34        |
| <b>3</b> | <b>Decomposition Method Applied to the Study of Filamentous Fungi</b> | <b>36</b> |
| 3.1      | A decomposition method . . . . .                                      | 36        |



|          |  |           |
|----------|--|-----------|
| 3.1.1    | Brief history . . . . .  | 37        |
| 3.1.2    | Adomian decomposition method . . . . .   | 38        |
| 3.1.2.1  | Example of ADM . . . . .   | 40        |
| 3.1.3    | Laplace decomposition method . . . . .   | 41        |
| 3.1.3.1  | Example of LDM . . . . .   | 43        |
| 3.1.4    | YWD Phenotype revisited . . . . .  | 44        |
| 3.1.4.1  | A particular solution . . . . .  | 44        |
| 3.1.4.2  | Applying LDM on phenotype YWD . . . . .  | 45        |
| 3.1.4.3  | Comparing LDM to numerical solutions . . . . .                                   | 47        |
| 3.1.5    | FHD Phenotype revisited . . . . .  | 51        |
| 3.2      | Application of LDM to track the position of leading edge of wave front . . . . . | 54        |
| 3.2.1    | Wave front of YWD . . . . .  | 55        |
| 3.2.2    | Wave front of FHD . . . . .  | 56        |
| 3.3      | Kinematic properties of an advancing wave front . . . . .                        | 57        |
| 3.3.1    | Inspiration and motivation . . . . .   | 57        |
| 3.3.2    | Formulation of method . . . . .  | 58        |
| 3.3.3    | LDM series solution utilisation . . . . .  | 60        |
| 3.3.3.1  | YWD phenotype: decoupled equations . . . . .                                     | 61        |
| 3.3.3.2  | FHD phenotype: coupled equations . . . . .                                       | 64        |
| 3.4      | Conclusion . . . . .   | 67        |
| <b>4</b> | <b>One Dimensional Models of Fungal Competition</b>                              | <b>71</b> |
| 4.1      | Competing fungi . . . . .  | 71        |
| 4.1.1    | Experimental studies . . . . .   | 71        |
| 4.1.2    | Historical modelling approaches . . . . .  | 74        |
| 4.2      | Nutrient independent interactions . . . . .                                      | 75        |
| 4.2.1    | Model equations . . . . .  | 75        |
| 4.2.2    | Mutual tip suppression equations . . . . .                                       | 77        |
| 4.2.2.1  | Analysis . . . . .   | 78        |
| 4.2.2.2  | Numerical results . . . . .  | 80        |
| 4.2.2.3  | Conclusion . . . . .   | 83        |
| 4.2.3    | Tips suppression and hyphal degradation in single species . . . . .              | 84        |
| 4.2.3.1  | Analysis . . . . .   | 84        |
| 4.2.3.2  | Numerical results . . . . .  | 85        |
| 4.2.3.3  | Conclusion . . . . .   | 89        |

|          |  |            |
|----------|--|------------|
| 4.3      | Nutrient dependent interactions . . . . .                              | 90         |
| 4.3.1    | Model equations . . . . .  | 90         |
| 4.3.2    | Model tip suppression only . . . . .                                   | 93         |
| 4.3.2.1  | Equilibria and stability . . . . .                                     | 93         |
| 4.3.2.2  | Phase-plane analysis . . . . .   | 97         |
| 4.3.2.3  | Numerical results . . . . .  | 101        |
| 4.3.3    | Mutual tip suppression and hyphal degradation . . . . .                | 105        |
| 4.3.3.1  | Equilibria and stability . . . . .                                     | 105        |
| 4.3.3.2  | Phase-plane analysis . . . . .   | 108        |
| 4.3.3.3  | Numerical results . . . . .  | 110        |
| 4.4      | Conclusion . . . . .   | 112        |
| <b>5</b> | <b>Fungal Interactions and Spatial Patterns in Planar Environments</b> | <b>116</b> |
| 5.1      | Boswell's modelling approach . . . . .                                 | 118        |
| 5.1.1    | Model formulation . . . . .  | 118        |
| 5.1.2    | Numerical simulation in COMSOL . . . . .                               | 122        |
| 5.2      | Fungal interactions model formulation . . . . .                        | 126        |
| 5.2.1    | Nutrient and competition variability . . . . .                         | 129        |
| 5.2.1.1  | Default calibration . . . . .  | 130        |
| 5.2.1.2  | Nutrient variability . . . . .   | 131        |
| 5.2.1.3  | Competitive variability . . . . .                                      | 133        |
| 5.2.1.4  | Nutrient and competition variability . . . . .                         | 135        |
| 5.2.2    | Continual nutrient replenishment . . . . .                             | 137        |
| 5.2.2.1  | Nutrient replenishment . . . . .                                       | 138        |
| 5.2.2.2  | Nutrient replenishment in an uneven domain . . . . .                   | 139        |
| 5.2.2.3  | Nutrient replenishment with competitive variability . . . . .          | 141        |
| 5.2.3    | Pulsed nutrient replenishment . . . . .                                | 143        |
| 5.2.3.1  | Competition under equality . . . . .                                   | 144        |
| 5.2.3.2  | Additional resource impact on competition . . . . .                    | 145        |
| 5.2.3.3  | Combative variability and resources . . . . .                          | 147        |
| 5.2.4    | Initial homogeneous resources . . . . .                                | 150        |
| 5.2.4.1  | Combative variability in an exhaustive nutrient domain . . . . .       | 150        |
| 5.2.4.2  | Combative variability in a biased nutrient domain . . . . .            | 152        |
| 5.3      | Single common resource . . . . .                                       | 154        |
| 5.3.1    | Competitive variability in a nutrient scarce domain . . . . .          | 156        |

|          |   |            |
|----------|---|------------|
| 5.3.2    | Competitive variability in a nutrient rich domain . . . . .   | 157        |
| 5.3.3    | Competitive and block nutrient . . . . .  | 159        |
| 5.4      | Conclusion . . . . .  | 161        |
| <b>6</b> | <b>Fungal Growth in Toxic Environments</b>  | <b>164</b> |
| 6.1      | Motivation . . . . .  | 164        |
| 6.2      | One dimensional model of fungal toxic interaction . . . . .   | 168        |
| 6.2.1    | Numerical simulation . . . . .  | 168        |
| 6.2.2    | Analysis of immobile toxicity . . . . .   | 169        |
| 6.2.3    | Conclusion from basic modelling . . . . .   | 171        |
| 6.3      | Two dimensional model of fungal growth in toxic environments . .  | 173        |
| 6.3.1    | Fomina <i>et al.</i> (2000) revisited . . . . .   | 174        |
| 6.3.1.1  | Biomass expansion in a toxic free environment . .   | 175        |
| 6.3.1.2  | Biomass expansion in low toxic domain with scarce<br>resources . . . . .                                | 178        |
| 6.3.1.3  | Biomass expansion in high toxic domain with<br>scarce resources . . . . .                               | 180        |
| 6.3.1.4  | Biomass expansion from a nutrient scarce domain<br>to a highly toxic domain with abundant resources     | 183        |
| 6.3.1.5  | Biomass expansion from a nutrient rich domain to<br>a highly toxic domain with scarce resources . . .   | 184        |
| 6.3.2    | Fomina <i>et al.</i> (2003) revisited . . . . .   | 187        |
| 6.3.2.1  | Biomass expansion in a toxic free environment . .   | 187        |
| 6.3.2.2  | Biomass expansion in a low toxicity environment   | 189        |
| 6.3.2.3  | Biomass expansion in a highly toxic domain. . . .   | 191        |
| 6.3.2.4  | Biomass expansion in a highly toxic domain with<br>scarce resources. . . . .                            | 194        |
| 6.3.2.5  | Biomass expansion from a nutrient rich region to<br>a highly toxic region with scarce resources . . . . | 195        |
| 6.3.3    | Biomass expansion across a pollutant strip . . . . .  | 198        |
| 6.3.3.1  | Biomass expansion from a rich nutrient source<br>across a highly toxic domain abundant in resources     | 199        |
| 6.3.3.2  | Biomass expansion from a limited nutrient domain<br>across a highly toxic region abundant in resources  | 201        |
| 6.3.3.3  | Biomass expansion from a scarce nutrient source<br>across a highly toxic region with limited resources  | 203        |

|          |  |            |
|----------|--|------------|
| 6.3.4    | Biomass expansion on toxic domain . . . . .                                  | 205        |
| 6.4      | Conclusion . . . . .   | 208        |
| <b>7</b> | <b>Iron in Fungi: Modelling the Role of Siderophores in Iron Acquisition</b> | <b>210</b> |
| 7.1      | Siderophore detection in laboratory experiments . . . . .                    | 212        |
| 7.2      | Mathematical model and numerical simulation . . . . .                        | 215        |
| 7.2.1    | Siderophore detection on a partitioned domain . . . . .                      | 217        |
| 7.2.2    | Variations in the external substrate . . . . .                               | 222        |
| 7.2.3    | Non-uniform nutrient distribution . . . . .                                  | 226        |
| 7.2.4    | Dependence on initial internal substrate . . . . .                           | 228        |
| 7.2.5    | Varying iron concentration . . . . .   | 230        |
| 7.3      | Conclusion . . . . .   | 232        |
| <b>8</b> | <b>Modelling Siderophore-Iron Interactions: An Analytical Approach</b>       | <b>235</b> |
| 8.1      | Analysis of siderophore-iron interaction . . . . .                           | 235        |
| 8.1.1    | Self similar solutions . . . . .   | 237        |
| 8.1.2    | Small time asymptotic limit . . . . .  | 239        |
| 8.1.3    | Large time asymptotic limit . . . . .  | 243        |
| 8.2      | Laplace decomposition method on wave speed approximation . . .               | 252        |
| 8.3      | Siderophore-iron complex . . . . .   | 255        |
| 8.3.1    | Siderophore distribution . . . . .   | 255        |
| 8.3.2    | Siderophore-iron complex distribution . . . . .                              | 258        |
| 8.3.3    | Equal diffusion of siderophore and siderophore-iron complex                  | 265        |
| 8.4      | Conclusion . . . . .   | 270        |
| <b>9</b> | <b>Conclusion</b>  | <b>272</b> |
| 9.1      | Concluding remarks . . . . .   | 272        |
| 9.2      | Future work . . . . .  | 277        |
|          | <b>Bibliography</b>  | <b>280</b> |

# List of Figures

|     |  |    |
|-----|--|----|
| 1.1 | Examples of fungal networks. . . . .   | 2  |
| 1.2 | Radial growth of fungi on a Petri dish (Online). . . . .   | 5  |
| 1.3 | Types of branching. . . . .  | 7  |
| 1.4 | Types of fusion. . . . .   | 8  |
| 2.1 | Plot of the initial function. . . . .  | 22 |
| 2.2 | Wave profile for FHD phenotype . . . . .   | 23 |
| 2.3 | Plot of the particular solution (2.25) with $\xi = 1$ at time $t = 1$ . . .                          | 24 |
| 2.4 | Wave profile for the FXD phenotype . . . . .   | 25 |
| 2.5 | Plot of the particular solution (2.29) with $\xi = 1$ at time $t = 1$ . . .                          | 26 |
| 2.6 | Wave profile for the YWD phenotype . . . . .   | 27 |
| 2.7 | Wave profile for the YHD phenotype . . . . .   | 30 |
| 2.8 | Phase plane diagrams for FHD, FXD, YWD and YHD phenotypes  | 33 |
| 3.1 | Plot of YWD using particular initial conditions . . . . .  | 48 |
| 3.2 | Numerical and LDM plot for YWD phenotype with 10 terms . . .   | 49 |
| 3.3 | Numerical and LDM plot for YWD phenotype with 20 terms . . .   | 50 |
| 3.4 | Numerical and LDM plot for YWD phenotype with 50 terms . . .   | 50 |
| 3.5 | Numerical and LDM plot for FHD phenotype with 30 terms . . .   | 53 |
| 3.6 | Numerical plot of YWD phenotype at $t = 2$ . . . . .   | 63 |
| 4.1 | Study of fungal interaction conducted by Ibarra-Medina et al. (2010)                                 | 72 |
| 4.2 | Study on fungal interactions by Iluyemi and Hanafi (2009) . . . .                                    | 73 |
| 4.3 | $A - B$ parameter space for equation (4.5) . . . . .   | 80 |
| 4.4 | Fungal interaction with tip suppression resulting in displacement .                                  | 81 |
| 4.5 | Fungal interaction with tip suppression resulting in coexistence . .                                 | 82 |
| 4.6 | Fungal interaction with tip suppression resulting in coexistence<br>with varying densities . . . . . | 83 |

|      |   |     |
|------|---|-----|
| 4.7  | Fungal interaction with a dominant species resulting in displacement  | 86  |
| 4.8  | Fungal interaction with dominant species displacing the non-dominant species at different rates . . . . .   | 87  |
| 4.9  | Fungal interaction showing coexistence with dominant species at higher density . . . . .  | 88  |
| 4.10 | Fungal interaction showing a non-dominant species tip and hyphal densities depleting at different rates . . . . .   | 89  |
| 4.11 | The $c_1$ - $c_2$ parameter space for equations (4.10) . . . . .  | 97  |
| 4.12 | Phase portraits of equations (4.15) with small $\psi$ for the cases outlined in Figure 4.11 . . . . .   | 99  |
| 4.13 | Phase portraits of equations (4.15) for the different regions outlined in Figure 4.11 . . . . .   | 101 |
| 4.14 | Numerical solutions of equations (4.11) with initial data (4.2) and (4.17) . . . . .  | 103 |
| 4.15 | Numerical solutions of equations (4.11) with initial data (4.2) and (4.17) . . . . .  | 104 |
| 4.16 | Numerical solutions of equations (4.10) with initial data (4.2) and (4.17) . . . . .  | 105 |
| 4.17 | Phase portraits of equations (4.19) for the different regions of Figure 4.11 . . . . .  | 110 |
| 4.18 | Numerical solutions of equations (4.10) with initial data (4.2) and (4.17) . . . . .  | 111 |
| 5.1  | Growth of fungi on a Petri dish . . . . .   | 117 |
| 5.2  | Solutions to equations (5.4) at times indicated with initial data in equation (5.5) and parameter values from Table 5.1 . . . . .   | 125 |
| 5.3  | 2d representation of the solutions to equations (5.10) with initial data (5.11) and parameter values from Table 5.2 with $s_{e1_0} = s_{e2_0} = 0.5$ , $G = H = 0$ and $A = B = 1000$ . . . . .       | 130 |
| 5.4  | Cross section of the solutions depicted in Figure 5.3. . . . .  | 131 |
| 5.5  | 2d representation of the solutions to equations (5.10) with initial data (5.11) and parameter values from Table 5.2 with $s_{e1_0} = 0.5$ , $s_{e2_0} = 1$ , $G = H = 0$ and $A = B = 1000$ . . . . . | 132 |
| 5.6  | Cross section of the solutions depicted in Figure 5.5. . . . .  | 133 |

|      |  |     |
|------|--|-----|
| 5.7  | 2d representation of the solutions to equations (5.10) with initial data (5.11) and parameter values from Table 5.2 with $s_{e1_0} = s_{e2_0} = 1$ , $G = H = 0$ , $A = 1000$ and $B = 300$ . . . . .  | 134 |
| 5.8  | Cross section of the solutions depicted in Figure 5.7. . . . .   | 135 |
| 5.9  | 2d representation of the solutions to equations (5.10) with initial data (5.11) and parameter values from Table 5.2 with $s_{e1_0} = 1$ , $s_{e2_0} = 0.5$ , $G = H = 0$ , $A = 1000$ and $B = 300$ . . . . .                                    | 136 |
| 5.10 | Cross section of the solutions depicted in Figure 5.9. . . . .   | 137 |
| 5.11 | 2d representation of the solutions to equations (5.10) with initial data (5.11), (5.13) and parameter values from Table 5.2 with $s_{e1_0} = s_{e2_0} = 0.5$ , $A = B = 1000$ , $G_0 = 0.3$ and $H = 0$ . . . . .                                | 138 |
| 5.12 | Cross section of the solutions depicted in Figure 5.11. . . . .  | 139 |
| 5.13 | 2d representation of the solutions to equations (5.10) with initial data (5.11), (5.13) and parameter values from Table 5.2 with $s_{e1_0} = 0.5$ , $s_{e2_0} = 1$ , $A = B = 1000$ , $G_0 = 0.3$ and $H = 0$ . . . . .                          | 140 |
| 5.14 | Cross section of the solutions depicted in Figure 5.13. . . . .  | 141 |
| 5.15 | 2d representation of the solutions to equations (5.10) with initial data (5.11), (5.13) and parameter values from Table 5.2 with $s_{e1_0} = s_{e2_0} = 0.5$ , $G_0 = 0.2$ , $H = 0$ , $A = 1000$ and $B = 300$ . . . . .                        | 142 |
| 5.16 | Cross section of the solutions depicted in Figure 5.15. . . . .  | 143 |
| 5.17 | 2d representation of the solutions to equations (5.10) with initial data (5.11), (5.14) and parameter values from Table 5.2 with $s_{e1_0} = s_{e2_0} = 0.5$ , $G = H = 1 + \sin(10t)$ and $A = B = 1000$ . . . . .                              | 144 |
| 5.18 | Cross section of the solutions depicted in Figure 5.17. . . . .  | 145 |
| 5.19 | 2d representation of the solutions to equations (5.10) with initial data (5.11), (5.14) and parameter values from Table 5.2 with $s_{e1_0} = s_{e2_0} = 0.5$ , $G = 2(1 + \sin(10t))$ , $H = 1 + \sin(10t)$ , $A = B = 1000$ . . . . .           | 146 |
| 5.20 | Cross section of the solutions depicted in Figure 5.19. . . . .  | 147 |
| 5.21 | 2d representation of the solutions to equations (5.10) with initial data (5.11), (5.14) and parameter values from Table 5.2 with $s_{e1_0} = s_{e2_0} = 0.5$ , $G = 2(1 + \sin(10t))$ , $H = 1 + \sin(10t)$ , $A = 1000$ and $B = 500$ . . . . . | 148 |
| 5.22 | Cross section of the solutions depicted in Figure 5.21. . . . .  | 149 |

|      |  |     |
|------|--|-----|
| 5.23 | 2d representation of the solutions to equations (5.10) with initial data (5.15) and parameter values from Table 5.2 with $s_{e1_0} = s_{e2_0} = 1$ , $G = H = 0$ , $A = 200$ and $B = 1000$ . . . . .          | 151 |
| 5.24 | Cross section of the solutions depicted in Figure 5.23. . . . .  | 152 |
| 5.25 | 2d representation of the solutions to equations (5.10) with initial data (5.15) and parameter values from Table 5.2 with $s_{e1_0} = 0.5$ , $s_{e2_0} = 1$ , $G = H = 0$ , $A = 200$ and $B = 1000$ . . . . .  | 153 |
| 5.26 | Cross section of the solutions depicted in Figure 5.25. . . . .  | 154 |
| 5.27 | 2d representation of the solutions to equations (5.16) with initial data (5.17) and parameter values from Table 5.2 with $s_{e_0} = 0.5$ , $A = 1000$ and $B = 300$ . . . . .                                  | 156 |
| 5.28 | Cross section of the solutions depicted in Figure 5.27. . . . .  | 157 |
| 5.29 | 2d representation of the solutions to equations (5.16) with initial data (5.17) and parameter values from Table 5.2 with $s_{e_0} = 1$ , $A = 1000$ and $B = 300$ . . . . .                                    | 158 |
| 5.30 | Cross section of the solutions depicted in Figure 5.29. . . . .  | 159 |
| 5.31 | 2d representation of the solutions to equations (5.16) with initial data (5.17) and (5.18) and parameter values from Table 5.2 with $\hat{s}_{e_0} = 1$ , $s_{e_0} = 0.5$ , $A = 1000$ and $B = 300$ . . . . . | 160 |
| 5.32 | Cross section of the solutions depicted in Figure 5.31. . . . .  | 161 |
| 6.1  | Experimental observations of fungal species <i>Clonostachys rosea</i> and <i>Trichoderma virens</i> by Fomina et al. (2003) . . . . .  | 166 |
| 6.2  | <i>T.virens</i> inoculating on a metal tile observed by (Fomina et al., 2003) . . . . .  | 167 |
| 6.3  | Numerical plot of equation (6.1) . . . . .   | 169 |
| 6.4  | Numerical solutions of equations (6.9) and (6.4) . . . . .   | 171 |
| 6.5  | Initial configuration used for the simulations. . . . .  | 174 |
| 6.6  | 2d representation of the solutions to equations (6.11) with initial data (6.12) and (6.14) using parameter values from Table 6.1 with $u_s = (0.5, 0)$ and $u_p = (0.5, 0)$ . . . . .                          | 177 |
| 6.7  | Cross section of the solutions depicted in Figure 6.6. . . . .   | 178 |
| 6.8  | 2d representation of the solutions to equations (6.11) with initial data (6.12) and (6.14) using parameter values from Table 6.1 with $u_S = (0.5, 0)$ and $u_P = (0.5, 0.1)$ . . . . .                        | 179 |
| 6.9  | Cross section of the solutions depicted in Figure 6.8. . . . .   | 180 |



|      |  |     |
|------|--|-----|
| 6.10 | 2d representation of the solutions to equations (6.11) with initial data (6.12) and (6.14) using parameter values from Table 6.1 i.e. $u_S = (0.5, 0)$ and $u_P = (0.5, 1)$ . . . . .                          | 181 |
| 6.11 | Cross section of the solutions depicted in Figure 6.10. . . . .  | 182 |
| 6.12 | 2d representation of the solutions to equations (6.11) with initial data (6.12) and (6.14) using parameter values from Table 6.1 with $u_S = (0.5, 0)$ and $u_P = (1, 1)$ . . . . .                            | 183 |
| 6.13 | Cross section of the solutions depicted in Figure 6.12. . . . .  | 184 |
| 6.14 | 2d representation of the solutions to equations (6.11) with initial data (6.12) and (6.14) using parameter values from Table 6.1 with $u_S = (2, 0)$ and $u_P = (0.5, 1)$ . . . . .                            | 185 |
| 6.15 | Cross section of the solutions depicted in Figure 6.14. . . . .  | 186 |
| 6.16 | Initial experimental configuration used in the simulations. . . . .  | 187 |
| 6.17 | 2d representation of the solutions to equations (6.11) with initial data (6.12), (6.14) and (6.15) using parameter values from Table 6.1 with $u_S = (0.5, 0)$ , $u_P = (1, 0)$ and $u_T = (1, 0)$ . . . . .   | 188 |
| 6.18 | Cross section of the solutions depicted in Figure 6.17. . . . .  | 189 |
| 6.19 | 2d representation of the solutions to equations (6.11) with initial data (6.12), (6.14) and (6.15) using parameter values from Table 6.1 with $u_S = (0.5, 0)$ , $u_P = (1, 0.1)$ and $u_T = (1, 0)$ . . . . . | 190 |
| 6.20 | Cross section of the solutions depicted in Figure 6.19. . . . .  | 191 |
| 6.21 | 2d representation of the solutions to equations (6.11) with initial data (6.12), (6.14) and (6.15) using parameter values from Table 6.1 with $u_S = (0.5, 0)$ , $u_P = (1, 1)$ and $u_T = (1, 0)$ . . . . .   | 192 |
| 6.22 | Cross section of the solutions depicted in Figure 6.21. . . . .  | 193 |
| 6.23 | 2d representation of the solutions to equations (6.11) with initial data (6.12), (6.14) and (6.15) using parameter values from Table 6.1 with $u_S = (0.5, 0)$ , $u_P = (0.1, 1)$ and $u_T = (1, 0)$ . . . . . | 194 |
| 6.24 | Cross section of the solutions depicted in Figure 6.23. . . . .  | 195 |
| 6.25 | 2d representation of the solutions to equations (6.11) with initial data (6.12), (6.14) and (6.15) using parameter values from Table 6.1 with $u_S = (2, 0)$ , $u_P = (0.1, 1)$ and $u_T = (1, 0)$ . . . . .   | 196 |
| 6.26 | Cross section of the solutions depicted in Figure 6.25. . . . .  | 197 |
| 6.27 | Initial experimental configuration depicting a toxic strip domain. . . . .   | 199 |

|      |   |     |
|------|---|-----|
| 6.28 | 2d representation of the solutions to equations (6.11) with initial data (6.12), (6.14) and (6.15) using parameter values from Table 6.1 with $u_S = (1, 0)$ , $u_P = (1, 1)$ and $u_T = (1, 0)$ . . . . .                    | 200 |
| 6.29 | Cross section of the solutions depicted in Figure 6.28. . . . .   | 201 |
| 6.30 | 2d representation of the solutions to equations (6.11) with initial data (6.12), (6.14) and (6.15) using parameter values from Table 6.1 with $u_S = (0.5, 0)$ , $u_P = (1, 1)$ and $u_T = (1, 0)$ . . . . .                  | 202 |
| 6.31 | Cross section of the solutions depicted in Figure 6.30. . . . .   | 203 |
| 6.32 | 2d representation of the solutions to equations (6.11) with initial data (6.12), (6.14) and (6.15) using parameter values from Table 6.1 with $u_S = (0.5, 0)$ , $u_P = (0.1, 1)$ and $u_T = (1, 0)$ . . . . .                | 204 |
| 6.33 | Cross section of the solutions depicted in Figure 6.32. . . . .   | 205 |
| 6.34 | Schematic representation depicting the formation of cluster of nutrients on a toxic strip domain. . . . .   | 206 |
| 6.35 | 2d representation of the solutions to equations (6.11) with initial data (6.12), (6.14), (6.15) and (6.16) using parameter values from Table 6.1 with $u_S = (0.5, 0)$ , $u_P = (0.1, 1)$ , $u_T = (2, 0)$ and $u_H = (1, 0)$ | 207 |
| 6.36 | 2d representation of the solutions in Figure 6.35 at longer times .   | 208 |
| 7.1  | Experimental observation by Bertrand et al. (2010) on the production of siderophores . . . . .  | 213 |
| 7.2  | Experimental observation by Srivastava et al. (2013) on the production of siderophores . . . . .  | 214 |
| 7.3  | Experimental observation by Indiragandhi et al. (2008) on the production of siderophores determined via colour change . . . . .   | 214 |
| 7.4  | Initial configuration used for the simulations. . . . .   | 218 |
| 7.5  | 2d representation of the solutions to equations (7.1) with initial data (7.3) and parameter values from Table 7.1 . . . . .   | 220 |
| 7.6  | The distribution of iron and siderophores of equations (7.1) solved with initial data (7.3) and parameter values from Table 7.1 . . . .   | 221 |
| 7.7  | 2d representation of the solutions to equations (7.1) with initial data (7.3) and parameter values from Table 7.1 with $s_{e0} = 0.1$ . .   | 223 |
| 7.8  | The distribution of iron and siderophores under the influence of nutrient depleted substrate. . . . .   | 224 |
| 7.9  | 2d representation of the solutions to equations (7.1) with initial data (7.3) and parameter values from Table 7.1 with $s_{e0} = 1$ . . .   | 225 |

|      |   |     |
|------|---|-----|
| 7.10 | The distribution of iron and siderophores under the influence of nutrient-rich substrate. . . . .   | 226 |
| 7.11 | 2d representation of the solutions to equations (7.1) with initial data (7.3), (7.4) and parameter values from Table 7.1 with $\hat{s}_{e0} = 1$ and $s_{e0} = 0.1$ . . . . .   | 227 |
| 7.12 | The distribution of iron and siderophores under the influence of varying substrate. . . . .   | 228 |
| 7.13 | The distribution of iron and siderophores with high initial internal substrate in a low nutrient environment. . . . .   | 229 |
| 7.14 | Equations (7.1) is solved with with initial data (7.3), (7.4) and parameter values from Table 7.1 with $I_0 = 1$ . . . . .  | 230 |
| 7.15 | Equations (7.1) are solved with initial data (7.3), (7.4) and parameter values from Table 7.1 with $I(x, y, 0) = 1$ . . . . .   | 231 |
| 7.16 | A cross section representation of iron $I$ (right hand side of each plot) and siderophores $C$ (left hand side of each plot) . . . . .  | 232 |
| 7.17 | Equations (7.1) are solved with initial data (7.3) and parameter values from Table 7.1 . . . . .  | 234 |
| 8.1  | A schematic drawing of the profiles of $C$ (blue, initially taking the value of zero everywhere except at $x = 0$ ) and $I$ (red, initially taking the value $I_0 > 0$ everywhere except at $x = 0$ ) at time $t = 0$ . . . . . | 237 |
| 8.2  | A schematic summary of the 3 cases for small time asymptotic solutions with $\bar{\beta}$ obtained from equation (8.14). . . . .  | 241 |
| 8.3  | Schematic drawing of the siderophore $C$ (blue) and iron $I$ (red) profiles around $\eta = \bar{\alpha}$ . . . . .  | 243 |
| 8.4  | A schematic summary of all cases when large time asymptotic solutions for $\bar{\alpha}$ obtained from equation (8.22) are valid. . . . .   | 251 |
| 8.5  | Plot of siderophore and iron concentration with 3 terms generated with LDM. . . . .   | 253 |
| 8.6  | Solutions of equations (8.58) and (8.72) from equations (8.70) and (8.89) using parameter values $k = 0.1$ , $D_c = 0.13$ , $D_v = 0.1$ , $L = 1$ . . . . .   | 264 |
| 8.7  | Solutions of equations (8.58) and (8.72) from equations (8.70) and (8.113) using parameter values $k = 0.1$ , $D = 1$ , $L = 1$ . . . . .   | 269 |

# List of Tables

|     |   |     |
|-----|---|-----|
| 2.1 | Description and notations of possible combinations of fungal branching and anastomosis. . . . .                                   | 20  |
| 3.1 | The position of the leading edge of hyphae for YWD phenotype and the truncated LDM series with the first 5, 10 and 50 terms. .    | 55  |
| 3.2 | The position of the leading edge for tips for the YWD phenotype and the truncated LDM series with the first 5, 10 and 50 terms. . | 55  |
| 3.3 | The position of the leading edge of hyphae for FHD phenotype and the truncated LDM series with first 5, 10 and 50 terms . . . . . | 56  |
| 3.4 | The position of the leading edge for tips for the FHD phenotype and the truncated LDM series with the first 5, 10 and 50 terms .  | 56  |
| 3.5 | Initial velocity and acceleration of the leading edge for the tip density of YWD phenotype . . . . .                              | 62  |
| 3.6 | Initial velocity and acceleration of the leading edge for the hyphal density of YWD phenotype . . . . .                           | 63  |
| 3.7 | Initial velocity and acceleration of the leading edge for the tip of FHD phenotype . . . . .                                      | 65  |
| 3.8 | Initial velocity and acceleration of the leading edge for the hyphal density of FHD phenotype . . . . .                           | 66  |
| 4.1 | Travelling wave solutions of equations (4.11) for small $\psi$ . . . . .  | 100 |
| 5.1 | The initial data and default parameter values used to solve model equations (5.4) . . . . .                                       | 124 |
| 5.2 | The initial data and default parameter values used to solve model equations (5.10) . . . . .                                      | 129 |
| 6.1 | The initial data and default parameter values used to solve model equations (6.11) . . . . .                                      | 175 |

|     |  |     |
|-----|--|-----|
| 7.1 | The initial data and parameter values used to solve model equations (7.1) . . . . .  | 219 |
| 8.1 | Small time asymptotic solution for $\bar{\alpha}$ , numerically solved for various parameter values and compared to analytical approximations. . . | 242 |
| 8.2 | Large time asymptotic solution for $\bar{\alpha}$ , numerically solved for varying parameter values. . . . .                                       | 251 |
| 8.3 | The initial velocity and acceleration of the leading edge for the siderophore concentration profile obtained analytically. . . . .                 | 254 |
| 8.4 | The initial velocity and acceleration of the leading edge for the iron concentration obtained analytically. . . . .                                | 255 |

# Chapter 1

## Introduction

### 1.1 Biology and uses of fungi

Until relatively recently, it was widely believed that fungi were part of the plant kingdom but this changed when ecologist Robert Whittaker separated fungi into their own respective kingdom (Myceteae) (Whittaker, 1959, 1969; Whittaker and Margulis, 1978; Hagen, 2012). Fungi are made of Eukaryote cells, which mean they are more closely related to animals than plants and hence their study is in fact more applicable to humans than to bacteria (Prokaryotes). It is estimated that there are between 700000 and 5.1 million species of fungi in the world (O'Brien et al., 2005; Taylor et al., 2010; Blackwell, 2011).

Fungi are widespread throughout the terrestrial and built environments and affect our everyday lives ranging from the food we consume to industrially important products to plant pathogens to human diseases. Hence the better we understand fungal biology, the more we will be able to control or exploit them for our own purposes. Fungi are tremendously important to human society. Many foods we consume are produced under the influence of fungi, e.g. bread, beer, blue cheese, soy sauce. The species of fungi that make citric acid used in fizzy drinks is of the *Aspergillus* species (see Efiuvweuwere and Chynyere, 2001; Flores-Maltos et al., 2011). Yeasts are also a species belonging to the kingdom of fungi (although their colonies often resemble that of bacteria, Váchová et al., 2012). Yeasts have been used for baking and brewing for many centuries. Fungi are also used as a meat substitute in branded products like 'Quorn' as Mycoprotein, (Peberdy, 1994). Indeed some studies have shown that a specific type of mushroom (*Boletus edulis*) even exceeds meat in protein content (Manjunathan et al., 2011). The

uses of fungi are not restricted to food production, but are also involved in plant life, medicine, science and industry to mention a few.

In the plant kingdom, many studies (e.g. Smith and Read, 1997; Selosse et al., 2006) have found that over 90% of plants in the terrestrial environment have a symbiotic connection with some species of fungi attached to their roots called *Mycorrhizae*, which help to uptake essential minerals from nutrient poor soils. This is due to the flexibility of fungi having the ability to scour greater distances to a nutrient source than the roots of the plant are able to achieve on their own (see Figure 1.1(a)).



(a) *Mycorrhiza* is the association between fungi and the roots of higher plants. Between 86% and 94% of plants are *mycorrhizal* (Brundrett, 2009; Asio, 2010).



(b) A culture of Royal Sun Blazei (*Agaricus brasiliensis*) growing on a Petri dish (Stamets, 2010).

**Figure 1.1:** *Examples of fungal networks.*

In the industrial sector many companies (e.g. Ecovative) are using fungi to create biodegradable structural products including building materials and packing materials (Bayer and McIntyre, 2011). A material being used recently in industry as an alternative to traditional petroleum polymer foam is called Mycobond, which is heat resistant, fire resistant and also biodegradable and is created out of the natural growth of the vegetative structure of fungal mycelium (Bayer and McIntyre, 2014). Fungal enzymes (*Trichoderma* species) are used to soften denim

jeans on large scales in industry (Carlile et al., 2001).

Mycoremediation is another use of fungi on an industrial scale to remove toxins from polluted landscapes (Sang et al., 2004; Gadd, 2010; Ramachandran and Gnanados, 2013; Gupta and Shrivastava, 2014, and references therein). It is an environmental and economical alternative to extracting, transporting and storing toxic waste. In agriculture huge losses occur due to various pathogenic species of fungi such as *Rhizoctonia*, *Sclerotinia*, *Phytophthora* and *Fusarium* (Lucca, 2007; Koutb and Ali, 2010). *Rhizoctonia* (root killer) is the causal agent of violet root rot of carrots, cucumber, sheath blight of rice, black scurf of potatoes and other vegetables (Chyu et al., 1996). Strains of *Sclerotinia* plant fungi are responsible for completely invading a plant host and having an adverse affect on carnation flowers and economically important crops including soybean, sunflower, lettuce, spinach, tomato, cabbage, pepper and sweet potatoes (Saharan and Mehta, 2008). *Phytophthora* fungus pathogen causes extensive damage and mortality to a wide range of trees and plants, e.g. oak trees (Brasier, 1996; Marçais et al., 2011). *Fusarium* produce mycotoxin in cereal crops that can affect human and animal health if they enter the food chain (Czembor et al., 2015). Some species of *Fusarium* affect plants e.g. barley, while others pervade humans directly when the immune system is weak (Olsen et al., 2011; Antonissen et al., 2014). The most widely used method for attempting to deal with these problems is via the use of chemicals (fungicides). This method is not particularly efficient as the fungicides need to be upgraded periodically due to fungi developing ways to become immune to the chemicals (Hobbelen et al., 2014). Although pathogenic fungi maybe controlled using fungicides, the chemicals used leave residues within the harvested crops which can be harmful for human/animal consumption (Shepherd, 2008; Wu and Khlangwiset, 2010; Zain, 2011). Thus an alternative biological control is sought (Sanzani et al., 2016). Several studies indicate the use of fungal species as promising, extremely effective and successful bio-control agents used against diseases of agronomic and vegetable crops caused by pathogenic fungi (Dorner et al., 2003; Cotty et al., 2007; Koutb and Ali, 2010; Mehl and Cotty, 2013; Vankudoth et al., 2016).

Common agents used in biological terrorism are bacterial, viral and fungal pathogens and toxins from living organisms. Indeed fungal strains such as *Fusarium*, *Aspergillus*, *Myrothecium*, *Trichoderma*, *Trichothecium*, *Cephalosporium*, *Verticimonosporium*, *Stachybotrys* and other filamentous fungi have had more



devastating effects on human populations than that of fission nuclear weapons (Dudley and Woodford, 2002; Bennett and Klich, 2003).

In medicine, the positive influence of fungi have been extraordinarily powerful and have provided advances that have revolutionised human health. Antibiotics such as *Penicillin* and *Cephalosporin* are produced by fungi. The immunosuppressive anti-rejection transplant drug Cyclosporin is produced by the fungus *Tolypocladium inflatum* (Bushley et al., 2013). Steroids, hormone and birth control pills are commercially produced by various fungi. In recent developments in medicine, particular species of fungi (*Trametes Versicolor*) have even been successfully used to treat patients with breast cancer and prostate cancer (Luk et al., 2011; Torkelson et al., 2012).

As fungi contribute to many attributes of our lives, it is important to pursue a greater understanding of its species in a scientifically sound manner. We can observe that some species of fungi span several kilometres but initial scale of growth are measured in microns (Boswell and Davidson, 2012). Most fungal research carried out in laboratories are of the order of a few centimetres as it is not always feasible to grow fungi on large acres of land for scientific purposes. Hence mathematical modelling provides a powerful augmentative tool for a number of reasons. Firstly, it provides the ability to carry out the research by naturally linking the different growth scales. Secondly, modelling is able to create quantitative predictions by focussing attention on key processes involved in growth. Also a mathematical model is able to quantify certain growth parameters, which is crucial to optimising strategies when fungi are used in industrial or biotechnological environments.

Furthermore, in addition to their direct use and application, fungi provide a good experimental system in which to study the control of shapes and growth rates of tissue. Due to their various species and forms, they can be easily cultured in a laboratory setting. This provides the opportunity to investigate variations of their colonies by varying the conditions of growth. This is usually undertaken by placing a small fungal colony on a nutrient-based medium Petri dish (see Figure 1.1(b)). Within a short period of time the fungi can be observed to develop into a radially expanding colony. After an initial transient phase, the expansion of a fungal colony usually takes place at a constant rate depending on the characteristics of its species and environment (Boswell et al., 2002).

An ideal approach is to construct a model of a fungal species and interpret

it using the laws of mathematics. As fungi are living organisms and due to their high complexity, it is conceivable that fungi can be described and understood in a comprehensive manner similar to that of a systems biology approach. It will not be feasible to explore every single variable. Thus, an appropriate model has to be devised carefully starting from a minimal model capturing the essential features of a fungal species and then try to incorporate additional features into the model to obtain realism in the outcome.

### 1.1.1 Fungal morphology and fungal interactions

Fungi consist of long branched filaments called *hyphae*. Hyphae only grow in their apical portion (tips) and thus hyphal tips possess the unique capability of continuously generating new growth (Edelstein, 1982; Jackson and Heath, 1993; Gooday, 1995; Schmitz et al., 2006). If a spore of cultivated fungi is placed on a suitable nutrient agar medium, a hypha may germinate. Nutrients are absorbed from the agar medium which excites growth, nuclear division and hyphal branching that blossom into a circular colony, increasing in diameter at a uniform rate (see Figure 1.2). The hyphae of a growing colony form a thick mat-like floor termed the *mycelium*.

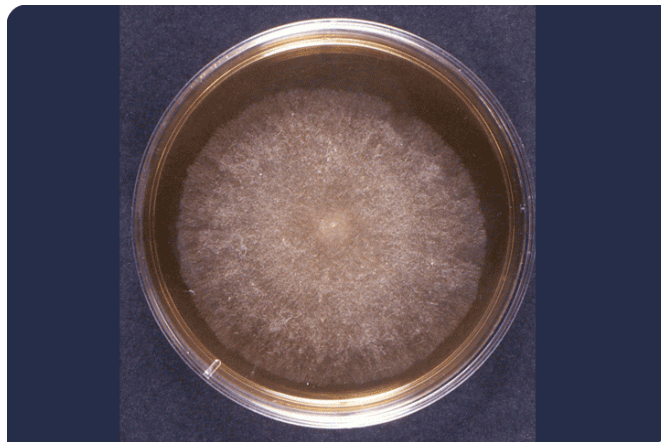


**Figure 1.2:** *Radial growth of fungi on a Petri dish (Online).*

Growth of a colony is achieved by a combination of two effects. A few leading hyphae proceed the colony in exploring uncolonised space. The branching of these hyphae produce secondary hyphae that fill the colonised space and give a characteristic shape to the colony interior.

There are many detailed accounts of the microscopic events that take place in a mycelium (Manteca et al., 2007). The two key processes that are deemed essential, at least for the current investigation, are branching and anastomosis.

*Branching* is the production of new growing tips, which can take place along the length of existing hyphae (lateral branching, Figure 1.3(a)). Branching could also take place by division of a single tip into two daughter tips (dichotomous branching, Figure 1.3(b)). Elongation and branching of hypha is the key mechanism in establishing a fungal mycelium. There are other types of branching (i.e. scorpioid and geniculate) that are observed in some species of fungi (e.g. *Monilinia laxa*) (Byrde and Willetts, 1977) but we will not be exploring these types in detail and instead focus on the more prevalent branching pattern, lateral branching (Harris, 2008). Nonetheless, the techniques developed in this thesis can easily be applied to these alternative morphologies. The branching of hyphae is highly effective in absorbing a substratum of nutrients. When a nutritionally rich location has been exhausted the fungus must reach other sources of nutrients to survive. Growth in areas lacking nutrients would quickly be terminated and inactive hyphae could be destroyed by insect attacks, autocatalytic behaviour or lysis by other microorganisms (Falconer et al., 2008, 2015).

Much research has been carried out where a single strand of hypha has been inspected microscopically (Carlile et al., 2001; Steinberg, 2007). It has been determined that the splitting of a single hypha is due to the accumulation of vesicles clustering in particular regions of the hyphal apex which lead to the birth of new branches. The *Spitzenkörper* is a region of the tip where the vesicles accumulate (Brunswik, 1924) and is an important feature for hyphal growth (Bartnicki-Garcia et al., 1995; Steinberg, 2007) since its position in the growing hyphae determines the direction of growth (Girbardt, 1969; Reynaga-Pena et al., 1997; Steinberg, 2007).

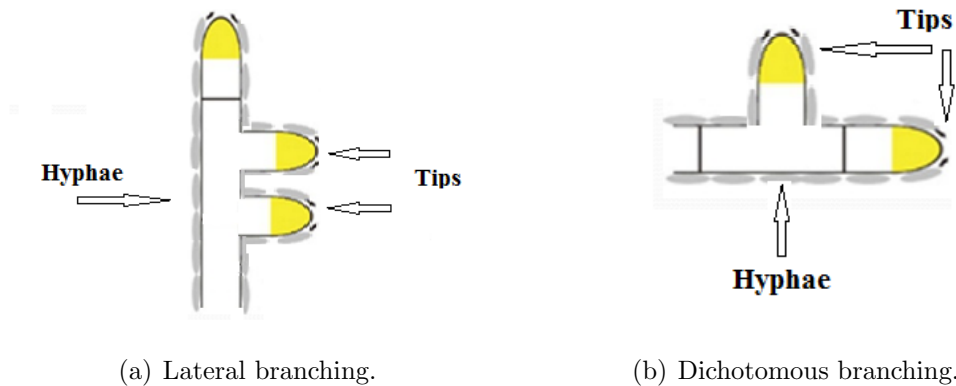


**Figure 1.3:** *Types of branching.*

*Anastomosis* is the reconnection of a hypha via its tip with a neighbouring hypha to form a complex interconnected network. It was found in a study by Buller (1931) that in the interior of a colony each hypha often produce side branches that grow towards each other and merge with hyphae to form closed networks. Such networks can facilitate the transportation of nutrients to any point in a mycelium and facilitate the growth of large fruiting bodies. An example is the common edible mushroom which is a fruiting body of the species *Agaricus bisporus*. Although the fruiting body is a unique feature of the cultivated mushroom, it is completely dependent on its mycelium for the absorption of nutrients. Examples of anastomosis are shown in Figure 1.4 and an in depth review of the anastomosis process can be found in the work of Providencia et al. (2005).

In their natural settings, fungi grow in environments where resources are heterogeneous. In such settings a fungal mycelium uptakes nutrients from its source and forms hyphal tubes around its colony margins. These hyphal tubes are called leading hyphae that propagate by elongation in search of new nutrient sources. As the existing nutrient source starts to deplete, the hyphae in the interior of the colony start to fuse with neighbouring hyphae to form closed networks and transport the nutrients efficiently to its leading hyphae via a process called *translocation*. Once the nutrient source reaches a critical level, cell walls and internal substrate of old hyphae in the colony interior are degraded and exported to new sites of growth where they are recycled. We do not intend to model recycling specifically and instead classify hyphae into two types depending on

whether they are actually involved in growth or not (see Falconer et al., 2005, 2010, for models including recycling, also known as autocatalytic behaviour).

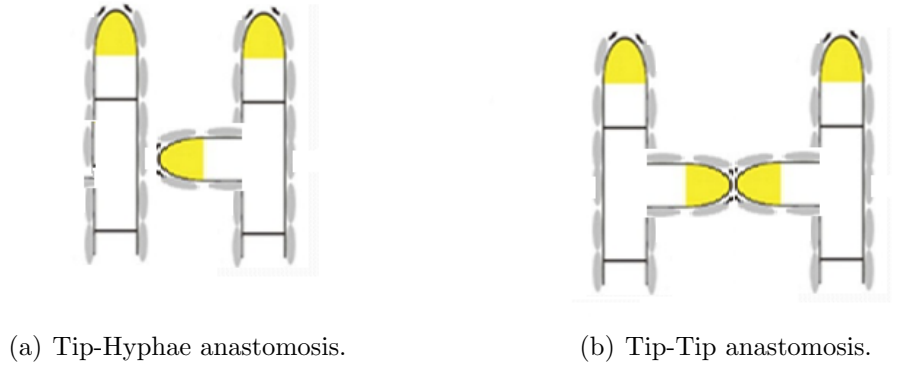


**Figure 1.4:** *Types of fusion.*

We will discuss a number of key existing fungal models found in the literature in the following section.

## 1.2 Historical modelling approaches

Over the last few decades, an enormous amount of research has been carried out in the field of mycology, in an attempt to understand the profuse complexities involved in fungal growth, mobility and interactions. Considerable attention has been devoted towards formulating concise mathematical models to try and identify parameters that capture the essence of organisms, without over simplification or unnecessary complication. One of the key issues faced by researchers modelling fungi is determining the correct choice of scale. This is in essence determined by the objective of the researcher.

Fungal models explored in this work fall into either the intermediate or “single colony” level. Models of the latter nature are typically continuous, discrete or both (i.e. hybrid). Each approach has their advantages and disadvantages as is now described.

There are numerous mathematical models that describe fungal function and morphology using a continuum approach. In a series of papers, Edelstein-Keshet (Edelstein, 1982; Edelstein and Segel, 1983) developed a simple pair of

hyperbolic partial differential equations modelling the motion of hyphal tips and subsequent creation of hyphae, initially in a single spatial dimension, and later in a two-dimensional setting (Edelstein and Ermentrout, 1989). Due to their simplistic nature, a variety of branching and anastomosis types were considered and through phase-plane analysis, a number of travelling wave solutions were shown to exist with some displaying morphology observed in laboratory settings, for example, the formation of striations along a colony radius. However, while these models captured the simple dynamics of an expanding mycelium, they do not relate this expansion to the nutrients essential for growth and hence the models are incapable of simulating biomass growth in heterogeneous environments.

Davidson and co-authors (e.g. Davidson, 1998) expanded Edelstein-Keshet’s models by using a set of reaction-diffusion equations. Unlike Edelstein-Keshet’s approach, these models incorporated an explicit nutrient responsible for biomass expansion and the movement of this nutrient, i.e. translocation, was explicitly included. Numerical simulations of the model equations were in good qualitative agreement with associated experimental configurations.

There is a major limitation with the use of reaction-diffusion equations, namely they allow the hyphal arrangements to diffuse whereas in practice they are static structures. While Davidson argued that biomass diffusion could represent the recycling of old hyphae, Boswell et al. (2002, 2003a) adopted an approach that combined the simplistic elegance of Edelstein-Keshet’s models with the explicit nutrient status outlined in Davidson’s approach. Boswell’s model were thus of mixed hyperbolic-parabolic type and were calibrated for the fungus *Rhizoctonia solani*. Due to the complexity of the model equations, bespoke integration routines were developed to obtain numerical solutions and these were shown to be in excellent qualitative and quantitative agreement with experimental data (Boswell et al., 2002). Falconer et al. (2005, 2008) expanded on Davidson’s models by including an explicit recycling component whereby biomass was reabsorbed into the model fungus, moved and used to generate further growth. While the resultant equations were far easier to work with than those of Boswell, their calibration was complicated because of the explicit diffusion of hyphal structures used in such models.

Cohen (1967) laid the foundation for discrete models by demonstrating how it was possible to generate realistic fungal structures with minimal growth parameters namely, extension and branching. The model was restricted to growth

only occurring at the apex of each branch, while branching occurred solely behind the growing tips. The fundamental disadvantage of Cohen’s model and with discrete approaches in general, is that only small networks are computationally efficient. That may suffice in modelling basic dynamics of a fungal growth on a microscopic level, but not containing enough complexity to develop a pattern of a realistic mycelium. Although Cohen did not aim to exclusively model fungal mycelia, his work inspired the work of Meskauskas et al. (2004a,b) that did.

Meskauskas et al. (2004a) proposed a discrete three-dimensional vector based model, termed a Neighbour-Sensing model, that investigated several forms of autotrophic behaviour in fungal networks. The paper discussed the vast quantity of structural forms that can be achieved by varying parameters such as fruiting-body like structures as well as the typical filamentous networks. However, despite the striking resemblance of actual fungal mycelium topology obtained using a discrete modelling approach, the model undoubtedly had severe limitations. For example focus of the model was primarily on rules designed to produce the desired outputs and little emphasis is on actual biological validation. Furthermore, the model was not sufficiently flexible to consider the fundamental biological phenomenon of anastomosis, which was a consequence of the three-dimensional approach employed and thus the model produced formations that were similar to tree structures rather than mycelial networks. Finally, the model also suffered the same restriction as with Cohen’s and in general most discrete models, i.e. large time simulations require significant computational resources.

By focussing on the advantages of the continuum and discrete modelling approaches various authors have proposed hybrid models (e.g. Yang et al., 1992; Boswell et al., 2007; Hopkins and Boswell, 2012). Yang et al. (1992) proposed a model that generated an explicit network representing the growth of filamentous fungi. The model divided the process of modelling into two stages; a deterministic approach was adopted to model biological and morphological development and a stochastic approach for factors that appear random like the direction of tip extension. Statistical data collected via quantitative analysis of genuine mycelial networks showed that branching and tip growth angles were normally distributed. Emphasis was on the identification that biological interpretations and a stochastic influence are both necessities to capture the true character of a developing fungal colony. Boswell et al. (2007) developed a hybrid model consisting of a Cellular automata approach to model filamentous fungi. The model allowed for the key

hyphal interactions of branching and anastomosis that could be simulated over heterogeneous environments. The model comprised the inclusion of uptake and active translocation, traditionally overlooked in discrete models, to be thoroughly investigated.

Hopkins and Boswell (2012) devised a model similar to Boswell et al. (2007) in that a generic substrate was assumed to exist in two forms: free in the external environment where it could diffuse and contained within the biomass network where it was translocated and used to fuel tip extension. An important feature of the model was the manner in which the orientation of hyphae were modelled. Previously, model tips were typically assumed to change direction according to a random variable drawn from a normal distribution (Yang et al., 1992). Therefore, restricting the predictive aspects of the reorientation of the tips to statistical properties obtained from experimental data limiting to situations resembling the calibration experiment. Hopkins and Boswell (2012) utilised a biased circular random walk to model tip orientation and related this to the corresponding Fokker-Planck partial differential equation, which described statistical properties of the random walk.

It is important to note that the hybrid models proposed by Boswell et al. (2007); Boswell (2008) are lattice-based. A Lattice-based random walk model typically represent the spatial domain as a one, two or three dimensional regular lattice. Computationally, the evolution of the system can be represented by a discrete time-stepping mechanism, in which, during each time step of duration  $t$ , each agent has problem-specific probabilities of moving and of proliferating (Plank and Sleeman, 2004). Therefore, non-interacting models are relevant only for problems where the density is so low that hypha to hypha contacts and crowding effects are unimportant (i.e. a discrete model requirement). Lattice-based models have achieved more in relating discrete processes to the mechanistic elements in a system but are hindered by their dependence on predefined geometry, for example limiting the angles at which hyphae extend and branch. Although the simplification allows the generation of a larger network, it places a bound on the accuracy of the processes of hyphal interactions within the model mycelium and could potentially impact on the quantitative and qualitative predictions of both fungal growth and function made by such models (Hopkins, 2011).

On the other hand, lattice-free random walk models represent motility and proliferation on a continuous domain (Hillen and Othmer, 2000) and are



more realistic than lattice-based models (Boswell and Carver, 2008; Hopkins and Boswell, 2012; Plank and Simpson, 2012). Lattice-free models allow the direction of movement to be a continuous variable, rather than restricting to a discrete set of directions corresponding to nearest neighbour lattice sites. A variety of lattice-free approaches have been developed over the last couple of decades, each offering differing degrees of flexibility and applicability (Boswell and Davidson, 2012). Almost all such models have relied on a mixture of deterministic and stochastic elements. The complexity and computational costs associated with such models often force compromises resulting in important biological features to be simplified or even omitted. The challenge is to find a meaningful balance between biological function and mathematical computability.

In a broad sense, discrete models are advantageous when explicit details of a development of a filamentous fungal structure is sought (e.g. growth of individual hyphae or vesicle influence on tip elongation Balmant et al., 2015). Simulations produced by discrete models can also provide accurate representation when compared to an actual fungal colony. The major disadvantage of discrete modelling is the intricate detail required to form an appropriate model which is computationally very expensive to simulate and the model is often limited to a single colony. Another major drawback of most discrete models is the lack of anastomosis which is sometimes even completely ignored due to computational difficulties. Anastomosis is a fundamental process responsible for hyphal growth, thus models without this process will not yield accurate representations of a fungal colony.

A hybrid approach consists of combining the discrete and continuum approach to form a model and is often very useful when using a lattice-free approach but a major limitation is the requirement of a predefined geometry in lattice based approaches. A large amount of data has to be recorded and processed which is problematic for large time based analysis due to the number of parameters growing exponentially (Hopkins, 2011).

A continuum approach generally prevails when attempting to capture the true biological functions of a moderately sized fungal mycelium. Complex structures of a fungal network are often simplified into biomass densities which allow for computational efficiency and simulations of large colonies. Although a continuum approach can simplify a complex fungal structure, exploring biological features such as translocation and uptake of nutrients can quickly over complicate the

formulation of a single colony model (Boswell et al., 2002; Falconer et al., 2005) and thus giving rise to difficulty in identifying key parameters or analysis of an investigation. Nevertheless, with the advancement of technology, powerful software are readily available to numerically integrate the model equations. Therefore a continuum approach, in the author's view, is the most appropriate choice for modelling fungal behaviour of the kind interested in this thesis, particularly since attention will be on the interactions between multiple fungal species.

Despite the plethora of laboratory based experimental studies involving fungal interactions, there are still only a hand-full of mathematical models that possess the capability to simulate such behaviours. Davidson et al. (1996) represented a fungal mycelium and its nutrients as activators and substrates and demonstrated that spatially heterogeneous structures could be formed through the collision of two fungal biomasses; however the abstract nature of the model meant it was unable to make qualitative predictions and was difficult to differentiate between the rival biomasses. Falconer et al. (2011) formed a system of partial differential equations accounting for the interactions between rival model fungal phenotypes in response to inhibitors. Through the creation of demarcation zones, this modelling showed that such inhibitors resulted in greater fungal biodiversity. More recently, Boswell (2012) investigated pairwise competition by using an alternative continuum model whose structure and formation allowed for its calibration and it was shown that nutrient availability influenced the outcome of competition. However, due to the complexity of the underlying partial differential equations, only numerical solutions could be obtained and consequently the predictive power of the model was limited and general principles could not be extracted. In particular, repeated numerical solutions provided the only mechanism to determine critical nutrient levels to alter the outcome of competition.

Our focus will essentially be on modelling fungal interactions utilising mathematical modelling techniques to formulate and provide solutions to complex systems of partial differential equations that portray typical behaviour such as biomass competing with other biomasses and biomass reacting to toxic compounds.

## 1.3 Summary

The above discussion provided clear motivation for studying fungi. The versatile nature of fungi having so much impact on our everyday lives cannot be ignored. Thus the need for a better understanding of fungi is crucial for the betterment of human well-being, survival, protection and much more. Mathematical modelling is a great tool to enhance our understanding of fungi. Many historical models have been proposed in the field of fungal studies ranging from continuous, discrete and hybrid models. A continuum modelling approach will be pursued in this body of work.

In Chapter 2 we explore the work of Edelstein-Keshet, who developed the pioneering model of fungal growth (Edelstein, 1982). Edelstein-Keshet's models will be investigated using a combination of numerical integration and algebraic techniques, including phase plane analysis. In particular, we also construct new solutions for the system of equations proposed by Edelstein-Keshet, modelling specific fungal phenotypes (i.e. specific branching and anastomosis morphologies).

In Chapter 3, we introduce a decomposition method (Laplace Decomposition Method (LDM)) and use it to validate novel solutions obtained in Chapter 2. Thereafter we use LDM to produce semi-analytical solutions for a coupled system of PDEs that hitherto have required the use of numerical methods. We exploit the technique further and propose a novel method that can predict the initial kinematics of an expanding fungal colony.

In Chapter 4, we extend the system of equations from Chapter 2 to model intra-species competition with limiting resources. A mathematical model is constructed to represent competition between two fungal colonies that have access to different resources. It is shown that the model equations display a multitude of travelling wave solutions and that the outcome of competition between two fungal biomasses can be controlled through the simple manipulation of the nutrient resources available to each species. The model equations are also numerically integrated to illustrate the range of outcomes arising from fungal competition and these results are placed in context of established experimental observations.

In Chapter 5 we extend the work from Chapter 4 to a more robust and realistic model comprising a mixed hyperbolic-parabolic system of partial differential equations to represent competing species in two dimensions (depicting experiments involving a Petri dish). The model is used to simulate various experimental studies and predictions are made on the outcome of specific nutrient

limited competition.

In Chapter 6 a two-dimensional model is formulated to investigate the influence of nutrient manipulation on fungi in a toxic domain. The primary inspiration for this work is based around the experimental work of Fomina et al. (2000, 2003). The model successfully captures the primary findings of Fomina et al. (2003) and provides further possible explanations for some previously unexplainable phenomenon observed in experimental studies.

In Chapter 7 we present a comprehensive continuous model involving siderophores. Siderophores are released by fungi to search for iron, which is a critical mineral required for fungal survival. We present a two-dimensional mathematical model that captures experimental observations seen in a laboratory setting and provides additional insight to potential causality for certain observations arising in experiments.

In Chapter 8 we investigate a reduced one-dimensional model involving siderophores and construct algebraic solutions on their spatial and temporal distributions.

Finally, in Chapter 9, a discussion on the main results of the thesis is presented and potential avenues for future work are stated.

## Chapter 2

# The Basis for Mathematical Modelling of Filamentous Fungi

### 2.1 Mathematical modelling fundamentals

For the purpose of constructing a mathematical model capturing the essential features of fungal growth, we will regard a mycelium and its constituents as continuous entities. Thus, rather than accounting for individual hypha, the average properties, such as distribution of hyphal densities, are described. Since hyphal length increment occurs only in the presence of a moving tip, the locations, density and flux of tips must be of significance in determining where growth takes place. Hence mycelial interactions can be summed up briefly as follows:

- Tip movement creates new hyphal filaments.
- Tips and hyphae can branch and create more tips or tips can vanish through anastomosis.
- Tips can cease to be active (i.e. ‘die’). Also, established hyphae can degrade.

### 2.2 Edelstein’s modelling approach

Edelstein-Keshet was the first to construct a continuous model of hyphal interactions in dense hyphal mycelia (Edelstein, 1982). Her approach was inspired by the work of Cohen (1967) where he identified the density of mycelium with respect to space as a key feature in fungal growth.

The work carried out by Edelstein (1982) will be revisited in this chapter as it lays the foundation of the work which follows in the forthcoming chapters of the thesis. Here we also present new solutions to her model equations.

It will initially be assumed that the mycelium grows over a continuously replenished nutrient supply so that all cellular events take place at maximal rates, which depend on the environmental conditions and fungal species. The following model is a one-dimensional model, representing growth along a radius of the colony, in line with the radially symmetric behaviour observed in experiments (Ryan et al., 1943; Rotheray et al., 2008; Boddy et al., 2010).

Let  $\rho(x, t)$  denote the hyphal density in units of filament length per unit area (measured in cm of hyphae  $\text{cm}^{-2}$ ) and  $n(x, t)$  denote the tip density number per unit area (number of tips  $\text{cm}^{-2}$ ). Note that this choice of units allows for the experimental testing of the model's predictions in a non-destructive manner; the length of hyphae or number of tips in a region of a mycelium can be easily obtained through the observation of enlarged images of a fungus. The radius of a fungal colony typically expands by the order of 1 cm per day and hence time is typically measured in days (e.g. Boswell et al., 2002). Since hyphae is fixed in space it can be regarded as the trail left behind a hyphal tip as it moves. Thus the rate at which hyphae are created is proportional to the number of tips present, with the constant of proportionality corresponding to the velocity of tips. Thus the model equations are

$$\frac{\partial \rho}{\partial t} = nv - d(\rho), \quad (2.1)$$

$$\frac{\partial n}{\partial t} = -\frac{\partial(nv)}{\partial x} + \sigma(n, \rho), \quad (2.2)$$

where  $v$  is the tip velocity (the rate of apex extension in length per unit time),  $\sigma(n, \rho)$  is the net creation of tips (the rate of tips created per unit area in time) and  $d(\rho)$  is the hyphal death rate (the rate of filament length loss per unit area in time). The quantity  $nv$  can be viewed as a tip flux and so corresponds to the rate of creation of new hyphae.

### 2.2.1 Formulation of $d(\rho)$ and $\sigma(n, \rho)$

The term  $d(\rho)$  represents the loss of hyphae, which may be a density-dependent process. However for simplicity it is assumed that autolysis of hyphae is modelled

as:

$$d(\rho) = \gamma\rho \quad (2.3)$$

where  $\gamma$  is the rate constant for hyphal loss per unit time.

Several forms can be used to represent the net creation of hyphal tips depending on the precise morphology of the fungus under study. *Dichotomous branching*, where a single hyphal tip splits in two (see Figure 1.3(b)), can be modelled via

$$\sigma = \alpha_1 n \quad (2.4)$$

where  $\alpha_1$  is the rate of splitting per unit time.

*Lateral branching* (or *Apical branching*), where a new branch emerges from a hyphal wall distant from a current tip (see Figure 1.3(a)), may be modelled by

$$\sigma = \alpha_2 \rho \quad (2.5)$$

where  $\alpha_2$  is the number of branches produced per unit hyphae length per unit time.

Tip elimination can also be incorporated into the process modelled by  $\sigma$  but with negative contributions. For simple tip death, which might result from atrophy of the apical compartment of hyphae (Edelstein, 1982; Al-Taie, 2011), the corresponding expression is

$$\sigma = -\alpha_3 n \quad (2.6)$$

where  $\alpha_3$  is the death rate (decay constant) of tips per unit time.

In interactions involving fusion (such as anastomosis, where a tip is eliminated at a potential site of extension) the encounter of two tips, or one tip and one of its neighbouring hyphae is required. The actual process of anastomosis is not well understood (Glass et al., 2000; Roca et al., 2003; Glass et al., 2004; Read et al., 2012) but appears to be governed by a combination of local and global conditions. For simplicity we will assume the fusion of a hyphal tip, with either another tip or a hyphae occurs at a rate proportional to the local density of either tips or hyphae respectively. Thus anastomosis can be modelled by

$$\sigma = -\beta_1 n^2 \quad (2.7)$$

or

$$\sigma = -\beta_2 n \rho \quad (2.8)$$

where  $\beta_1$  and  $\beta_2$  are the rate of fusion per *Tip-Tip* and *Tip-Hyphae* encounter respectively.

Other cellular interactions have also been hypothesised (Edelstein, 1982). For example, suppose an overcrowding of hyphae causes accumulation of (toxic) substances to growing tips. A term representing this could be

$$\sigma = -\beta_3\rho^2 \quad (2.9)$$

where  $\beta_3$  is the rate of *tip elimination* per unit time by the effect of neighbouring hyphae. The term is quadratic in  $\rho$  so that this term would dominate over *lateral branching* (2.5) for large hyphal densities.

Combining a single branching type with a single tip-degrading influence yields numerous distinct phenotypes of fungi. Of these, four apply somewhat more broadly to fungi in which true anastomosis is absent (Edelstein, 1982) and potential anastomosis is present. These are

$$\sigma = \rho(\alpha_2 - \beta_2 n), \quad (2.10)$$

$$\sigma = \rho(\alpha_2 - \beta_3 \rho), \quad (2.11)$$

$$\sigma = n(\alpha_1 - \beta_1 n), \quad (2.12)$$

$$\sigma = n(\alpha_1 - \beta_2 \rho). \quad (2.13)$$

These could be interpreted as density dependent branching rates that diminish as filament or tip crowding reach threshold levels. Above these thresholds, such terms predict negative branching or a cumulative effect tending to reduce the population of tips. Also tips formed in their places would be eliminated as they grow through a location in which  $\sigma$  is negative.

In theory, a combination of any number of the branching types could be expressed during phases of growth of a particular species of fungi. For ease of notation these will be abbreviated as indicated in Table 2.1, consistent with the notation of Edelstein (1982).



| Biological Type        | Mathematical Notation      | Symbol |
|------------------------|----------------------------|--------|
| Lateral Branching      | $\sigma = \alpha_2 \rho$   | F      |
| Dichotomous Branching  | $\sigma = \alpha_1 n$      | Y      |
| Tip-Hyphae Anastomosis | $\sigma = -\beta_2 n \rho$ | H      |
| Tip-Tip Anastomosis    | $\sigma = -\beta_1 n^2$    | W      |
| Tip Death              | $\sigma = -\alpha_3 n$     | T      |
| Tip Death Overcrowding | $\sigma = -\beta_3 \rho^2$ | X      |
| Hyphal Death           | $d = \gamma \rho$          | D      |

**Table 2.1:** *Description and notations of possible combinations of fungal branching and anastomosis.*

### 2.2.2 Non-dimensionalisation of model equations

Incorporating (2.3)-(2.9) into equations (2.1) and (2.2) yields

$$\frac{\partial \rho}{\partial t} = nv - \gamma \rho, \quad (2.14)$$

$$\frac{\partial n}{\partial t} = -\frac{\partial(nv)}{\partial x} + (\alpha_1 - \alpha_3)n + \alpha_2 \rho - \beta_1 n^2 - \beta_2 n \rho - \beta_3 \rho^2, \quad (2.15)$$

where the parameters have been previously described.

It is convenient to reformulate equations (2.14) and (2.15) in terms of dimensionless quantities. Hence introducing  $\tau$ ,  $\bar{x}$ ,  $\bar{\rho}$  and  $\bar{n}$ , which are to be determined, so that  $t^* = t/\tau$ ,  $x^* = x/\bar{x}$ ,  $\rho^* = \rho/\bar{\rho}$ ,  $n^* = n/\bar{n}$ , where  $t^*$ ,  $x^*$ ,  $\rho^*$  and  $n^*$  are now dimensionless variables. Therefore equation (2.14) is non-dimensionalised to

$$\frac{\partial \rho^*}{\partial t^*} = \left( \frac{\tau \bar{n} v}{\bar{\rho}} \right) n^* - (\gamma \tau) \rho^*. \quad (2.16)$$

Equation (2.15) is non-dimensionalised to

$$\begin{aligned} \frac{\partial n^*}{\partial t^*} = & - \left( \frac{\tau v}{\bar{x}} \right) \frac{\partial n^*}{\partial x^*} + (\alpha_1 - \alpha_3) \tau n^* + \left( \frac{\alpha_2 \tau \bar{\rho}}{\bar{n}} \right) \rho^* \\ & - (\beta_1 \bar{n} \tau) n^{*2} - (\beta_2 \tau \bar{\rho}) n^* \rho^* - \left( \frac{\beta_3 \tau \bar{\rho}^2}{\bar{n}} \right) \rho^{*2}. \end{aligned} \quad (2.17)$$

The form of the leading coefficients in equations (2.16) and (2.17), (which are retained for all fungal types since they represent the basic feature of tip growth) suggest the particular choices  $\bar{x} = \tau v$ ,  $\tau = \gamma^{-1}$  and  $\bar{\rho} = \bar{x} \bar{n}$ . After dropping stars

for convenience, (2.16) and (2.17) become,

$$\frac{\partial \rho}{\partial t} = n - \rho, \quad (2.18)$$

$$\frac{\partial n}{\partial t} = -\frac{\partial n}{\partial x} + (\alpha_1 - \alpha_3)\tau n + (\alpha_2\tau^2 v)\rho - \tau\bar{n} [\beta_1 n^2 + (\beta_2\tau v)n\rho + \beta_3(\tau v)^2\rho^2]. \quad (2.19)$$

Depending on the exact processes in the model fungus, (i.e. whether  $\alpha_1$ ,  $\alpha_2$ ,  $\alpha_3$ ,  $\beta_1$ ,  $\beta_2$  or  $\beta_3$  are non-zero) further simplification is possible by choosing  $\bar{n}$  suitably.

## 2.3 Specific phenotype of fungi

To illustrate the basic behaviour of the non-dimensional model equations (2.18) and (2.19), four particular forms for  $\sigma(n, \rho)$  will be considered, focussing on the branching and anastomosis process represented by

- FHD (i.e. lateral branching, tip-hypha anastomosis)
- FXD (i.e. lateral branching, tip death due to overcrowding)
- YWD (i.e. dichotomous branching, tip-tip anastomosis)
- YHD (i.e. dichotomous branching, tip-hypha anastomosis)

and are modelled by dimensionless versions of the equations (2.10), (2.11), (2.12) and (2.13) respectively. These represent four distinct phenotypes.

These four cases are now investigated in more detail, using a combination of numerical and algebraic approaches where possible. Somewhat unexpectedly, algebraic solutions for these model phenotypes have not been published previously. The models have been numerically integrated in Matlab using ‘pdepe’ and typical solutions with zero-flux boundary conditions are shown at time intervals of 2 for  $0 \leq t \leq 20$  over the domain  $x \in [0, 50]$ . A zero-flux boundary condition was appropriate for our investigation as the behaviour at the boundaries of the system was not investigated because it has been assumed that no material enters or leaves the domain at the edges. This is consistent with laboratory experiments where material is confined to the interior of a Petri dish. Note that the simulations are halted before the biomass visibly arrives at the boundary. The initial conditions

were chosen to be

$$\begin{aligned}\rho(x, 0) &= \begin{cases} \rho_0, & \text{if } x \leq x_0 \\ 0, & \text{if } x > x_0 \end{cases} \\ n(x, 0) &= \begin{cases} n_0, & \text{if } x \leq x_0 \\ 0, & \text{if } x > x_0 \end{cases}\end{aligned}\tag{2.20}$$

with  $x_0 = 3$ , where

$$\rho_0 = n_0 = \frac{1 - \tanh(x)}{2}.\tag{2.21}$$

A depiction of the function in equation (2.21) is shown in Figure 2.1.

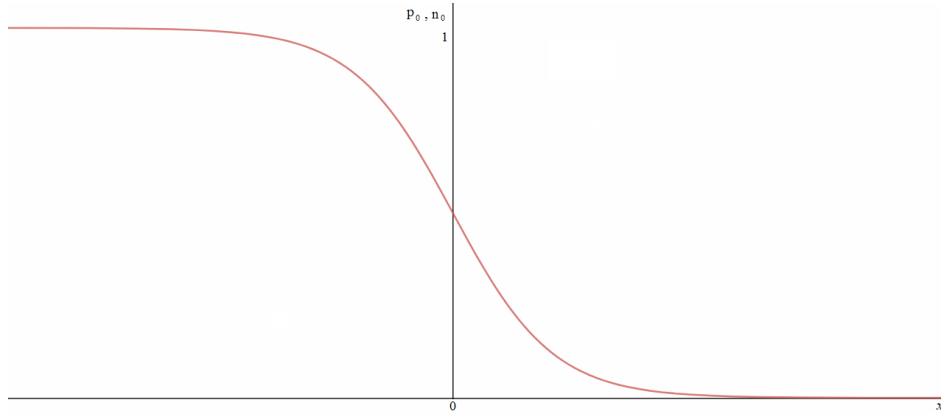


**Figure 2.1:** *Plot of the initial function.*

Notice there is a discontinuity at  $x_0$  for the initial data. This was selected to avoid non-zero densities for large values of  $x$  at small times but did not cause any integration issues in Matlab.

### 2.3.1 Phenotype FHD

The phenotype FHD models fungi that display lateral branching coupled with tip-hypha anastomosis. These two processes are represented by  $\sigma = \alpha_2\rho - \beta_2n\rho$ . By choosing the dimensional parameters  $\bar{n} = \frac{\alpha_2}{\beta_2}$ , with  $\alpha_1 = \alpha_3 = \beta_1 = \beta_3 = 0$ , (2.19) is further simplified. The mathematical equations that model the basic

characteristics of this phenotype are

$$\frac{\partial \rho}{\partial t} = n - \rho, \quad (2.22)$$

$$\frac{\partial n}{\partial t} = -\frac{\partial n}{\partial x} + \xi \rho(1 - n), \quad (2.23)$$

where  $\xi = \frac{\alpha_2 v}{\gamma^2}$ . Numerical solutions (Figure 2.2(a) and 2.2(b)) suggest that the hyphae and tips propagate in a uniform manner in time as a travelling wave, where profiles move at a constant speed in one direction without altering their shape.

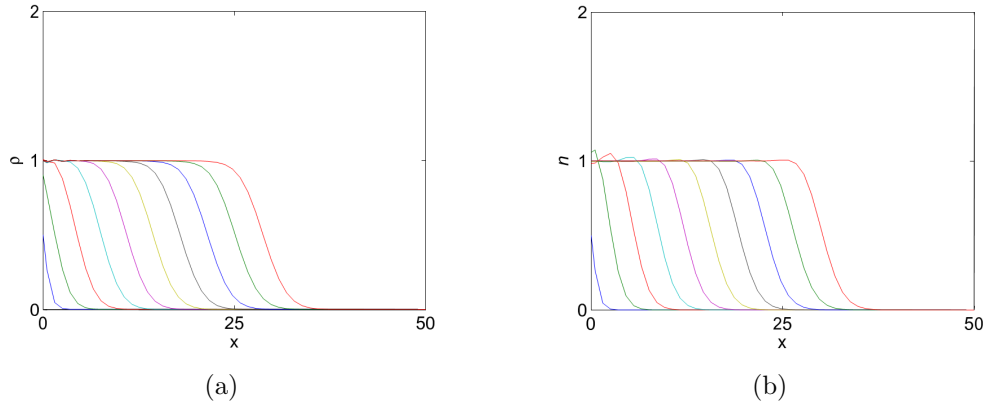


**Figure 2.2:** Wave profile for the FHD phenotype with (2.20) and  $\xi = 1$  shown at time intervals of 2 from left to right for  $0 \leq t \leq 20$  over the domain  $0 \leq x \leq 50$  where (a) is biomass ( $\rho$ ) and (b) is tips ( $n$ ).

### 2.3.1.1 Particular travelling wave solution for FHD

Previous studies have investigated the system of equations (2.22) and (2.23) using numerical solutions or phase-plane analysis (see later). However, it is possible to construct a particular travelling wave solution of these equations by seeking a solution of the form

$$\rho(x, t) = a + b \tanh(\theta x + ct) \quad (2.24)$$

where  $a$ ,  $b$ ,  $c$  and  $\theta$  are chosen so that equation (2.23) is satisfied. Substituting the function in equation (2.24) with  $n = \rho + \rho_t$  from equation (2.22) into (2.23) and comparing terms, we obtain a set of values for the parameters  $a = \frac{1}{2}$ ,  $b = c = -\frac{1}{2}$  and  $\theta = \frac{1}{2} - \frac{\xi}{4}$  that satisfies the equations and thus provides the following particular

travelling wave solution

$$\begin{aligned} n(x, t) &= \frac{1}{4} (1 - \Lambda) (3 + \Lambda), \\ \rho(x, t) &= \frac{1}{2} - \frac{\Lambda}{2}, \end{aligned} \tag{2.25}$$

where  $\Lambda = \tanh\left(\left(\frac{2-\xi}{4}\right)x - \frac{t}{2}\right)$  which is physically realistic for  $\xi < 2$ . An illustration of equations (2.25) is shown in Figure 2.3.

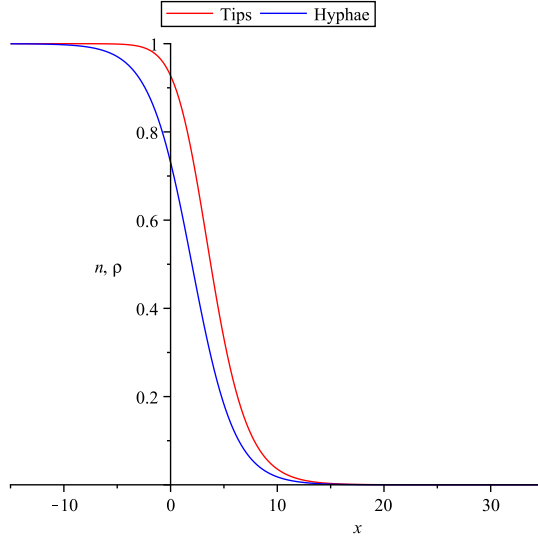


**Figure 2.3:** Plot of the particular solution (2.25) with  $\xi = 1$  at time  $t = 1$ .

We see in Figure 2.3 that  $n$  and  $\rho$  are monotonic decreasing in  $x$  and the wave is propagating to the right with a speed of  $\frac{2}{2-\xi}$ . To the author's knowledge, this is the first time a closed form solution has been obtained to the “tip and trail” equations widely used in the mathematical modelling of fungi.

### 2.3.2 Phenotype FXD

The phenotype FXD models lateral branching coupled with tip death due to overcrowding of hyphae. The biological interpretation is that the hyphae create a toxic substance in its tips which kills off other tips. These two processes are modelled by equation (2.11), namely  $\sigma = \rho(\alpha_2 - \beta_3\rho)$ . By choosing  $\bar{n} = \frac{\alpha_2\gamma}{\beta_3v}$  with  $\alpha_1 = \alpha_3 = \beta_1 = \beta_2 = 0$ , equation (2.19) is further simplified. The mathematical

equations that model the basic characteristics of this phenotype are

$$\frac{\partial \rho}{\partial t} = n - \rho, \quad (2.26)$$

$$\frac{\partial n}{\partial t} = -\frac{\partial n}{\partial x} + \xi \rho(1 - \rho), \quad (2.27)$$

where  $\xi = \frac{\alpha_2 v}{\gamma^2}$ .

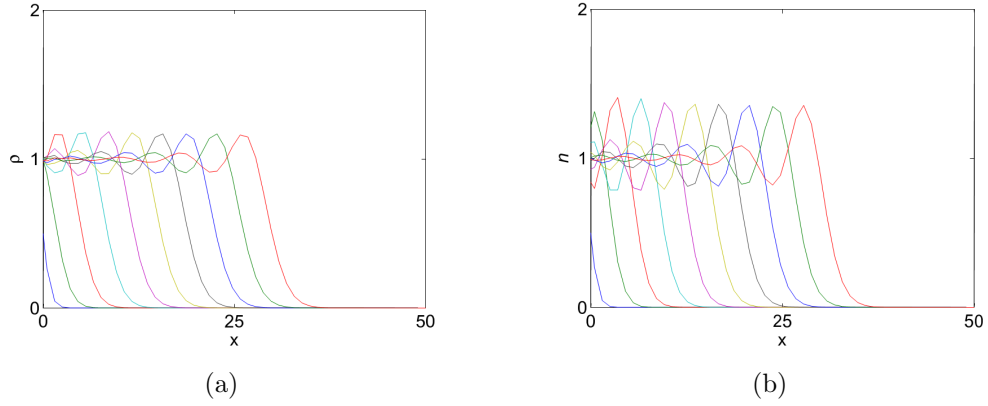


**Figure 2.4:** Wave profile for the FXD phenotype with equation (2.20) and  $\xi = 1$  shown at time intervals of 2 from left to right for  $0 \leq t \leq 20$  over the domain  $0 \leq x \leq 50$  where (a) is biomass ( $\rho$ ) and (b) is tips ( $n$ ).

Through numerical integration (Figures 2.4(a) and 2.4(b)) it can be seen that a propagating behaviour is present in both hypha and tip distributions. Interestingly the densities can be seen to proliferate in an alternating manner. This phenomenon is observed for various species of fungi in laboratory based experiments (e.g. Nissen, 2012) where mycelia are seen to form concentric rings in solid medium. A possible cause for such behaviour was proposed as being due to circadian rhythm, where a fungi is exposed to alternating exposure to light and temperature during growth (Nissen, 2012), but the above shows an alternative possible cause.

### 2.3.2.1 A particular travelling wave solution for FXD

A similar approach as used in Section 2.3.1.1 for the FHD phenotype can be applied to the FXD phenotype to yield particular travelling wave solutions. We seek a solution to the equations (2.26) and (2.27) of the form

$$\rho(x, t) = a + b \tanh(\theta x + ct) + d \tanh(\theta x + ct)^2 \quad (2.28)$$

where  $a, b, c, d$  and  $\theta$  are chosen so that equation (2.27) is satisfied. Substituting the function in equation (2.28) with  $n = \rho + \rho_t$  from equation (2.26) into (2.27) and comparing terms, we find that  $a = \frac{3}{4}$ ,  $b = -\frac{1}{2}$ ,  $c = -\frac{1}{10}$ ,  $d = -\frac{1}{4}$  and  $\theta = \frac{1}{10} - \frac{5\xi}{12}$  that satisfies the equations and thus provides the following particular travelling wave solution

$$\begin{aligned} n(x, t) &= \frac{1}{20}(1 - \Upsilon)(16 + 7\Upsilon + \Upsilon^2), \\ \rho(x, t) &= \frac{1}{4}(1 - \Upsilon)(3 + \Upsilon), \end{aligned} \quad (2.29)$$

where  $\Upsilon = \tanh\left(\left(\frac{6-25\xi}{60}\right)x - \frac{t}{10}\right)$  which is physically realistic for  $\xi < \frac{6}{25}$ . An illustration of equations (2.29) is shown in Figure 2.5.

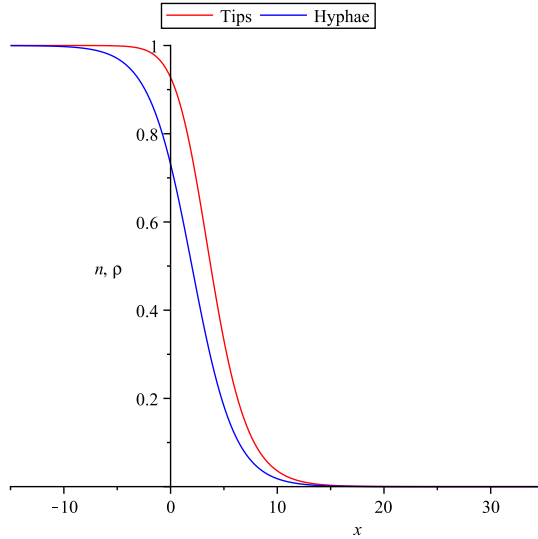


**Figure 2.5:** Plot of the particular solution (2.29) with  $\xi = 1$  at time  $t = 1$ .

We see in Figure 2.5 that  $n$  and  $\rho$  are monotonic decreasing in  $x$  and the wave is propagating to the right with a speed of  $\frac{6}{6-25\xi}$ .

### 2.3.3 Phenotype YWD

This phenotype represents dichotomous branching coupled with tip-tip anastomosis and the corresponding branching and anastomosis terms are modelled by

$\sigma = (\alpha_1 - \alpha_3)n - \beta_1 n^2$ . In respect to modelling the phenotype YWD, we will only consider  $\alpha_1 n$  in our model as this depicts the splitting of hyphae into two tips whereas the term  $-\alpha_3 n$  represents tip elimination/death. Hence using the dimensional parameters  $\bar{n} = \frac{\alpha_1}{\beta_1}$  in (2.19) and by setting  $\alpha_2 = \alpha_3 = \beta_2 = \beta_3 = 0$ , the mathematical equations formed are

$$\begin{aligned} \frac{\partial \rho}{\partial t} &= n - \rho, \\ \frac{\partial n}{\partial t} &= -\frac{\partial n}{\partial x} + \zeta n(1 - n), \end{aligned} \quad (2.30)$$

where  $\zeta = \frac{\alpha_1}{\gamma}$ .

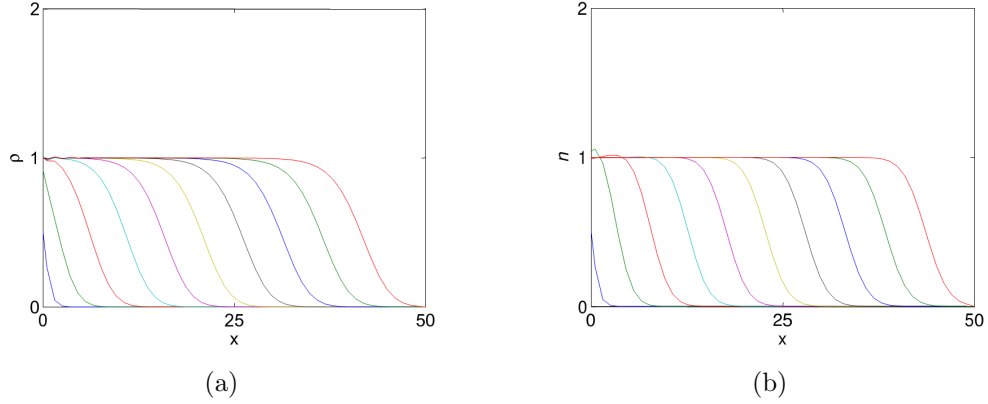


**Figure 2.6:** Wave profile for the YWD phenotype with (2.20) and  $\zeta = 1$  shown at time intervals of 2 from left to right for  $0 \leq t \leq 20$  over the domain  $0 \leq x \leq 50$  where (a) is biomass ( $\rho$ ) and (b) is tips ( $n$ ).

The numerical simulation of equation (2.30) (Figures 2.6(a) and 2.6(b)) show that again a uniform propagation behaviour is present in both hyphae and tips.

### 2.3.3.1 General analytical solution

It is interesting to note that these model equations can be solved analytically but no solution has, to the author's knowledge, previously been published. This aspect of this model was not explored by Edelstein-Keshet. The dimensionless



form of the system of equations will be used, i.e.

$$\begin{aligned}\frac{\partial \rho}{\partial t} &= n - \rho, \\ \frac{\partial n}{\partial t} &= -\frac{\partial n}{\partial x} + \zeta(n - n^2),\end{aligned}\tag{2.31}$$

which can be more conveniently expressed as

$$\begin{aligned}\frac{\partial \rho}{\partial t} + \rho &= n, \\ \frac{\partial n}{\partial x} + \frac{\partial n}{\partial t} &= \zeta(n - n^2).\end{aligned}\tag{2.32}$$

The first equation of (2.32) can be solved using the integrating factor method to give the solution

$$\rho(x, t) = e^{-t} \left( \int_0^t n(x, \hat{t}) e^{\hat{t}} d\hat{t} + F(x) \right)\tag{2.33}$$

where  $F(x) = \rho(x, 0)$  is introduced through integration. The second equation of (2.32) can be solved using the method of characteristics. The characteristic equations of (2.32) can be expressed as

$$dx = dt = \frac{dn}{\zeta(n - n^2)}.\tag{2.34}$$

Integrating the first two terms

$$\int dx = \int dt\tag{2.35}$$

gives  $x = t + \bar{s}$  where  $\bar{s}$  was obtained from integration. The second term in equation (2.34) can be integrated in two parts

$$\int dt = \int \frac{dn}{\zeta(n - n^2)}\tag{2.36}$$

i.e.

$$t = \int \frac{dn}{\zeta(n - n^2)}\tag{2.37}$$

where  $\zeta \neq 0$ . The right hand side of (2.37) can be expressed in terms of its partial

fractions and then integrated to give

$$\zeta t = \ln \left( \frac{n}{1-n} \right) + \zeta G(\bar{s}) \quad (2.38)$$

where  $G(\bar{s})$  is introduced via integration. Rearranging equation (2.38) yields

$$n = \frac{1}{e^{-\zeta(t-G(\bar{s}))} + 1}. \quad (2.39)$$

Therefore the analytical solution of equation (2.31) is

$$\begin{aligned} \rho &= e^{-t} \left( \int_0^t n(x, \hat{t}) e^{\hat{t}} d\hat{t} + F(x) \right), \\ n &= \frac{1}{1 + e^{-\zeta(t-G(x-t))}}. \end{aligned} \quad (2.40)$$

If  $\rho(x, 0) = \rho_0(x)$  and  $n(x, 0) = n_0(x)$  then equation (2.40) can be expressed as the following

$$\begin{aligned} \rho(x, t) &= e^{-t} \left( \int_0^t n(x, \hat{t}) e^{\hat{t}} d\hat{t} + \rho_0(x) \right), \\ n(x, t) &= \frac{1}{1 + e^{-\zeta t} \left( \frac{1}{n_0(x-t)} - 1 \right)}. \end{aligned} \quad (2.41)$$

This is the only type of phenotype out of the four we have chosen to analyse that provides us with a general closed form solution for any initial data. We will use this result in later analysis.

### 2.3.4 Phenotype YHD

This phenotype represents dichotomous branching coupled with tip-hyphae anastomosis and the corresponding branching and anastomosis terms are modelled by  $\sigma = \alpha_1 n - \beta_2 n \rho$ . In respect to modelling the phenotype YHD, we will only consider  $\alpha_1 n$  in our model as this depicts the splitting of hyphae into two tips whereas the term  $-\alpha_3 n$  represents tip death. Hence using the dimensional parameters  $\bar{n} = \frac{\alpha_1 \gamma}{\beta_2 v}$  and setting  $\alpha_2 = \alpha_3 = \beta_1 = \beta_3 = 0$  in (2.19), the mathematical

equations formed are

$$\begin{aligned}\frac{\partial \rho}{\partial t} &= n - \rho \\ \frac{\partial n}{\partial t} &= -\frac{\partial n}{\partial x} + \zeta n(1 - \rho)\end{aligned}\tag{2.42}$$

where  $\zeta = \frac{\alpha_1}{\gamma}$ .

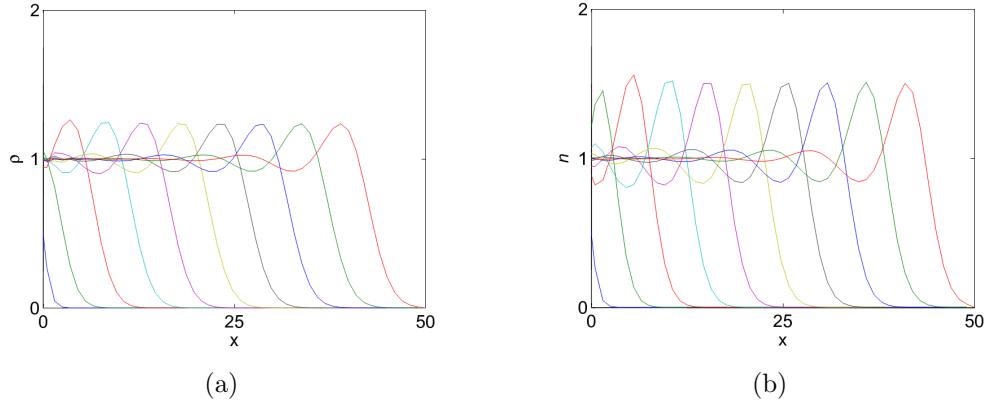


**Figure 2.7:** Wave profile for the YHD phenotype with (2.20) and  $\zeta = 1$  shown at time intervals of 2 from left to right for  $0 \leq t \leq 20$  over the domain  $0 \leq x \leq 50$  where (a) is biomass ( $\rho$ ) and (b) is tips ( $n$ ).

The numerical solutions (Figures 2.7(a) and 2.7(b)) show a propagating distribution of hyphal and tip populations. Notice, striations similar to that observed in FXD phenotype are also seen here. We were unable to obtain physically realistic travelling wave solutions of the form similar to the other phenotypes above.

## 2.4 Phase space analysis

### 2.4.1 Travelling wave solutions

One of the features of fungal colonies is their ability to spread over space as has been seen in the previous simulations. The radial expansion of a colony normally occurs at a constant rate. This can be described mathematically by saying that the density distributions behave like travelling waves. Hence, in such circumstances,

the particular solutions to equations (2.1) and (2.2) can be given by

$$\begin{aligned}\rho(x, t) &= P(z), \\ n(x, t) &= N(z),\end{aligned}$$

where  $z = x - ct$ . Here  $P(z)$  and  $N(z)$  represent density profiles and  $c$  is the speed of propagation of the colony.  $P$  and  $N$  are bounded, non-negative functions of  $z$ . Hence equations (2.1) and (2.2) can be written as

$$-c \frac{dP}{dz} = N - d(P) \quad (2.43)$$

and

$$(1 - c) \frac{dN}{dz} = \sigma(N, P) \quad (2.44)$$

where the equations are now a pair of ordinary differential equations in which the distance and the death term has been non-dimensionalised. These equations can be analyzed using phase plane techniques by looking for bounded, non-negative solutions to these equations. For the solutions to represent a travelling wave the following conditions must be satisfied (Edelstein, 1982):

1. The system has more than one equilibrium point (i.e.  $\frac{dP}{dz} = 0, \frac{dN}{dz} = 0$ )
2. There is a heteroclinic trajectory connecting these in the  $(P, N)$  plane
3. The trajectory remains in the positive  $(P, N)$  quadrant
4. One of the steady states is necessarily  $(P_0, N_0) = (0, 0)$

Condition (4) is necessary since ahead of the colony before growth has arrived no hyphae or tips are present. Hence this steady state must be the attractor for flow along the heteroclinic trajectory since it represents the limit as  $z \rightarrow +\infty$  densities. If it exists, a second equilibrium of equations (2.43) and (2.44)  $(P_1, N_1)$  would represent density levels into the interior of the colony as  $z \rightarrow -\infty$ .

## 2.4.2 Phase plane analysis

Here the attention is focussed on travelling wave solutions of the models considered in the previous section, namely equations (2.23), (2.26), (2.30) and (2.42) coupled with the hyphae equation

$$-c \frac{dP}{dz} = N - P$$

1. FHD:  $(1 - c) \frac{dN}{dz} = \xi P(1 - N),$
2. FXD:  $(1 - c) \frac{dN}{dz} = \xi P(1 - P),$
3. YWD:  $(1 - c) \frac{dN}{dz} = \zeta N(1 - N),$
4. YHD:  $(1 - c) \frac{dN}{dz} = \zeta N(1 - P).$

To illustrate the construction and analysis of the phase plane, consider the FHD phenotype.

$$\begin{aligned} -c \frac{dP}{dz} &= N - P, \\ (1 - c) \frac{dN}{dz} &= \xi P(1 - N). \end{aligned} \tag{2.45}$$

From equation (2.45) we obtain the coordinates for the stationary points, which are  $(0, 0)$  and  $(1, 1)$  respectively. The eigenvalues,  $\lambda$ , of the Jacobian matrix evaluated at  $(0, 0)$  are the roots of

$$\lambda^2 - \frac{1}{c}\lambda + \frac{\xi}{c(1 - c)} = 0. \tag{2.46}$$

For a travelling wave solution to exist there has to be a trajectory connecting the two stationary points that lie in the positive quadrant. If  $0 < c < \frac{1}{4\xi+1}$  then both  $\lambda$  are positive and so  $(0, 0)$  is an unstable node and if  $\frac{1}{4\xi+1} < c < 1$  then  $\lambda$  are complex conjugates with positive real parts and so  $(0, 0)$  is an unstable spiral, implying the existence of trajectories that leave the positive quadrant. If  $c > 1$  then the eigenvalues have opposite signs which would suggest that  $(0, 0)$  is a saddle point.

The eigenvalues of the Jacobian matrix evaluated at  $(1, 1)$  are given by solutions of

$$\left(\lambda - \frac{1}{c}\right) \left(\lambda + \frac{\xi}{1 - c}\right) = 0 \tag{2.47}$$

i.e.  $\lambda = \frac{1}{c}$  and  $\lambda = \frac{\xi}{c-1}$ . If  $c > 1$  then both eigenvalues are positive and so  $(1, 1)$  is an unstable node, if  $0 < c < 1$  then the eigenvalues have opposite signs which would suggest that  $(1, 1)$  is a saddle point. If  $c < 0$  then both eigenvalues are negative, so  $(1, 1)$  is a stable node.

The results for the other phenotypes can be determined in a similar manner and have been conducted by other authors (e.g. Edelstein, 1982). Figure 2.8 show sample phase plane diagrams for different phenotypes, obtained using `pplane8` in Matlab.

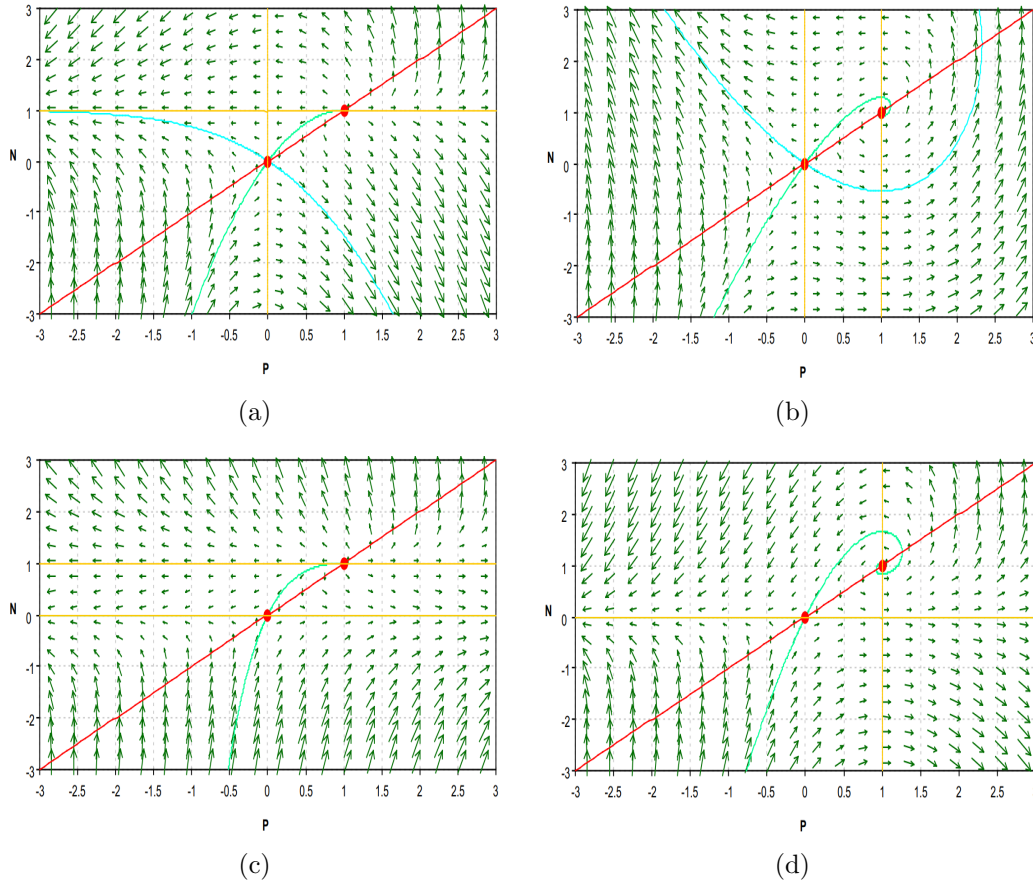


**Figure 2.8:** Phase plane diagrams for (a) FHD, (b) FXD, (c) YWD and (d) YHD phenotype, plotted using `pplane8` with  $c = 2$  and  $\xi = \zeta = 1$ . Travelling wave solutions are illustrated by the light blue trajectories connecting  $(1, 1)$  to  $(0, 0)$ . The red and orange lines correspond to the  $P$  and  $N$  nullclines respectively.

## 2.5 Summary

We have computed numerical simulations of four distinct phenotypes explored by Edelstein-Keshet and briefly explained their behaviour. We have shown that all four phenotypes (i.e. FHD, FXD, YWD and YHD) display propagating behaviour. This is true provided a death term is included in the model equations to represent hyphal death. This result is also confirmed by Edelstein (1982) where she used phase plane techniques to carry out an in depth analysis to determine which of the phenotypes had bounded non-negative solutions. We have briefly explored the key aspect of phase plane analysis from her work.

We also carried out a phase portrait analysis to reproduce Edelstein-Keshet's results. Edelstein-Keshet stressed that an expectation for all fungal colonies to propagate is not realistic or possible if only reliance is on reaction terms alone, which correspond to branching and anastomosis. Hence the death/autolysis term is as important to fungi as branching and anastomosis and is necessary to produce a travelling wave solution.

The numerical solutions for the FHD and YWD phenotypes depicted 'tiny' oscillations for small times ( $t = 2$  and  $t = 4$ ). These oscillations are numerical errors that smoothed out over time to yield monotonic propagation of a travelling wave (see Figures 2.2 and 2.6). However, the oscillations observed for the FXD and YHD phenotypes are not numerical artefacts; rather these are intrinsic behaviours of the model system and are predicted from the phase plane analysis (see Figure 2.8) that depicted a spiral heteroclinic trajectory from the stationary point  $(1, 1)$  to  $(0, 0)$  for the FXD and YHD phenotype. There is no single driving force that defines this different characteristic and thus the only conclusion is that the growth characteristic arises as a response to a combination of branching, anastomosis and hyphal death. A more in depth analysis can be found in Edelstein (1982).

We have seen in this section some analysis of the four common phenotypes observed in fungal development. They all can be solved numerically as shown in each respective subsections. We have also obtained a general analytical solution for the phenotype YWD and a particular analytical solution for the FHD and FXD phenotypes, which to the author's knowledge has not been obtained in previous studies.

The objective of this chapter has been to illustrate how different branching and anastomosis processes (as well as tip death) can influence the morphology of a fungal mycelium. It should be noted that these models have been investigated

in the Cartesian coordinate system, and so are consistent with the previous investigations of Edelstein (1982), Boswell and Davidson (2012), and as a consequence have generated travelling wave solutions for certain model phenotypes. Due to the circular growth of fungal colonies, at least in uniform domains, an alternative analysis using polar coordinates could have been presented. While travelling waves would no longer have arisen, for large times the leading edge of the resultant distributions would still resemble those constructed above due to the similarity between polar coordinate systems for large  $r$  and the Cartesian coordinate system.

In the following chapter we construct semi-analytical solutions for particular phenotypes and develop a method that describes the initial kinematics of an expanding colony.



## Chapter 3

# Decomposition Method Applied to the Study of Filamentous Fungi

### 3.1 A decomposition method

In Section 2.3.1.1 we determined a closed form solution (2.25) to the lateral branching coupled with tip-hypha anastomosis phenotype (FHD). The solution was restricted by choosing initial data of a specific form. In Section 2.3.3.1 for the dichotomous branching coupled with tip-tip anastomosis phenotype (YWD), a general solution (2.40) was obtained for the tips but for the hyphae only an integral solution was obtained. In this section we will venture an alternative approach to obtain an approximate solution and verify the results with the closed form solution. We will then use this new approach to generate an approximate semi-analytical solution for the lateral branching coupled with tip-hypha anastomosis phenotype (FHD), which in general is required to be solved numerically. This alternative approach is the technique called the Laplace Decomposition Method (LDM) inspired from the work developed by George Adomian. We choose to focus on two phenotypes. Firstly YWD, as it was the only phenotype that resulted in a general analytical solution. Thus the forthcoming technique developed in this chapter can be tested against an exact result. The FHD phenotype is frequently observed in experiments involving filamentous fungi and indeed it was found in Boswell et al. (2002) that the fungi *R. solani* adheres to the morphological pattern FHD and hence this phenotype is also considered here. Note, however, that the

methods developed here can be applied to all possible phenotypes proposed in the previous chapter.

### 3.1.1 Brief history

George Adomian developed the Adomian Decomposition Method (ADM) in a series of papers starting in the 1980s (Adomian, 1986, 1988, 1991a). It is based on the search for a solution in the form of a series by decomposing the terms (linear or non-linear) into a series in which the terms are calculated recursively using Adomian polynomials (Adomian, 1991b; Adomian and Rach, 1991; Adomian, 1994; Biazar et al., 2004).

The formation of mathematical models related to actual physical problems arising in various areas of applied science (e.g. hydraulics), biology (e.g. population models), engineering (e.g. transfer of heat) and physics (e.g. plasma physics) often requires the investigation of a class of ordinary differential equations (ODEs) and partial differential equations (PDEs) or a system of these, which are often strongly non-linear or even stochastic. The models are usually formed with the most realistic representation of the key attributes of interest of the problem. Due to the complexity of the equations there is usually the need for simplifying assumptions, typically linearisation. Although linearisation has been greatly useful for problems of this nature, sometimes its use may mean the problem being solved has skewed away from the realism of the physical problem (Adomian, 1991a; Khan et al., 2010; Mohamed and Torky, 2013). Thus the result obtained, however elegant, may not be physically realistic. The decomposition method does not change the problem into a convenient approximate form, but instead provides a non-linear algebraic solution.

Adomian and co-workers have solved many differential equations in a wide class of non-linear problems including polynomials (Adomian and Rach, 1985a), exponentials (Adomian and Rach, 1985b), hyperbolic (Adomian and Rach, 1984) and negative-powers (Adomian and Rach, 1985c). Hence ADM can be used to determine a series solution for many types of non-linear problems. It can be found in literature that the decomposition method provides the solution in a convergent series. The rapid convergence of the solution is guaranteed by the work conducted by Cherruault (1990) and Dehghan and Tataru (2006).

Shueil Kuhri introduced a variation on the ADM termed Laplace Decomposition Method (LDM) (Khuri, 2001, 2004). This algebraic technique illustrates

how the Laplace transform may be utilised to approximate the solution of nonlinear PDEs by manipulating the decomposition method (Khuri, 2001, 2004; Fadaei, 2011). The Laplace decomposition method has assisted in the work of many authors to determine the solution to a variety of problems as well as many complex systems (Agadjanov, 2006; Elgazery, 2008; Fadaei, 2011; Safari and Danesh, 2011; Mohamed and Torky, 2013; Al-Hayani, 2013). There have also been modifications to the LDM introduced by numerous authors (e.g. Wazwaz, 2006; Hussain and Khan, 2010; Fadaei, 2011).

### 3.1.2 Adomian decomposition method

We will now discuss the processes involved in the Adomian decomposition method. The ADM will be explained first because the LDM is simply a manipulated version of the ADM. We begin with an equation of the form  $Fu(x, t) = h(x, t)$ , where  $F$  represents a general differential operator involving both linear and nonlinear terms. The linear terms can be decomposed into  $L$  and  $R$ , where  $L$  is easily invertible and  $R$  is the remainder of the linear operator. The equation may be written as follows

$$Lu(x, t) + Ru(x, t) + Nu(x, t) = h(x, t) \quad (3.1)$$

where  $L$ , for the current application, will be regarded as  $L = \frac{\partial}{\partial t}$  (but  $L$  may be taken as the highest order derivative in general),  $R$  is the remainder of the linear operator of the equation,  $N$  represents a general nonlinear operator acting on  $u$  and  $h(x, t)$  is a source term. Equation (3.1) can be rearranged to

$$Lu(x, t) = h(x, t) - Ru(x, t) - Nu(x, t). \quad (3.2)$$

Since  $L$  is linear, it is invertible and so an equivalent equation is

$$L^{-1}Lu(x, t) = L^{-1}h(x, t) - L^{-1}Ru(x, t) - L^{-1}Nu(x, t). \quad (3.3)$$

If equation (3.1) corresponds to an initial/boundary value problem, the inverse operator  $L^{-1}$  may be regarded as integration where the constants are evaluated from the given conditions. Thus equation (3.3) can be written as

$$u(x, t) = K(x, t) - L^{-1}Ru(x, t) - L^{-1}Nu(x, t) \quad (3.4)$$

where  $K(x, t) = L^{-1}h(x, t)$ . The next step is to express the solution as an infinite series

$$u(x, t) = \sum_{n=0}^{\infty} u_n \quad (3.5)$$

where  $u_n$  are functions of  $x$  and  $t$ . The nonlinear operation on  $u(x, t)$  is decomposed into a second series

$$Nu(x, t) = \sum_{n=0}^{\infty} A_n \quad (3.6)$$

where  $A_n$  are the Adomian polynomials (Adomian, 1991b) of  $u_0, u_1, u_2 \dots$  and are functions of  $x$  and  $t$ . These polynomials can be generated from the standard definition of the Adomian polynomials

$$A_n = \frac{1}{n!} \frac{d^n}{d\lambda^n} \left[ N \left( \sum_{i=0}^{\infty} \lambda^i u_i \right) \right]_{\lambda=0} \quad \text{for } n = 0, 1, 2, \dots \quad (3.7)$$

but in application can be more readily formed from applying the nonlinear operator onto the series solution for  $u$ . Thus substituting (3.5) and (3.6) into (3.4) we obtain

$$\sum_{n=0}^{\infty} u_n = K(x, t) - L^{-1}R \sum_{n=0}^{\infty} u_n - L^{-1} \sum_{n=0}^{\infty} A_n. \quad (3.8)$$

The polynomials of  $A_n$  are generated for each nonlinearity so  $A_0$  depends only on  $u_0$ ,  $A_1$  depends on  $u_0$  and  $u_1$ ,  $A_2$  depends on  $u_0, u_1$  and  $u_2$  and so on. It can be seen that the series  $\sum_{n=0}^{\infty} A_n$  for  $Nu(x, t)$  is equal to a generalised Taylor series about  $u = u_0$  and  $\sum_{n=0}^{\infty} u_n$  is a generalised Taylor series about  $u = u_0$ . Therefore we can write equation (3.8) in iterative form as

$$\begin{aligned} u_0 &= K(x, t) \\ u_1 &= -L^{-1}Ru_0 - L^{-1}A_0 \\ u_2 &= -L^{-1}Ru_1 - L^{-1}A_1 \\ u_3 &= -L^{-1}Ru_2 - L^{-1}A_2 \\ &\vdots \\ u_{n+1} &= -L^{-1}Ru_n - L^{-1}A_n. \end{aligned} \quad (3.9)$$

Thus the solution  $u$  can be constructed by summing its constituent parts (the

$u_n s)$ .

### 3.1.2.1 Example of ADM

To illustrate the Adomian decomposition method, consider the following transport equation

$$\frac{\partial u}{\partial t} = -\frac{\partial u}{\partial x} \quad (3.10)$$

with initial data

$$u(x, 0) = \sin(x). \quad (3.11)$$

The closed form solution of equation (3.10) is clearly  $u(x, t) = \sin(x - t)$ , which can be easily verified by differentiation. To apply the ADM, we write equation (3.10) in the form of equation (3.3), i.e.

$$L^{-1} \left( \frac{\partial u}{\partial t} \right) = L^{-1} \left( -\frac{\partial u}{\partial x} \right) \quad (3.12)$$

where the differential operator  $L = \frac{\partial}{\partial t}$  and the inverse operator  $L^{-1}(\cdot) = \int_0^t (\cdot) dt$  (and so consistent with Adomian's notation: Adomian, 1986, 1988, 1991a). Hence equation (3.12) becomes

$$u(x, t) = - \int_0^t \left( \frac{\partial u}{\partial x} \right) dt. \quad (3.13)$$

The Adomian Decomposition Method assumes that the unknown function  $u(x, t)$  can be expressed by an infinite series of the form

$$u(x, t) = \sum_{n=0}^{\infty} u_n, \quad (3.14)$$

where  $u_{n+1} = - \int_0^t \frac{\partial u_n}{\partial x} dt$ . From (3.11), we set  $u_0 = \sin(x)$  and use the iterative formula from equation (3.9). In equation (3.10) there is no source term hence the  $h(x, t)$  term in equation (3.1) is zero here. Thus our initial function ( $u_0$ ) is only a function of  $x$ , i.e. independent of  $t$ . Hence the first few terms are

$$\begin{aligned}
u_0 &= \sin(x) \\
u_1 &= - \int_0^t \left( \frac{\partial u_0}{\partial x} \right) dt = -\cos(x)t \\
u_2 &= - \int_0^t \left( \frac{\partial u_1}{\partial x} \right) dt = -\sin(x) \frac{t^2}{2!} \\
&\vdots
\end{aligned} \tag{3.15}$$

Therefore using the general formula to generate a few more consecutive terms and summing them we get

$$\begin{aligned}
u(x, t) &= \sin(x) - \cos(x) t - \sin(x) \frac{t^2}{2!} + \cos(x) \frac{t^3}{3!} + \sin(x) \frac{t^4}{4!} - \cos(x) \frac{t^5}{5!} + \dots \\
&= \sin(x) \left[ 1 - \frac{t^2}{2!} + \frac{t^4}{4!} + \dots \right] + \cos(x) \left[ -t + \frac{t^3}{3!} - \frac{t^5}{5!} + \dots \right] \\
&= \sin(x) \cos(t) - \cos(x) \sin(t) \\
&= \sin(x - t)
\end{aligned} \tag{3.16}$$

which is the exact solution of equation (3.10) stated at the start of this example.

### 3.1.3 Laplace decomposition method

As mentioned earlier, the Laplace decomposition method was introduced by Khuri (2001). Consider the general form of an inhomogeneous nonlinear partial differential equation:

$$Lu(x, t) = h(x, t) - Ru(x, t) - Nu(x, t), \tag{3.17}$$

with initial data

$$u(x, 0) = f(x), \tag{3.18}$$

where all the operators are the same as before except  $f(x)$  represents the initial conditions. We first take the Laplace transform of both sides of equation (3.17)

$$\mathcal{L}[Lu(x, t)] = \mathcal{L}[h(x, t)] - \mathcal{L}[Ru(x, t)] - \mathcal{L}[Nu(x, t)], \tag{3.19}$$

and using the standard differential property of the Laplace transform we obtain

$$s\mathcal{L}[u(x, t)] - f(x) = \mathcal{L}[h(x, t)] - \mathcal{L}[Ru(x, t)] - \mathcal{L}[Nu(x, t)]. \quad (3.20)$$

Thus rearranging equation (3.20) we obtain

$$\mathcal{L}[u(x, t)] = \frac{f(x)}{s} + \frac{1}{s}\mathcal{L}[h(x, t)] - \frac{1}{s}\mathcal{L}[Ru(x, t)] - \frac{1}{s}\mathcal{L}[Nu(x, t)]. \quad (3.21)$$

We use the same representation for  $u_n$  and  $Nu$  as we did for the ADM in equations (3.5), (3.6) and (3.7), thus

$$u(x, t) = \sum_{n=0}^{\infty} u_n \quad \text{and} \quad Nu(x, t) = \sum_{n=0}^{\infty} A_n. \quad (3.22)$$

Substituting equation (3.22) in equation (3.21) we get

$$\mathcal{L}\left[\sum_{n=0}^{\infty} u_n\right] = \frac{f(x)}{s} + \frac{1}{s}\mathcal{L}[h(x, t)] - \frac{1}{s}\mathcal{L}\left[R\sum_{n=0}^{\infty} u_n\right] - \frac{1}{s}\mathcal{L}\left[\sum_{n=0}^{\infty} A_n\right]. \quad (3.23)$$

Hence by grouping terms carefully we obtain

$$\mathcal{L}[u_0] = \frac{f(x)}{s} + \frac{1}{s}\mathcal{L}[h(x, t)] = K(x, s), \quad (3.24)$$

$$\mathcal{L}[u_1] = -\frac{1}{s}\mathcal{L}[Ru_0] - \frac{1}{s}\mathcal{L}[A_0],$$

$\vdots$

$$\mathcal{L}[u_{n+1}] = -\frac{1}{s}\mathcal{L}[Ru_n] - \frac{1}{s}\mathcal{L}[A_n], \quad \text{for } n \geq 0 \quad (3.25)$$

where  $K(x, s)$  is used to represent the Laplace transformed source term and the initial condition. Now we take the inverse Laplace transform of equations (3.24) and (3.25) to get

$$u_0 = \mathcal{L}^{-1}[K(x, s)], \quad (3.26)$$

$$u_{n+1} = -\mathcal{L}^{-1}\left[\frac{1}{s}\mathcal{L}[Ru_n] + \frac{1}{s}\mathcal{L}[A_n]\right], \quad \text{for } n \geq 0.$$

Therefore we obtain the functions for  $u_1, u_2, u_3, \dots$  from equation (3.26) allowing one to construct a series solution.

### 3.1.3.1 Example of LDM

We will solve the same first order transport equation, solved earlier using ADM, by the Laplace decomposition method, i.e.

$$\frac{\partial u}{\partial t} = -\frac{\partial u}{\partial x} \quad \text{with} \quad u(x, 0) = \sin(x).$$

We write the equation in the same form as equation (3.19):

$$\mathcal{L} \left[ \frac{\partial u}{\partial t} \right] = -\mathcal{L} \left[ \frac{\partial u}{\partial x} \right], \quad (3.27)$$

where the differential operator  $\mathcal{L}$  is the Laplace transform operator. Hence evaluating the Laplace transform in equation (3.27) we obtain:

$$s\mathcal{L}[u] - u(x, 0) = -\mathcal{L} \left[ \frac{\partial u}{\partial x} \right]. \quad (3.28)$$

We rearrange equation (3.28) and take the inverse Laplace transform to get

$$u(x, t) = \mathcal{L}^{-1} \left[ \frac{u(x, 0)}{s} \right] - \mathcal{L}^{-1} \left[ \frac{1}{s} \mathcal{L} \left[ \frac{\partial u}{\partial x} \right] \right]. \quad (3.29)$$

We know that the unknown function can be written as an infinite series shown in equation (3.22). Hence we have

$$\sum_{n=0}^{\infty} u_n = u(x, 0) - \mathcal{L}^{-1} \left[ \frac{1}{s} \mathcal{L} \left[ \frac{\partial}{\partial x} \left( \sum_{n=0}^{\infty} u_n \right) \right] \right]. \quad (3.30)$$

Hence we obtain

$$\begin{aligned} u_0 &= u(x, 0) = \sin(x) \\ u_1 &= -\mathcal{L}^{-1} \left[ \frac{1}{s} \mathcal{L} \left[ \frac{\partial(u_0)}{\partial x} \right] \right] = -\mathcal{L}^{-1} \left[ \frac{1}{s^2} \cos(x) \right] = -\cos(x) \, t \\ u_2 &= -\mathcal{L}^{-1} \left[ \frac{1}{s} \mathcal{L} \left[ \frac{\partial(u_1)}{\partial x} \right] \right] = -\mathcal{L}^{-1} \left[ \frac{1}{s^3} \sin(x) \right] = -\sin(x) \, \frac{t^2}{2!} \\ &\vdots \end{aligned}$$

As before, we can clearly see,  $u(x, t) = \sin(x - t)$ .

In practice, the series will be truncated after a given number of terms.



The convergence or divergence of a series is typically not known, thus choosing the point to truncate a series should be considered in obtaining a useful result.

### 3.1.4 YWD Phenotype revisited

#### 3.1.4.1 A particular solution

In Section 2.3.3.1 a closed form solution was obtained for the phenotype YWD (the fungal colony with the dichotomous branching and tip-tip anastomosis characteristics) for non-dimensionalised parameters. Edelstein (1982) stressed that some parameters are crucial to ensure propagating behaviour in fungi and thus should not be overlooked. Crucial parameters such as the speed of the tips, death of hyphae and the branching and anastomosis terms were not explicitly included in the non-dimensionalised models seen in the previous chapter. These parameters are fundamental to understanding important properties of fungal kinematics. Therefore we will use the dimensional form of the system of equations for the phenotypes YWD and FHD in this chapter.

We start by writing equation (2.31) in an alternative but equivalent form and use particular initial conditions to obtain an analytical solution

$$\rho_t = nv - \gamma\rho, \tag{3.31}$$

$$n_t = -vn_x + \alpha n - \beta n^2.$$

The general solutions to the equations in (3.31) are given by

$$\rho = e^{-\gamma t} \left( \int_0^t v n e^{\gamma \hat{t}} d\hat{t} + F(x) \right), \tag{3.32}$$

$$n = \frac{\alpha}{\beta + e^{-\alpha t} G(x - vt)}, \tag{3.33}$$

where  $F(x)$  and  $G$  are the same as before but for notational convenience we set  $\alpha = \alpha_1$  and  $\beta = \beta_1$ . For illustrative purposes, suppose the following initial conditions are used

$$\rho(x, 0) = \frac{\alpha v}{2\beta\gamma} (1 - \tanh(\theta x)), \quad n(x, 0) = \frac{\alpha}{2\beta} (1 - \tanh(\phi x)). \tag{3.34}$$

This choice of initial conditions were influenced by the anticipation of a heteroclinic orbit between the two equilibrium points, often seen in these studies

(Edelstein, 1982) and where the behaviour at the boundaries matches the spatially uniform equilibria. Hence using simple algebra, the initial condition for the tip equation (3.33) is

$$G(x) = \beta \left( \frac{1 + \tanh(\phi x)}{1 - \tanh(\phi x)} \right) = \beta e^{2\phi x}. \quad (3.35)$$

Therefore

$$n(x, t) = \frac{\alpha}{\beta(1 + e^{2\phi(x - (\frac{\alpha}{2\phi} + v)t})} = \frac{\alpha}{2\beta} \left( 1 - \tanh \left( \phi \left( x - \left( \frac{\alpha}{2\phi} + v \right) t \right) \right) \right)$$

and so the distribution propagates as a travelling wave with velocity  $\frac{\alpha}{2\phi} + v$ . Substituting the above into equation (3.32) we obtain the analytical solutions for the system of equations (3.31)

$$\rho(x, t) = e^{-\gamma t} \left( v \int_0^t \frac{\alpha}{2\beta} \left( 1 - \tanh \left( \phi \left( x - \left( \frac{\alpha}{2\phi} + v \right) \hat{t} \right) \right) \right) e^{\gamma \hat{t}} d\hat{t} + F(x) \right), \quad (3.36)$$

$$n(x, t) = \frac{\alpha}{2\beta} \left( 1 - \tanh \left( \phi \left( x - \left( \frac{\alpha}{2\phi} + v \right) t \right) \right) \right). \quad (3.37)$$

#### 3.1.4.2 Applying LDM on phenotype YWD

In this section we will apply the Laplace decomposition method to phenotype YWD. The model equations are

$$\begin{aligned} \rho_t &= nv - \gamma\rho, \\ n_t &= -vn_x + \alpha n - \beta n^2. \end{aligned}$$

Applying Laplace transforms to both equations we obtain

$$\begin{aligned} \mathcal{L}[\rho_t] &= \mathcal{L}[nv - \gamma\rho], \\ \mathcal{L}[n_t] &= \mathcal{L}[-vn_x + \alpha n - \beta n^2]. \end{aligned} \quad (3.38)$$

Hence

$$\begin{aligned} s\mathcal{L}[\rho] - \rho(x, 0) &= \mathcal{L}[nv - \gamma\rho], \\ s\mathcal{L}[n] - n(x, 0) &= \mathcal{L}[-vn_x + \alpha n - \beta n^2]. \end{aligned} \quad (3.39)$$

Rearranging and applying inverse Laplace transforms, we get

$$\begin{aligned}\rho(x, t) &= \rho(x, 0) + \mathcal{L}^{-1} \left[ \frac{1}{s} \mathcal{L}[nv - \gamma\rho] \right], \\ n(x, t) &= n(x, 0) + \mathcal{L}^{-1} \left[ \frac{1}{s} \mathcal{L}[-vn_x + \alpha n - \beta n^2] \right].\end{aligned}\quad (3.40)$$

LDM assumes a series solution of the functions  $\rho(x, t)$  and  $n(x, t)$ , so we suppose

$$\begin{aligned}\rho(x, t) &= \sum_{m=0}^{\infty} \hat{\rho}_m(x, t), \\ n(x, t) &= \sum_{m=0}^{\infty} \hat{n}_m(x, t).\end{aligned}\quad (3.41)$$

Therefore substituting (3.41) into (3.40) we obtain

$$\begin{aligned}\sum_{m=0}^{\infty} \hat{\rho}_m(x, t) &= \rho(x, 0) + \mathcal{L}^{-1} \left[ \frac{1}{s} \mathcal{L} \left[ v \sum_{m=0}^{\infty} \hat{n}_m(x, t) - \gamma \sum_{m=0}^{\infty} \hat{\rho}_m(x, t) \right] \right] \\ \sum_{m=0}^{\infty} \hat{n}_m(x, t) &= n(x, 0) + \\ &\quad \mathcal{L}^{-1} \left[ \frac{\mathcal{L}[-v \sum_{m=0}^{\infty} (\hat{n}_m(x, t))_x + \alpha \sum_{m=0}^{\infty} \hat{n}_m(x, t) - \sum_{m=0}^{\infty} A_m]}{s} \right]\end{aligned}\quad (3.42)$$

where the nonlinear term  $\beta n^2$  is decomposed as

$$A_m = \beta \sum_{i=0}^m (\hat{n}_i \times \hat{n}_{m-i}), \quad \text{for } m = 0, 1, 2, \dots \quad (3.43)$$

where  $A_m$  are Adomian polynomials of  $\hat{n}_0, \hat{n}_1, \hat{n}_2, \dots, \hat{n}_m$ . The  $A_m$  terms are therefore

$$\begin{aligned}A_0 &= \beta(\hat{n}_0 \hat{n}_0) \\ A_1 &= \beta(\hat{n}_0 \hat{n}_1 + \hat{n}_1 \hat{n}_0) \\ A_2 &= \beta(\hat{n}_0 \hat{n}_2 + \hat{n}_1 \hat{n}_1 + \hat{n}_2 \hat{n}_0) \\ &\vdots\end{aligned}$$

From equation (3.42) we can deduce the recursive relation for  $\rho(x, t)$  and  $n(x, t)$  using

$$\begin{aligned}\hat{\rho}_0(x, t) &= \rho(x, 0), \\ \hat{\rho}_{m+1}(x, t) &= \mathcal{L}^{-1} \left[ \frac{\mathcal{L}[v \sum_{m=0}^{\infty} \hat{n}_m(x, t) - \gamma \sum_{m=0}^{\infty} \hat{\rho}_m(x, t)]}{s} \right] \quad \text{for } m \geq 0\end{aligned}\quad (3.44)$$

$$\begin{aligned}\hat{n}_0(x, t) &= n(x, 0), \\ \hat{n}_{m+1}(x, t) &= \mathcal{L}^{-1} \left[ \frac{\mathcal{L}[-v \sum_{m=0}^{\infty} (\hat{n}_m(x, t))_x + \alpha \sum_{m=0}^{\infty} \hat{n}_m(x, t) - A_m]}{s} \right], \quad \text{for } m \geq 0.\end{aligned}\quad (3.45)$$

Hence using the same initial conditions from equation (3.34), we obtain the series solution for  $\rho$  and  $n$ , which for convenience were computed using Maple:

$$\begin{aligned}\rho(x, t) &= \frac{\alpha v}{2\beta\gamma}(1 - \tanh(\theta x)) - \frac{\alpha v}{2\beta}(\tanh(\phi x) - \tanh(\theta x)) t \\ &\quad + \frac{\alpha v}{8\beta}((2\phi v + \alpha) \operatorname{sech}^2(\phi x) + 2\gamma(\tanh(\phi x) - \tanh(\theta x))) t^2 + \dots\end{aligned}\quad (3.46)$$

$$\begin{aligned}n(x, t) &= \frac{\alpha}{2\beta}(1 - \tanh(\phi x)) + \frac{\alpha}{4\beta}(2\phi v + \alpha) \operatorname{sech}^2(\phi x) t \\ &\quad + \frac{\alpha}{8\beta}(2\phi v + \alpha)^2 \operatorname{sech}^2(\phi x) \tanh(\phi x) t^2 + \dots\end{aligned}\quad (3.47)$$

From equation (3.47) we notice that these terms are identical to the Taylor series about  $t = 0$  of the closed form solution  $n(x, t) = \frac{\alpha}{2\beta} \left( 1 - \tanh \left( \phi \left( x - \left( \frac{\alpha}{2\phi} + v \right) t \right) \right) \right)$ . We cannot easily conclude the same for the series generated for  $\rho$  in equation (3.46), since the series for equation (3.36) cannot be easily generated. However the result obtained for  $\rho$  can still be used to plot the distribution of the hyphae and predict the kinematic state of the system (see Section 3.3). Furthermore using computer software such as Maple, we can take the small  $t$  limit of (3.32) and find that it does indeed equal (3.46).

### 3.1.4.3 Comparing LDM to numerical solutions

The numerical solution to the system of equations in equation (3.31) representing the YWD phenotype, has been plotted in Maple with initial conditions (3.34) using '*pdesolve*'. This will be used to compare to the series solution for equation (3.46) and (3.47). All parameters will be set to unity (i.e.  $\alpha, \beta, \gamma, \theta, \phi$  and  $v$ ) for simplicity in this section.

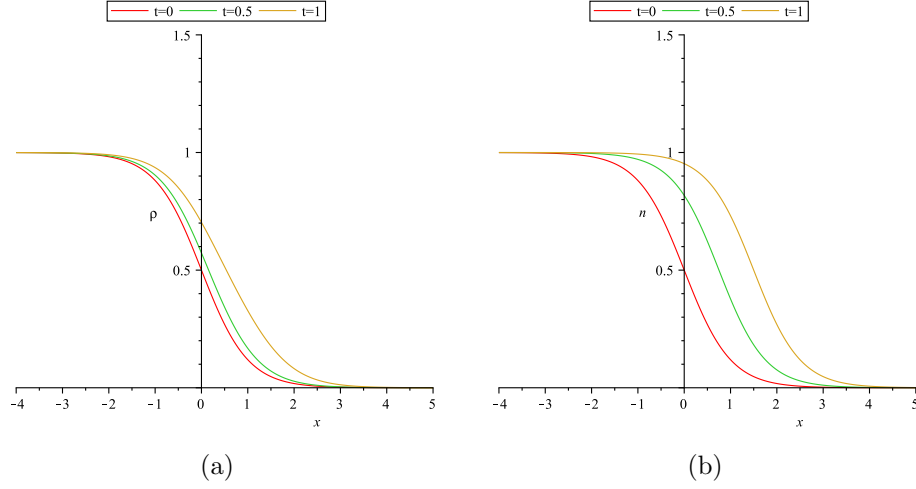


**Figure 3.1:** *Plot of YWD phenotype propagation represented by equation (3.31) with initial conditions in (3.34) using parameter values  $\alpha = \beta = \gamma = \theta = \phi = v = 1$  shown at times  $t = 0, 0.5$  and  $1$ . (a) shows typical propagation of hyphae and (b) shows typical propagation of tips.*

A propagating wave can be seen in Figures 3.1(a) and 3.1(b). This kind of behaviour was observed earlier in Section 2.3.3, where the system of equations were solved numerically in Matlab (see Figure 2.6(b)). Interestingly a delay in the proliferation of  $\rho$  is observed prior to forming a travelling wave in Figure 3.1(a). This delay is expected since  $\rho$  should follow behind  $n$ , but this shift is not included in the initial conditions for  $\rho$  and  $n$ .

Using the Laplace decomposition method with initial conditions (3.34), the leading terms for  $\rho$  and  $n$  were generated, as depicted in equations (3.46) and (3.47), by utilising Maple to perform the algebraic manipulations. Figure 3.2 compares the sum of the first 10 terms for  $n(x, t)$  against the exact solution.

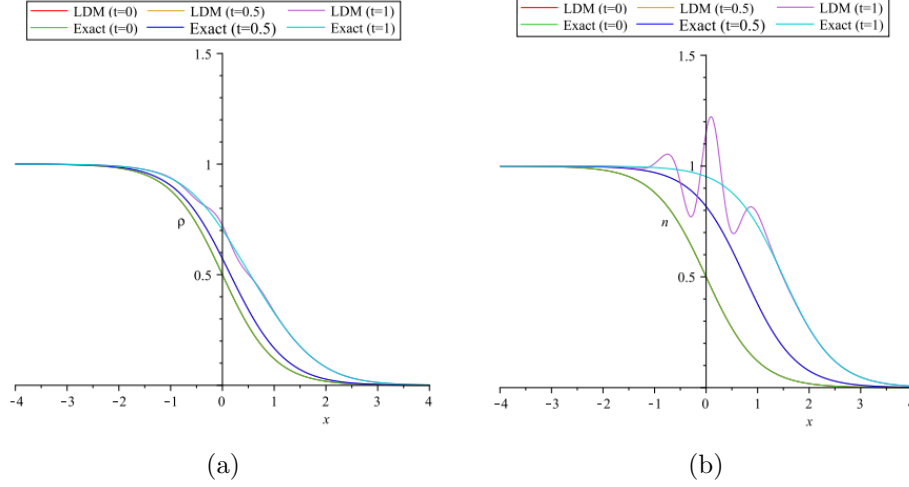


**Figure 3.2:** A comparison plot of the numerical solutions generated from equations (3.36) and (3.37) of YWD phenotype with initial data (3.34) with 10 terms generated using LDM from equations (3.44) and (3.45) using parameter values  $\alpha = \beta = \gamma = \theta = \phi = v = 1$  are shown at times  $t = 0, 0.5$  and  $1$ . Figure (a) is a plot of hyphae and (b) is a plot of tips.

It can be seen that for small times, 10 terms in the truncated series are more than sufficient to produce propagating behaviour at the leading edge. However, for larger times oscillations seems to arise at the peaks of the curve behind the leading edge suggesting the series diverges but the leading edge of the wave front appear to be in good agreement with the exact solution. This maybe due to the number of Adomian polynomials used. Hence in our example, our series for  $n(x, t)$  was truncated at  $n_{10}$ , so as time increases, it creates spurious oscillations. If we compute more terms for  $n(x, t)$  then we should anticipate a smoother plot at later times and a more accurate result. This can be observed in Figures 3.3 and 3.4 where the series has been computed for 20 and 50 terms respectively.

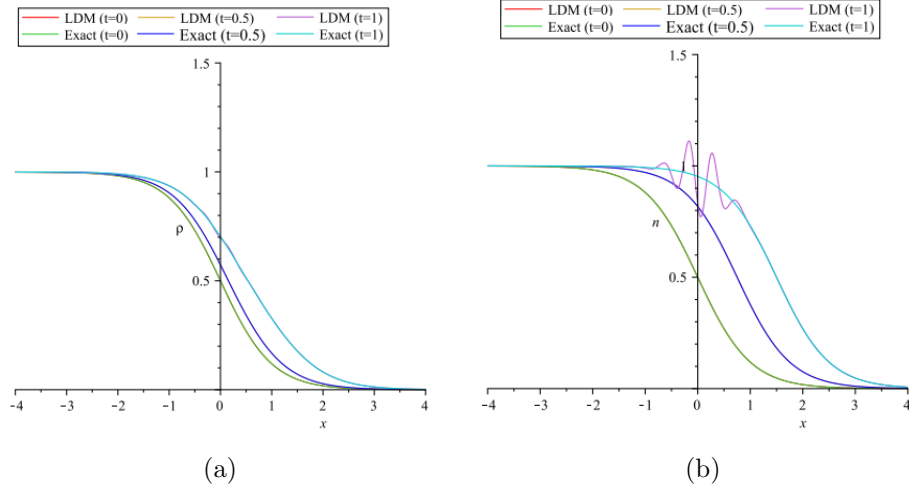


**Figure 3.3:** A comparison plot of the numerical solutions generated from equations (3.36) and (3.37) of YWD phenotype with initial data (3.34) with 20 terms generated using LDM from equations (3.44) and (3.45) using parameter values  $\alpha = \beta = \gamma = \theta = \phi = v = 1$  are shown at times  $t = 0, 0.5$  and 1. (a) is a plot of hyphae and (b) is a plot of tips.

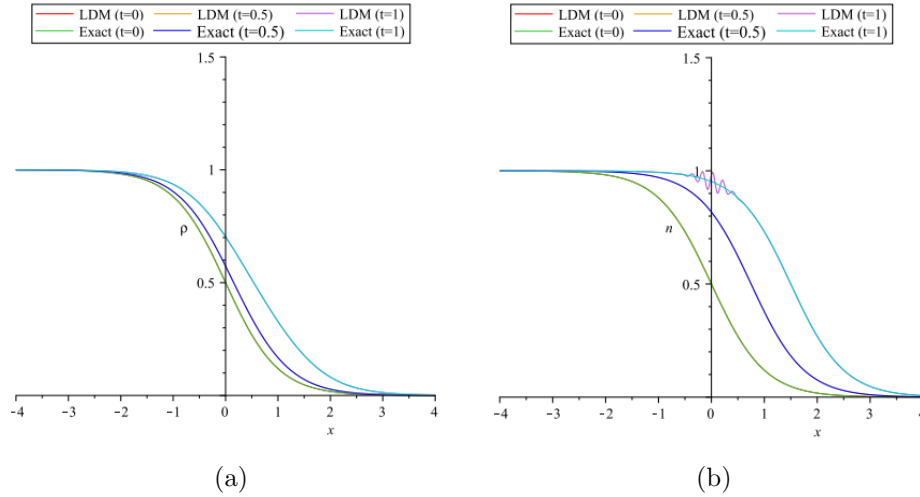


**Figure 3.4:** A comparison plot of the numerical solutions generated from equations (3.36) and (3.37) of YWD phenotype with initial data (3.34) with 50 terms generated using LDM from equations (3.44) and (3.45) using parameter values  $\alpha = \beta = \gamma = \theta = \phi = v = 1$  are shown at times  $t = 0, 0.5$  and 1. (a) is a plot of hyphae propagation and (b) is a plot of tip propagation.

Clearly from Figures 3.2 to 3.4 as the number of terms in the series approximation for  $n(x, t)$  increases, the series solution generated via LDM produce a smoother distribution that more closely resembles the exact solution (Figure 3.1(b)).

For the LDM-generated solutions to avoid spurious oscillations, it is essential that the resultant series converges. This convergence is guaranteed for small times but not necessarily for larger times. The convergence theory of ADM or LDM will not be explored in this thesis but has been extensively discussed by various authors (Cherruault, 1990; Abbaoui and Cherruault, 1994a,b; Abdelrazec, 2008; Rach, 2008; Abdelrazec and Pelinovsky, 2011). Therefore we conclude that the semi-analytical solution produced by the Laplace decomposition method is a very good approximation, at least for small times, for the fungal phenotype YWD.

### 3.1.5 FHD Phenotype revisited

The phenotype FHD introduced in Chapter 2 corresponds to

$$\begin{aligned}\rho_t &= vn - \gamma\rho, \\ n_t &= -vn_x + \alpha\rho - \beta\rho n,\end{aligned}\tag{3.48}$$

and had no general solution, except for specific initial data. Hence, solving equation (3.48) using initial conditions (3.34) we obtain the following particular solutions:

$$\rho(x, t) = \frac{\alpha v}{2\beta\gamma} - \frac{\alpha v}{2\beta\gamma} \tanh\left(\left(\frac{2\gamma^2 - \alpha v}{4\gamma v}\right)x - \left(\frac{\gamma}{2}\right)t\right),\tag{3.49}$$

$$\begin{aligned}n(x, t) &= \frac{3\alpha}{4\beta} - \frac{\alpha}{2\beta} \tanh\left(\left(\frac{2\gamma^2 - \alpha v}{4\gamma v}\right)x - \left(\frac{\gamma}{2}\right)t\right) \\ &\quad - \frac{\alpha}{4\beta} \tanh\left(\left(\frac{2\gamma^2 - \alpha v}{4\gamma v}\right)x - \left(\frac{\gamma}{2}\right)t\right)^2.\end{aligned}\tag{3.50}$$

Similar to the previous section, we apply the Laplace transform to both equations (3.48), rearrange and apply inverse Laplace transforms, to get

$$\begin{aligned}\rho(x, t) &= \rho(x, 0) + \mathcal{L}^{-1}\left[\frac{\mathcal{L}[vn - \gamma\rho]}{s}\right], \\ n(x, t) &= n(x, 0) + \mathcal{L}^{-1}\left[\frac{\mathcal{L}[-vn_x + \alpha\rho - \beta\rho n]}{s}\right].\end{aligned}\tag{3.51}$$



LDM assumes a series solution of the functions  $\rho(x, t)$  and  $n(x, t)$ , thus we suppose

$$\begin{aligned}\rho(x, t) &= \sum_{m=0}^{\infty} \hat{\rho}_m(x, t), \\ n(x, t) &= \sum_{m=0}^{\infty} \hat{n}_m(x, t).\end{aligned}\tag{3.52}$$

Therefore substituting equations in (3.52) into (3.51) we obtain

$$\begin{aligned}\sum_{m=0}^{\infty} \hat{\rho}_m(x, t) &= \rho(x, 0) + \mathcal{L}^{-1} \left[ \frac{\mathcal{L}[v \sum_{m=0}^{\infty} \hat{n}_m(x, t) - \gamma \sum_{m=0}^{\infty} \hat{\rho}_m(x, t)]}{s} \right] \\ \sum_{m=0}^{\infty} \hat{n}_m(x, t) &= n(x, 0) + \\ &\mathcal{L}^{-1} \left[ \frac{\mathcal{L}[-v \sum_{m=0}^{\infty} (\hat{n}_m(x, t))_x + \alpha \sum_{m=0}^{\infty} \hat{\rho}_m(x, t) - \sum_{m=0}^{\infty} A_m]}{s} \right]\end{aligned}\tag{3.53}$$

where the non-linear term  $\beta \rho n$  is decomposed as

$$A_m = \beta \sum_{i=0}^m (\hat{\rho}_i \times \hat{n}_{m-i}), \quad \text{for } m = 0, 1, 2, \dots\tag{3.54}$$

where  $A_m$  are Adomian polynomials and are given by

$$\begin{aligned}A_0 &= \beta \hat{\rho}_0 \hat{n}_0 \\ A_1 &= \beta (\hat{\rho}_0 \hat{n}_1 + \hat{\rho}_1 \hat{n}_0) \\ A_2 &= \beta (\hat{\rho}_0 \hat{n}_2 + \hat{\rho}_1 \hat{n}_1 + \hat{\rho}_2 \hat{n}_0) \\ &\vdots\end{aligned}$$

Therefore from equation (3.53) we can deduce the recursive relation for  $\hat{\rho}_m(x, t)$  and  $\hat{n}_m(x, t)$  to be

$$\begin{aligned}\hat{\rho}_0(x, t) &= \rho(x, 0), \\ \hat{\rho}_{m+1}(x, t) &= \mathcal{L}^{-1} \left[ \frac{\mathcal{L}[v \hat{n}_m(x, t) - \gamma \hat{\rho}_m(x, t)]}{s} \right], \quad \text{for } m \geq 0\end{aligned}\tag{3.55}$$

$$\begin{aligned}\hat{n}_0(x, t) &= n(x, 0), \\ \hat{n}_{m+1}(x, t) &= \mathcal{L}^{-1} \left[ \frac{\mathcal{L}[-v (\hat{n}_m(x, t))_x + \alpha \hat{\rho}_m(x, t) - A_m]}{s} \right], \quad \text{for } m \geq 0.\end{aligned}\tag{3.56}$$

Hence using the same initial conditions from equation (3.34), we obtain the leading terms for  $\rho$  and  $n$  which for convenience were computed using Maple.

$$\rho(x, t) = \frac{\alpha v}{2\beta\gamma}(1 - \tanh(\theta x)) - \frac{\alpha v}{2\beta}(\tanh(\phi x) - \tanh(\theta x)) t \quad (3.57)$$

$$\begin{aligned} & -\frac{\alpha v}{8\beta\gamma} [-2\phi\gamma v - \alpha v + (\alpha v + 2\gamma^2 + \alpha v \tanh(\phi x)) \tanh(\theta x) + \\ & (-\alpha v - 2\gamma^2 + 2\phi\gamma v \tanh(\phi x)) \tanh(\phi x)] t^2 + \dots \\ n(x, t) &= \frac{\alpha}{2\beta}(1 - \tanh(\phi x)) \quad (3.58) \\ & -\frac{\alpha v}{4\beta\gamma} [(\tanh(\phi x) + 1)(2\phi\gamma \tanh(\phi x) + \alpha \tanh(\theta x) - 2\phi\gamma - \alpha)] t + \dots \end{aligned}$$

The results were obtained on a machine with ‘AMD E-300 APU with Radeon(tm) HD Graphics 1.30 GHz’ processor and 8GB of RAM. The total time taken to generate 30 terms on average was 2000 seconds. Setting all parameters to unity and plotting the first 30 terms for  $\rho$  and  $n$  we obtain a familiar travelling wave profile (Figure 3.5).

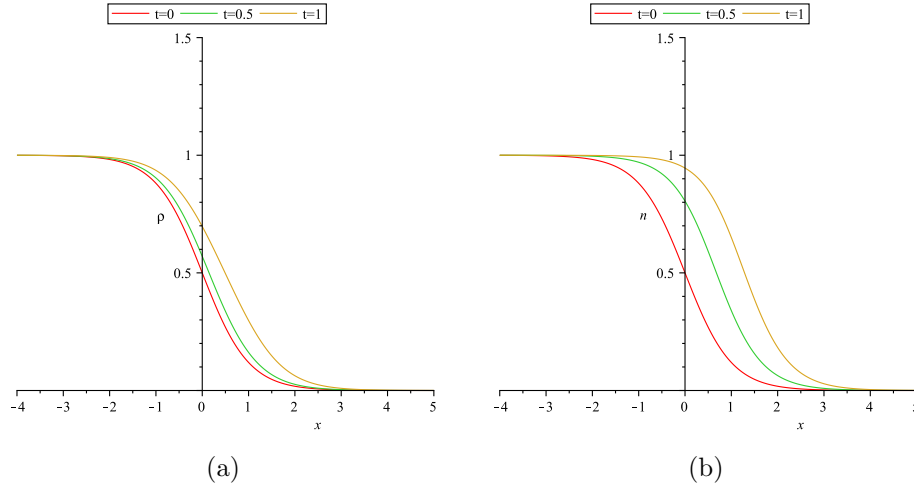


**Figure 3.5:** A comparison plot of the numerical solution for equations in (3.48) with initial data (3.34) of FHD phenotype propagation with 30 terms generated using LDM from equations (3.55) and (3.56) using parameter values  $\alpha = \beta = \gamma = \theta = \phi = v = 1$  shown at times  $t = 0, 0.5$  and  $1$ . Figure (a) is a plot of hyphae propagation and Figure (b) is a plot of tip propagation.

We have successfully constructed a semi-analytical approach to solving a system of partial differential equations using the Laplace decomposition method,

which has not been previously obtained. The LDM produces a good approximation as we can observe by comparing Figure 3.5 to the behaviour we saw earlier when we solved the set of equations numerically in Matlab (Figure 2.2(b)). Further investigation is required to compare the accuracy of the solution for larger times. Initially we have explored the current system for large times and found that the wave front is accurately depicted by the series, whereas behind the wave front was not very accurate, as will now be explained.

## 3.2 Application of LDM to track the position of leading edge of wave front

In this section we will explore the dynamics of the leading wave front for large times for the YWD and FHD phenotypes. The system of equations for the YWD phenotype in (3.31) and FHD phenotype (3.48) was shown previously to display a travelling wave distribution.

It was shown previously that the series generated with LDM for the system of equations in (3.31) is in excellent agreement with the closed form solutions for small time (e.g. Figures 3.1, 3.2, 3.3 and 3.4). As more terms were added, the plot of the profile became smoother and approached the closed form solution and for large times there appeared to be spurious oscillations forming behind the leading edge. However, the leading edge did not seem to be affected and we found that by adding more terms to the series, the position of the wave front for larger times could be obtained with greater accuracy.

To track the leading wave position we suppose  $x_0$  is the greatest value of  $x$  such that the distribution is equal to some arbitrary value at time  $t_0$ , (e.g. for tips,  $n(x_0, t_0) = n_c$ ). The position  $x_0$  at time  $t_0$  will then be compared between the closed form solutions (3.36) and (3.37) (for YWD phenotype) and the series generated using LDM, i.e. (3.44) and (3.45). Due to the lack of an explicit solution, the FHD phenotype in equation (3.48) with initial condition (3.34), will be solved numerically and the solution will be compared to the series generated via LDM in equations (3.55) and (3.56).

### 3.2.1 Wave front of YWD

The closed form solution (3.36) and (3.37) was used to determine the position  $x$  of the leading edge of the distribution at various times  $t$ , i.e. the greatest value  $x_c$  such that  $n(x_c, t) = n_c$  or  $\rho(x_c, t) = \rho_c$  where  $n_c = \rho_c = 0.1$  and other parameters were taken to be unity. These critical values of  $x$  were solved numerically using Maple (Tables 3.1 and 3.2). Additionally the LDM generated series (3.46) and (3.47) were used to determine the same position but where different numbers of terms were used in the series expansion.

| Time | Equation (3.36) | Series (3.46): 5 terms | Series (3.46): 10 terms | Series (3.46): 50 terms |
|------|-----------------|------------------------|-------------------------|-------------------------|
| 0    | 1.0986          | 1.0986                 | 1.0986                  | 1.0986                  |
| 2    | 3.3369          | 3.0426                 | 3.3883                  | 3.3369                  |
| 4    | 6.3361          | 4.5081                 | 5.9282                  | 6.3386                  |
| 6    | 9.3361          | 5.4382                 | 7.7109                  | 9.2996                  |
| 8    | 12.3361         | 6.1172                 | 9.0456                  | 12.3585                 |
| 10   | 15.3361         | 6.6515                 | 10.1037                 | 15.4451                 |

**Table 3.1:** *The position of the leading edge of hyphae for YWD phenotype from the system of equations (3.31) determined by the greatest value of  $x_c$  where  $\rho(x_c, t) = 0.1$  with  $\alpha = \beta = \gamma = \theta = \phi = v = 1$  and with initial data (3.34) is calculated using the analytical solution (3.36) and from truncated series in equation (3.46) comprising respectively the first 5, 10 and 50 terms.*

| Time | Equation (3.37) | Series (3.47): 5 terms | Series (3.47): 10 terms | Series (3.47): 50 terms |
|------|-----------------|------------------------|-------------------------|-------------------------|
| 0    | 1.0986          | 1.0986                 | 1.0986                  | 1.0986                  |
| 2    | 4.0986          | 3.7420                 | 4.1096                  | 4.0986                  |
| 4    | 7.0986          | 5.2033                 | 6.6219                  | 7.0987                  |
| 6    | 10.0986         | 6.1338                 | 7.7109                  | 10.0948                 |
| 8    | 13.0986         | 6.8133                 | 9.7382                  | 13.1151                 |
| 10   | 16.0986         | 7.3480                 | 10.7969                 | 16.1456                 |

**Table 3.2:** *The position of the leading edge for tips for the YWD phenotype from system of equations in (3.31) determined by the greatest value of  $x_c$  where  $n(x_c, t) = 0.1$  with  $\alpha = \beta = \gamma = \theta = \phi = v = 1$  and with initial data (3.34) is calculated using the analytical solution (3.37) and from truncated series in equation (3.47) comprising respectively the first 5, 10 and 50 terms.*

It is clear from Tables 3.2 and 3.1, as more terms are added to the series generated by LDM the accuracy for the position of the leading edge for the tips and hyphae do indeed increase greatly.

### 3.2.2 Wave front of FHD

Using the same approach as in the previous section we obtain Tables 3.3 and 3.4 containing information regarding the comparisons made between the semi-analytical result generated via LDM and numerical solutions for the tips and hyphae of the FHD phenotype. The position of the leading wave of the distributions have been calculated at an arbitrary critical value of  $n_c = \rho_c = 0.1$ .

| Time | Equation (3.49) | Series (3.57): 5 terms | Series (3.57): 10 terms | Series (3.57): 50 terms |
|------|-----------------|------------------------|-------------------------|-------------------------|
| 0    | 1.0986          | 1.0986                 | 1.0986                  | 1.0986                  |
| 2    | 2.8600          | 2.8779                 | 2.8779                  | 2.8606                  |
| 4    | 5.1686          | 4.0981                 | 5.0514                  | 5.1690                  |
| 6    | 7.4762          | 7.4751                 | 6.7156                  | 7.4751                  |
| 8    | 9.7831          | 5.6531                 | 8.001                   | 9.7691                  |
| 10   | 12.0902         | 6.1761                 | 9.0359                  | 12.0937                 |

**Table 3.3:** *The position of the leading edge of hyphae for FHD phenotype from the system of equations (3.48) determined by the greatest value of  $x_c$  where  $\rho(x_c, t) = 0.1$  with  $\alpha = \beta = \gamma = \theta = \phi = v = 1$  and with initial data (3.34) is calculated numerically. The truncated series in equation (3.57) comprising respectively the first 5, 10 and 50 terms are shown at times  $t \geq 0$ .*

| Time | Equation (3.50) | Series (3.58): 5 terms | Series (3.58): 10 terms | Series (3.58): 50 terms |
|------|-----------------|------------------------|-------------------------|-------------------------|
| 0    | 1.0986          | 1.0986                 | 1.0986                  | 1.0986                  |
| 2    | 3.5000          | 3.5079                 | 3.5079                  | 3.4997                  |
| 4    | 5.8078          | 4.7112                 | 5.6507                  | 5.8057                  |
| 6    | 8.1148          | 8.1097                 | 7.3126                  | 8.1097                  |
| 8    | 10.4214         | 6.2788                 | 8.5982                  | 10.4118                 |
| 10   | 12.7276         | 6.8059                 | 9.6323                  | 12.7245                 |

**Table 3.4:** *The position of the leading edge for tips for the FHD phenotype from system of equations in (3.48) determined by the greatest value of  $x_c$  where  $n(x_c, t) = 0.1$  with  $\alpha = \beta = \gamma = \theta = \phi = v = 1$  and with initial data (3.34) is calculated numerically. The truncated series in equation (3.58) comprising respectively the first 5, 10 and 50 terms is shown at times  $t \geq 0$ .*

From Tables 3.4 and 3.3 it can be seen that the accuracy for large times of the position of the leading wave front increases with the addition of higher order terms.

Our investigation in this section demonstrates that the Laplace decomposition method accurately tracks the position of the leading wave. Its advantages over numerical methods lies in the fact that cumulative errors are not introduced

as in other numerical methods, while also boundary conditions do not need to be considered to obtain useful results. Also once a general series is determined, solutions can be obtained for different parameters without the need for solving the system of equations with each change.

Despite the advantages, there is also a noticeable disadvantage, namely the solution behind the leading edge is problematic. In Figures 3.2 - 3.4 ‘wiggles’ can be seen immediately behind the leading edge for large times. These wiggles seem to reduce by including more terms in the series generated.

### **3.3 Kinematic properties of an advancing wave front**

#### **3.3.1 Inspiration and motivation**

Many systems of partial differential equations (PDEs) display travelling wave solutions. Traditionally, and especially in a single spatial dimension, the development of such systems is investigated analytically, e.g. by using substitutions of the form  $z = x - ct$ . However, for highly non-linear functions, or complicated initial data, it may be too complex to extract such solutions, even if they exist. While numerical simulations can provide insight into the behaviour of the system, parameter values and initial data have to be chosen in advance and it is therefore often difficult to isolate the influence of either on the entire system. Furthermore, such solutions may only describe the long term behaviour and not the initial development of the system which is influenced by initial data (Safuan et al., 2016) and can be especially important when considering population dynamics. For example, in infectious diseases, the early dynamics of the disease in a spatially organised population is determined by its initial distribution (Keeling and Rohani, 2008), in ecology the progress of non-native species invading an otherwise empty environment is of interest (Lockwood et al., 2013) and in medicine the progress of a drug towards a tumour is dependent on the initial concentration of the drug (Giráldez and Herrero, 2009).

An additional problem faced in applications when using PDEs is that the equations can predict the presence of a population at low densities that are in practice, impossible to measure in the physical system being considered. Thus the tracking of a leading edge of the population, namely the position at which a

population can be measured, is crucial to allow comparison between theoretical and experimental results. This is certainly the case with fungi where hyphae can have diameters of order 10 microns. In the following section, an analytical approach is proposed that can be used to describe the initial behaviour of such leading edges by constructing algebraic expressions for their initial velocity and acceleration. This novel approach is based on constructing a series solution of the model equations utilising the Laplace decomposition method (LDM) and allows the influence of the initial data and all model parameters to be easily observed. To illustrate the method we will use many of the same PDEs used in the previous section in particular the YWD and FHD phenotypes, i.e. equations (3.31) and (3.48) respectively.

### 3.3.2 Formulation of method

Suppose  $u(x, t)$  satisfies  $u_t = f(x, t, u_x, u_{xx}, \dots)$  for a specified function  $f$ , which may also include a large number of parameters, with given initial data  $u(x, 0) = u_0(x)$  representing an ‘invasive’ population, i.e.  $u_0(x) \rightarrow 0$  as  $x \rightarrow \infty$  and  $u_0(x) > 0$  as  $x \rightarrow -\infty$ . As time passes, the function  $u$  moves. To track how the distribution of  $u$  develops over time, suppose  $x_0$  is the greatest value of  $x$  such that  $u(x_0, t_0) = u_c$  for some arbitrary  $u_c$  at time  $t_0$  taken to be in the range of  $u$  and that satisfies  $u_x(x_0, t_0) < 0$ . The value  $u_c$ , denoting the leading edge of the distribution, could represent a critical density below which the population cannot be detected. After a time  $\Delta t$  has elapsed, suppose the leading edge has moved a distance  $\Delta x$  so that  $u(x_0 + \Delta x, t_0 + \Delta t) = u_c$ . More precisely, suppose

$$\Delta x = a_1 \Delta t + a_2 \Delta t^2 + a_3 \Delta t^3 + \dots \quad (3.59)$$

since  $\Delta x$  is position and  $\Delta t$  is time. The velocity is given by

$$\frac{d\Delta x}{d\Delta t} = a_1 + 2a_2 \Delta t + 3a_3 \Delta t^2 + \dots$$

while acceleration is

$$\frac{d^2 \Delta x}{d\Delta t^2} = 2a_2 + 6a_3 \Delta t + \dots$$

Thus the instantaneous velocity and acceleration are  $a_1$  and  $2a_2$  respectively. Using Taylor series about  $(x_0, t_0)$  i.e.  $\Delta x \rightarrow 0$  and  $\Delta t \rightarrow 0$  we get

$$\begin{aligned} u(x_0 + \Delta x, t_0 + \Delta t) &= u(x_0, t_0) + \Delta x \frac{\partial u}{\partial x} + \Delta t \frac{\partial u}{\partial t} \\ &+ \frac{1}{2!} \left[ \Delta x^2 \frac{\partial^2 u}{\partial x^2} + 2\Delta x \Delta t \frac{\partial^2 u}{\partial x \partial t} + \Delta t^2 \frac{\partial^2 u}{\partial t^2} \right] + \dots \end{aligned}$$

When tracking the position of the leading edge, at the critical value then  $u(x_0 + \Delta x, t_0 + \Delta t) = u(x_0, t_0) = u_c$ . It follows that

$$0 = \Delta x \frac{\partial u}{\partial x} + \Delta t \frac{\partial u}{\partial t} + \frac{1}{2!} \left[ \Delta x^2 \frac{\partial^2 u}{\partial x^2} + 2\Delta x \Delta t \frac{\partial^2 u}{\partial x \partial t} + \Delta t^2 \frac{\partial^2 u}{\partial t^2} \right] + \dots \quad (3.60)$$

Substituting (3.59) into equation (3.60) and collecting terms in  $\Delta t$ ,  $\Delta t^2$  etc, we obtain the following

$$0 = \Delta t [a_1 u_x + u_t] + \Delta t^2 \left[ a_2 u_x + \frac{a_1^2}{2} u_{xx} + a_1 u_{xt} + \frac{1}{2} u_{tt} \right] + \mathcal{O}(\Delta t^3). \quad (3.61)$$

Neglecting higher order terms and comparing coefficients allows  $a_1$  and  $a_2$  to be determined. Hence comparing  $\Delta t$  terms the instantaneous velocity of the wave front at  $(x_0, t_0)$  is

$$\begin{aligned} 0 &= a_1 u_x + u_t \\ \therefore \text{Initial velocity} &= -\frac{u_t}{u_x}. \end{aligned} \quad (3.62)$$

The acceleration is determined by comparing the  $\Delta t^2$  terms and substituting equation (3.62) into equation (3.61), i.e.

$$2a_2 = 2 \frac{u_{xt} u_t}{u_x^2} - \frac{u_{xx} u_t^2}{u_x^3} - \frac{u_{tt}}{u_x}. \quad (3.63)$$

After some algebraic manipulation the acceleration equation in (3.63) can be expressed as

$$\text{Initial acceleration} = \frac{2u_t u_x u_{xt} - u_x^2 u_{tt} - u_t^2 u_{xx}}{u_x^3} \quad (3.64)$$

provided  $u_x$  is non-zero.



### Simple example: transport equation

The equation  $u_t = -vu_x$  has a solution  $u(x, t) = u_0(x - vt)$  corresponding to the initial distribution  $u(x, 0) = u_0(x)$  propagating with a constant velocity  $v$ . Notice  $-u_t/u_x = v$  as above. Further, by noting that  $u_{tt} = -vu_{xt}$ , the acceleration is easily shown to be zero. More examples on the utilisation of this technique can be found in Choudhury et al. (2016).

While these formulae provide simple estimates of the velocity and acceleration of the leading edge of an advancing wave front, they often require the solution of the corresponding PDE to be known. If such a solution is unknown, a series solution can be obtained using the Laplace Decomposition Method to generate the corresponding formulae in terms of the original model parameters.

### 3.3.3 LDM series solution utilisation

We observed in Section 3.1 that the series generated by the decomposition method corresponds to a Taylor series about  $t = 0$  of the solution. The resultant series can therefore be written as,

$$u(x, t) = \bar{u}_0 + \bar{u}_1(x)t + \bar{u}_2(x)t^2 + \dots$$

which note, is only true for homogeneous PDEs. Hence the initial velocity of the leading wave front (i.e. when  $t = 0$  at  $x = x_0$ ) is from equation (3.62)

$$-\frac{u_t}{u_x} = -\frac{\bar{u}_1}{\bar{u}_0'} \quad (3.65)$$

and from equation (3.64) the initial acceleration is

$$\frac{2u_t u_x u_{xt} - u_{tt} u_x^2 - u_t^2 u_{xx}}{u_x^3} = \frac{2\bar{u}_0' \bar{u}_1 \bar{u}_1' - 2\bar{u}_2 (\bar{u}_0')^2 - \bar{u}_1^2 \bar{u}_0''}{(\bar{u}_0')^3} \quad (3.66)$$

where primes denotes differentiation with respect to  $x$  and the functions are evaluated at  $x = x_0$ .

### 3.3.3.1 YWD phenotype: decoupled equations

In the previous chapter we looked at a model which depicted the fungal phenotype YWD and was represented by the system of equations

$$\rho_t = nv - \gamma\rho, \quad (3.67)$$

$$n_t = -vn_x + \alpha n - \beta n^2. \quad (3.68)$$

These equations have previously been shown to display a travelling wave solution. For particular initial data, it was even possible to construct a closed form solution (see Section 2.3.3.1). Since the equations (3.67) and (3.68) are decoupled, the second equation (3.68) can be considered in isolation. Recall the initial conditions used previously

$$\rho(x, 0) = \frac{\alpha v}{\beta \gamma} \left( \frac{1 - \tanh(\theta x)}{2} \right), \quad n(x, 0) = \frac{\alpha}{\beta} \left( \frac{1 - \tanh(\phi x)}{2} \right), \quad (3.69)$$

where  $\alpha v/\beta \gamma$  and  $\alpha/\beta$  correspond to the non-zero equilibria of the system of equations in (3.67) and (3.68). Equation (3.68) then has the closed form solution

$$n(x, t) = \frac{\alpha}{2\beta} \left( 1 - \tanh \left( \phi \left( x - \left[ v + \frac{\alpha}{2\phi} \right] t \right) \right) \right). \quad (3.70)$$

It can clearly be seen that this is a travelling wave solution with wave speed  $v + \alpha/2\phi$ . Upon applying the LDM to equations (3.67) and (3.68) with the initial conditions in (3.69) generates

$$\rho(x, t) = \frac{\alpha v}{2\beta \gamma} (1 - \tanh(\theta x)) - \frac{\alpha v}{2\beta} (\tanh(\phi x) - \tanh(\theta x)) t \quad (3.71)$$

$$+ \frac{\alpha v}{8\beta} ((2\phi v + \alpha) \operatorname{sech}^2(\phi x) + 2\gamma (\tanh(\phi x) - \tanh(\theta x))) t^2 + \dots$$

$$n(x, t) = \frac{\alpha}{2\beta} (1 - \tanh(\phi x)) + \frac{\alpha}{4\beta} (2\phi v + \alpha) \operatorname{sech}^2(\phi x) t \quad (3.72)$$

$$+ \frac{\alpha}{8\beta} (2\phi v + \alpha)^2 \operatorname{sech}^2(\phi x) \tanh(\phi x) t^2 + \dots$$

(see Section 3.1.4.2). Thus using the terms from equation (3.72) and substituting them into equations (3.65) and (3.66) accordingly, we see that for the tip

distribution gives an initial velocity of

$$-\frac{\bar{n}_1}{\bar{n}_0'} = v + \frac{\alpha}{2\phi}, \quad (3.73)$$

and the initial acceleration is

$$\frac{2\bar{n}_0'\bar{n}_1\bar{n}_1' - 2\bar{n}_2(\bar{n}_0')^2 - \bar{n}_1^2\bar{n}_0''}{(\bar{n}_0')^3} = 0. \quad (3.74)$$

Equations (3.67) and (3.68) were solved numerically using initial data from (3.69) and the velocities and acceleration of the wave front were computed at small times and compared against those predicted by equations (3.73) and (3.74) (Table 3.5). Clearly there is excellent agreement between the analytical and numerical methods over small times.

| $v$ | Parameters |         |          |        |          | Wave front velocity |             |            |           |         | Wave front acceleration |              |
|-----|------------|---------|----------|--------|----------|---------------------|-------------|------------|-----------|---------|-------------------------|--------------|
|     | $\alpha$   | $\beta$ | $\gamma$ | $\phi$ | $\theta$ | Equation (3.73)     | $t = 0.001$ | $t = 0.01$ | $t = 0.1$ | $t = 1$ | Equation (3.74)         | $t = 0.0001$ |
| 1   | 1          | 1       | 1        | 1      | 1        | 1.50                | 1.50        | 1.50       | 1.50      | 1.50    | 0                       | 0.00         |
| 2   | 1          | 2       | 2        | 2      | 3        | 2.25                | 2.25        | 2.25       | 2.25      | 2.25    | 0                       | 0.00         |
| 4   | 2          | 3       | 1        | 2      | 2        | 4.50                | 4.51        | 4.47       | 4.47      | 3.26    | 0                       | 0.00         |

**Table 3.5:** *Equation (3.67) and (3.68) were solved numerically and the velocities and accelerations of the leading edge of the wave fronts starting at  $x_0 = 0$  were calculated at the times indicated. The initial velocity and acceleration of the leading edge for the tip density of YWD phenotype obtained analytically from equations (3.73) and (3.74) are shown for comparison.*

The above analysis focused entirely on the propagation of the tips. However, the same technique can be applied to the hyphal density denoted by  $\rho$ .

Using the terms generated via LDM in equation (3.71), we see that at  $x_0 = 0$  the velocity is

$$-\frac{\bar{\rho}_1}{\bar{\rho}_0'} = 0, \quad (3.75)$$

and the acceleration is

$$\frac{2\bar{\rho}_0'\bar{\rho}_1\bar{\rho}_1' - 2\bar{\rho}_2(\bar{\rho}_0')^2 - \bar{\rho}_1^2\bar{\rho}_0''}{(\bar{\rho}_0')^3} = \frac{\gamma\phi}{\theta} \left( v + \frac{\alpha}{2\phi} \right). \quad (3.76)$$

| Parameters |          |         |          |        |          | Wave front acceleration |             |            |           |         | Wave front velocity |              |
|------------|----------|---------|----------|--------|----------|-------------------------|-------------|------------|-----------|---------|---------------------|--------------|
| $v$        | $\alpha$ | $\beta$ | $\gamma$ | $\phi$ | $\theta$ | Equation (3.76)         | $t = 0.001$ | $t = 0.01$ | $t = 0.1$ | $t = 1$ | Equation (3.75)     | $t = 0.0001$ |
| 1          | 1        | 1       | 1        | 1      | 1        | 1.50                    | 1.44        | 1.49       | 1.34      | 0.74    | 0                   | 0.00         |
| 2          | 1        | 2       | 2        | 2      | 3        | 3.00                    | 3.04        | 3.04       | 2.69      | 2.24    | 0                   | 0.00         |
| 4          | 2        | 3       | 1        | 2      | 2        | 4.50                    | 4.56        | 5.02       | 8.85      | 3.27    | 0                   | 0.00         |

**Table 3.6:** Equations (3.67) and (3.68) were solved numerically and the velocities and accelerations of the leading edge of the wave fronts starting at  $x_0 = 0$  were calculated at the times indicated. The initial velocity and acceleration of the leading edge for the hyphal density of YWD phenotype obtained analytically from equations (3.75) and (3.76) are shown for comparison.

From Table 3.6 it can be seen that the initial velocity at the wave front of hyphae is zero, due to the growth of hyphae being solely dependent upon the movement of the tips. The initial acceleration of hyphae on the other hand is positive and identical to the velocity of the leading tips multiplied by a scalar. This is because as the velocity of tip density increase from its initial state, the velocity of hyphal density is zero but quickly accelerates to match the velocity of the tips. This seems to indicate a ‘lagging’ effect between the hyphae and tips. This is indeed the case and if we look at the structure of the model equations for all phenotypes, notice that the ‘creation’ term for hyphae is identical to the flux term for the tips. Therefore there must be a distance between the tip and the hyphae. Indeed a plot of the hyphal and tip densities for the YWD phenotype on the same graph illustrates the lag clearly (Figure 3.6).

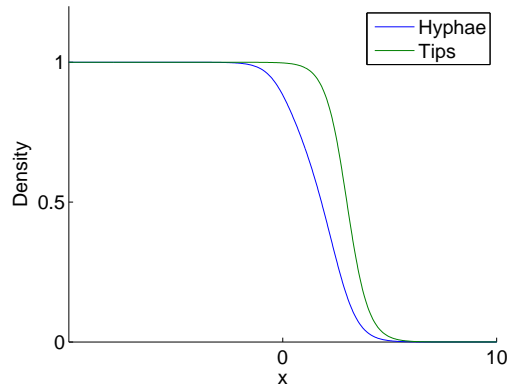


**Figure 3.6:** Plot of YWD phenotype (3.67) and (3.68) numerically solved using initial conditions in (3.69) with parameters values  $\alpha = \beta = \gamma = \theta = \phi = v = 1$  shown at time  $t=2$ .

### 3.3.3.2 FHD phenotype: coupled equations

The fungal phenotype ‘FHD’ investigated in earlier chapters is a coupled system of PDEs with no known analytical solution, except for specific initial data. Recall, the model equations are

$$\rho_t = nv - \gamma\rho, \quad (3.77)$$

$$n_t = -vn_x + \alpha\rho - \beta n\rho. \quad (3.78)$$

Since the equations in (3.77) and (3.78) are coupled, they cannot be considered in isolation. Applying the LDM with initial data (3.69) generates

$$\begin{aligned} \rho(x, t) &= \frac{\alpha v}{2\beta\gamma}(1 - \tanh(\theta x)) - \frac{\alpha v}{2\beta}(\tanh(\phi x) - \tanh(\theta x)) t + \\ &\quad - \frac{\alpha v}{8\beta\gamma} [(-2\phi\gamma v - \alpha v) + (\alpha v + 2\gamma^2 + \alpha v \tanh(\phi x)) \tanh(\theta x) + \\ &\quad (-\alpha v - 2\gamma^2 + 2\phi\gamma v \tanh(\phi x)) \tanh(\phi x)] t^2 + \dots \end{aligned} \quad (3.79)$$

$$\begin{aligned} n(x, t) &= \frac{\alpha}{2\beta}(1 - \tanh(\phi x)) - \frac{\alpha v}{4\beta\gamma} [(\tanh(\phi x) + 1) \\ &\quad (2\phi\gamma \tanh(\phi x) + \alpha \tanh(\theta x) - 2\phi\gamma - \alpha)] t + \dots \end{aligned} \quad (3.80)$$

(see Section 3.1.5). Thus substituting the terms generated by LDM equations (3.79) and (3.80) into equations (3.65) and (3.66) we obtain the initial tip velocity

$$-\frac{\bar{n}_1}{\bar{n}_0'} = v + \frac{\alpha v}{2\phi\gamma}, \quad (3.81)$$

while the initial tip acceleration is given by

$$\frac{2\bar{n}_0'\bar{n}_1\bar{n}_1' - 2\bar{n}_2(\bar{n}_0')^2 - \bar{n}_1^2\bar{n}_0''}{(\bar{n}_0')^3} = \frac{\alpha v^2(\alpha\phi - 2\alpha\theta - 2\gamma\phi\theta)}{4\phi^2\gamma^2}. \quad (3.82)$$

As there is no analytical solution to compare this result, we shall resort to using numerical methods to gain some insight into the initial state of the system for a selection of parameter values.

| Parameters |          |         |          |        |          | Wave front velocity |             |            |           |         | Wave front acceleration |              |
|------------|----------|---------|----------|--------|----------|---------------------|-------------|------------|-----------|---------|-------------------------|--------------|
| $v$        | $\alpha$ | $\beta$ | $\gamma$ | $\phi$ | $\theta$ | Equation (3.81)     | $t = 0.001$ | $t = 0.01$ | $t = 0.1$ | $t = 1$ | Equation (3.82)         | $t = 0.0001$ |
| 1          | 1        | 1       | 1        | 1      | 1        | 1.50                | 1.50        | 1.49       | 1.43      | 1.16    | -0.75                   | -0.75        |
| 2          | 1        | 2       | 2        | 2      | 3        | 2.25                | 2.25        | 2.23       | 2.11      | 1.80    | -1.75                   | -1.75        |
| 4          | 2        | 3       | 1        | 2      | 2        | 6.00                | 5.98        | 5.77       | 4.30      | 3.04    | -24.00                  | -24.21       |

**Table 3.7:** *Equations (3.77) and (3.78) were solved numerically and the velocities and accelerations of the leading edge of the tip wave fronts starting at  $x_0 = 0$  were calculated at the times indicated. The initial velocity and acceleration of the leading edge for the tip of FHD phenotype obtained analytically from equations (3.81) and (3.82) are shown for comparison.*

From Table 3.7 it can be seen that the values for the acceleration from equation (3.82) are all negative, predicting that the tips may be slowing down from its initial state. When we compare with numerical results, we can see there is some indication that the initial velocity is decelerating from its initial state as predicted by equation (3.82). As our approximation is centred around  $x_0 = 0$ , the result produced via (3.81) and (3.82) are in excellent agreement near zero as shown in Table 3.7.

An interesting observation, similar to the YWD phenotype, is that using the terms generated from the LDM in equation (3.79) we see that at  $x_0 = 0$  the hyphal velocity is

$$-\frac{\bar{\rho}_1}{\bar{\rho}_0} = 0 \quad (3.83)$$

and the hyphal acceleration is

$$\frac{2\bar{\rho}_0'\bar{\rho}_1\bar{\rho}_1' - 2\bar{\rho}_2(\bar{\rho}_0')^2 - \bar{\rho}_1^2\bar{\rho}_0''}{(\bar{\rho}_0')^3} = \frac{\alpha v}{2\theta} + \frac{\gamma\phi v}{\theta}. \quad (3.84)$$

For small times (i.e.  $t = 0.0001$ ) it was found that the velocity of the hyphae is indeed zero (see Table 3.8), thus confirming equation (3.83). Similar to the tips, the hyphal acceleration for small times (i.e.  $t = 0.001$ ) was found to be identical to tip velocity (see Table 3.7) as predicted.

| Parameters |          |         |          |        |          | Wave front acceleration |             |            |           |         | Wave front velocity |              |
|------------|----------|---------|----------|--------|----------|-------------------------|-------------|------------|-----------|---------|---------------------|--------------|
| $v$        | $\alpha$ | $\beta$ | $\gamma$ | $\phi$ | $\theta$ | Equation (3.84)         | $t = 0.001$ | $t = 0.01$ | $t = 0.1$ | $t = 1$ | Equation (3.83)     | $t = 0.0001$ |
| 1          | 1        | 1       | 1        | 1      | 1        | 1.50                    | 1.48        | 1.44       | 1.30      | 0.6252  | 0                   | 0.00         |
| 2          | 1        | 2       | 2        | 2      | 3        | 3.00                    | 3.05        | 3.03       | 2.68      | -0.54   | 0                   | 0.00         |
| 4          | 2        | 3       | 1        | 2      | 2        | 6.00                    | 5.98        | 5.77       | 4.30      | 3.04    | 0                   | 0.00         |

**Table 3.8:** *Equations (3.77) and (3.78) were solved numerically and the velocities and accelerations of the leading edge of the hyphal wave fronts starting at  $x_0 = 0$  were calculated at the times indicated. The initial velocity and acceleration of the leading edge for the hyphal density of FHD phenotype obtained analytically from equations (3.83) and (3.84) are shown for comparison.*

Again this is in agreement with the biology of the system. Initially the wave front velocity of hyphae is indeed zero due to the growth of hyphae solely being dependent upon the movement of the tips. The initial acceleration of the hyphae is positive and identical to the velocity of the leading tips. Therefore we can predict that the initial state of the hyphae for a fungal colony that satisfies the phenotype modelled (FHD) in the system of equations in (3.77) and (3.78) which also satisfies the initial conditions used, will have zero initial velocity but will accelerate up to the same rate as the tips of the colony and then may decelerate to its asymptotic speed for large times.

It must be emphasised, the accuracy of the velocity and acceleration results obtained in the analysis are highly dependent on the choice of initial conditions. Under different initial conditions the conclusion for FHD phenotype would be different. For illustration purposes consider the particular solution obtained in Section 3.1.5 (from equations (3.49) and (3.50)) and set the initial data to be

$$\rho(x, 0) = \frac{\alpha v}{2\beta\gamma} - \frac{\alpha v}{2\beta\gamma} \tanh\left(\left(\frac{2\gamma^2 - \alpha v}{4\gamma v}\right)x\right), \quad (3.85)$$

$$n(x, 0) = \frac{3\alpha}{4\beta} - \frac{\alpha}{2\beta} \tanh\left(\left(\frac{2\gamma^2 - \alpha v}{4\gamma v}\right)x\right) - \frac{\alpha}{4\beta} \tanh\left(\left(\frac{2\gamma^2 - \alpha v}{4\gamma v}\right)x\right)^2. \quad (3.86)$$

Constructing the first three terms using LDM and substituting into (3.65) and (3.66) yields the initial velocity of the tips as

$$-\frac{\bar{n}_1}{\bar{n}_0'} = \frac{2\gamma^2 v}{2\gamma^2 - \alpha v} \quad (3.87)$$

and the initial acceleration for the tips as

$$\frac{2\bar{n}'_0\bar{n}_1\bar{n}'_1 - 2\bar{n}_2(\bar{n}'_0)^2 - \bar{n}_1^2\bar{n}''_0}{(\bar{n}'_0)^3} = 0. \quad (3.88)$$

Likewise the equations for hyphal velocity is given by

$$-\frac{\bar{\rho}_1}{\bar{\rho}'_0} = \frac{2\gamma^2 v}{2\gamma^2 - \alpha v} \quad (3.89)$$

and hyphal acceleration is given by

$$\frac{2\bar{\rho}'_0\bar{\rho}_1\bar{\rho}'_1 - 2\bar{\rho}_2(\bar{\rho}'_0)^2 - \bar{\rho}_1^2\bar{\rho}''_0}{(\bar{\rho}'_0)^3} = 0. \quad (3.90)$$

Solving the system of equations (3.77) and (3.78) numerically with initial conditions (3.85) and with all parameters set to unity, we get the velocity for tips and hyphae to be equal to 2 and acceleration to be zero. Using the same parameters in equations (3.87), (3.88), (3.89) and (3.90), we get the approximation solution to be in perfect agreement with the analytical and numerical solution.

Notice under these initial conditions, the approximations successfully determined the wave speed of tips and hyphae for the FHD phenotype. Also notice the acceleration when all parameters are set to unity is zero indicating constant velocity.

### 3.4 Conclusion

The decomposition method has been utilised by many researchers who have stressed the advantages the technique offers e.g. its efficiency, the ability to solve problems without linearisation and the range of applicability to various types of problems and fields.

However, the technique undeniably has some limitations. First, the series solution must be truncated for practical application, which hinders the accuracy of the solution in a wider region. Also the region of convergence of the series must be considered and this is potentially a major weakness of the technique, especially for problems where results are required for larger times. For example, we have seen in Section 2.3.3.1 that an analytical solution exists for the YWD phenotype and using the initial conditions in equation (3.34), we observed that



LDM computed the first few terms of a Taylor series of the analytical solution for the tips (3.72). Thus we could infer that the series converges to the solution.

However, the approximate series solution is usually only valid for a small region in the space - time plane regardless of the number of terms generated in the series. It was hypothesised initially that greater number of terms included in the series could determine the convergence for larger times. Due to the recursive nature of the decomposition methods, the computation of terms greater than 50 can be computationally expensive. For example the FHD phenotype, equations (3.55) and (3.56), took several hours to compute only 50 terms on a standard computer.

To overcome the computation limitation, techniques such as the reduced differential transform method (RDTM) (Keskin and Oturan, 2009, 2010) can be utilised. The RDTM produces identical terms to that of the LDM. The RDTM is a modification of the differential transform method and is much more robust and efficient when implementing in a computer when computing terms of higher order of an infinite series. Thus we computed terms exceeding 100 terms and observed that the solution did not get any better for  $t > 1$  (data not shown). Furthermore, the solution was good only at locating the position of the leading wave and extremely weak behind the wave front which consisted of ‘wiggles’ for large times regardless of the number of terms used. From this it is reasonable to deduce that the series could possibly be of a divergent nature.

There have been a number of studies on the convergence of the Laplace decomposition method (Cherruault, 1990; Abbaoui and Cherruault, 1994a,b). It is difficult to prove the convergence of a decomposition method when it is applied to PDEs with initial and boundary conditions (Ngarhasta et al., 2002) using traditional approaches used by Cherruault et al. but in recent publications there have been promising results which prove the existence and uniqueness of a series solution produced via decomposition methods (El-Kalla, 2007; Ray, 2014). We did not focus on the convergence analysis as this diverges away from the applied nature of this thesis, but note that this remains an important open problem.

In the plethora of literature related to the Adomian/Laplace decomposition method (and other decomposition techniques of similar nature) it is clear that the semi-analytical solutions of problems are usually in excellent agreement with the closed form solution (if one exists) and thus must converge. Such results have been of immense benefit in real life applications e.g. food and chemical industries,

firefighting, structural material sciences to mention a few (Tataria et al., 2007; Helal and Mehanna, 2007; Meher and Meher, 2013; Gledson et al., 2013).

It is worthy of mention that despite the potential lack of convergence of the generated series, we observed an interesting phenomena occurring in our system of equations for the fungal YWD phenotypes. Using a number of terms from the semi-analytical solution, the position of the leading wave did not appear to be affected by the spurious oscillations behind it and seemed to be in perfect alignment with the closed form solution for large times. Due to the nature of the system of equations used to model fungal phenotypes, there are similarities in the structure of the equations (i.e. FHD, FXD, YWD and YHD). Hence, despite the lack of any known analytical solutions for the other phenotypes, we expect the methodology used for the YWD phenotype to gain crucial information regarding the wave properties of other phenotypes. As an example, the series generated via LDM for the FHD phenotype was shown to be in excellent agreement with the numerical solution.

In addition to approximating the initial kinematic properties of the leading edge, we provided an alternative means of tracking the position of the leading edge of the distribution for larger times. Truncated series of equations (3.44) and (3.45) were constructed and solved to determine the position of the leading edge of the distribution, i.e. the maximum value of  $x$  such that  $u_c = \sum_{m=0}^k u_m(x, t)$  for different series length  $k$  at various times  $t$ , where  $u_c = 0.1$  (Tables 3.2 and 3.1). When compared with the exact solution obtained from equation (3.37), the accuracy of the position of the leading edge obtained from the series decreases with time but improves with the inclusion of more terms, similar to a Taylor series approximation of a function (Adomian, 1988). The methods developed to determine the initial velocity and acceleration ((3.62) and (3.64)) can be extended further to include initial jerk, snap, crackle and pop.

Typically the development of the type of system of equations investigated in this chapter is achieved by looking for travelling wave solutions of the corresponding model equations but these may be too complex to extract such solutions, even if they exist. Alternatively, numerical simulations can provide insight into the behaviour of the system. One main drawback of relying on numerical solutions is that parameter values have to be calibrated in advance and it is therefore often difficult to isolate the influence of one parameter on the system. Numerical solutions are also useful in determining asymptotic behaviour for large times but

often fail to provide any information around its initial state. Hence using the velocity and acceleration equations (3.65) and (3.66) proposed, we can predict with great accuracy the initial development of a system. This information can be of great relevance for researchers concerned with determining the initial speed of a complex system of equations. In the context of fungi, testing the predictions of this approach in relation to the initial movement of the leading edge of the colony is complicated by the discrete nature of individual hyphae and the continuum approximation required to generate the partial differential equation model. Nonetheless, by visually inspecting enlarged images of the position of the edge of a mycelia, it should be possible to detect, and hence quantify, how that position changes over time. However, the greatest difficulty in comparing these model predictions to experimental data relates around the correct choice of the initial data in the model.

We explored some well established fungal species models in Chapters 2 and 3, providing insight that have not been explored previously i.e. analytical solutions for YWD and FHD phenotypes. An elegant derivation to determine key information of initial wave properties was proposed and explored. It is worthy to mention the analysis in this section is not limited to fungal models but can be applied to various systems.

All the analysis seen thus far has been concerned with a single fungal colony growing in a homogenous environment. One of the most important observations in a real life fungal habitat is that of fungi competing with other fungi for survival. We will explore this phenomena in the following chapters and make use of the methodology developed here to understand the initial kinematics of fungi growing in toxic domains.

## Chapter 4

# One Dimensional Models of Fungal Competition

### 4.1 Competing fungi

Fungi rarely grow in isolation and instead compete against other species for common resources including various nutrients (e.g. carbon, nitrogen and oxygen), water and even simply territory (which influences the ability of the fungus to acquire further resources). Consequently the success of any application of fungi depends on its ability to grow and suitably function in the presence of rival species.

#### 4.1.1 Experimental studies

Such interactions are usually investigated experimentally by inoculating a Petri dish with two non-mutually compatible species and observing their subsequent growth and behaviour over a range of conditions (Boddy, 2000; Evans et al., 2008; Boddy et al., 2010). Typically the early growth of both species is radially symmetric until the periphery of the colonies collide after which one of three distinct outcomes are observed. Certain combinations of fungi display *intermingling* (also termed overgrowth or coexistence), where there is a continued and increasing overlap in the extent of both species. Other fungal pairings display *deadlock*, where neither species is able to invade territory held by the other and a stalemate is reached. The third outcome is *displacement* where one fungus takes over the territory held by the other and thereby locally eliminating its rival. The mechanisms behind these outcomes have been well studied (e.g. Carlile et al., 2001; Utermark

and Karlovsky, 2007; Sempere and Santamarina, 2010). The experiment carried out by Ibarra-Medina et al. (2010) depicted some of these behaviours explicitly, between the fungi strains of *Trichoderma* against phytopathogenic fungi *Sclerotinia sclerotiorum* (Figure 4.1).

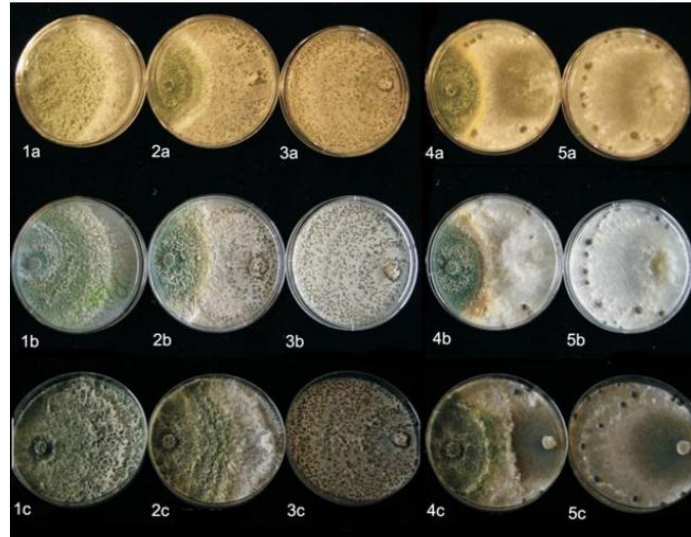


**Figure 4.1:** Study of fungal interaction conducted by Ibarra-Medina et al. (2010). Control strains of *Trichoderma*(T) (1a, b, c), Control strains of *Sclerotinia sclerotiorum*(Ss) (3a, b, c) and *Sclerotinia minor*(Sm) (5a, b, c). Interaction of T vs Ss (2a, b, c) and T vs Sm (4a, b, c).

Under laboratory conditions the two species were placed on a Petri dish and left for a significant amount of time, on average between “8 - 10 days”. In Figure 4.1 displacement can be seen in 2b and 2c whereas a state of deadlock can be seen in 2a, 4a, 4b and 4c. Another study conducted by Iluyemi and Hanafi (2009) using 5 strains of fungi, *Sclerotium rolfsii*, *Aspergillus niger*, *Trichoderma harzianum*, *Trichoderma longibrachiatum* and *Trichoderma koningii* show intermingling behaviours between various type of fungi (see Figure 4.2).

The fungal interactions in Figure 4.2 also display common fungal behaviours. Figures (e) and (f) shows dominance (displacement) of *S.rolfsii* by *T.longibrachiatum* and *T.koningii* by *S.rolfsii*. Figures (a), (b) and (g) show deadlock between the species. Figure (d) show stalemate with the right fungi covering greater surface area (a mutual line can be seen where neither fungi grew over). Lastly, Figure (c) also shows intermingling (coexistence) where *T. harzianum* has grown over *A.niger* but *A.niger* still exists at a lower density seen

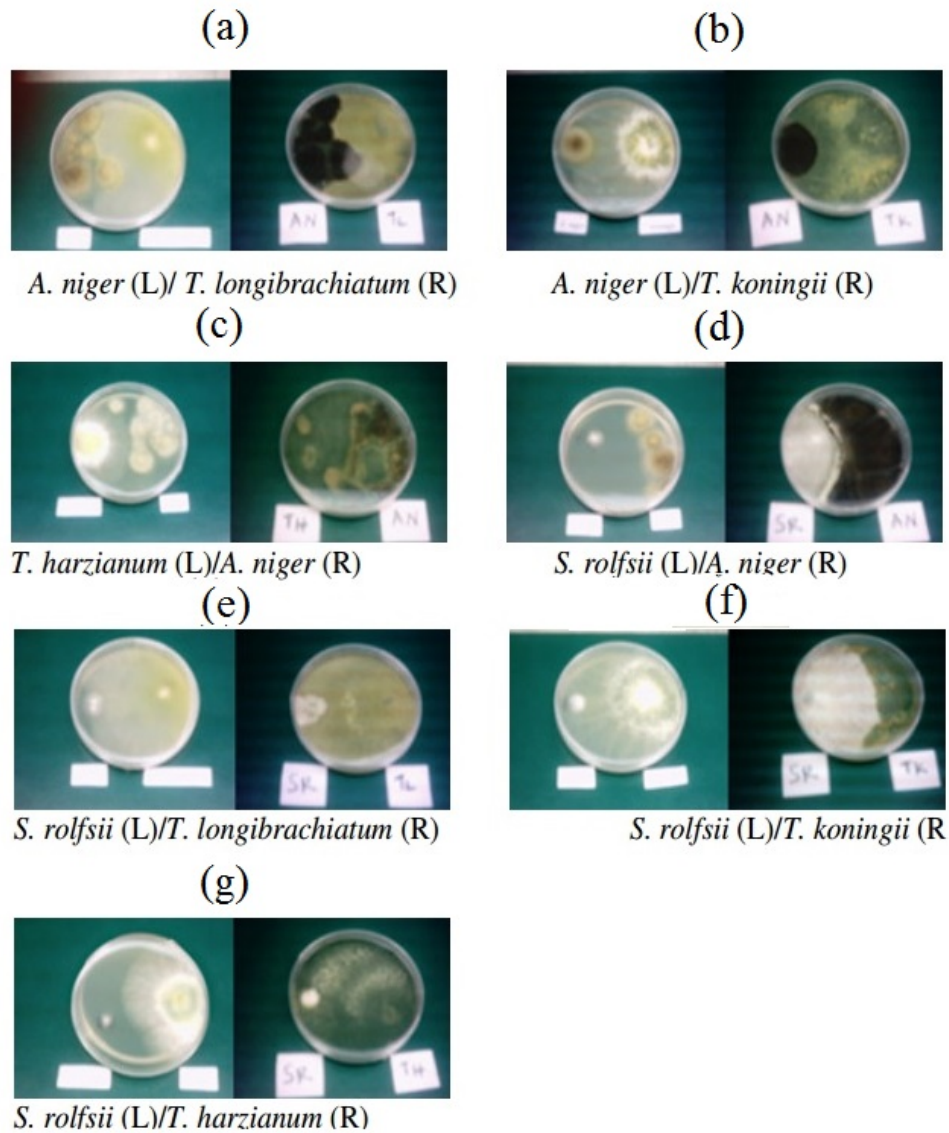


**Figure 4.2:** *Experimental study on fungal interactions by Iluyemi and Hanafi (2009). Interactions of 5 fungal strains where left Petri dish contains 2nd day of inoculation and the right Petri dish is 13<sup>th</sup> day of inoculation.*

on the upper and lower surfaces of the Petri dish. Barua et al. (2012) is yet another experimental-based paper depicting the intermingling behaviours discussed above.

### 4.1.2 Historical modelling approaches

The outcomes seen above arise because fungi produce a combination of volatile organic compounds (VOCs) and toxic metabolites that inhibit the growth of rivals and degrade their existing biomass (Hynes et al., 2007). Most commonly, one fungus will lyse its rival on contact as observed by the bursting of cells, the vacuolisation of compartments and the withdrawal of cytoplasm (Horio and Oakley, 2005). These mechanisms are resource intensive and experimental studies have shown that the outcome of pairwise interactions is in part determined by the availability of nutrient resources (Kennedy, 2010; Mehl and Cotty, 2013). Therefore the success of any biotechnological application involving fungi depends on the provision of suitable nutrients.

There have been a multitude of mathematical models describing fungal growth and function as discussed in Chapter 1. However the most useful models of fungal interactions have been based on continuum approaches since they efficiently represent entire fungal communities while capturing the microscopic characteristics of colony dynamics (but see Halley et al., 1994, for a cellular automaton formulation).

In this chapter a mathematical model of fungal pairwise competition will be constructed that simulates observed experiments and allows general principles to emerge. To maintain the generality of the model, the resource being competed for is regarded as space or territory rather than an explicit source of nutrient. Thus, the outcome of competition is solely governed by independent resources available to the two fungi and this scenario is designed to reflect experiments investigating the outgrowth of fungi from isolated nutrient resources (see, for example, Tlalka et al., 2008).

We initialize our investigation by exploring nutrient independent interactions before extending to nutrient dependent interactions.

## 4.2 Nutrient independent interactions

### 4.2.1 Model equations

In laboratory-based experiments a Petri dish is inoculated with a species of fungi that expand outwards in a radially symmetric manner and the overall outcome of pairwise competition is determined by observing how the colony peripheries behave immediately before and then following their collision. Thus, due to the radial symmetry involved, a one-dimensional mathematical model is sufficient to investigate such competition corresponding to the growth along the line connecting the centres of the inoculation sites.

In Chapter 2 we explored the models formulated by Edelstein (1982) where fungal growth was modelled by the populations of hyphae and hyphal tips. The creation of hyphae corresponded to the trail left behind a moving tip. This same “tip and trail” structure has been used successfully in other investigations (e.g. Boswell et al., 2002). Thus we introduce  $\rho_j$  and  $n_j$  to denote the density of hyphae and the density of hyphal tips respectively in fungal biomass  $j$  where  $j = 1, 2$  represent two different fungal phenotypes. During fungal competition, combinations of VOCs and toxic metabolites are produced along the lengths of hyphae that comprise the mycelium. Since these compounds restrict the ability of a rival biomass to create new hyphal material as well as degrading existing hyphae, they essentially cause hyphal tips in a rival to cease functioning and reduce the density of existing biomass. For convenience these substances are not represented explicitly but instead their influence on rival biomasses is modelled. Therefore the process of tip inhibition/degradation and hyphal degradation in biomass  $j$  by biomass  $i$  ( $i \neq j$ ) is modelled using terms proportional to  $\rho_i n_j$  and  $\rho_i \rho_j$ , respectively.

The mathematical model is described by four coupled partial differential equations

$$\begin{aligned}\frac{\partial \rho_1}{\partial t} &= v_1 n_1 - \gamma_1 \rho_1 - E \rho_2 \rho_1, \\ \frac{\partial n_1}{\partial t} &= -\frac{\partial(v_1 n_1)}{\partial x} + \alpha_1 \rho_1 - \beta_1 \rho_1 n_1 - A \rho_2 n_1, \\ \frac{\partial \rho_2}{\partial t} &= v_2 n_2 - \gamma_2 \rho_2 - F \rho_1 \rho_2, \\ \frac{\partial n_2}{\partial t} &= \frac{\partial(v_2 n_2)}{\partial x} + \alpha_2 \rho_2 - \beta_2 \rho_2 n_2 - B \rho_1 n_2,\end{aligned}\tag{4.1}$$



where constants  $\gamma_j$  denote the natural loss of hyphae,  $\alpha_j$  represent the branching rates,  $\beta_j$  represent the anastomosis rates and  $A$ ,  $B$ ,  $E$  and  $F$  are the proportionality constants of the rates of degradation of biomass and associated tips due to competition, which may be different between the two biomass “phenotypes”. Notice that the sign of the fluxes for the hyphal tips are reversed ensuring that both biomasses expand in opposite directions and thus will collide with suitable initial data; an approach that has successfully been used in previous studies (e.g. Boswell, 2012). [Note: The equations in (4.1) are simply two FHD phenotype equations (3.48) seen in Section 3.1.5 with combat ability.]

The model equations are to be solved on the spatial interval  $(-L, L)$  and to be consistent with typical experimental protocols described above require zero-flux boundary conditions because in the associated experimental configuration no material enters or leaves the Petri dish after inoculation. Furthermore, suitable initial data, representing the inoculation of the Petri dish, requires that the two rival biomasses start on opposite sides of the interval with no overlap. Hence the initial data is taken to be of the form

$$\begin{aligned}\rho_1(x, 0) &= \begin{cases} 0, & \text{if } x \geq 0 \\ \hat{\rho}_1(x), & \text{otherwise} \end{cases} \\ \rho_2(x, 0) &= \begin{cases} \hat{\rho}_2(x), & \text{if } x \geq 0 \\ 0, & \text{otherwise} \end{cases} \\ n_1(x, 0) &= \begin{cases} 0, & \text{if } x \geq 0 \\ \hat{n}_1(x), & \text{otherwise} \end{cases} \\ n_2(x, 0) &= \begin{cases} \hat{n}_2(x), & \text{if } x \geq 0 \\ 0, & \text{otherwise} \end{cases}\end{aligned}\tag{4.2}$$

where  $\hat{\rho}_j$  and  $\hat{n}_j$  are specified functions. Hence we assume biomass 1 starts on the left hand side of the domain and biomass 2 starts on the right hand side of the domain.

When considered in isolation, each of the biomasses and corresponding tips from equation (4.1) generate a stable travelling wave solution (see Chapter 2). Thus to ensure the biomasses have attained stable distributions prior to their contact, the initial distributions  $\hat{\rho}_j(x)$  and  $\hat{n}_j(x)$  are chosen to be similar to their travelling wave profile. Consequently, and solely for the purpose of numerical integration of the system of equations in (4.1), the initial data in equation (4.2)

is

$$\begin{aligned}\hat{\rho}_1(x) &= \frac{\alpha_1 v_1}{2\beta_1 \gamma_1} \operatorname{erfc}\left(\frac{\bar{x} + x}{2}\right), & \hat{n}_1(x) &= \frac{\alpha_1}{2\beta_1} \operatorname{erfc}\left(\frac{\bar{x} + x}{2}\right), \\ \hat{\rho}_2(x) &= \frac{\alpha_2 v_2}{2\beta_2 \gamma_2} \operatorname{erfc}\left(\frac{\bar{x} - x}{2}\right), & \hat{n}_2(x) &= \frac{\alpha_2}{2\beta_2} \operatorname{erfc}\left(\frac{\bar{x} - x}{2}\right),\end{aligned}\quad (4.3)$$

where  $2\bar{x}$  represents the initial distance between the two model biomasses and  $\operatorname{erfc}(x)$  is the complementary error function. Note that while these functions are not the final travelling wave profiles obtained by the biomasses, when considered in isolation of each other, provided  $\bar{x}$  is sufficiently large, these initial profiles quickly converge to their stable distributions before any interactions hence why the biomass terms have been multiplied by  $\frac{\alpha_i v_i}{2\beta_i \gamma_i}$  and the tip terms by  $\frac{\alpha_i}{2\beta_i}$ .

In order to isolate the key parameters of the system, it is reasonably assumed that the two rival biomasses have similar growth characteristics and differ only in their ability to degrade and inhibit the growth of their rivals. Thus we henceforth set  $v_1 = v_2 = v$ ,  $\alpha_1 = \alpha_2 = \alpha$ ,  $\beta_1 = \beta_2 = \beta$  and  $\gamma_1 = \gamma_2 = \gamma$ . The resultant model equation (4.1) can be non-dimensionalised by introducing  $\rho_j^* = \frac{\rho_j \beta \gamma}{\alpha v}$ ,  $n_j^* = \frac{n_j \beta}{\alpha}$ ,  $\psi = \frac{\alpha v}{\gamma^2}$ ,  $A^* = \frac{A}{\beta}$ ,  $B^* = \frac{B}{\beta}$ ,  $E^* = \frac{\alpha v}{\beta \gamma^2} E$ ,  $F^* = \frac{\alpha v}{\beta \gamma^2} F$ ,  $x^* = \frac{\gamma x}{v}$  and  $t^* = \gamma t$  giving rise to

$$\begin{aligned}\frac{\partial \rho_1}{\partial t} &= n_1 - \rho_1 - E \rho_2 \rho_1, \\ \frac{\partial n_1}{\partial t} &= -\frac{\partial n_1}{\partial x} + \psi(\rho_1 - \rho_1 n_1 - A \rho_2 n_1), \\ \frac{\partial \rho_2}{\partial t} &= n_2 - \rho_2 - F \rho_1 \rho_2, \\ \frac{\partial n_2}{\partial t} &= \frac{\partial n_2}{\partial x} + \psi(\rho_2 - \rho_2 n_2 - B \rho_1 n_2),\end{aligned}\quad (4.4)$$

where asterisks have been dropped for notational convenience.

### 4.2.2 Mutual tip suppression equations

In this scenario both species are assumed to be able to produce some toxic metabolite proportional to its biomass (i.e. hyphae), which can suppress the tips of its competitor only. Thus to model this effect, attention is focussed on the impact of tip suppression when hyphal degradation is neglected (i.e. by assuming  $E$  and  $F$  are both zero). The corresponding non-dimensionalised model equations are

therefore

$$\begin{aligned}
\frac{\partial \rho_1}{\partial t} &= n_1 - \rho_1, \\
\frac{\partial n_1}{\partial t} &= -\frac{\partial n_1}{\partial x} + \psi(\rho_1 - \rho_1 n_1 - A\rho_2 n_1), \\
\frac{\partial \rho_2}{\partial t} &= n_2 - \rho_2, \\
\frac{\partial n_2}{\partial t} &= \frac{\partial n_2}{\partial x} + \psi(\rho_2 - \rho_2 n_2 - B\rho_1 n_2).
\end{aligned} \tag{4.5}$$

#### 4.2.2.1 Analysis

The equilibria of equation (4.5) satisfy

$$\begin{aligned}
0 &= n_1 - \rho_1, \\
0 &= \psi(\rho_1 - \rho_1 n_1 - A\rho_2 n_1), \\
0 &= n_2 - \rho_2, \\
0 &= \psi(\rho_2 - \rho_2 n_2 - B\rho_1 n_2),
\end{aligned}$$

generating the four stationary points,

$$\begin{aligned}
(\rho_1^*, n_1^*, \rho_2^*, n_2^*) &= (0, 0, 0, 0), (1, 1, 0, 0), (0, 0, 1, 1), \\
&\left( \frac{1-A}{1-AB}, \frac{1-A}{1-AB}, \frac{1-B}{1-AB}, \frac{1-B}{1-AB} \right).
\end{aligned}$$

In order for the fourth stationary point to be biologically realistic it is required that either  $A, B < 1$  or  $A, B > 1$ . The corresponding Jacobian matrix  $J(\rho_1, n_1, \rho_2, n_2)$  has characteristic equation

$$\begin{vmatrix}
-1-\lambda & 1 & 0 & 0 \\
\psi(1-n_1) & -\psi(\rho_1 + A\rho_2) - \lambda & -\psi A n_1 & 0 \\
0 & 0 & -1-\lambda & 1 \\
-\psi B n_2 & 0 & \psi(1-n_2) & -\psi(\rho_2 + B\rho_1) - \lambda
\end{vmatrix} = 0$$

and can be expressed as the product of two quadratics minus a constant term

$$\begin{aligned}
&(\lambda^2 + (1 + \psi(B\rho_1 + \rho_2))\lambda + \psi(B\rho_1 + \rho_2 + n_2 - 1)) \times \\
&(\lambda^2 + (1 + \psi(A\rho_2 + \rho_1))\lambda + \psi(A\rho_2 + \rho_1 + n_1 - 1)) - \psi^2 AB n_1 n_2 = 0.
\end{aligned} \tag{4.6}$$

Now we analyze the stationary points. Substituting the first, second and third stationary points into equation (4.6) yields respectively

$$\begin{aligned}(\lambda^2 + \lambda - \psi) (\lambda^2 + \lambda - \psi) &= 0, \\(\lambda + 1)(\lambda + \psi) (\lambda^2 + (1 + \psi B) \lambda + \psi(B - 1)) &= 0, \\(\lambda + 1)(\lambda + \psi) (\lambda^2 + (1 + \psi A) \lambda + \psi(A - 1)) &= 0.\end{aligned}$$

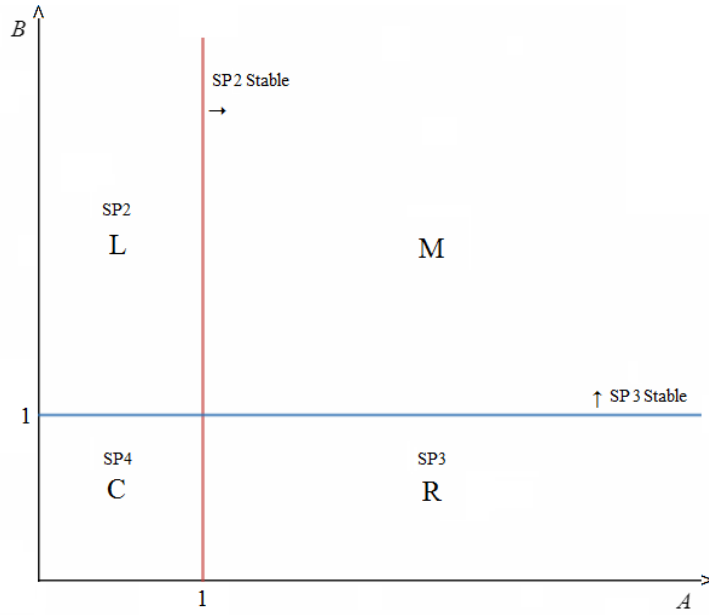
Using the Routh-Hurwitz criteria, it can be seen that the first stationary point is unstable. The second stationary point is stable iff  $B > 1$  and the third stationary point is stable iff  $A > 1$ .

The eigenvalues of the Jacobian evaluated at the fourth stationary point produces an equation that can be factorised

$$(\lambda + 1)(\lambda + \psi) \left( \lambda^2 + (1 + \psi)\lambda + \frac{\psi(A - 1)(1 - B)}{AB - 1} \right) = 0.$$

Thus  $-1$  and  $-\psi$  are two of the eigenvalues, both being negative. Hence the quadratic factor determines the stability of the fourth equilibria. From the quadratic factor, the eigenvalues have negative real part iff  $1 + \psi > 0$  and  $\frac{\psi(A-1)(1-B)}{AB-1} > 0$  which is satisfied when  $1 > A$  and  $1 > B$ . Hence the fourth stationary point corresponding to coexistence is stable iff  $1 > A$  and  $1 > B$ . Thus there will always be coexistence between the species if these inequalities are satisfied.

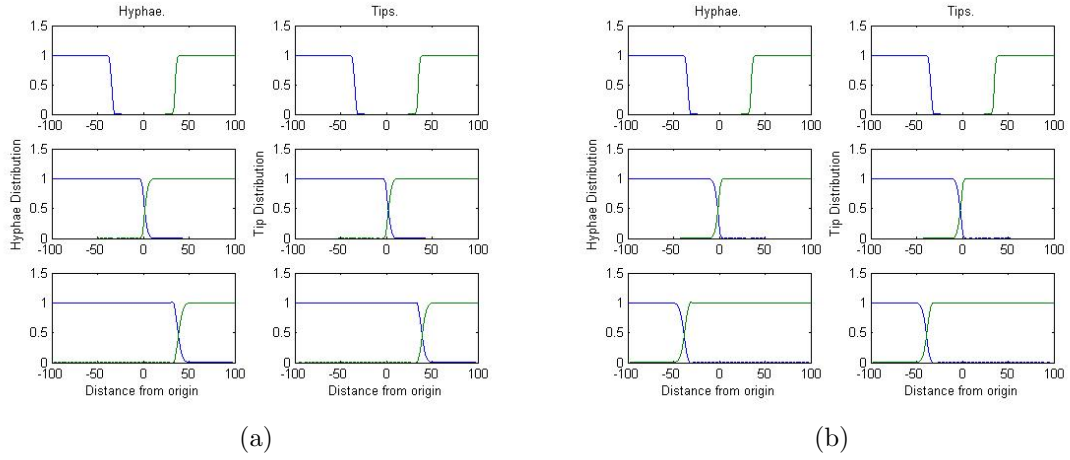
The stationary point analysis above can be represented on a  $A - B$  parameter space divided into four regions (Figure 4.3).



**Figure 4.3:** The  $A - B$  parameter space for equation (4.5) for the different regions where the stationary points are stable.  $SP2$  corresponds to the stationary point  $(1, 1, 0, 0)$ ,  $SP3$  corresponds to the stationary point  $(0, 0, 1, 1)$  and  $SP4$  corresponds to the stationary point  $(\frac{1-A}{1-AB}, \frac{1-A}{1-AB}, \frac{1-B}{1-AB}, \frac{1-B}{1-AB})$ . Region  $R$  corresponds to where the biomass initially starting on the right will displace that initially on the left. Region  $L$  corresponds to where the biomass initially starting on the left will displace that initially on the right. Region  $C$  corresponds to where coexistence (or intermingling) of biomasses arises. Region  $M$  corresponds to where multiple stable equilibria are found, which can include deadlock.

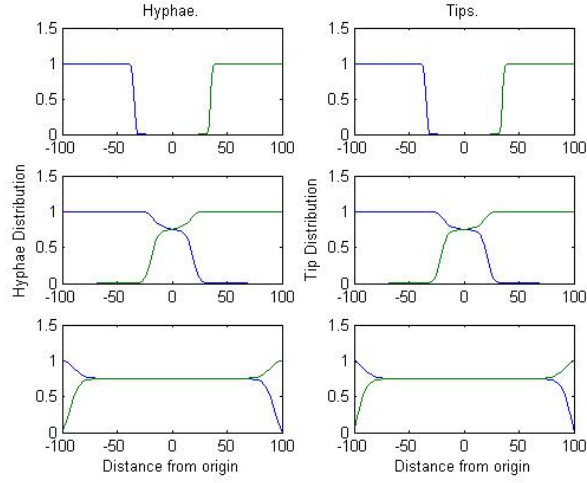
#### 4.2.2.2 Numerical results

The system of equations in (4.5) with initial conditions (4.2) and (4.3) are solved in Matlab using the routine *pdepe* (see Figures 4.4 - 4.6). Notice that due to the nondimensionalisation applied, the corresponding initial data (4.3) are monotonic functions taking values between 0 and 1 and consequently there is a symmetry between the initial profiles.



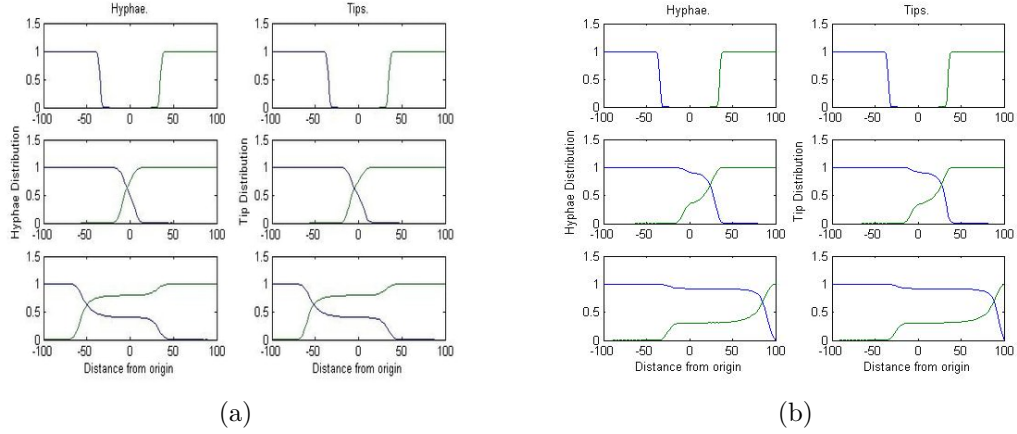
**Figure 4.4:** *System of equations in (4.5) with initial conditions (4.2) and (4.3) are solved with parameters  $\alpha = \beta = \gamma = v = 1$  and therefore  $\psi = 1$  is represented in (a) with  $A = 1$  and  $B = 3$ . The species on the left is displacing the species on the right. Solving the system of equations with parameters values,  $A = 3$ ,  $B = 1$  and  $\psi = 1$  is represented in (b) where it can be seen that species on the right is displacing the species on the left. All shown at times  $t = 0, 25$  and  $75$ .*

Figure 4.4(a) shows that species 1 (starting on the left) is the dominant biomass as it is able to displace its rival's tips faster than the rival species. Therefore both species approach the second stationary point  $(1, 1, 0, 0)$  and the left biomass displaces the right. Similarly, if  $A > 1$  (and  $B < A$ ) then the parameter values of  $A$  and  $B$  are reversed and species 2 (starting on the right) displaces its rival species (see Figure 4.4(b)).



**Figure 4.5:** *System of equations in (4.5) with initial conditions (4.2) and (4.3) are solved with parameters using parameter values  $\alpha = 3$ ,  $\beta = \gamma = v = 1$ ,  $A = B = \frac{1}{3}$  and  $1 > AB$ . Coexistence can be seen between both species. All shown at times  $t = 0, 25$  and  $75$ .*

The analysis above predicted the species would coexist if  $1 > A$  and  $1 > B$ . This is illustrated in Figure 4.5 where  $A = B = \frac{1}{3}$  and  $\psi = 3$ . If we use the values  $B = \frac{1}{2}$ ,  $A = \frac{3}{4}$  and  $\psi = 2$  we also get coexistence of both species but with species 2 at a greater density (Figure 4.6(a)). Similarly species 1 has a greater density level with appropriate parameter values (Figure 4.6(b)).



**Figure 4.6:** System of equations in (4.5) with initial conditions (4.2) and (4.3) are solved with parameters  $\alpha = 2$ ,  $\beta = \gamma = v = 1$ ,  $A = \frac{3}{4}$ ,  $B = \frac{1}{2}$  and  $\psi = 2$  is represented in (a) where coexistence of both species with the species on the right at greater density. Solving with parameter values  $\alpha = 4$ ,  $\beta = \gamma = v = 1$ ,  $A = \frac{1}{4}$ ,  $B = \frac{3}{4}$  and  $\psi = 4$  is represented in (b) where coexistence of both species with species on the left at greater density. All shown at times  $t = 0, 25$  and  $50$ .

#### 4.2.2.3 Conclusion

In this model we have successfully modelled the basic interaction of two species of fungi. Both species have been assumed to have developed the ability to compete against each other via releasing a form of toxic material at a rate proportional to its hyphal density which eliminates the rival's tips. In the analysis we have obtained four stationary points. The first was always unstable, which makes sense as it is the trivial point, corresponding to the complete absence of biomass. A second stationary point, corresponding to the right-starting biomass displacing the left arose if  $A > 1 > B$  with the reverse arising when  $B > 1 > A$  from a third stationary point. If both  $A, B > 1$  then since both the second and third equilibria are stable, the initial data along with relative values of  $A$  and  $B$  determine which equilibria is reached. A fourth stationary point, corresponding to co-existence, was asymptotically stable provided  $A, B < 1$ .



### 4.2.3 Tips suppression and hyphal degradation in single species

Some species of fungi do not evolve with attacking abilities but have instead developed great defensive capabilities e.g. *Cytostereum murraini* and *Phlebia centrifuga* (Boddy, 2000). In this section we model an invasive fungi attacking a rival's hyphae as well as its tips using the relevant reaction terms seen in Section 4.2.1. To model the impact of tip suppression and hyphal degradation by one species we set  $B$  and  $F$  to zero. Thus equation (4.4) becomes the following,

$$\begin{aligned}\frac{\partial \rho_1}{\partial t} &= n_1 - \rho_1 - E\rho_1\rho_2, \\ \frac{\partial n_1}{\partial t} &= -\frac{\partial n_1}{\partial x} + \psi(\rho_1 - \rho_1 n_1 - A\rho_2 n_1), \\ \frac{\partial \rho_2}{\partial t} &= n_2 - \rho_2, \\ \frac{\partial n_2}{\partial t} &= \frac{\partial n_2}{\partial x} + \psi(\rho_2 - \rho_2 n_2).\end{aligned}\tag{4.7}$$

#### 4.2.3.1 Analysis

The corresponding stationary points from equation (4.7) are,

$$\begin{aligned}(\rho_1^*, n_1^*, \rho_2^*, n_2^*) &= (0, 0, 0, 0), (1, 1, 0, 0), (0, 0, 1, 1), \\ &\left(\frac{1 - A - AE}{1 + E}, 1 - A - AE, 1, 1\right),\end{aligned}$$

which is biologically realistic provided  $A(1 + E) < 1$ . To determine the stability of the stationary points the characteristic equation is required,

$$\begin{vmatrix} -1 - E\rho_2 - \lambda & 1 & -E\rho_1 & 0 \\ \psi(1 - n_1) & -\psi(\rho_1 + A\rho_2) - \lambda & -\psi A n_1 & 0 \\ 0 & 0 & -1 - \lambda & 1 \\ 0 & 0 & \psi(1 - n_2) & -\psi\rho_2 - \lambda \end{vmatrix} = 0.$$

The characteristic equation can be expressed as the product of two quadratics

$$\begin{aligned} &(\lambda^2 + (1 + \psi\rho_2)\lambda + \psi(\rho_2 + n_2 - 1)) \times \\ &(\lambda^2 + (1 + E\rho_2 + \psi(A\rho_2 + \rho_1))\lambda + \psi(EA\rho_2^2 + E\rho_1\rho_2 \\ &+ A\rho_2 + \rho_1 + n_1 - 1)) = 0.\end{aligned}\tag{4.8}$$

Now we analyze the stationary points. Substituting the stationary points into equation (4.8) gives

$$\begin{aligned}
& (\lambda^2 + \lambda - \psi) (\lambda^2 + \lambda - \psi) = 0 \\
& (\lambda + 1)(\lambda + \psi) (\lambda^2 + \lambda - \psi) = 0 \\
& (\lambda + 1)(\lambda + \psi) (\lambda^2 + (1 + E + \psi A)\lambda + \psi(AE + A - 1)) = 0 \\
& (\lambda + 1)(\lambda + \psi) \left( \lambda^2 + \left( 1 + E + \left( \frac{\psi}{1 + E} \right) \right) \lambda + \psi(1 - A(E + 1)) \right) = 0.
\end{aligned}$$

Using the Routh-Hurwitz criteria, it can easily be seen that the first two stationary points are unstable. The third stationary point is stable iff  $A(E + 1) > 1$ .

The eigenvalues of the first two factors of the final stationary point are always negative. The Routh-Hurwitz criteria applied to the third factor ensure stability iff the real part of  $1 + E + (\frac{\psi}{1+E}) > 0$  and  $\psi(1 - A(E + 1)) > 0$ . The former is always true and the latter is only true iff  $1 > A(E + 1)$  which, recall, is the condition for the existence of the stationary point. Thus both species of fungi can coexist if these conditions are satisfied.

#### 4.2.3.2 Numerical results

The system of equations in (4.7) have been solved numerically in Matlab using the built in function *pdepe* with the values  $E = A = \psi = 1$  and so satisfy  $(A(E + 1) > 1)$  (Figure 4.7).

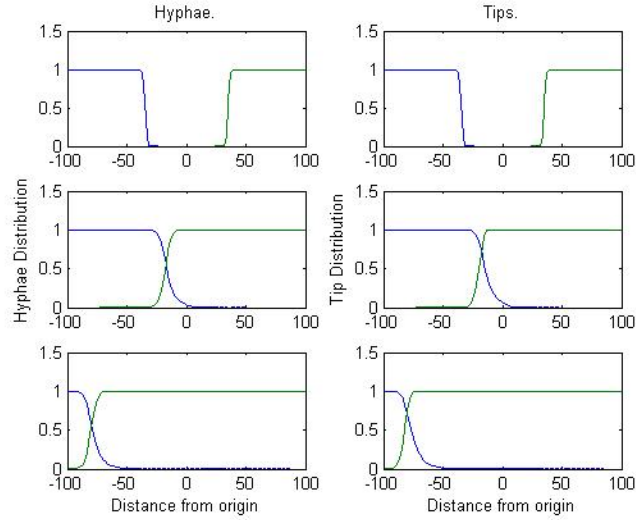


**Figure 4.7:** *System of equations in (4.7) with initial condition (4.2) have been solved numerically using parameter values  $\alpha = \beta = \gamma = v = 1$ ,  $E = A = 1$  and  $\psi = 1$ , so to satisfy  $A(E + 1) > 1$ . All shown at times  $t = 0, 25$  and  $50$ . Species on the right displaces species on the left.*

In Figure 4.7 it can be seen that species 2 (which starts on the right) eliminates species 1 (which starts on the left), corresponding to the solution of equation (4.7) approaching the third stationary point  $(0, 0, 1, 1)$ . It is interesting to note that if the elimination of tips is less than the elimination of hyphae i.e.  $A < E$  then it takes longer for the extinction of the entire species. On the other hand, if the elimination of tips is greater than the elimination of hyphae i.e.  $A > E$  then the species approaches its demise quicker. This is illustrated with values of  $A = \frac{1}{2}$  and  $E = 3$  in Figure 4.8(a) and  $A = 3$  and  $E = \frac{1}{2}$  in Figure 4.8(b) (with all other parameters remaining the same).

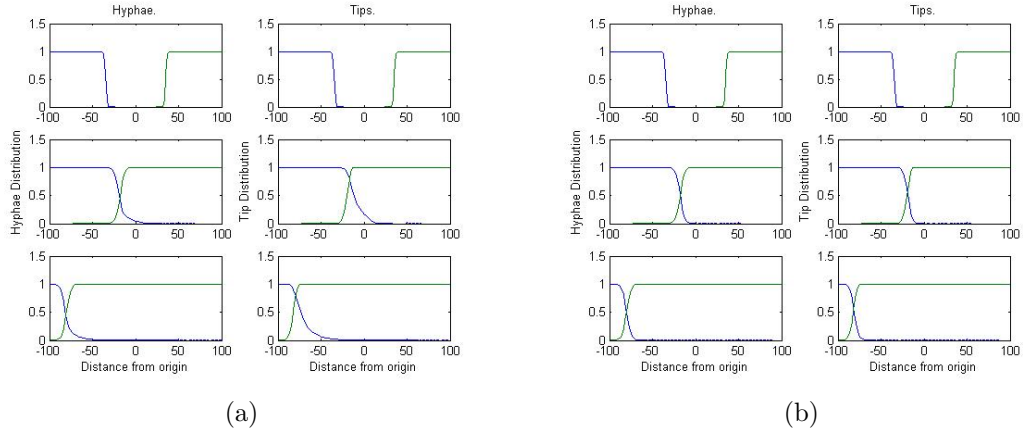


**Figure 4.8:** *System of equations in (4.5) with initial conditions (4.2) and (4.3) are solved with parameters  $\alpha = \beta = \gamma = v = 1$ ,  $A = \frac{1}{2}$ ,  $E = 3$  and  $\psi = 1$  is represented in (a) where species on the right displaces species on the left at a slower rate. Solving with parameter values  $\psi = 1$ ,  $A = 3$  and  $E = \frac{1}{2}$  is represented in (b) where species on the right displaces species on the left at a faster rate. All shown at times  $t = 0, 25$  and  $50$ .*

We will now numerically solve the system of equations in (4.7) with initial conditions in (4.2) using the parameter values  $E = A = \frac{2}{5}$  and  $\psi = \frac{5}{2}$  so that  $A(E + 1) < 1$ . Thus the first three stationary points are unstable and the fourth stationary point corresponding to coexistence is stable (Figure 4.9).

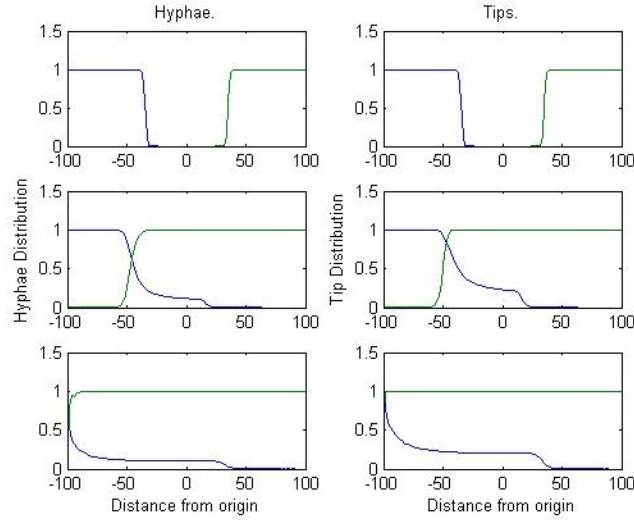


**Figure 4.9:** *System of equations in (4.7) with initial condition (4.2) have been solved numerically using parameter values  $\alpha = \frac{5}{2}$ ,  $\beta = \frac{25}{4}$ ,  $\gamma = v = 1$ ,  $E = A = \frac{2}{5}$  and  $\psi = \frac{5}{2}$ . All shown at times  $t = 0, 25$  and  $50$ . Both species can be seen to coexist with species on the right dominating.*

It can be seen from Figure 4.9 that both species coexist with species 1 existing at a reduced density than species 2. This is due to the reduction of hyphae and tips of species 1 by species 2. As the growth term imbedded in  $\psi$  is greater than the rate of the attack ( $A$  and  $E$ ), it is able to survive.

We have so far observed that there will always be coexistence between the species as long as  $A(E + 1) < 1$  is satisfied. By assuming that the rate of attack of the hyphae and tips in species 1 by species 2 is the same, it has been established that species 1 will survive at a lower density. We will now examine the effect of varying these parameter values to observe the behaviour. The result is similar to that obtained earlier (where it was found that when the depletion of tips is lower than the depletion of hyphae, species 1 takes longer to reach extinction and vice versa, see Figure 4.10(a) and 4.10(b)).

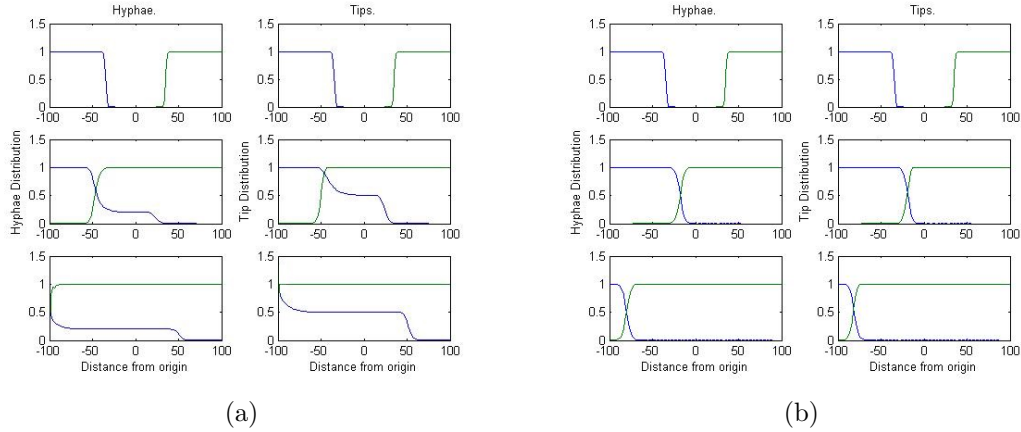


**Figure 4.10:** *System of equations in (4.5) with initial conditions (4.2) and (4.3) are solved with parameters  $\alpha = \frac{5}{2}$ ,  $\beta = \frac{25}{6}$ ,  $\gamma = v = 1$ ,  $A = \frac{1}{5}$ ,  $E = \frac{3}{5}$  and  $\psi = \frac{5}{2}$  is represented in (a) where species on the left's hyphal and tip densities are depleting slower. Solving with parameter values  $\alpha = \frac{5}{2}$ ,  $\beta = \frac{25}{6}$ ,  $\gamma = v = 1$ ,  $A = \frac{3}{5}$ ,  $E = \frac{1}{5}$  and  $\psi = \frac{5}{2}$  is represented in (b) where species on the left's hyphal and tip densities are depleting faster. All shown at times  $t = 0, 25$  and  $50$ .*

The results obtained show that the hyphae density of species 1 depend on the rate of interaction of its tips with the hyphae of species 2. If species 2 tend to target the hyphae of its rival more than its tips, then it could dominate the species without pushing it to extinction and letting it coexist in the same vicinity but at a reduced density.

#### 4.2.3.3 Conclusion

In this model we have explored the effect of two species of fungi, one of which has the ability to reduce its rivals tips and hyphae and the other does not. We have found that both species can survive and coexist together with the less dominant fungi existing with a lower density than its rival only if the rival fungi eliminates the hyphae of the opponent at a greater rate than it reduces its tips (see Figure 4.8 where  $A < E$ ). On the other hand if the fungi reduces the tips of its opponent at a faster rate than its hyphae, then the less dominant species of fungi is displaced (Figure 4.10(b)). If the dominant species eliminates the tips and hyphae at the same rate ( $A = E$ ) but the defending fungi is able to generate tips faster then coexistence would occur (Figure 4.9). In this type of environment the dominant fungi can benefit from its rival in many ways, for example the existing fungi can

have farther reach of nutrient or might even be contributing by bonding to a nutrient source, which is favourable to its rival.

For the species of fungi to coexist it has been determined in the analysis the inequality  $1 > A(E + 1)$  must hold true. Thus, if the growing fungus cannot generate growth faster than it is being attacked then it is bound to be eliminated. The rate of elimination can depend on the style of attack from its rival. If the rival targets its hyphae more rapidly than it targets the tips, the fungi will remain in existence for a longer period of time but its ultimate fate still depends on the relative values of the model parameters  $A$  and  $E$ .

## 4.3 Nutrient dependent interactions

In the previous section, it was tacitly assumed there was a constant and uncontrollable quantity of nutrient available to the fungi. In particular, the nutrient influence on hyphal extension, branching and toxin production was not explicitly incorporated in to the model for simplicity purposes. This hinders the applicability of the results obtained and is contrary to some studies that have shown hyphal extension rates and branching rates are influenced by localised nutrient concentrations (e.g Gruhn et al., 1992). Therefore in this section we will extend the model to include nutrient influence.

### 4.3.1 Model equations

Since the process of hyphal tip extension is the culmination of a cascade of metabolic processes each requiring suitable nutrients, consistent with previous studies (e.g. Prosser and Trinci, 1979) it is reasonably assumed that the speed of tip movement is proportional to the concentration of nutrients available to that fungal biomass. Nutrient uptake in fungal models are usually represented by the Michaelis-Menton kinetics (e.g. Goyal et al., 2013). Since the purpose of the current investigation is to understand the role of nutrient availability on the outcome of competition, it is assumed that the nutrients are represented by a single generic substrate and that  $c_j$  denotes the concentration of that substrate available to biomass  $j$ . Thus the speed of the model tip movement in biomass  $j$  is given by  $v_j c_j$  and the creation of biomass is given by the corresponding flux of the model tips. Also, to capture the natural turnover in hyphal segments, it is assumed that

material in biomass  $j$  has a constant degradation rate of  $\gamma_j$  independent of any competition.

Experimental investigations have long since established that an increase in glucose concentrations within a mycelium is associated with an increase in hyphal branching (Gruhn et al., 1992). Consequently, and consistent with previous modelling studies (Boswell et al., 2003a, 2007; Boswell and Davidson, 2012; Hopkins and Boswell, 2012), it is assumed that the production of new model tips in biomass  $j$  is proportional to  $c_j\rho_j$  capturing the dependence of this process on both the concentration of substrate and the hyphal length from which new tips can emerge. Anastomosis, the fusion of tips with other hyphae, is a process that regulates the density of hyphal tips. Again, consistent with previous studies (Edelstein, 1982; Boswell and Davidson, 2012), it is assumed that the per capita loss of model tips in biomass  $j$  is proportional to the density of biomass  $j$ , namely  $\rho_j$ .

During fungal competition, combinations of VOCs and toxic metabolites are produced along the lengths of hyphae that comprise the mycelium. Due to the concomitant energy costs, the production of these compounds is reasonably assumed to be proportional to the energy available to the biomass, i.e. proportional to  $c_1$  or  $c_2$ . Further, since these compounds restrict the ability of a rival biomass to create new hyphal material as well as degrading existing hyphae, they essentially cause hyphal tips in a rival to cease functioning and reduce the density of existing biomass. For convenience these substances are not represented explicitly but instead their influence on rival biomasses is modelled. Therefore the process of tip inhibition/degradation and hyphal degradation in biomass  $j$  by biomass  $i$  ( $i \neq j$ ) is modelled using terms proportional to  $c_i\rho_i n_j$  and  $c_i\rho_i\rho_j$  respectively. This approach is consistent with observed behaviour of competing fungi where the amount of VOCs produced changes during competition and depends on the degree of contact between the two species (Hynes et al., 2007).

Thus the mathematical model is described by four coupled partial differ-



ential equations

$$\begin{aligned}
\frac{\partial \rho_1}{\partial t} &= v_1 c_1 n_1 - \gamma_1 \rho_1 - E c_2 \rho_2 \rho_1, \\
\frac{\partial n_1}{\partial t} &= -\frac{\partial(v_1 c_1 n_1)}{\partial x} + \alpha_1 c_1 \rho_1 - \beta_1 \rho_1 n_1 - A c_2 \rho_2 n_1, \\
\frac{\partial \rho_2}{\partial t} &= v_2 c_2 n_2 - \gamma_2 \rho_2 - F c_1 \rho_1 \rho_2, \\
\frac{\partial n_2}{\partial t} &= \frac{\partial(v_2 c_2 n_2)}{\partial x} + \alpha_2 c_2 \rho_2 - \beta_2 \rho_2 n_2 - B c_1 \rho_1 n_2,
\end{aligned} \tag{4.9}$$

where all the parameters are consistent with equations (4.1).

The main purpose of the current investigation is to focus on the role of nutrient availability and its involvement in determining the outcome of pairwise competition between fungi. As previous studies have shown (e.g. Edelstein, 1982), tip velocity and local branching and anastomosis rates dictate the densities achieved by biomasses in the absence of competition which in turn impact on the competitive ability of the biomass. Therefore, in order to isolate the key role of nutrient availability on competition, it is reasonably assumed that the two rival biomasses have similar growth characteristics and only differ in their local nutrient resources and their ability to degrade and inhibit the growth of their rivals. Thus nutrient resources provide the main drivers for differences in biomass competition. Therefore, we use the same assumption and non-dimensionalisation parameters as in Section 4.2.1 to get

$$\begin{aligned}
\frac{\partial \rho_1}{\partial t} &= c_1 n_1 - \rho_1 - E c_2 \rho_2 \rho_1, \\
\frac{\partial n_1}{\partial t} &= -\frac{\partial(c_1 n_1)}{\partial x} + \psi c_1 \rho_1 - \psi \rho_1 n_1 - A \psi c_2 \rho_2 n_1, \\
\frac{\partial \rho_2}{\partial t} &= c_2 n_2 - \rho_2 - F c_1 \rho_1 \rho_2, \\
\frac{\partial n_2}{\partial t} &= \frac{\partial(c_2 n_2)}{\partial x} + \psi c_2 \rho_2 - \psi \rho_2 n_2 - B \psi c_1 \rho_1 n_2,
\end{aligned} \tag{4.10}$$

where stars have been dropped for notational convenience. While alternative non-dimensionalisations are possible, the particular choice adopted here, which retains independent parameters relating to the two substrate concentrations, is central to the results obtained from the following analysis.

Previous modelling investigations (e.g. Boswell et al., 2002, 2003a) explicitly simulated the distribution of a substrate, representing a growth promoting

carbon, inside the biomass structure, accounting for not only its uptake from the external environment and depletion due to growth costs, but also its movement within the biomass network. Indeed, when the external resource was continually replenished, the internally-held substrate distribution was the same order of magnitude throughout the majority of the biomass (Boswell, 2012). Consequently, it is assumed that the variables  $c_1$  and  $c_2$  are constant throughout the biomass and also do not change over time corresponding to biomass expansion and competition in a continually-replenished or nutrient-rich environment.

As previously explained, the suppression of hyphal tip extension and the degradation of hyphae represent the two major processes used by fungal biomasses during competition. To isolate the effect of each, attention is focussed first on the impact of tip suppression when hyphal degradation is neglected (by assuming  $E$  and  $F$  are both zero) before extending the analysis to include both processes acting simultaneously.

### 4.3.2 Model tip suppression only

In the absence of hyphal degradation ( $E = F = 0$ ), the corresponding model equations (4.10) become

$$\begin{aligned}\frac{\partial \rho_1}{\partial t} &= c_1 n_1 - \rho_1, \\ \frac{\partial n_1}{\partial t} &= -\frac{\partial(c_1 n_1)}{\partial x} + \psi(c_1 \rho_1 - \rho_1 n_1 - A c_2 \rho_2 n_1), \\ \frac{\partial \rho_2}{\partial t} &= c_2 n_2 - \rho_2, \\ \frac{\partial n_2}{\partial t} &= \frac{\partial(c_2 n_2)}{\partial x} + \psi(c_2 \rho_2 - \rho_2 n_2 - B c_1 \rho_1 n_2).\end{aligned}\tag{4.11}$$

#### 4.3.2.1 Equilibria and stability

Edelstein (1982) and work in Chapter 2 showed that model equations similar to those in equation (4.11) gave rise to travelling wave solutions and hence if there are travelling wave solutions the spatially-uniform stationary points provide information on such solutions. The system of equations in (4.11) has four such stationary points that can be found and classified. The spatially-uniform equilibria

of the non-dimensionalised equations (4.11) satisfy

$$\begin{aligned}
0 &= c_1 n_1 - \rho_1, \\
0 &= \psi(c_1 \rho_1 - \rho_1 n_1 - A c_2 \rho_2 n_1), \\
0 &= c_2 n_2 - \rho_2, \\
0 &= \psi(c_2 \rho_2 - \rho_2 n_2 - B c_1 \rho_1 n_2).
\end{aligned}$$

There are four equilibria, three of which can be easily determined after some trivial algebraic manipulation

$$(\rho_1^*, n_1^*, \rho_2^*, n_2^*) = (0, 0, 0, 0), \quad (\text{SP0})$$

$$(c_1^2, c_1, 0, 0), \quad (\text{SP1})$$

$$(0, 0, c_2^2, c_2). \quad (\text{SP2})$$

There is a fourth stationary point corresponding to coexistence (or intermingling). After some lengthy algebra the stationary point is shown below

$$\left( \frac{Ac_2^3 - c_1^2}{ABc_1c_2 - 1}, \frac{Ac_2^3 - c_1^2}{c_1(ABc_1c_2 - 1)}, \frac{Bc_1^3 - c_2^2}{ABc_1c_2 - 1}, \frac{Bc_1^3 - c_2^2}{c_2(ABc_1c_2 - 1)} \right), \quad (\text{SP3a})$$

which is biologically realistic when both  $Ac_2^3 < c_1^2$  and  $Bc_1^3 < c_2^2$ , or when both  $Ac_2^3 > c_1^2$  and  $Bc_1^3 > c_2^2$ . Clearly stationary points (SP0), (SP1) and (SP2) are biologically realistic (i.e. non-negative) for all non-negative parameter values. The stability of the stationary points found above are determined from the characteristic equation

$$\begin{vmatrix}
-1 - \lambda & c_1 & 0 & 0 \\
\psi(c_1 - n_1) & -\psi\rho_1 - A\psi c_2 \rho_2 - \lambda & -A\psi c_2 n_1 & 0 \\
0 & 0 & -1 - \lambda & c_2 \\
-B\psi c_1 n_2 & 0 & \psi(c_2 - n_2) & -\psi\rho_2 - B\psi c_1 \rho_1 - \lambda
\end{vmatrix} = 0.$$

### SP0

The characteristic equation obtained from the above matrix evaluated at the stationary point  $(0, 0, 0, 0)$  can be easily factorised into two quadratics

$$(\lambda^2 + \lambda - \psi c_2^2)(\lambda^2 + \lambda - \psi c_1^2) = 0.$$

Hence the stability of this stationary point is determined by the roots of two quadratic equations. Since the coefficient of the constant term is negative in at least one of the quadratics, the Routh-Hurwitz criteria for polynomials of degree 2 implies that there is an eigenvalue with a positive real part and hence the stationary point (SP0) is unstable. Furthermore, due to the structure of the quadratics, this stationary point is clearly a saddle point.

### SP1

Substituting the equilibria  $(c_1^2, c_1, 0, 0)$  into the above characteristic equation yields an equation that can be easily factorised:

$$(\lambda + 1)(\lambda + \psi c_1^2) (\lambda^2 + (1 + \psi B c_1^3)\lambda + \psi B c_1^3 - \psi c_2^2) = 0.$$

Since two of the eigenvalues are clearly negative, the roots of the quadratic determine the stability of stationary point (SP1). Again, using the Routh-Hurwitz criteria for polynomials of degree 2, the stationary point (SP1) is stable provided the constant term is positive, i.e.  $B c_1^3 > c_2^2$  and hence is otherwise a saddle point.

### SP2

Similar to above, the characteristic equation evaluated at the stationary point (SP2) can be factorised:

$$(\lambda + 1)(\lambda + \psi c_2^2) (\lambda^2 + (1 + \psi A c_2^3)\lambda + \psi A c_2^3 - \psi c_1^2) = 0.$$

Hence an application of the Routh-Hurwitz criteria implies that stationary point (SP2) is stable provided  $A c_2^3 > c_1^2$  and is otherwise a saddle point.

### SP3a

After significant algebraic manipulation, the characteristic equation evaluated at the fourth stationary point (SP3a) can be written as

$$(\lambda + 1) \left[ \lambda^3 + (1 + \psi(c_1^2 + c_2^2)) \lambda^2 + \psi \left( \frac{c_1^2(u-1) + c_2^2(w-1)}{uw-1} + \psi c_1^2 c_2^2 \right) \lambda - \psi^2 c_1^2 c_2^2 \left( \frac{(u-1)(w-1)}{uw-1} \right) \right] = 0, \quad (4.12)$$

where,  $u = Ac_2^3/c_1^2$  and  $w = Bc_1^3/c_2^2$ . Clearly  $\lambda = -1$  is an eigenvalue and hence the roots of the remaining cubic determines the stability of the equilibria. Recall the stationary point (SP3a) is biologically realistic (i.e. the variables are non-negative) provided either  $u, w > 1$  or  $u, w < 1$ . We investigate these two cases below but first recall from the Routh-Hurwitz criteria that the cubic equation  $\lambda^3 + a\lambda^2 + b\lambda + c = 0$  has all roots with negative real parts if  $a, b, c > 0$  and  $ab - c > 0$ . With  $u, w > 1$  the constant term in the cubic of equation (4.12) is negative and so the Routh-Hurwitz condition fails. Therefore the coexistence stationary point (SP3a) is unstable when  $u, w > 1$ .

Assuming  $u, w < 1$  and then by examining the cubic in equation (4.12) it is easily seen that  $a, b, c > 0$  is satisfied (i.e. the quadratic, linear and constant coefficients are all positive). The remaining condition for stability is investigated by examining the term  $ab - c$ . After some lengthy algebra, the expression  $ab - c$  can be written as

$$\begin{aligned} & \left( \frac{c_1^2(u-1) + c_2^2(w-1)}{uw-1} \right) \psi \\ & + \left( \frac{c_1^4(u-1) + c_2^4(w-1) + 2(uw-1)c_1^2c_2^2}{uw-1} \right) \psi^2 \\ & + (c_1^4c_2^2 + c_2^4c_1^2) \psi^3. \end{aligned} \tag{4.13}$$

Since  $u, w < 1$  and the remaining parameters are positive, it is clear that all three terms in (4.13) are positive. Therefore the Routh-Hurwitz criteria implies that the stationary point (SP3a) is stable provided  $u, w < 1$ , i.e. provided  $Ac_2^3 < c_1^2$  and  $Bc_1^3 < c_2^2$ , and is otherwise a saddle point (or biologically unrealistic if it takes negative values).

Consequently from the above analysis the  $c_1$ - $c_2$  parameter space is divided into four regions by the curves  $Ac_2^3 = c_1^2$  and  $Bc_1^3 = c_2^2$  (Figure 4.11 with  $E = F = 0$ ).

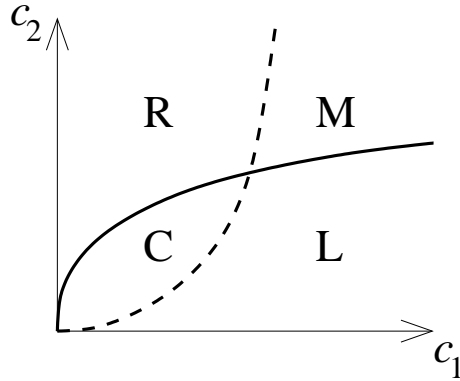


**Figure 4.11:** The  $c_1$ - $c_2$  parameter space for equations (4.10) is divided into regions by the curves  $Ac_2^3(1 + Ec_2^3) = c_1^2$  (solid line) and  $Bc_1^3(1 + Fc_1^3) = c_2^2$  (dashed line). Region R corresponds to where the biomass initially starting on the right will displace that initially on the left. Region L corresponds to where the biomass initially starting on the left will displace that initially on the right. Region C corresponds to where coexistence (or intermingling) of biomasses arises. Region M corresponds to where multiple stable equilibria are found, which can include deadlock.

In essence, when either  $c_1$  is significantly larger than  $c_2$ , or  $c_2$  is significantly larger than  $c_1$ , one fungal biomass will displace the other. If both  $c_1$  and  $c_2$  are sufficiently large then multiple stable equilibria arise and so precise values of  $c_1$  and  $c_2$ , along with initial data, determine the outcome of competition. Finally, if both  $c_1$  and  $c_2$  are similarly and sufficiently small then the only stable equilibrium corresponds to the coexistence (i.e. intermingling) of biomasses.

The area of the region between the curves in Figure 4.11 can be determined using integration and is equal to  $1/(5AB)$  (for  $E = F = 0$ ). Thus it is clear that the region of coexistence gets smaller as the competitive ability of the biomass increases, which is intuitively appealing.

#### 4.3.2.2 Phase-plane analysis

To prove the existence of travelling wave solutions, it is necessary to prove the existence of trajectories in the four-dimensional state space connecting the equilibria constructed above. To this end, introduce  $z = x - st$ , where  $s$  is a constant corresponding to the speed of a travelling wave. Equations (4.11) can then be

represented as

$$\begin{aligned}
\rho'_1 &= -\frac{1}{s}(c_1 n_1 - \rho_1), \\
n'_1 &= -\frac{\psi}{s - c_1}(c_1 \rho_1 - \rho_1 n_1 - A c_2 \rho_2 n_1), \\
\rho'_2 &= -\frac{1}{s}(c_2 n_2 - \rho_2), \\
n'_2 &= -\frac{\psi}{s + c_2}(c_2 \rho_2 - \rho_2 n_2 - B c_1 \rho_1 n_2),
\end{aligned} \tag{4.14}$$

where prime denotes differentiation with respect to the wave variable  $z$ . The parameter  $\psi$  can be regarded as separating the reaction terms of equation (4.11) into two classes: those that change in proportion to  $\psi$ , representing the change of the hyphal tip population, and those independent of  $\psi$ , representing the change of the hyphal biomass population.

For small values of  $\psi$  the change in the model variables  $n_1$  and  $n_2$  can be regarded as varying slower than the change in both  $\rho_1$  and  $\rho_2$ . Due to the construction of the model equations, in particular that the change in the biomass concentrations  $\rho_j$  ( $j = 1, 2$ ) is dictated by the movement of model tips  $n_j$ , the change in biomass concentration lags behind a change in tip concentration (effectively the biomass concentration is continually “catching up” with the tip concentration). Thus there is an inherent stability embedded in the model equations for  $\rho_j$  and therefore it is reasonable to take the approximations  $\rho_1 = c_1 n_1$  and  $\rho_2 = c_2 n_2$  along trajectories in the four-dimensional state space. Thus the system of equations (4.14) then reduces to

$$\begin{aligned}
n'_1 &= -\frac{\psi n_1}{s - c_1}(c_1^2 - c_1 n_1 - A c_2^2 n_2), \\
n'_2 &= -\frac{\psi n_2}{s + c_2}(c_2^2 - c_2 n_2 - B c_1^2 n_1).
\end{aligned} \tag{4.15}$$

This pair of equations can be investigated using standard phase plane analysis. Consistent with the construction of Figure 4.11, there are four distinct ways in which the nullclines of equations (4.15) can intersect. Additionally, the direction of flow in the phase planes of each of these instances depends on the sign of the expressions  $s - c_1$  and  $s + c_2$  corresponding to the three cases  $s > c_1$ ,  $-c_2 < s < c_1$  and  $s < -c_2$ . The twelve possible phase portraits are illustrated in Figure 4.12.

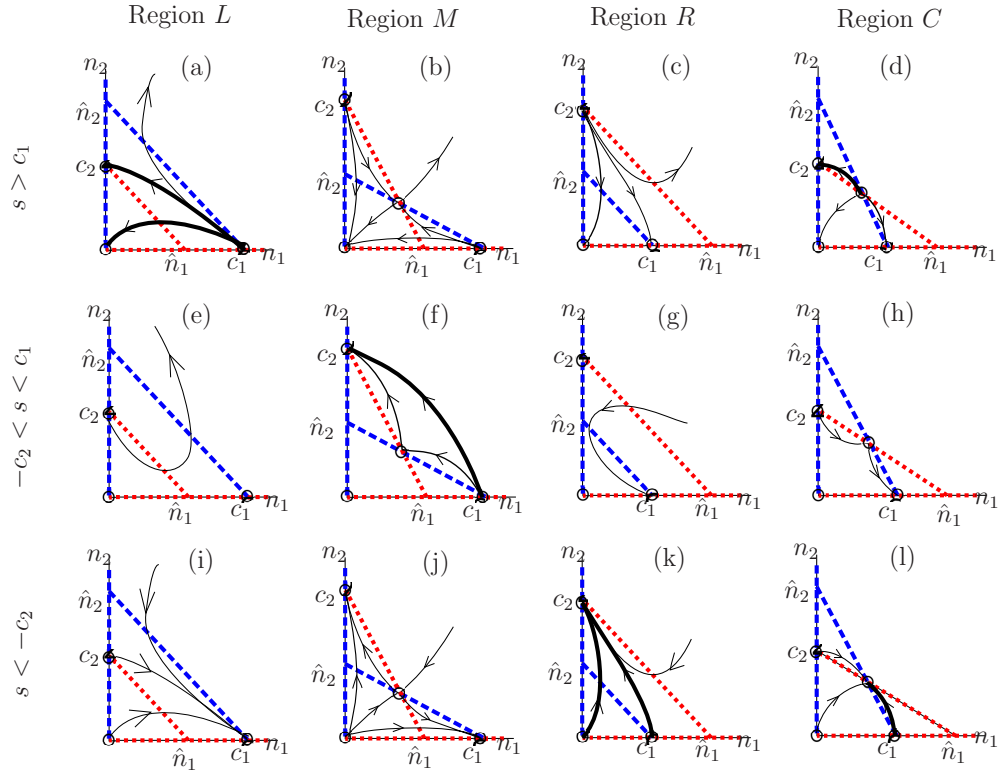


**Figure 4.12:** Phase portraits of equations (4.15) with small  $\psi$  for the cases outlined in Figure 4.11 where  $s$  takes the values indicated and  $\hat{n}_1 = c_2^2/(Bc_1^2)$ ,  $\hat{n}_2 = c_1^2/(Ac_2^2)$ . The  $n_1$ - and  $n_2$ -nullclines are represented by the dashed (blue) and dotted (red) lines respectively with typical trajectories represented by solid black lines. Trajectories in bold illustrate biologically relevant travelling wave solutions of equations (4.11) for small  $\psi$  with  $E = F = 0$ .

The existence of travelling wave solutions in model equations (4.11) requires the presence of trajectories in the phase portraits connecting equilibria in a meaningful manner (e.g. the direction of flow in the state space is consistent with the sign of  $s$  and corresponds to biomass expansion in the appropriate direction). In region  $L$  of the parameter space of Figure 4.11 (where the biomass starting on the left displaces that on the right, and hence indicates a positive value of  $s$ ), the only physically realistic trajectories connecting equilibria arise when  $s > c_1$  (Figure 4.12(a)), thus generating a lower bound for the travelling wave speed. Notice that there are two heteroclinic trajectories in this instance representing the movement of biomass into an empty domain and the movement following collision with the biomass initially starting on the right. A similar situation arises in region  $R$  of Figure 4.11, except the wave speed satisfies  $s < -c_2$  (Figure 4.12(k)).



In region  $M$  of Figure 4.11, where multiple outcomes of biomass competition are possible, the only travelling waves that can exist must satisfy  $-c_2 < s < c_1$  (Figure 4.12(f)). Finally, in region  $C$  of Figure 4.11, corresponding to the coexistence (or intermingling) of biomasses, the only physically realistic trajectories satisfy either  $s > c_1$  or  $s < -c_2$  (Figure 4.12(d), (l)). (Note that in Figure 4.12 (e), (g) there are no heteroclinic orbits and hence no corresponding travelling waves while in Figure 4.12(b, c, h, i, j) the direction of the trajectories is incompatible for the existence of travelling wave solutions for the corresponding values of  $s$  or is not consistent with the stability of the four equilibria of equations (4.11) found above.) The resultant bounds on wave speed for the small  $\psi$  case are summarised in Table 4.1. Consequently, given the bounds on the wave speeds constructed above, the instance of deadlock, which corresponds to stationary distributions, can only arise for values of  $c_1$  and  $c_2$  lying in Region  $M$  of Figure 4.11.

| Figure 4.11 Region | Outcome                      | Condition                        | Wave speed ( $s$ )      |
|--------------------|------------------------------|----------------------------------|-------------------------|
| L                  | Left biomass displaces right | $c_2^2 < Bc_1^3, Ac_2^3 < c_1^2$ | $s > c_1$               |
| M                  | Multiple outcomes            | $c_2^2 < Bc_1^3, Ac_2^3 > c_1^2$ | $-c_2 < s < c_1$        |
| R                  | Right biomass displaces left | $c_2^2 > Bc_1^3, Ac_2^3 > c_1^2$ | $s < -c_2$              |
| C                  | Coexistence / intermingling  | $c_2^2 > Bc_1^3, Ac_2^3 < c_1^2$ | $s > c_1$ or $s < -c_2$ |

**Table 4.1:** *Travelling wave solutions of equations (4.11) for small  $\psi$ .*

A similar technique can be applied when  $\psi$  is large so that it is reasonable to make the approximations  $n_1 = c_1\rho_1/(\rho_1 + Ac_2\rho_2)$  and  $n_2 = c_2\rho_2/(\rho_2 + Bc_1\rho_1)$  along trajectories. Under these conditions equation (4.14) reduces to the pair of equations

$$\begin{aligned}\rho_1' &= -\frac{\rho_1}{s(\rho_1 + Ac_2\rho_2)} (c_1^2 - \rho_1 - Ac_2\rho_2), \\ \rho_2' &= -\frac{\rho_2}{s(\rho_2 + Bc_1\rho_1)} (c_2^2 - \rho_2 - Bc_1\rho_1).\end{aligned}\tag{4.16}$$

As before, there are four alternative ways the nullclines can intersect and the direction of flow depends on the sign of  $s$  yielding a total of 8 distinct phase portraits (Figure 4.13). Depending on parameter values, there are trajectories connecting various equilibria similar to the previous case for small  $\psi$  but in this instance there are no restrictions on  $s$  and hence no bounds on the speed of the travelling waves can be constructed.

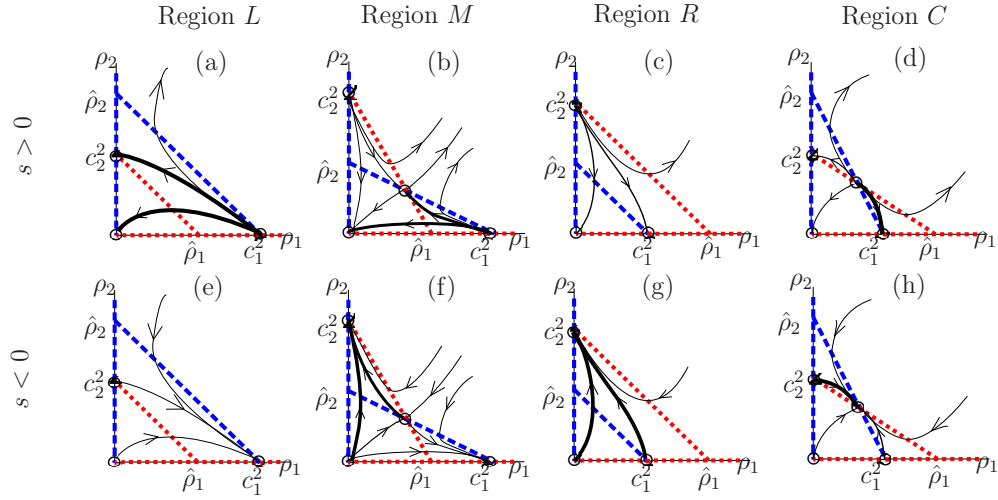


**Figure 4.13:** Phase portraits of equations (4.16) for the different regions of Figure 4.11 where  $s > 0$  and  $s < 0$  as indicated and  $\hat{\rho}_1 = c_2^2/(Bc_1)$ ,  $\hat{\rho}_2 = c_1^2/(Ac_2)$ . The  $\rho_1$ - and  $\rho_2$ -nullclines are represented by the dashed (blue) and dotted (red) lines respectively. Sample trajectories are indicated along with specific trajectories (in bold) connecting equilibria illustrating biologically relevant travelling wave solutions of equations (4.11) for large  $\psi$  with  $E = F = 0$ .

#### 4.3.2.3 Numerical results

When considered in isolation, each of the biomasses and corresponding tips from equation (4.11) generate a stable travelling wave solution. Thus to ensure the biomasses have attained stable distributions prior to their contact, the initial distributions  $\hat{\rho}_j(x)$  and  $\hat{n}_j(x)$  are chosen to be similar to their travelling wave profile. Consequently, and solely for the purpose of numerical integration of the system of equations in (4.9), the nondimensionalised version of the initial data in equation (4.2) is

$$\begin{aligned}\hat{\rho}_1(x) &= \frac{c_1^2}{2} \operatorname{erfc}\left(\frac{\bar{x} + x}{2}\right), & \hat{n}_1(x) &= \frac{c_1}{2} \operatorname{erfc}\left(\frac{\bar{x} + x}{2}\right), \\ \hat{\rho}_2(x) &= \frac{c_2^2}{2} \operatorname{erfc}\left(\frac{\bar{x} - x}{2}\right), & \hat{n}_2(x) &= \frac{c_2}{2} \operatorname{erfc}\left(\frac{\bar{x} - x}{2}\right),\end{aligned}\quad (4.17)$$

where  $2\bar{x}$  represents the initial distance between the two model biomasses and  $\operatorname{erfc}$  is the complementary error function. Note that while these functions are not the final travelling wave profiles obtained by the biomasses when considered in isolation of each other, provided  $\bar{x}$  is sufficiently large, using these initial profiles,  $n_j$  and  $\rho_j$  quickly converge to their stable distributions before any interactions.

The model equations (4.11) with initial data (4.2), (4.17) were solved numerically for a range of parameter values  $c_1$  and  $c_2$  for small and large values of  $\psi$  (Figs. 4.14, 4.15, 4.16). In all instances, the initial distributions of model biomass  $\rho_j$  and model tips  $n_j$  ( $j = 1, 2$ ) rapidly converged on a stable travelling wave profile taking values of zero in front of the wave and  $\rho_j = c_j^2$  and  $n_j = c_j$  ( $j = 1, 2$ ) behind it, consistent with the equilibria found above. These profiles propagated towards the centre of the domain with a constant velocity  $s_j$  ( $j = 1, 2$ ), that was calculated numerically, and in all cases  $s_1 > c_1$  and  $s_2 < -c_2$ , in line with the above analysis. The leading edge of the model tips marginally preceded the leading edge of the model biomasses, which is consistent with the model structure where biomass creation was proportional to tip flux and further justifies the methodology applied in the small and large  $\psi$  analysis investigated above. The rival distributions collided with each other close to the origin but the exact position varied with the values of  $c_1$  and  $c_2$  due to the differences in the propagation speeds  $s_1$  and  $s_2$ . Following their collisions, the distributions took numerous forms depending on parameter values and the speed of the travelling fronts changed accordingly.

For  $\psi = 0.1$ , representing a small value of this parameter, the outcome depended upon the values of  $A, B, c_1$  and  $c_2$ . When  $c_2 < A^{-3/5}B^{-2/5}$  (corresponding to the value of  $c_2$  at the non-trivial intersection of the curves identified in Figure 4.11) three outcomes arose consistent with the above analysis. If  $c_1$  was sufficiently small, i.e.  $c_1 < (Ac_2^3)^{1/2}$  and so in Region  $R$  of Figure 4.11, then the biomass initially starting on the right displaced that initially starting on the left and a corresponding travelling wave solution arose (Figure 4.14(a)) where the resultant wave speed satisfied  $s < -c_2$ . If  $(Ac_2^3)^{1/2} < c_1 < (c_2^2/B)^{1/3}$ , corresponding to Region  $C$  of Figure 4.11, then the biomasses coexisted after their collision at reduced densities and both wave fronts continued to propagate at reduced speeds (Figure 4.14(b)) where  $s_1 > c_1$  and  $s_2 < -c_2$ . If  $c_1 > (c_2^2/B)^{1/3}$ , corresponding to Region  $L$  of Figure 4.11, then the biomass initially starting on the left displaced that on the right (Figure 4.14(c)) and the resultant wave speed satisfied  $s > c_1$ . When  $c_2 > A^{-3/5}B^{-2/5}$ , consistent with the parameter space of Figure 4.11, the biomass initially starting on the right displaced that on the left if  $c_1 < (c_2^2/B)^{1/3}$  (i.e. in Region  $R$ ) and vice-versa if  $c_1 > (Ac_2^3)^{1/2}$  (i.e. in Region  $L$ ). However, for  $(c_2^2/B)^{1/3} < c_1 < (Ac_2^3)^{1/2}$  (corresponding to region  $M$  in Figure 4.11) different solutions were obtained depending on the precise values of  $c_1$  and  $c_2$  corresponding to the right biomass displacing the left (Figure 4.15(a)); deadlock, where nei-

ther distribution moved following collision (Figure 4.15(b)); and the left biomass displacing the right (Figure 4.15(c)). In all these cases, the speeds of the travelling wave fronts satisfied  $-c_2 < s < c_1$ , consistent with the bounds presented in Table 4.1.

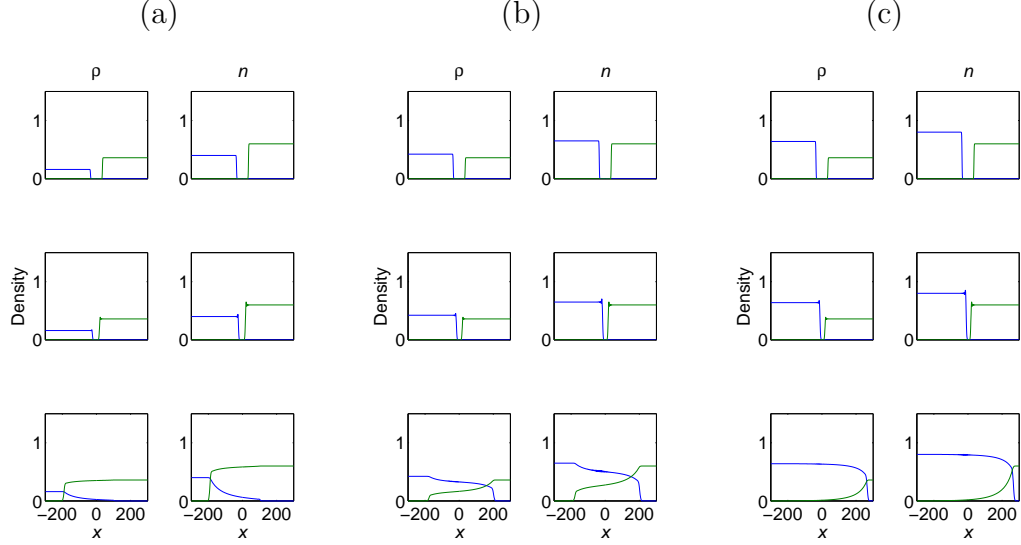


**Figure 4.14:** Numerical solutions of equations (4.11) with initial data (4.2), (4.17) over the interval  $(-300, 300)$  with  $\bar{x} = 35$ ,  $A = B = 1$  and  $\psi = 0.1$ . Distributions are shown at times  $t = 0, 30$  and  $350$  where values of  $c_1$  and  $c_2$  belong to (a) region  $R$ , (b) region  $C$  and (c) region  $L$  of Figure 4.11. (a)  $c_1 = 0.4$ ,  $c_2 = 0.6$  (with travelling wave speeds of  $s_1 = 0.43$ ,  $s_2 = -0.65$  before collision,  $s_1 = s_2 = -0.64$  after collision). (b)  $c_1 = 0.65$ ,  $c_2 = 0.6$  (with travelling wave speeds of  $s_1 = 0.72$ ,  $s_2 = -0.65$  before collision,  $s_1 = 0.69$ ,  $s_2 = -0.61$  after collision). (c)  $c_1 = 0.8$ ,  $c_2 = 0.6$  (with travelling wave speeds of  $s_1 = 0.87$ ,  $s_2 = -0.65$  before collision,  $s_1 = s_2 = 0.87$  after collision).

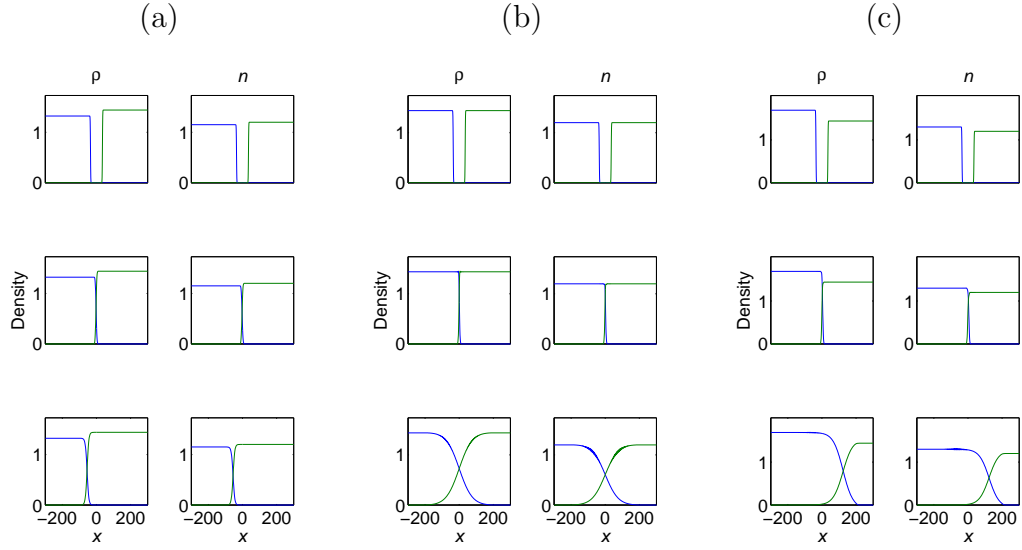


**Figure 4.15:** Numerical solutions of equations (4.11) with initial data (4.2), (4.17) over the interval  $(-300, 300)$  with  $\bar{x} = 35$ ,  $A = B = 1$  and  $\psi = 0.1$ . Distributions are shown at times  $t = 0, 30$  and  $200$  where values of  $c_1$  and  $c_2$  belong to region  $M$  of Figure 4.11, where multiple outcomes from competition are possible. (a)  $c_1 = 1.15$ ,  $c_2 = 1.2$  (with travelling wave speeds of  $s_1 = 1.30$ ,  $s_2 = -1.35$  before collision,  $s_1 = s_2 = -0.33$  after collision). (b)  $c_1 = 1.2$ ,  $c_2 = 1.2$  (with travelling wave speeds of  $s_1 = 1.35$ ,  $s_2 = -1.35$  before collision,  $s_1 = s_2 = 0$  after collision, i.e. deadlock). (c)  $c_1 = 1.3$ ,  $c_2 = 1.2$  (with travelling wave speeds of  $s_1 = 1.59$ ,  $s_2 = -1.35$  before collision,  $s_1 = s_2 = 1.13$  after collision).

The bounds on the travelling wave speeds for small  $\psi$  (Table 4.1) do not apply to larger values of  $\psi$  (Figure 4.16). For example, in Figure 4.16(a), following collision of biomasses, the speed of the advancing wave fronts satisfied  $s_1 > c_1$  and  $s_2 < -c_2$  while in Figure 4.16(c), their speeds satisfied  $s_1 < c_1$  and  $s_2 > -c_2$ , despite both these combinations of  $c_1$  and  $c_2$  belonging to region  $C$  of Figure 4.11.

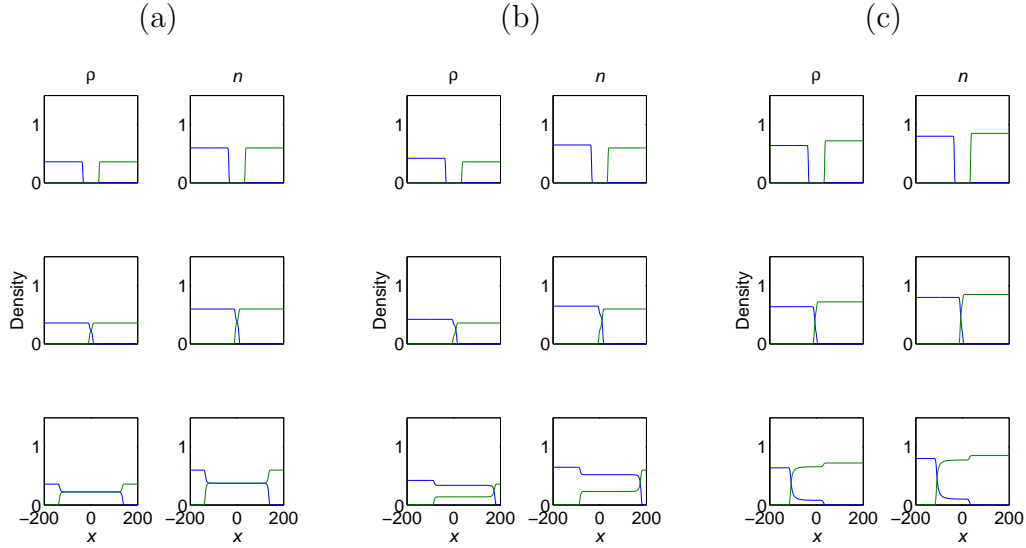


**Figure 4.16:** Numerical solutions of equations (4.10) with initial data (4.2), (4.17) over the interval  $(-200, 200)$  with  $\bar{x} = 35$  and  $A = B = 1$ ,  $E = F = 0$  and  $\psi = 10$ . Distributions are shown at times  $t = 0, 30$  and  $200$  for values of  $c_1$  and  $c_2$  in the region  $C$  of Figure 4.11, ensuring coexistence (or intermingling) of biomasses. (a)  $c_1 = 0.6$ ,  $c_2 = 0.6$  (with travelling wave speeds of  $s_1 = 2.07$ ,  $s_2 = -2.07$  before collision,  $s_1 = 0.77$ ,  $s_2 = -0.77$  after collision). (b)  $c_1 = 0.65$ ,  $c_2 = 0.6$  (with travelling wave speeds of  $s_1 = 2.27$ ,  $s_2 = -2.07$  before collision,  $s_1 = 0.98$ ,  $s_2 = -0.49$  after collision). (c)  $c_1 = 0.8$ ,  $c_2 = 0.85$  (with travelling wave speeds of  $s_1 = 2.92$ ,  $s_2 = -3.07$  before collision,  $s_1 = 0.18$ ,  $s_2 = -0.61$  after collision).

### 4.3.3 Mutual tip suppression and hyphal degradation

#### 4.3.3.1 Equilibria and stability

When the processes of both tip suppression and hyphal degradation are considered to be acting simultaneously, the same qualitative features arose as obtained above. The system of equations in (4.10) has four stationary points, three of which can be easily found and classified. A fourth stationary point can be found in certain special and interesting cases. The spatially-uniform stationary points take more complicated forms than before and correspond to the absence of both biomasses, the presence of only one biomass, and the coexistence of biomasses. The spatially-

uniform equilibria of the non-dimensionalised equations (4.10) satisfy

$$\begin{aligned}
0 &= c_1 n_1 - \rho_1 - E c_2 \rho_1 \rho_2, \\
0 &= \psi(c_1 \rho_1 - \rho_1 n_1 - A c_2 \rho_2 n_1), \\
0 &= c_2 n_2 - \rho_2 - F c_1 \rho_1 \rho_2, \\
0 &= \psi(c_2 \rho_2 - \rho_2 n_2 - B c_1 \rho_1 n_2).
\end{aligned}$$

Similar to the previous cases, three equilibria are given by

$$\begin{aligned}
(\rho_1^*, n_1^*, \rho_2^*, n_2^*) &= (0, 0, 0, 0), & (\text{SP0}) \\
(c_1^2, c_1, 0, 0), & & (\text{SP1}) \\
(0, 0, c_2^2, c_2), & & (\text{SP2})
\end{aligned}$$

and are identical to the previous case with  $E = F = 0$ . The remaining stationary point, corresponding to coexistence, cannot be expressed in a convenient closed form. However, there are a number of exceptions. One insightful exception arises when  $A = B = 0$  (i.e. in the absence of tip suppression) in which case the stationary point (SP3b) is  $(\bar{\rho}_1, \bar{n}_1, \bar{\rho}_2, \bar{n}_2)$  where

$$\begin{aligned}
\bar{\rho}_1 &= \frac{F c_1^3 - E c_2^3 - 1 + \sqrt{(F c_1^3 - E c_2^3 - 1)^2 + 4 F c_1^3}}{2 F c_1}, & \bar{n}_1 &= c_1, \\
\bar{\rho}_2 &= \frac{E c_2^3 - F c_1^3 - 1 + \sqrt{(E c_2^3 - F c_1^3 - 1)^2 + 4 E c_2^3}}{2 E c_2}, & \bar{n}_2 &= c_2.
\end{aligned}$$

Notice that  $\bar{\rho}_1$  increases with  $c_1$  but decreases with  $c_2$  (and vice-versa for  $\bar{\rho}_2$ ). Therefore the density of one model biomass increases with the availability of nutrients but is inhibited by the presence of a rival.

The stability of the stationary points found above are determined from the following characteristic equation

$$\begin{vmatrix}
-1 - E c_2 \rho_2 - \lambda & c_1 & -E c_2 \rho_1 & 0 \\
\psi(c_1 - n_1) & -\psi \rho_1 - A \psi c_2 \rho_2 - \lambda & -A \psi c_2 n_1 & 0 \\
-F c_1 \rho_2 & 0 & -1 - F c_1 \rho_1 - \lambda & c_2 \\
-B \psi c_1 n_2 & 0 & \psi(c_2 - n_2) & -\psi \rho_2 - B \psi c_1 \rho_1 - \lambda
\end{vmatrix} = 0.$$

### SP0

The characteristic equation obtained from the above matrix evaluated at the stationary point  $(0, 0, 0, 0)$  can be easily factorised into two quadratics

$$(\lambda^2 + \lambda - \psi c_2^2)(\lambda^2 + \lambda - \psi c_1^2) = 0.$$

By the Routh-Hurwitz criteria for polynomials of degree 2 this stationary point is clearly a saddle point.

### SP1

Substituting the equilibria  $(c_1^2, c_1, 0, 0)$  into the above characteristic equation yields an equation that can be easily factorised:

$$(\lambda + 1)(\lambda + \psi c_1^2) (\lambda^2 + (1 + Fc_1^3 + \psi Bc_1^3)\lambda + \psi Bc_1^3(1 + Fc_1^3) - \psi c_2^2) = 0.$$

Two of the eigenvalues are clearly negative. Again, using the Routh-Hurwitz criteria for polynomials of degree 2, the stationary point (SP1) is stable provided the constant term in the quadratic is positive, i.e.  $Bc_1^3(1 + Fc_1^3) > c_2^2$  and hence is otherwise a saddle point.

### SP2

Similar to above, the characteristic equation evaluated at the stationary point (SP2) can be factorised:

$$(\lambda + 1)(\lambda + \psi c_2^2) (\lambda^2 + (1 + Ec_2^3 + \psi Ac_2^3)\lambda + \psi Ac_2^3(1 + Ec_2^3) - \psi c_1^2) = 0.$$

Hence an application of the Routh-Hurwitz criteria implies that stationary point (SP2) is stable provided  $Ac_2^3(1 + Ec_2^3) > c_1^2$  and is otherwise a saddle point.

### SP3b

The characteristic equation evaluated at the stationary point (SP3b) for the special case  $A = B = 0$  can be factorised to give

$$0 = (\lambda + \psi \rho_1^*)(\lambda + \psi \rho_2^*)(\lambda + 1) (\lambda + 1 + Ec_2 \rho_2^* + Fc_1 \rho_1^*)$$



where  $\rho_1^*$  and  $\rho_2^*$  are the values of  $\rho_1$  and  $\rho_2$  at the stationary point (SP3b) respectively. Clearly, since  $\rho_1^*$  and  $\rho_2^*$  are positive, the stationary point (SP3b) is asymptotically stable. Notice also that in this special case of  $A = B = 0$ , coexistence is always a stable stationary point and therefore the suppression of hyphal tips (which corresponds to  $A, B > 0$ ) clearly occupies a central role in the diversity of outcomes of competition.

Similar to Section 4.3.2.1, and provided  $A$  and  $B$  are not both zero, the  $c_1$ - $c_2$  parameter space is divided by the curves  $Bc_1^3(1 + Fc_1^3) = c_2^2$  and  $Ac_2^3(1 + Ec_2^3) = c_1^2$  into the four regions identical to that found previously (Figure 4.11). Hence if  $c_1$  is significantly larger than  $c_2$  the only stable equilibria corresponds to the presence of the model biomass  $\rho_1$  and its model tips  $n_1$ , with the reverse case if  $c_2$  is significantly larger than  $c_1$ . If  $c_1$  and  $c_2$  are both large then there are multiple stable equilibria and provided  $c_1$  and  $c_2$  are sufficiently and similarly small then coexistence (i.e. intermingling) is observed.

#### 4.3.3.2 Phase-plane analysis

As in the previous case, the existence of travelling wave solutions connecting the equilibria identified above can be determined by setting  $z = x - st$  in equations (4.10) where  $A, B, E$  and  $F$  are non-zero:

$$\begin{aligned}\rho_1' &= -\frac{1}{s}(c_1 n_1 - \rho_1 - Ec_2 \rho_1 \rho_2), \\ n_1' &= -\frac{\psi}{s - c_1}(c_1 \rho_1 - \rho_1 n_1 - Ac_2 \rho_2 n_1), \\ \rho_2' &= -\frac{1}{s}(c_2 n_2 - \rho_2 - Fc_1 \rho_1 \rho_2), \\ n_2' &= -\frac{\psi}{s + c_2}(c_2 \rho_2 - \rho_2 n_2 - Bc_1 \rho_1 n_2),\end{aligned}\tag{4.18}$$

where prime denotes differentiation with respect to the wave variable  $z$ . Similar to the approach in Section 4.3.2.1 and for the same reasons, if  $\psi$  is large it is reasonable to make the approximations  $n_1 = c_1 \rho_1 / (\rho_1 + Ac_2 \rho_2)$ ,  $n_2 = c_2 \rho_2 / (\rho_2 + Bc_1 \rho_1)$  and hence the system of equations (4.18) reduces to

$$\begin{aligned}\rho_1' &= -\frac{\rho_1}{s} \left( \frac{c_1^2}{\rho_1 + Ac_2 \rho_2} - 1 - Ec_2 \rho_2 \right), \\ \rho_2' &= -\frac{\rho_2}{s} \left( \frac{c_2^2}{\rho_2 + Bc_1 \rho_1} - 1 - Fc_1 \rho_1 \right),\end{aligned}\tag{4.19}$$

and standard phase space analysis in the  $\rho_1$ - $\rho_2$  plane can be used to investigate this system. From equations (4.19), the  $\rho_2$ -nullclines are the line  $\rho_2 = 0$  and the curve  $\rho_2 = \frac{c_2^2}{1 + Fc_1\rho_1} - Bc_1\rho_1$ , which is defined for all  $\rho_1 \neq -1/(Fc_1)$ . The second of these satisfies

$$\begin{aligned}\frac{d\rho_2}{d\rho_1} &= -\frac{Fc_1c_2^2}{(1 + Fc_1\rho_1)^2} - Bc_1, \\ \frac{d^2\rho_2}{d\rho_1^2} &= \frac{2F^2c_1^2c_2^2}{(1 + Fc_1\rho_1)^3}.\end{aligned}$$

Notice that the first derivative of the non-zero nullcline is negative for all values of  $\rho_1 \neq -1/(Fc_1)$  while the second derivative is positive provided  $\rho_1 > -1/(Fc_1)$ . In particular, this demonstrates that the non-zero  $\rho_2$ -nullcline decreases from the vertical asymptote  $\rho_1 = -1/(Fc_1)$ , crosses the  $\rho_2$ -axis at  $(0, c_2^2)$  and tends to the oblique asymptote  $\rho_2 = -Bc_1\rho_1$ .

Through the symmetry in equations (4.19), the  $\rho_1$ -nullclines have equivalent properties where the model variables and parameters are suitably transposed; namely the non-zero  $\rho_1$ -nullcline has negative first derivative and positive second derivative provided  $\rho_2 > -1/(Ec_2)$ . In particular, in the  $\rho_1$ - $\rho_2$  phase space, the non-zero  $\rho_1$ -nullcline declines from the oblique asymptote  $\rho_2 = -\rho_1/(Ac_2)$ , crosses the  $\rho_1$ -axis at  $(c_1^2, 0)$  before tending to the horizontal asymptote  $\rho_2 = -1/(Ec_2)$ . Thus in the region  $\rho_1 > -1/(Fc_1)$  and  $\rho_2 > -1/(Ec_2)$  the non-zero  $\rho_1$ - and  $\rho_2$ -nullclines intersect precisely once. Depending on parameter values, this intersection may arise inside or outside the biologically relevant portion of the phase space (i.e.  $\rho_1, \rho_2 \geq 0$ ). Consequently there are four ways the nullclines can intersect in the biologically-relevant portion of the phase space depending on parameter values but where the direction of flow depends on the sign of  $s$  generating a total of 8 distinct phase portraits (Figure 4.17). This analysis demonstrates the existence of travelling wave solutions but, as in the case of the reduced system for large  $\psi$  in equations (4.16), no bounds on the wave speed can be obtained. Unfortunately, the case for small  $\psi$  does not yield any tractable analytical results.

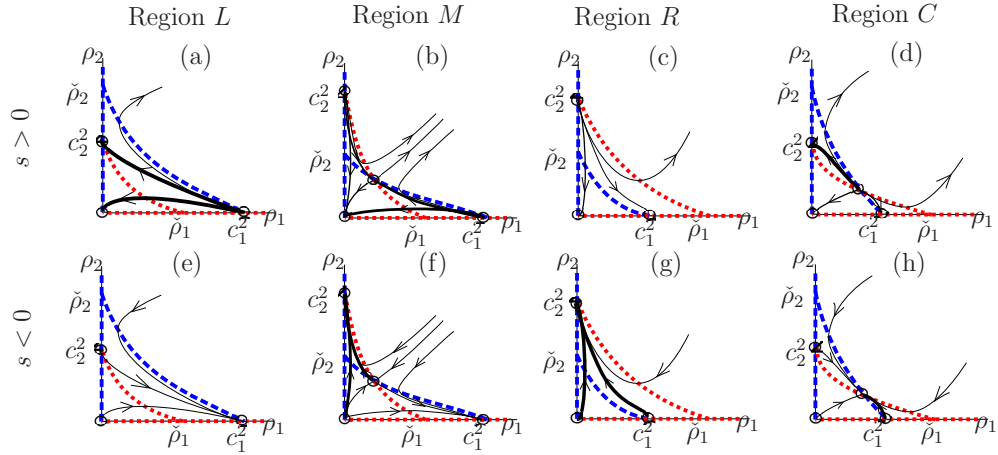


**Figure 4.17:** Phase portraits of equations (4.19) for the different regions of Figure 4.11 where  $s > 0$  and  $s < 0$  as indicated. The  $\rho_1$ - and  $\rho_2$ -nullclines are represented by the dashed (blue) and dotted (red) lines respectively where  $\check{\rho}_1 = (\sqrt{B^2 + 4BFc_2^2} - B)/(2BFc_1)$  and  $\check{\rho}_2 = (\sqrt{A^2 + 4AEC_1^2} - A)/(2AEC_2)$ . Sample trajectories are indicated along with specific trajectories (in bold) connecting equilibria illustrating biologically relevant travelling wave solutions of equations (4.10) for large  $\psi$ .

#### 4.3.3.3 Numerical results

The model equations (4.10) with initial data (4.2), (4.17) were solved numerically for a range of parameter values  $c_1$  and  $c_2$  (Figure 4.18), with positive values used for all parameters and the speed of the travelling waves were calculated numerically before and after biomass collision. In all cases, the qualitative behaviour of the solutions were similar to that described in Section 4.3.2.1. In particular, for pairings of the parameters  $c_1$  and  $c_2$  in the region denoted by  $C$  in Figure 4.11 where neither of the model biomasses in isolation were stable, the only observed outcome of competition was coexistence (or intermingling) of biomasses (Figure 4.18(b)). Furthermore, different pairings of the parameters  $c_1$  and  $c_2$  that lay within the multiple equilibria region  $M$  in Figure 4.11 generated three distinct outcomes; the biomass initially starting on the right displaced that on the left (Figure 4.18(d)), the biomasses reached a state of deadlock (Figure 4.18(e)), and the biomass initially starting on the left displaced that on the right (Figure 4.18(f)).

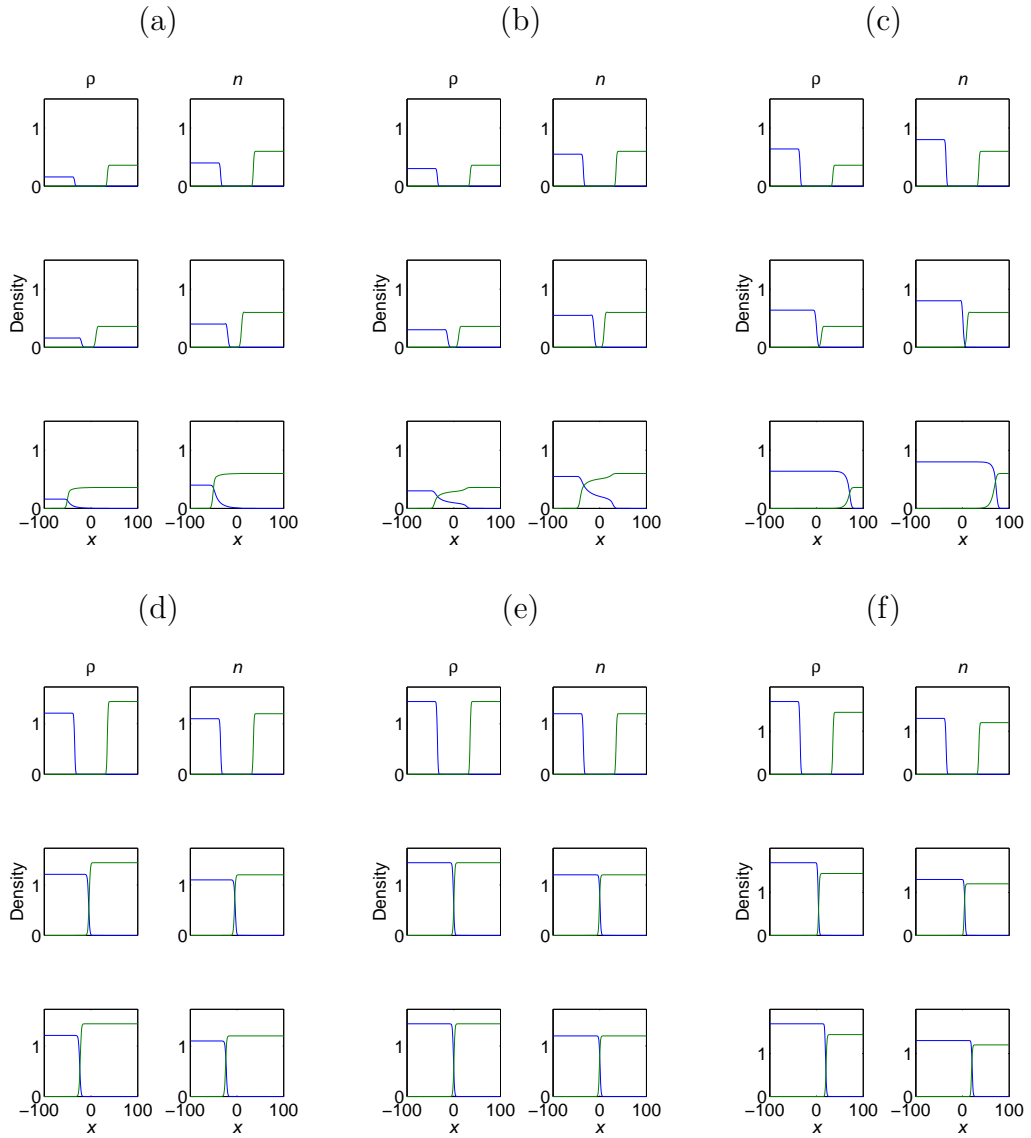


**Figure 4.18:** Numerical solutions of equations (4.10) with initial data (4.2), (4.17) over the interval  $(-100, 100)$  with  $\bar{x} = 35$  and  $\psi = A = B = E = F = 1$ . Distributions are shown at times  $t = 0, 30$  and  $100$  where  $c_1$  and  $c_2$  belong to regions (a)  $R$ , (b)  $C$ , (c)  $L$ , (d-f)  $M$  in Figure 4.11. (a)  $c_1 = 0.4, c_2 = 0.6$  (with travelling wave speeds of  $s_1 = 0.54, s_2 = -0.86$  before collision,  $s_1 = s_2 = -0.84$  after collision). (b)  $c_1 = 0.55, c_2 = 0.6$  (with travelling wave speeds of  $s_1 = 0.81, s_2 = -0.88$  before collision,  $s_1 = 0.52, s_2 = -0.71$  after collision). (c)  $c_1 = 0.8, c_2 = 0.6$  (with travelling wave speeds of  $s_1 = 1.21, s_2 = -0.87$  before collision,  $s_1 = s_2 = 1.03$  after collision). (d)  $c_1 = 1.1, c_2 = 1.2$  (with travelling wave speeds of  $s_1 = 1.75, s_2 = -1.94$  before collision,  $s_1 = s_2 = -0.27$  after collision). (e)  $c_1 = 1.2, c_2 = 1.2$  (with travelling wave speeds of  $s_1 = 1.94, s_2 = -1.94$  before collision,  $s_1 = s_2 = 0$  after collision). (f)  $c_1 = 1.3, c_2 = 1.2$  (with travelling wave speeds of  $s_1 = 2.24, s_2 = -1.94$  before collision,  $s_1 = s_2 = 0.22$  after collision).

## 4.4 Conclusion

In biotechnological applications that involve the introduction of a species of fungus to an environment, such as biological control and biological remediation, the interaction between it and other fungal species already present in the environment impacts on the success of the treatment. The investigation in this chapter has primarily focused on how nutrient availability can influence the outcome of fungal interactions by altering the rate at which they degrade rival's hyphae and hyphal tips and the concomitant spatial reorganisation. In particular, the mathematical model predicted the circumstances under which pairwise competition would result in the displacement of one species by another, the intermingling (or coexistence) of multiple species and the emergence of deadlock where a stalemate is reached.

In the instances of displacement or intermingling, the numerical solutions of the model equations suggested that the corresponding model biomasses advanced as a travelling wave. Indeed, through phase-space analysis, the existence of travelling wave solutions in the model equations were demonstrated for certain values of the parameter  $\psi$ , which essentially can be regarded as comparing the production of new biomass material through hyphal tip branching and extension to that lost through natural degradation. Furthermore, bounds on the travelling wave speed were also obtained in certain cases. Previous studies (Boswell et al., 2002; Boswell and Davidson, 2012) have calibrated these parameter values for the fungus *Rhizoctonia solani* growing on a standard agar mixture from which  $\psi$  can be deduced to take values between  $10^{12}$  and  $10^{14}$ . Thus, since  $\psi$  is significantly larger than values taken by other parameters in the nondimensionalised model equations (4.10), there is strong experimental evidence to support the large  $\psi$  analysis used in the current investigation and the corresponding model equations essentially reduce to a pair of differential equations that exhibit Lotka-Volterra competition (e.g. Allen, 2007). However, the complete proof of the existence of travelling wave solutions for all values of  $\psi$  in equations (4.10), which involves proving the existence of heteroclinic trajectories in four-dimensional state space, remains an interesting open problem.

A key feature of the modelling was the distinction between the two major processes involved in fungal competition, namely the degradation of existing hyphae and the degradation of hyphal tips by rival fungi. The suppression of hyphal tips alone was shown to be a sufficient mechanism to generate the main observed behaviours in fungal interactions, i.e. displacement, intermingling and deadlock.

Indeed, by not degrading hyphal tips, a mycelium was shown to be unable to completely displace its rival (Section 4.3.3 with  $A = B = 0$ ) and therefore the only outcomes of competition with this singular regime are intermingling or its own displacement. Intuitively this is appealing: hyphal tip extension is the sole means by which mycelia expand and therefore the possibility of continued growth cannot be eliminated unless the hyphal tips are inhibited or degraded. However, the degradation of hyphal structures impacts on the ability of a mycelium to redistribute internally-held supplies, which is essential for continued growth, and therefore such degradation can reduce its ability to function effectively (e.g. Lee et al., 2017). This possibility cannot be captured in the current model because of its continuous nature, but hybrid approaches that explicitly simulate the discrete network of a mycelium have been used with some success (Boswell, 2012). Nonetheless, our modelling has shown that hyphal degradation plays an important role in pairwise fungal competition; it significantly reduces the region of parameter space where intermingling (or coexistence) can arise and extends the regions corresponding to displacement (Figure 4.11) and therefore provides a further competitive advantage to a fungus.

The modelling demonstrated that the availability of nutrients plays a central role on the outcomes of pairwise competition between fungal species. Coexistence, or intermingling, was shown to be possible only when the concentrations of nutrients provided to both model fungi were similarly small and deadlock was only possible when the nutrient concentrations were similarly large (Figure 4.11). This result supports many of the findings in Boswell (2012) where numerical simulations showed that deadlock could arise when the suppression of hyphal tips and the degradation of biomass occurred at sufficiently large rates and coexistence arose when both rates were sufficiently small. However, in that study, the explicit dependence of nutrients on those two processes was neglected and instead the nutrients only influenced the branching and tip movement processes. Further, it was shown in Boswell (2012) that deadlock could be achieved when there was a significant disparity between nutrient availability in two fungal biomasses provided their tip suppression and hyphal degradation rates were also different. The results here (also reported in Choudhury et al., 2018) extend these findings; the modelling predicts that further increasing the nutrient disparity will change the outcome of competition resulting in the displacement of one biomass by another since it corresponds to the movement from region  $M$  in Figure 4.11 to either region  $L$  or  $R$ ,

depending on the nutrient concentration changed. Indeed, additional numerical simulations using the model of Boswell (2012) have shown precisely this outcome (Choudhury et al., 2018), thus demonstrating the additional insight gained from the current approach.

It has been shown in a number of experimental studies (e.g. Boddy, 1993, 2000) that under certain triggers, such as the presence of a rival biomass, fungi will construct structures, often termed barrages, to protect themselves. Such structures were not observed in our modelling and thus certain potential causes of these structures can be eliminated. In particular, the degradation of hyphal tips (or biomass) by a rival fungus is not sufficient on its own to generate defensive structures; other mechanisms must be employed. These alternative mechanisms could potentially include a change in the redistribution of internally-located nutrients or a change in the movement habit of hyphal tips themselves in response to an anticipated attack. Such a change in the movement habit of tips may require additional spatial dimensions in the model, and consequently the basic structure of the model equations, especially tip flux and creation of biomass, would need careful revision, potentially by including their movement in response to different biomass distributions, see e.g. Boswell et al. (2003a). Nonetheless, the modelling has demonstrated that fungi are better able to defend themselves when supplied with sufficient resources and hence the reallocation of internally-held resources to the colony periphery provides increased defensive capabilities for mycelia.

In experiments involving mycelial networks, the majority of the variables cannot be controlled but can be measured experimentally (e.g. the speed of tip growth, branching and the death rate of a fungal network hyphae see Rotheray et al. (2010)). One variable that can be controlled, however, is the nutrient concentration. Nutrients play a key role in many fungal interactions, such as in the effect of grazing (Hogervorst et al., 2003; Heaton et al., 2012), toxin removal (Gadd, 1993; Fomina et al., 2003; Goyal et al., 2013) and pathogenic fungi neutralisation (Sempere and Santamarina, 2010; Ibarra-Medina et al., 2010). In this chapter we have provided a simple yet powerful description of how nutrient concentrations can influence interactions between different fungi species. However, additional factors, including temperature (Hiscox et al., 2016) and water activity (Sempere and Santamarina, 2010) can also influence the outcome of pairwise competition and so could be incorporated into future models of fungal interactions.

A key limitation of the modelling approach in this chapter relates to the

reduction of the biomass expansion to a single spatial dimension. In experimental configurations, and indeed often in the terrestrial environments, growth is essentially planar and hence there may be inherent differences in the biomass structures produced in such settings. Thus in the following chapter the model equations (4.9) will be re-expressed in a two-dimensional setting. A two-dimensional representation of interactions will capture the dynamics of the entire fungus colonies of fungi seen in experimental studies rather than focussing on the periphery alone. However, key aspects of the model equations themselves need to be revised as a result of the dimensional change since opportunities for growth are different.



## Chapter 5

# Fungal Interactions and Spatial Patterns in Planar Environments

The previous chapter investigated how nutrient resources can influence the outcome of competition between two rival biomasses, which is clearly an important consideration for their biotechnological applications (see also Choudhury et al., 2018). The mathematical models formed were one-dimensional in nature, primarily to focus attention on the interaction zone at their periphery where the fungi interact with each other. The simple models provided insightful results including predicting common behaviour seen in experimental fungal studies such as displacement, coexistence and deadlock via manipulating the nutrient concentration provided to the fungi.

In laboratory experiments, as well as in their natural settings, fungal colonies in isolation grow radially from a food source (Figure 5.1(a)). This growth is often two dimensional; for example in a Petri dish or on the surface of organic matter. However Figure 5.1(b) demonstrates how fungal colonies cease exhibiting radial symmetry when they start interacting with each other. The preceding models thus lacked the ability to capture the intricate growth structure observed in practice.

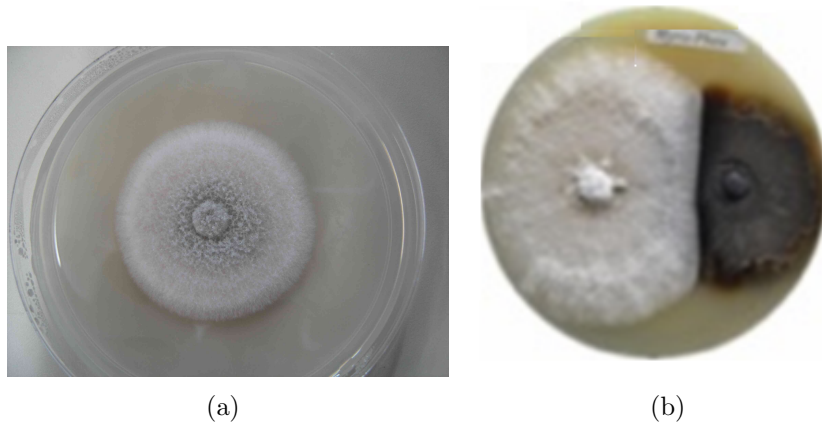


**Figure 5.1:** (a) The radial growth of *colletotrichum gloeosporioides* species grown on a Petri dish (Duarte, 2004), (b) Competition between fungal species *M. roridum* and *P. eupyrena* causes the cessation of radial symmetry on a Petri dish (Morón-Ríos et al., 2017).

In heterogeneous environments, nutrients are unevenly distributed forcing fungi to seek out distal additional sources of nutrients. This process is carried out by the leading hyphal tips of the colony and is supported by the mycelium by providing the necessary energy required to the tips. Thus there is some redistribution of energy within the fungal colony termed translocation. It is through this process that many fungi are able to grow in low nutrient or even polluted habitats by exploiting the resources available to other parts of the mycelium (Schütte, 1956; Ritz, 1995; Persson et al., 2000).

For the one-dimensional models considered previously, it was reasonable to represent tip growth via simple convective flux and nutrient influence as a constant where the primary focus was on capturing the essence of the model without over complicating the model in addition to observing steady state behaviours. There are several complexities involved in formulating a two-dimensional model of filamentous fungal growth that must be considered. For example, the geometry of the network is of importance as the possibility of fusions (anastomosis) occurring depends on the density of the colony as well as the direction the branches are growing. However the biggest failing of the one-dimensional model considered thus far is the lack of translocation.

Boswell et al. (2002, 2003a), engineered an exquisite model that captured the growth of a strain of *Rhizoctonia solani* fungi and found it to be in excellent agreement with calibrated experimental data. The devised model consisted of

mixed hyperbolic-parabolic type equations. We will use this model as the basis of our investigation and extend it further to capture fungal interactions in two-dimensional domains.

## 5.1 Boswell's modelling approach

We will continue to regard a mycelium and its constituents as continuous entities. Thus, rather than accounting for individual hypha growth, the average properties, such as the distribution of hyphal densities, are described. Since hyphal length increment occurs only in the presence of a moving tip, the locations, density and flux of tips is of immense importance in determining where growth takes place. Hence the mycelium will be considered as a continuous distribution consisting of three key features: active hyphal density, inactive hyphal density and hyphal tip density. Active hyphae refers to those hyphae involved in the translocation of internal metabolites while hyphal tips denote the ends of these hyphae. Inactive hyphae denote hyphae no longer directly involved in translocation, branching or anastomosis but still form part of the observable mycelium. Therefore to summarise:

- Tip movements creates new hyphal filaments.
- Tips and hyphae can branch and create more tips or vanish through anastomosis.
- Hyphae can become inactive and inactive hyphae can also degrade.
- Internal nutrients influence tip extension and hyphal growth.
- Internal nutrients held within the hyphae are different to external nutrients.

### 5.1.1 Model formulation

Consistent with the notation used in previous chapters, let  $\rho(\underline{x}, t)$  denotes active hyphal density where  $\underline{x}$  and  $t$  are spatial and temporal coordinates respectively,  $\rho'(\underline{x}, t)$  denotes inactive hyphal density,  $n(\underline{x}, t)$  denotes the tip density,  $s_i(\underline{x}, t)$  denotes internal substrate concentration and  $s_e(\underline{x}, t)$  denotes external substrate concentration. Notice here we differentiate between nutrients free in the growth domain and those acquired by the biomass. Hyphae are fixed in space and can be

regarded as the trail left behind a hyphal tip as it moves. Thus the rate at which hyphae are created is proportional to the number of tips present and the rate at which they move.

In the one-dimensional models constructed previously the model tips simply moved along the growth domain. However, this approach is not sufficient to model growth in higher spatial dimensions since in practice hyphal tips will reorient themselves. Hence there are assumed to be two processes involved in tip movement that capture the motile behaviour seen in nature: a convective element and a diffusive element. There is a linear relationship between tip growth, tip velocity and internal substrate as growth is only possible when energy is supplied to the tips. The tips must be modelled as convecting away from its biomass density so that tips avoid their own biomass trail. In a sparse mycelial network a convective element alone is not sufficient for growth as anastomosis would be neglected therefore to overcome this a diffusive term must also be included in the tip flux. The diffusive term will ensure anastomosis as well as capture the small random growth behaviour of tip growth observed in experiments (Giovannetti et al., 2001). Thus the tip flux is modelled as

$$-vs_in\nabla\rho - D_ns_i\nabla n, \quad (5.1)$$

where  $v$  and  $D_n$  are non-negative constants. Notice if the internal substrate term  $s_i$  is zero, then there is no flux. The inactivation of hyphae is assumed to occur at a constant rate  $d_\rho$ . Inactive hyphae, while still forming part of the biomass structure, play no role in growth, uptake or translocation and are assumed to degrade at a rate of  $d_i$  (note, the recycling of inactive hyphae has been modelled in a series of papers by Falconer et al., 2011).

The reaction terms that corresponds to the creation and loss of hyphal tips is modelled using the FHD phenotype seen in Chapter 2. Indeed, it was found in Boswell et al. (2002) that the fungi *R. solani* adheres to the morphological pattern FHD. Therefore the branching and anastomosis processes were represented by the terms  $\alpha s_i \rho$  and  $\beta n \rho$  respectively, where  $\alpha$  denotes the branching rate and  $\beta$  denotes the anastomosis rate. (Notice that the nutrient concentration here is denoted by the variable  $s_i$  while in the one-dimensional models previously constructed it was denoted by a constant  $c$ .)

The flux terms for the movement of internal substrate consists of two pro-

cesses, simple diffusion and an active transport.

$$\text{Passive flux} = -D_i \rho \nabla s_i, \quad (5.2)$$

$$\text{Active flux} = D_a \rho s_i \nabla n, \quad (5.3)$$

where  $D_i$  and  $D_a$  are non-negative constants. Passive flux corresponds to the diffusion of internal substrate within the mycelium. The flux is dependent on the density of the mycelium, since the substrate movement increases with network density. Since hyphal tips are the primary source of fungal growth, numerous experimental studies have shown that internally located material is usually directed towards them or more specifically, internal substrate moves locally to the greatest concentrations of hyphal tips (Steinberg, 2007; Balmant et al., 2015). The uptake process of substrate is modelled in a linear manner,  $c_1 s_i \rho s_e$ , where  $c_1$  is a positive constant representing the cost or energy involved in substrate uptake. It is also reasonable to include the energy cost of tip movement and active flux terms. As the elongation of tips require energy and active translocation of substrate also requires energy it is assumed the costs are proportional to the flux terms, i.e.  $c_2 |v s_i n \nabla \rho + D_n s_i \nabla n|$  and  $c_4 |D_a \rho s_i \nabla n|$ , where  $c_2$  and  $c_4$  are non-negative constants.

The external substrate movement is modelled using the standard law of Fickian diffusion and the reaction term corresponds to the depletion from the environment. This term is similar to the uptake form for the internal substrate due to conservation laws and is denoted by  $c_3 s_i \rho s_e$ , where  $c_3$  is a non-negative constant. Some features of microbial life, such as growth rate and yield (where yield is the portion of consumed substrate that is converted into biomass), will not be explicitly modelled. There are certainly some trade-offs that occurs between the growth rate and yield depending on the requirement of the specific microorganism (Lipson, 2015). In the context of modelling the phenotypic relation between substrate uptake, metabolism and biomass growth, there is great interest in developing quantitative descriptions of the relationship between the growth rate and yield (Cheng et al., 2019). The yield is typically depicted as the ratio between the specific growth rate and the rate of substrate consumption, however we denote this feature simply via the constant terms  $c_2$  and  $c_4$  respectively, to avoid unnecessary complication to our model. To capture the imperfection of substrate

uptake it is mandatory that  $c_1 < c_3$ . Thus the model equations are of the form

$$\begin{aligned}
\frac{\partial \rho}{\partial t} &= \underbrace{|vs_i n \nabla \rho + D_n s_i \nabla n|}_{\text{trail of tips}} - \underbrace{d_\rho \rho}_{\text{inactive hyphae}}, \\
\frac{\partial \rho'}{\partial t} &= \underbrace{d_\rho \rho}_{\text{inactive hyphae}} - \underbrace{d_i \rho'}_{\text{hyphae degradation}}, \\
\frac{\partial n}{\partial t} &= \nabla \cdot \underbrace{(vs_i n \nabla \rho + D_n s_i \nabla n)}_{\text{tip flux}} + \underbrace{\alpha s_i \rho}_{\text{branching}} - \underbrace{\beta n \rho}_{\text{anastomosis}}, \\
\frac{\partial s_i}{\partial t} &= \underbrace{\nabla \cdot (D_i \rho \nabla s_i - D_a \rho s_i \nabla n)}_{\text{movement of internal substrate}} + \underbrace{c_1 s_i \rho s_e}_{\text{substrate uptake}} - \underbrace{c_2 |vs_i n \nabla \rho + D_n s_i \nabla n|}_{\text{cost of growth}} \\
&\quad - \underbrace{c_4 |D_a \rho s_i \nabla n|}_{\text{translocation cost}}, \\
\frac{\partial s_e}{\partial t} &= \underbrace{D_e \nabla^2 s_e}_{\text{diffusion of external substrate}} - \underbrace{c_3 s_i \rho s_e}_{\text{substrate depletion}}.
\end{aligned} \tag{5.4}$$

Despite the growth dynamics of fungal colonies being influenced greatly by physical boundaries (e.g. soil-particles or the edge of a Petri dish) we will not consider such influences in our investigations but rather focus on nutritional influences to be consistent with the one-dimensional model in Chapter 4. Typical experiments involving fungi are carried out on Petri dishes of diameter 9 cm but we will consider a diameter of 4 cm to focus on the growth of the mycelium at the centre of the domain to reduce computation time. We thus solve the equations in a circular domain representing radius 2 cm in COMSOL and we define another circle of radius  $R = 0.2$  cm within to represent the initial inoculation site. Note in experimental conditions fungi are grown on a separate Petri dish where once grown a portion is cut and placed onto another Petri dish with fresh substrate. Hence there will be some quantity of biomass and internal substrate within the initial plug. Thus, and consistent with experimental protocol, the model equations are to be solved in a circular domain of radius  $L$  (not to be confused with the standard symbol used for dimensions representing length  $L$  (see Table 5.1)) with zero flux boundary conditions. The initial data thus can be represented using the

following

$$\begin{aligned}\frac{\rho(x, y, 0)}{\rho_0} &= \frac{n(x, y, 0)}{n_0} = \frac{s_i(x, y, 0)}{s_{i_0}} = \frac{1 - \tanh(\phi(r - R))}{2}, \\ \rho'(x, y, 0) &= \rho'_0 \\ s_e(x, y, 0) &= s_{e_0},\end{aligned}\tag{5.5}$$

where  $\phi$  are scalar constants,  $r = \sqrt{x^2 + y^2}$  denotes the distance from the centre of the domain,  $R$  corresponds to the radius of the fungal inoculum where we have assumed it is circular in shape. The initial conditions for hyphae, tips and internal substrate thus correspond to the initial plug of mycelium placed on the Petri dish at  $(0, 0)$  of radius  $R$  respectively. The initial properties for the fungal species is proportional to the function  $\frac{1}{2}(1 - \tanh(\phi(r - R)))$  and is consistent to that used for the one-dimensional models.

### 5.1.2 Numerical simulation in COMSOL

COMSOL Multiphysics will be used to solve the model equations. COMSOL, formally known as Femlab, uses finite element methods to solve systems of partial differential equations.

We will solve the system of equations in (5.4) with initial conditions (5.5) using the calibrated data given in Boswell et al. (2003a). Although the results have been published and are well known, we will demonstrate that COMSOL does indeed produce solutions consistent with Boswell et al. (2003a). In COMSOL the user must first specify the dimension of the problem (i.e. 1D, 2D or 3D) and select the relative physics, which are predefined PDE interfaces for different types of model equations. The most appropriate for equation (5.4) are ‘Coefficient form PDE’ template. The template for entering equations (5.4) is

$$e_a \frac{\partial^2 u}{\partial t^2} + d_a \frac{\partial u}{\partial t} + \nabla \cdot (-c \nabla u - \hat{\alpha} u + \hat{\gamma}) + \hat{\beta} \cdot \nabla u + a u = f,\tag{5.6}$$

where  $u = [\rho, \rho', n, s_i, s_e]^T$  and  $\nabla = [\frac{\partial}{\partial x}, \frac{\partial}{\partial y}]$ . Hence model equation (5.4) can be

entered by defining  $e_a = a = \hat{\beta} = \hat{\gamma} = 0$ ,  $d_a = I_5$  (the  $5 \times 5$  identity matrix) and

$$c = \begin{pmatrix} 0 & 0 & 0 & 0 & 0 \\ 0 & 0 & 0 & 0 & 0 \\ 0 & 0 & D_n s_i & 0 & 0 \\ 0 & 0 & 0 & D_i \rho & 0 \\ 0 & 0 & 0 & 0 & D_e \end{pmatrix}, \quad (5.7)$$

$$\hat{\alpha} = \begin{pmatrix} 0 & 0 & 0 & 0 & 0 \\ 0 & 0 & 0 & 0 & 0 \\ 0 & 0 & v s_i \nabla \rho & 0 & 0 \\ 0 & 0 & 0 & -D_a \rho \nabla n & 0 \\ 0 & 0 & 0 & 0 & 0 \end{pmatrix}, \quad (5.8)$$

$$f = \begin{pmatrix} \sqrt{|v s_i n \nabla \rho + D_n s_i \nabla n|^2 + \epsilon} - d_\rho \rho \\ d_\rho \rho - d_i \rho' \\ \alpha s_i \rho - \beta n \rho \\ c_1 s_i \rho s_e - c_2 \sqrt{|v s_i n \nabla \rho + D_n s_i \nabla n|^2 + \epsilon} - c_4 \sqrt{|D_a \rho s_i \nabla n|^2 + \epsilon} \\ -c_3 s_i \rho s_e \end{pmatrix}, \quad (5.9)$$

where the matrix  $\hat{\alpha}$  is of course distinct from the previously defined branching rate  $\alpha$ . Similarly  $\hat{\beta} \neq \beta$  and  $\hat{\gamma} \neq \gamma$ . Notice that (5.9) has introduced a constant  $\epsilon$  which is a small value to counteract possible singularities which can occur due to the calculation of the Jacobian of the vector  $f$  when evaluated at certain points. This is a standard approach designed to bypass numerical problems related to the precision of the computer used. We will take  $\epsilon = 10^{-16}$  in all that follows. The calibrated values obtained from a specific experiment for the fungal species *R. Solani* in Boswell et al. (2002) were used in Boswell et al. (2003a) and are shown in Table 5.1.



| Initial data/Parameters | Rescaled Value | Dimensions          | Description                              |
|-------------------------|----------------|---------------------|--|
| $v$                     | 0.5            | $L^5 T^{-1} N^{-1}$ | Directed tip velocity                    |
| $d_\rho$                | 0.5            | $T^{-1}$            | Hyphal inactivation rate                 |
| $d_i$                   | 0              | $T^{-1}$            | Inactive hyphae loss rate                |
| $\alpha$                | $10^3$         | $LT^{-1} N^{-1}$    | Branching rate                           |
| $\beta$                 | $10^4$         | $LT^{-1}$           | Anastomosis rate                         |
| $c_1$                   | 900            | $L^3 T^{-1} N^{-1}$ | Uptake rate of external substrate        |
| $c_2$                   | 1              | $NL^{-1}$           | Growth cost                              |
| $c_3$                   | $10^3$         | $L^3 T^{-1} N^{-1}$ | Uptake of external substrate             |
| $c_4$                   | $10^{-8}$      | $L^{-1}$            | Active translocation cost                |
| $D_n$                   | 0.1            | $L^4 T^{-1} N^{-1}$ | Tip avoidance cost                       |
| $D_i$                   | 10             | $L^3 T^{-1}$        | Internal substrate diffusion coefficient |
| $D_a$                   | 10             | $L^5 T^{-1}$        | Active translocation rate                |
| $D_e$                   | 0.3456         | $L^2 T^{-1}$        | External substrate diffusion coefficient |
| $R$                     | 0.2            | $L$                 | Radius of active hyphal plug             |
| $\phi$                  | 20             | -                   | Scalar constant of initial data          |
| $L$                     | 30             | $L$                 | Radius of domain                         |
| $\rho_0$                | 0.1            | $L^{-1}$            | Initial active hyphal density            |
| $\rho'_0$               | 0              | $L^{-1}$            | Initial inactive hyphal density          |
| $n_0$                   | 0.1            | $L^{-2}$            | Initial tip density                      |
| $s_{i0}$                | 0.4            | $NL^{-2}$           | Initial internal substrate               |
| $s_{e0}$                | 0.3            | $NL^{-2}$           | External substrate                       |

**Table 5.1:** *The initial data and default parameter values used to solve model equations (5.4). The parameter values used for fungal growth are from the calibration experiments carried out by Boswell et al. (2003a).*

For direct comparisons with experimental results, an experiment was carried out to determine values for the model parameters and initial data in Boswell et al. (2002). The approximate length of hyphae and number of hyphal tips per unit area were determined to be  $\rho = 100 \text{ cm}^{-1}$  and  $n = 100 \text{ hyphal tip cm}^{-2}$  respectively. By counting the number of branches and anastomosis events over a known time period (a few hours), the corresponding branching and anastomosis rates were estimated,  $\alpha = 10^7 \text{ branches cm}^{-1} \text{ hyphae day}^{-1}$  and  $\beta = 10 \text{ fusions in cm of hyphae day}^{-1}$ . Hyphal tip velocity was similarly estimated to be  $v = 5 \times 10^{-1} \text{ cm mol}^{-1} \text{ day}^{-1}$  and hyphal death  $d = 0.5 \text{ day}^{-1}$ . The internal substrate and external substrate both are similar in order of magnitudes. Thus through knowledge of the composition of the agar growth media, the initial concentration of  $s_i$  was estimated to be  $4 \times 10^{-5} \text{ mol glucose cm}^{-2}$  (dimensions are represented in Table 5.1 as moles per unit area  $NL^{-2}$ ) and  $s_e$  was estimated to be  $3 \times 10^{-5} \text{ mol glucose cm}^{-2}$  respectively (for full detail see Boswell et al., 2002). The system variables have vastly different magnitudes which complicates the procedure required to accurately and efficiently solve the system numerically,

especially when implementing variable time step methods to efficiently integrate the equations. Thus the model variables and consequently model parameters were rescaled such that the variables in the rescaled system are all similar in magnitude and so simplified the numerical integration of the model equations. Notice that quantitative comparisons between model and experimental systems are still possible by simply multiplying the rescaled densities by their scaling factors. All figures in this and forthcoming chapters are the rescaled variables consistent with Boswell et al. (2003a) and thus represents predictions and hypotheses concerning the observed qualitative and quantitative properties of mycelial growth and function.

The model equation (5.4) were solved using COMSOL with initial data (5.5) and zero-flux boundary conditions. The results are illustrated in Figure 5.2.

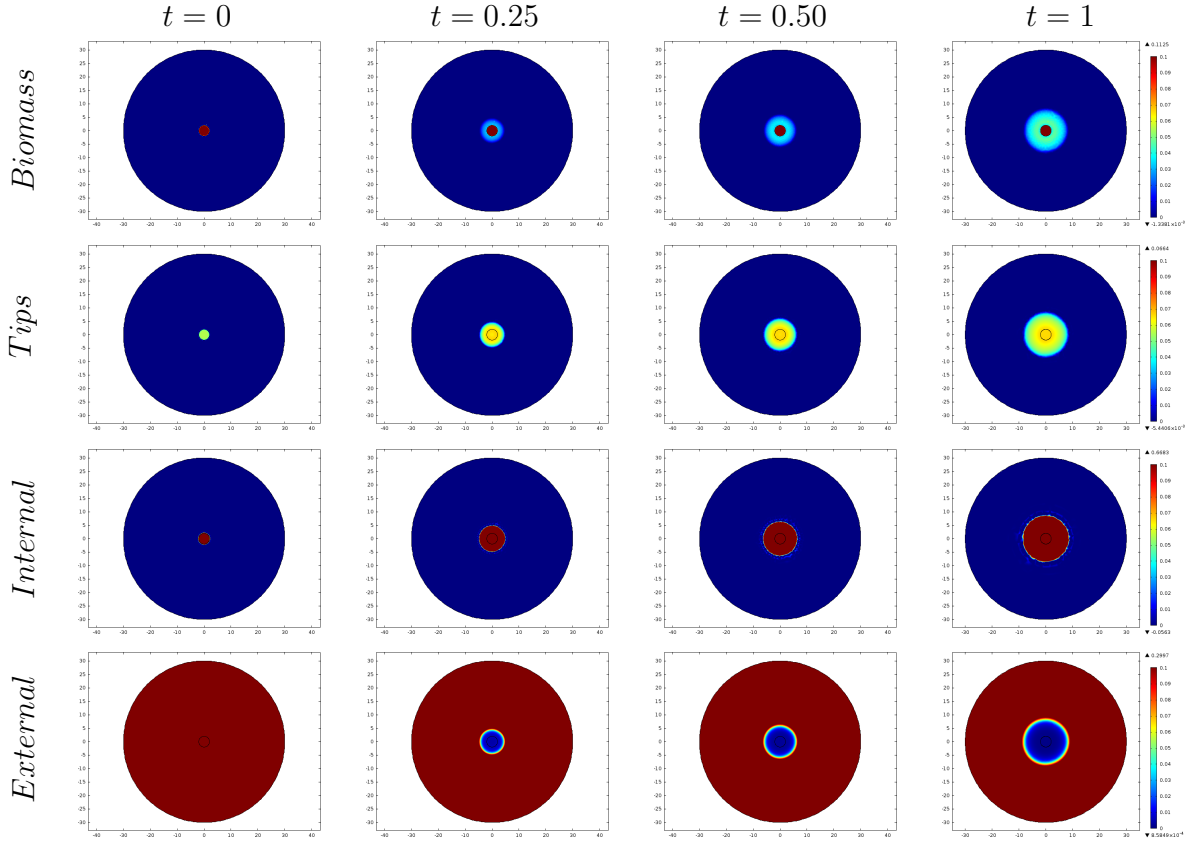


**Figure 5.2:** Solutions to equations (5.4) at times indicated with initial data in equation (5.5) and parameter values from Table 5.1. Biomass corresponds to  $(\rho + \rho')$ , the sum of active and inactive hyphal densities.

Figure 5.2 shows the radially symmetric growth commonly seen in uniform

growth conditions (see Figure 5.1). As the biomass extends overtime the red circular region in the centre corresponds to predominantly inactive hyphae whereas active hyphae can be seen in the outer green region. Notice the extent of hyphal tips is slightly greater than that of the hyphal biomass since the tips lead the colony and hyphae are the trail left behind as they move. The internal substrate closely resemble hyphal tip density, due to the active translocation of internal substrate towards the tip. As the model biomass expands over the domain, the depletion of external substrate is observed to be relative to the hyphal biomass density.

The model equations in (5.4) successfully captured the common radial growth observed in fungal studies and results are similar to Boswell et al. (2003a) who required a bespoke numerical routine (Boswell et al., 2003b). Although calibrated for a specific fungi (*R. Solani*), the filamentous blossoming manner of fungal growth is observed in various other species of fungi. We now extend this model to consider fungal interactions.

## 5.2 Fungal interactions model formulation

As previously explored in Chapter 4 during fungal competition, combinations of VOCs and toxic metabolites are produced along the lengths of hyphae that comprise the mycelium. Due to the energy costs involved, the production of these compounds is reasonably assumed to be proportional to the energy available to the biomass. Further, since these compounds restrict the ability of a rival biomass to create new hyphal material as well as degrading existing hyphae, they essentially cause hyphal tips in a rival to cease functioning and reduce the density of existing biomass. For convenience these substances are not represented explicitly, but instead their influence on rival biomasses is modelled. The system of equations in (5.10) represents the interaction of two species of fungi where the subscript on the model variables and parameters is used to distinguish between the two colonies. The process of tip inhibition/degradation and hyphal degradation in biomass 2 by biomass 1 is modelled using terms proportional to  $s_{i2}n_2\rho_1$  and  $s_{i1}n_1\rho_2$ , respectively. Using notation developed previously, the mathematical

model is described by the following ten coupled partial differential equations:

$$\begin{aligned}
\frac{\partial \rho_1}{\partial t} &= |v_1 s_{i1} n_1 \nabla \rho_1 + D_{n1} s_{i1} \nabla n_1| - d_{\rho_1} \rho_1 - E s_{i2} \rho_2 \rho_1 \\
\frac{\partial \rho'_1}{\partial t} &= d_{\rho_1} \rho_1 - d_{i1} \rho'_1 \\
\frac{\partial n_1}{\partial t} &= \nabla \cdot (v_1 s_{i1} n_1 \nabla \rho_1 + D_{n1} s_{i1} \nabla n_1) + \alpha_1 s_{i1} \rho_1 - \beta_1 n_1 \rho_1 - A s_{i2} \rho_2 n_1 \\
\frac{\partial s_{i1}}{\partial t} &= \nabla \cdot (D_{i1} \rho_1 \nabla s_{i1} - D_{a1} \rho_1 s_{i1} \nabla n_1) + c_1 s_{i1} \rho_1 s_{e1} \\
&\quad - c_2 |v_1 s_{i1} n_1 \nabla \rho_1 + D_{n1} s_{i1} \nabla n_1| - c_4 |D_{a1} \rho_1 s_{i1} \nabla n_1| \\
\frac{\partial s_{e1}}{\partial t} &= D_{e1} \nabla^2 s_{e1} - c_3 s_{i1} \rho_1 s_{e1} + G(\underline{x}, t) \\
\frac{\partial \rho_2}{\partial t} &= |v_2 s_{i2} n_2 \nabla \rho_2 + D_{n2} s_{i2} \nabla n_2| - d_{\rho_2} \rho_2 - F s_{i1} \rho_1 \rho_2 \\
\frac{\partial \rho'_2}{\partial t} &= d_{\rho_2} \rho_2 - d_{i2} \rho'_2 \\
\frac{\partial n_2}{\partial t} &= \nabla \cdot (v_2 s_{i2} n_2 \nabla \rho_2 + D_{n2} s_{i2} \nabla n_2) + \alpha_2 s_{i2} \rho_2 - \beta_2 n_2 \rho_2 - B s_{i1} \rho_1 n_2 \\
\frac{\partial s_{i2}}{\partial t} &= \nabla \cdot (D_{i2} \rho_2 \nabla s_{i2} - D_{a2} \rho_2 s_{i2} \nabla n_2) + \overline{c}_1 s_{i2} \rho_2 s_{e2} \\
&\quad - \overline{c}_2 |v_2 s_{i2} n_2 \nabla \rho_2 + D_{n2} s_{i2} \nabla n_2| - \overline{c}_4 |D_{a2} \rho_2 s_{i2} \nabla n_2| \\
\frac{\partial s_{e2}}{\partial t} &= D_{e2} \nabla^2 s_{e2} - \overline{c}_3 s_{i2} \rho_2 s_{e2} + H(\underline{x}, t)
\end{aligned} \tag{5.10}$$

where constants  $A$ ,  $B$ ,  $E$  and  $F$  are the proportionality constants of the rate of degradation of biomass and associated tips due to competition and which may be different between the two biomass “phenotypes”. For all numerical simulations in this chapter we set  $A = E$  and  $B = F$  to represent equal rate of degradation of tips and hyphae respective to the individual species so that attention can be focussed on the rate of nutrient (i.e. substrate) availability. The terms  $G$  and  $H$  represent additional supply of substrate provided to the domain which may depend on both space and time. The terms  $\overline{c}_1$ ,  $\overline{c}_2$ ,  $\overline{c}_3$  and  $\overline{c}_4$  are similar to  $c_1$ ,  $c_2$ ,  $c_3$  and  $c_4$  respectively, except they correspond to the parameters for the second biomass.

We solve the system of PDEs (5.10) numerically using COMSOL in a circular domain, representing a Petri dish, with initial data representing experimental protocol. Zero flux boundary conditions are assumed since in laboratory experiments there are no external addition or loss of biomass or nutrient at the

boundaries.

## Fungal interactions: Initial conditions and parameter values

We numerically integrate equations (5.10) in COMSOL using a ‘2d time dependent model’ for a ‘coefficient form’ type PDE as described earlier in Section 5.1.2. Since the sought after behaviour occurs primarily at the centre of the domain, having a large domain adds unnecessary costs and therefore our simulated Petri dish will be depicted having the same size as previously described. The domain comprises of two semi-circular regions joined together to form a complete circle, one half of which is inoculated by fungal species 1 (left hand side) and the other half by fungal species 2 (right hand side). Following earlier work, the initial conditions are taken to be

$$\begin{aligned}
\frac{\rho_1(x, y, 0)}{\rho_{10}} &= \frac{n_1(x, y, 0)}{n_{10}} = \frac{s_{i1}(x, y, 0)}{s_{i10}} = \frac{1 - \tanh(\phi(r - R))}{2} \\
\rho'_1(x, y, 0) &= 0, \quad \frac{s_{e1}(x, y, 0)}{s_{e10}} = \frac{1 - \tanh(\phi x)}{2} \\
\frac{\rho_2(x, y, 0)}{\rho_{20}} &= \frac{n_2(x, y, 0)}{n_{20}} = \frac{s_{i2}(x, y, 0)}{s_{i20}} = \frac{1 - \tanh(\theta(\bar{r} - R))}{2} \\
\rho'_2(x, y, 0) &= 0, \quad \frac{s_{e2}(x, y, 0)}{s_{e20}} = \frac{1 - \tanh(\theta x)}{2}
\end{aligned} \tag{5.11}$$

where  $\phi$  and  $\theta$  are scalar constants controlling the profiles of the “inoculum” of the biomass and  $r$  and  $\bar{r}$  are defined as below. The parameter  $R = 0.2$  corresponds to the radius of the fungal inoculum where we have assumed they are circular in shape. The variables  $r$  and  $\bar{r}$  are defined as

$$\begin{aligned}
r &= \sqrt{(x + M)^2 + y^2}, \\
\bar{r} &= \sqrt{(x - M)^2 + y^2},
\end{aligned} \tag{5.12}$$

and correspond to the distance from the centre of the two inoculation sites. We set  $M = 0.3$  corresponding to the centre of each plug of mycelium (not to be confused with the standard symbol used for dimensions representing mass  $M$  in Table 6.1). These initial conditions for hyphae, tips and internal substrate corresponds to the initial plug of mycelium placed on the Petri dish at  $(-M, 0)$  and  $(M, 0)$  of radius  $R$  respectively. The initial properties for fungal species 1 are proportional to the function  $\frac{1}{2}(1 - \tanh(\phi(r - R)))$ , which is placed mainly on the left hand side of

the Petri dish and the initial properties for fungal species 2 are proportional to the function  $\frac{1}{2}(1 - \tanh(\theta(\bar{r} - R)))$  denoting the right hand side of the Petri dish. The precise form is used so that the derivatives can be easily computed.

The parameter values used are given in Table 5.2 and are consistent with those used previously. In all cases the simulations are stopped before the biomasses collide with the boundaries.

| Initial Parameters |              | Rescaled Value | Dimensions          | Description                                |
|--------------------|--------------|----------------|---------------------|--|
| $v_1$              | $v_2$        | 0.5            | $L^5 T^{-1} N^{-1}$ | Directed tip velocity                      |
| $d_{\rho 1}$       | $d_{\rho 2}$ | 0.2            | $T^{-1}$            | Hyphal inactivation rate                   |
| $d_{i1}$           | $d_{i2}$     | 0              | $T^{-1}$            | Inactive hyphae loss rate                  |
| $\alpha_1$         | $\alpha_2$   | $10^4$         | $LT^{-1}N^{-1}$     | Branching rate                             |
| $\beta_1$          | $\beta_2$    | $10^4$         | $LT^{-1}$           | Anastomosis rate                           |
| $c_1$              | $\bar{c}_1$  | 900            | $L^3 T^{-1} N^{-1}$ | Uptake rate of external substrate          |
| $c_2$              | $\bar{c}_2$  | 1              | $NL^{-1}$           | Growth cost                                |
| $c_3$              | $\bar{c}_3$  | $10^3$         | $L^3 T^{-1} N^{-1}$ | Uptake of external substrate               |
| $c_4$              | $\bar{c}_4$  | $10^{-8}$      | $L^{-1}$            | Active translocation cost                  |
| $D_{n1}$           | $D_{n2}$     | 0.1            | $L^4 T^{-1} N^{-1}$ | Tip avoidance of biomass                   |
| $D_{i1}$           | $D_{i2}$     | 10             | $L^3 T^{-1}$        | Internal substrate diffusion coefficient   |
| $D_{a1}$           | $D_{a2}$     | 10             | $L^5 T^{-1}$        | Active translocation rate                  |
| $D_{e1}$           | $D_{e2}$     | $10^{-4}$      | $L^2 T^{-1}$        | External substrate diffusion coefficient   |
| $\phi$             | $\theta$     | 20             | -                   | Scalar constant of initial data            |
| $L$                | $L$          | 2              | $L$                 | Radius of domain                           |
| $F$                | $E$          | $10^3$         | $L^3 T^{-1} N^{-1}$ | Degradation rate of biomass by competition |
| $B$                | $A$          | $10^3$         | $L^3 T^{-1} N^{-1}$ | Degradation rate of tips by competition    |
| $G$                | $H$          | 0              | $NL^{-2} T^{-1}$    | Additional substrate                       |
| $\rho_{10}$        | $\rho_{20}$  | 0.1            | $L^{-1}$            | Initial active hyphal density              |
| $n_{10}$           | $n_{20}$     | 0.1            | $L^{-2}$            | Initial tip density                        |
| $s_{i10}$          | $s_{i20}$    | 0.4            | $NL^{-2}$           | Initial internal substrate density         |
| $s_{e10}$          | $s_{e20}$    | 0.5            | $NL^{-2}$           | Initial external substrate density         |

**Table 5.2:** *The initial data and default parameter values used to solve model equations (5.10) as used in Boswell et al. (2003a) augmented with assumed values where necessary based on known similar calibrated processes.*

### 5.2.1 Nutrient and competition variability

In this section we explore the interaction of two fungal biomasses modelled by equations (5.10). Following work in Chapter 4, the primary focus of attention in this section will be how variations in substrate concentrations and combat ability influence the outcome of pairwise biomass competition.

### 5.2.1.1 Default calibration

The model equations (5.10) were solved in COMSOL with the initial data in equation (5.11) and zero flux boundary conditions using the default parameters in Table 5.2. Using similar techniques to those in Section 5.1, typical results are shown in Figure 5.3. In all forthcoming figures ‘Biomass’ corresponds to  $(\rho_1 + \rho_2 + \rho'_1 + \rho'_2)$ , ‘Tips’ corresponds to  $(n_1 + n_2)$ , ‘Internal’ corresponds to  $(s_{i1} + s_{i2})$  and ‘External’ corresponds to  $(s_{e1} + s_{e2})$  respectively.

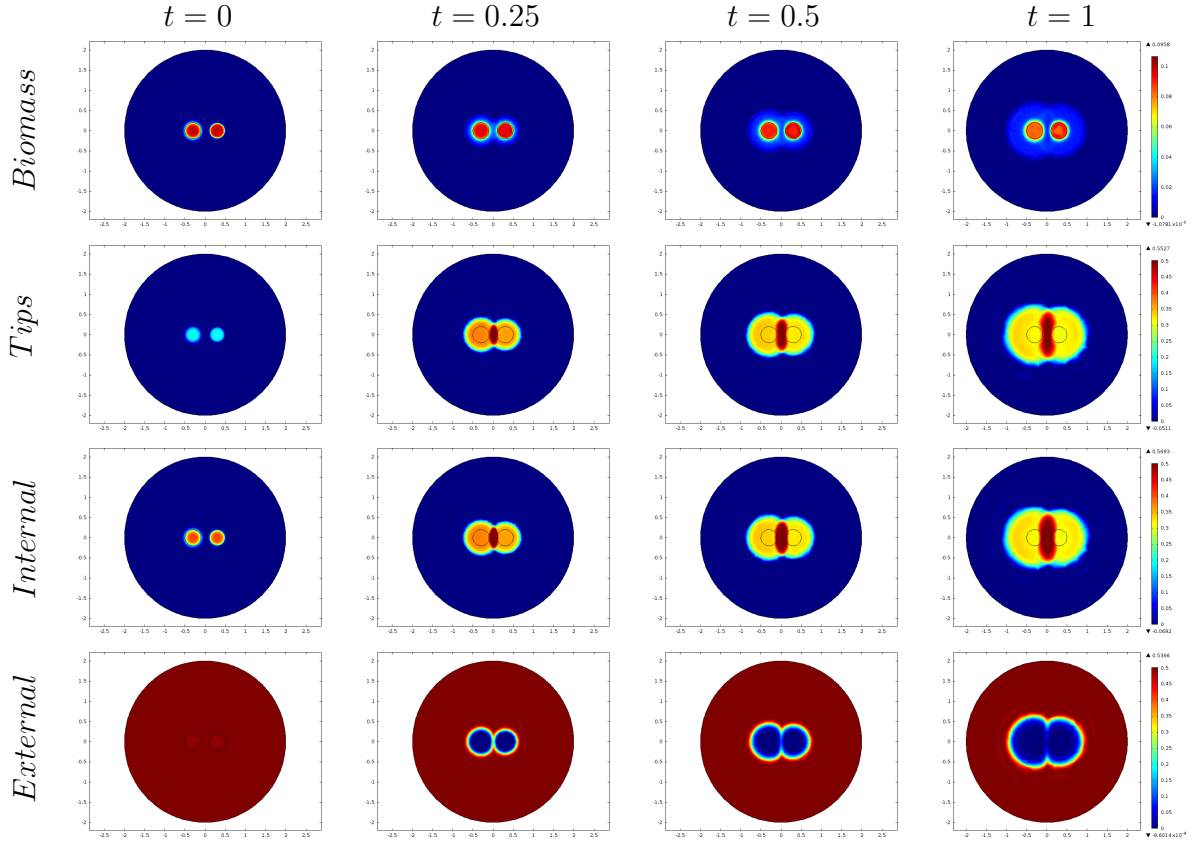


**Figure 5.3:** 2d representation of the solutions to equations (5.10) with initial data (5.11) and parameter values from Table 5.2. Notice the parameters  $s_{e10} = s_{e20} = 0.5$ ,  $G = H = 0$  and  $A = B = 1000$ . A state of stalemate is observed. [For a movie of these plots please see external folder labelled: Comsol - Movie\_files - Fig-5.3]

The simulation in Figure 5.3 shows the growth and interaction of two fungal species with equal capabilities and depicts the well-known ‘stalemate’ behaviour defined in Chapter 4. The hyphal biomasses expand in a radial manner from their initial inoculum sites and initially interact at the centre of the domain. An

accumulation of tips and internal substrate can be seen at this interaction zone. The external substrate levels deplete according to the growth of the biomasses, i.e. the larger the radius of biomass, the larger the area of external substrate depletion.

To get an alternative view of what is happening at the biomass periphery and to relate this simulation to the work in Chapter 4, we take a cross section of the domain (along the line  $y = 0$  passing through the centre of the “inoculation” sites (see Figure 5.4)). The one-dimensional plots of the biomass and tip distributions shown in Figure 5.4 clearly show that the two fungal species enter a state of deadlock since they cease expanding at their interaction zone (see movie file *Fig\_5.3* and *Fig\_5.4*).

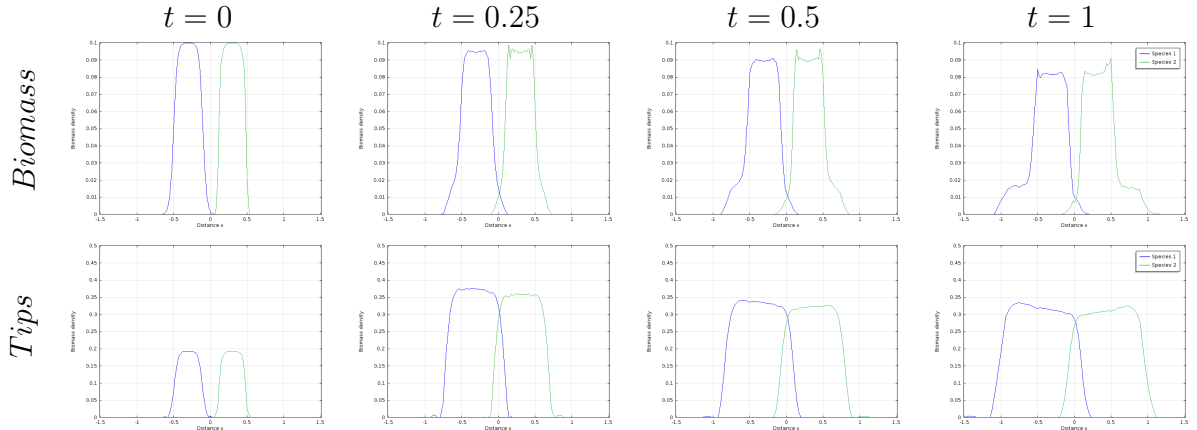


**Figure 5.4:** Cross section of the solutions to equations (5.10) with initial data (5.11) and parameter values from Table 5.2. The parameters  $s_{e1_0} = s_{e2_0} = 0.5$ ,  $G = H = 0$  and  $A = B = 1000$ . A state of stalemate is observed. [For a movie of these plots please see external folder labelled:- Comsol - Movie\_files Fig\_5.4]

### 5.2.1.2 Nutrient variability

In Chapter 4 it was shown that the outcome of fungal competition was influenced by substrate availability. However, the precise impact on the morphology could not be obtained due to the one-dimensional nature of the modelling. Thus we now consider the influence of nutritional variability in the planar setting. The model equations (5.10) with initial data (5.11) are solved as above except with  $s_{e2_0} = 1$  to create nutrient heterogeneity (Figure 5.5).



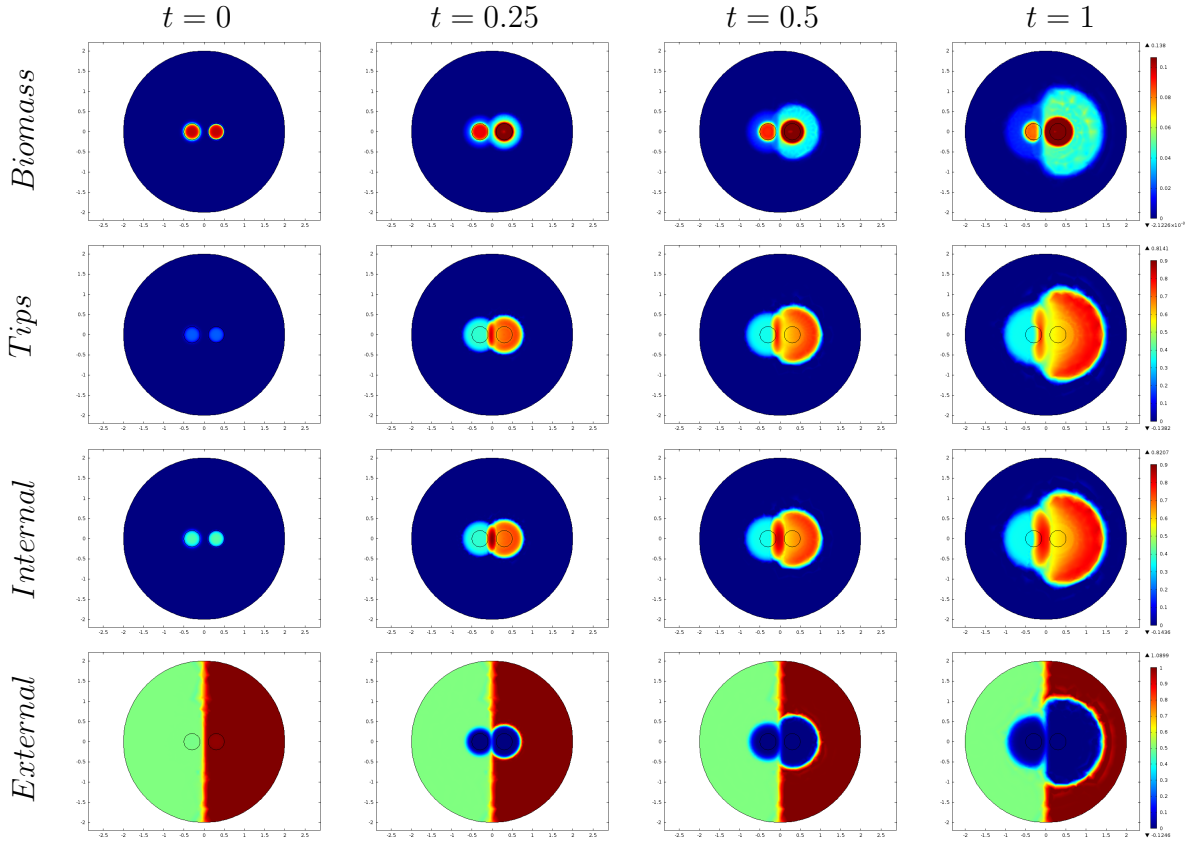


**Figure 5.5:** 2d representation of the solutions to equations (5.10) with initial data (5.11) and parameter values from Table 5.2. The parameters  $s_{e1_0} = 0.5$ ,  $s_{e2_0} = 1$ ,  $G = H = 0$  and  $A = B = 1000$ . Clearly the right biomass is dominating the left. [For a movie of these plots please see external folder labelled:- Comsol - Movie\_files- Fig-5.5]

The biomass starting on the right hand side expands more rapidly than that starting on the left due to additional substrate. Having access to greater resources, the biomass starting on the right hand side is able to dominate and displace the biomass starting on the left hand side. The cross-sectional view in Figure 5.6 more clearly illustrates biomass displacement (see also movie files *Fig\_5.5* and *Fig\_5.6*). This result is in agreement with the findings of Chapter 4 and Choudhury et al. (2018).

The typical behaviour seen in Figure 5.5 can occur in heterogeneous environments where a fungal species germinate and release spores to occupy an inhabited space. Two spores may land in neighbouring locations but have access to different resources and the species with greater access to resource can be ex-

pected to dominate or displace the competitor. Alternatively, in the context of biotechnology, the manipulation of the nutrient concentration can influence the outcome of fungal competition.

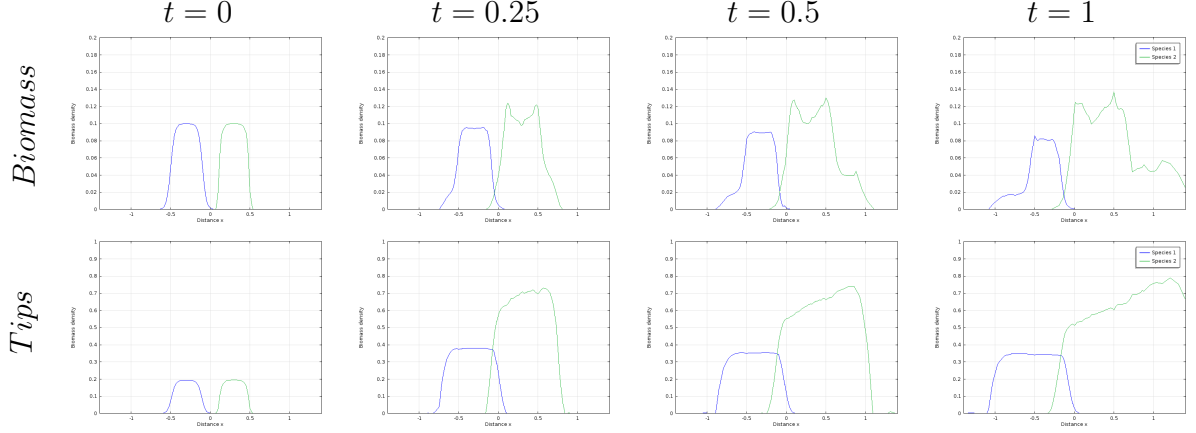


**Figure 5.6:** *Cross section of the solutions to equations (5.10) with initial data (5.11) and parameter values from Table 5.2. The parameters  $s_{e1_0} = 0.5$ ,  $s_{e2_0} = 1$ ,  $G = H = 0$  and  $A = B = 1000$ . Clearly displacement is observed (right biomass is displacing the left). [For a movie of these plots please see external folder labelled:- Comsol - Movie\_files - Fig\_5.6]*

### 5.2.1.3 Competitive variability

In the terrestrial environment fungi often vary in their abilities to compete against rival species (Boddy, 2000). In the previous simulations the fungi had identical combat ability for both species so we will now explore how the model behaves where there is such variation between the species, i.e.  $A \neq B$ . Numerically integrating equations (5.10) using initial conditions in equation (5.11) with the parameter values given in Table 5.2 except  $s_{e1_0} = s_{e2_0} = 1$ ,  $A = 1000$  and  $B = 300$ , illustrates the impact of variations in combat ability (see Figures 5.7 and 5.8).

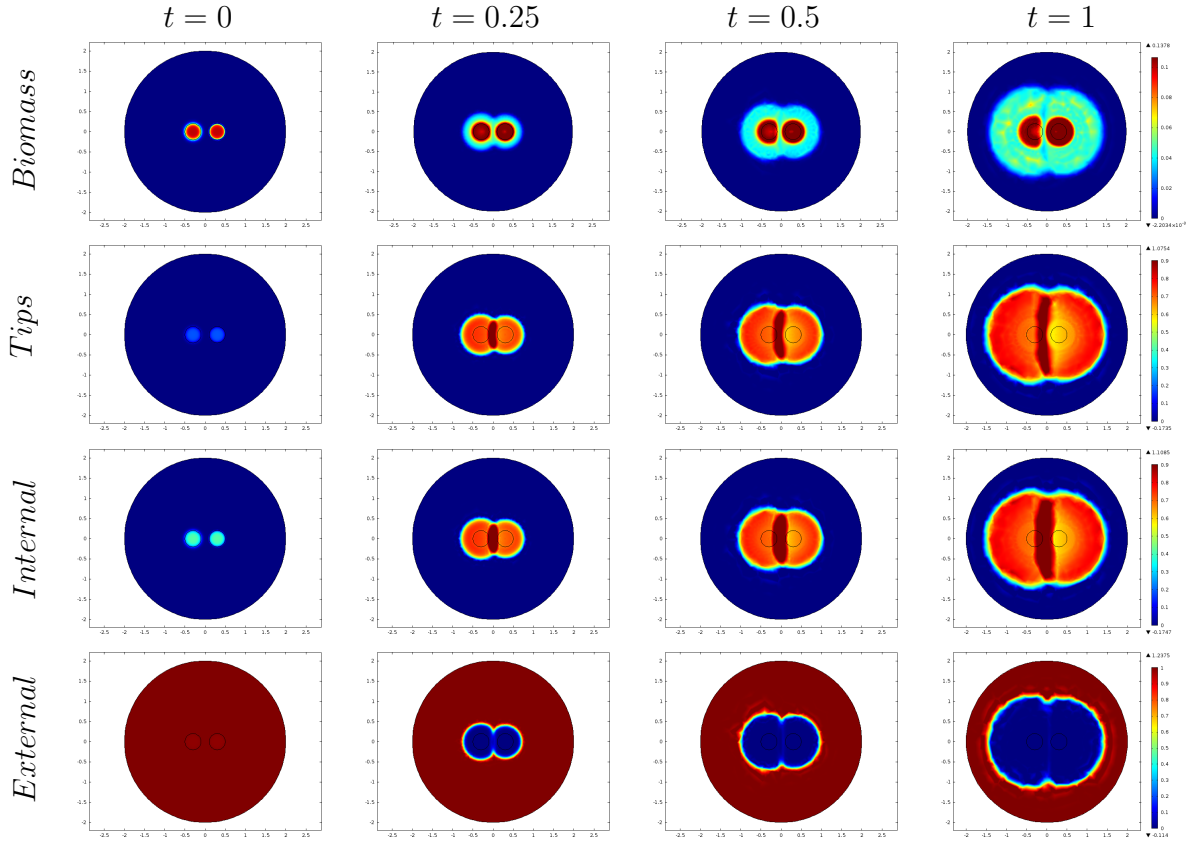


**Figure 5.7:** 2d representation of the solutions to equations (5.10) with initial data (5.11) and parameter values from Table 5.2 with  $s_{e1_0} = s_{e2_0} = 1$ ,  $G = H = 0$ ,  $A = 1000$  and  $B = 300$ . Clearly displacement can be observed (right biomass is displacing the left). [For a movie of these plots please see external folder labelled:- Comsol -Movie\_files - Fig\_5.7]

Clearly the biomass starting on the right is faster at degrading its rival biomass than vice-versa and so there is a steady displacement of one biomass by another (see movie files *Fig\_5.7* and *Fig\_5.8*). Notice there is an increased concentration of hyphal tips at the interaction zone in the displaced biomass, compared to the default case (see Figure 5.3).

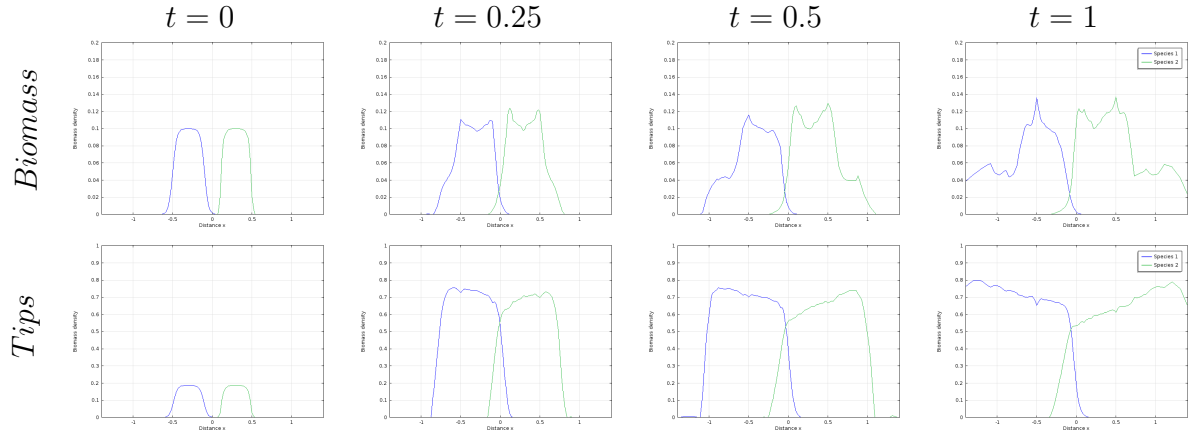


**Figure 5.8:** *Cross section representation of the solutions to equations (5.10) with initial data (5.11) and parameter values from Table 5.2 with  $s_{e1_0} = s_{e2_0} = 1$ ,  $G = H = 0$ ,  $A = 1000$  and  $B = 300$ . Clearly displacement can be observed (right biomass is displacing the left). [For a movie of these plots please see external folder labelled:- Comsol - Movie\_files - Fig-5.8]*

#### 5.2.1.4 Nutrient and competition variability

It was seen above that a better natural competitor will displace an inferior one if the resource available to both biomasses are equal. However, in Chapter 4 we showed that an inferior competitor can displace a superior one provided sufficient resources are made available. We investigate that scenario here to more fully understand the morphological changes. Model equations (5.10) with initial data (5.11) are solved as described above using the same parameters in Table 5.2 except  $s_{e1_0} = 1$ ,  $s_{e2_0} = 0.5$ ,  $A = 1000$  and  $B = 300$  (see Figures 5.9 and 5.10).

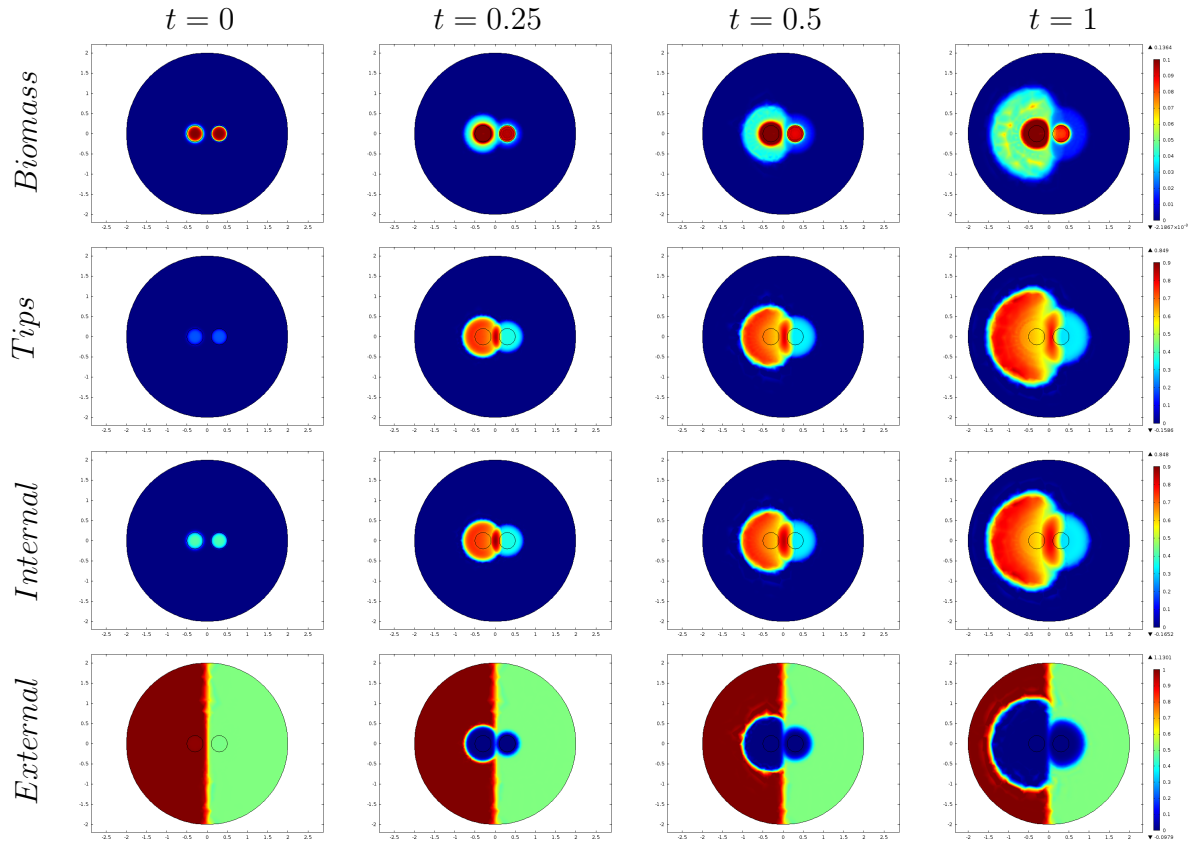


**Figure 5.9:** 2d representation of the solutions to equations (5.10) with initial data (5.11) and parameter values from Table 5.2 with  $s_{e1_0} = 1$ ,  $s_{e2_0} = 0.5$ ,  $G = H = 0$ ,  $A = 1000$  and  $B = 300$ . Displacement can be observed (left biomass is displacing the right). [For a movie of these plots please see external folder labelled:- Comsol - Movie\_files - Fig\_5.9]

The biomass starting on the left expands more rapidly than that on the right due to the extra resources available. Thus following biomass collision at time  $t = 0.25$ , the increased biomass density of the biomass on the left means it is able to prevent its displacement by the apparent superior competitor starting on the right (see movie files *Fig\_5.9* and *Fig\_5.10*).

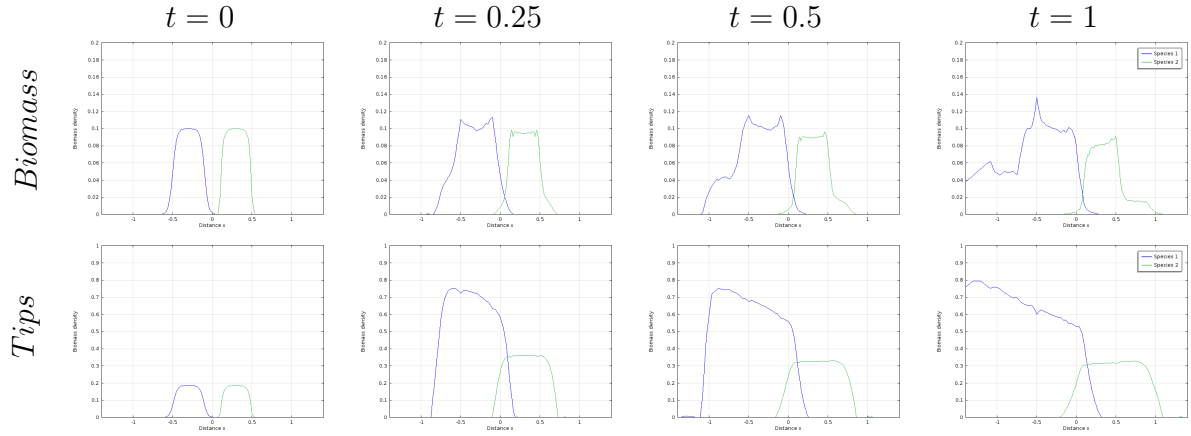


**Figure 5.10:** Cross section of the solutions to equations (5.10) with initial data (5.11) and parameter values from Table 5.2 with  $s_{e10} = 1$ ,  $s_{e20} = 0.5$ ,  $G = H = 0$ ,  $A = 1000$  and  $B = 300$ . Clearly displacement can be observed (left biomass is displacing the right). [For a movie of these plots please see external folder labelled:- Comsol - Movie\_files - Fig-5.10]

### 5.2.2 Continual nutrient replenishment

The previous section examined how variations in the initial substrate concentration could impact on competition between two fungal biomasses. In particular, it was shown that an otherwise inferior competitor could displace a superior competitor if provided with sufficient resources. However, once the resource has been exhausted, the inferior competitor loses any advantage. To overcome this, additional substrate can be supplied. This feature of manipulating resources is especially important in biotechnological applications. This may represent a steady release of nutrient from naturally degrading vegetation or a deliberate release of nutrients designed to promote fungal growth. Either way, this process can be modelled by including a suitable reaction term in the equations for the external substrate  $s_e$ . In particular we consider the case:

$$G(x, y, t) = \begin{cases} G_0, & \text{if } x < 0, \\ 0, & \text{otherwise.} \end{cases} \quad (5.13)$$

$$H(x, y, t) = 0$$

representing the continual release of nutrients to the biomass starting on the left hand side.

### 5.2.2.1 Nutrient replenishment

Model equations (5.10) with initial data (5.11) are solved as previously described with parameter values in Table 5.2 with equation (5.13), where  $G_0 = 0.3$ .

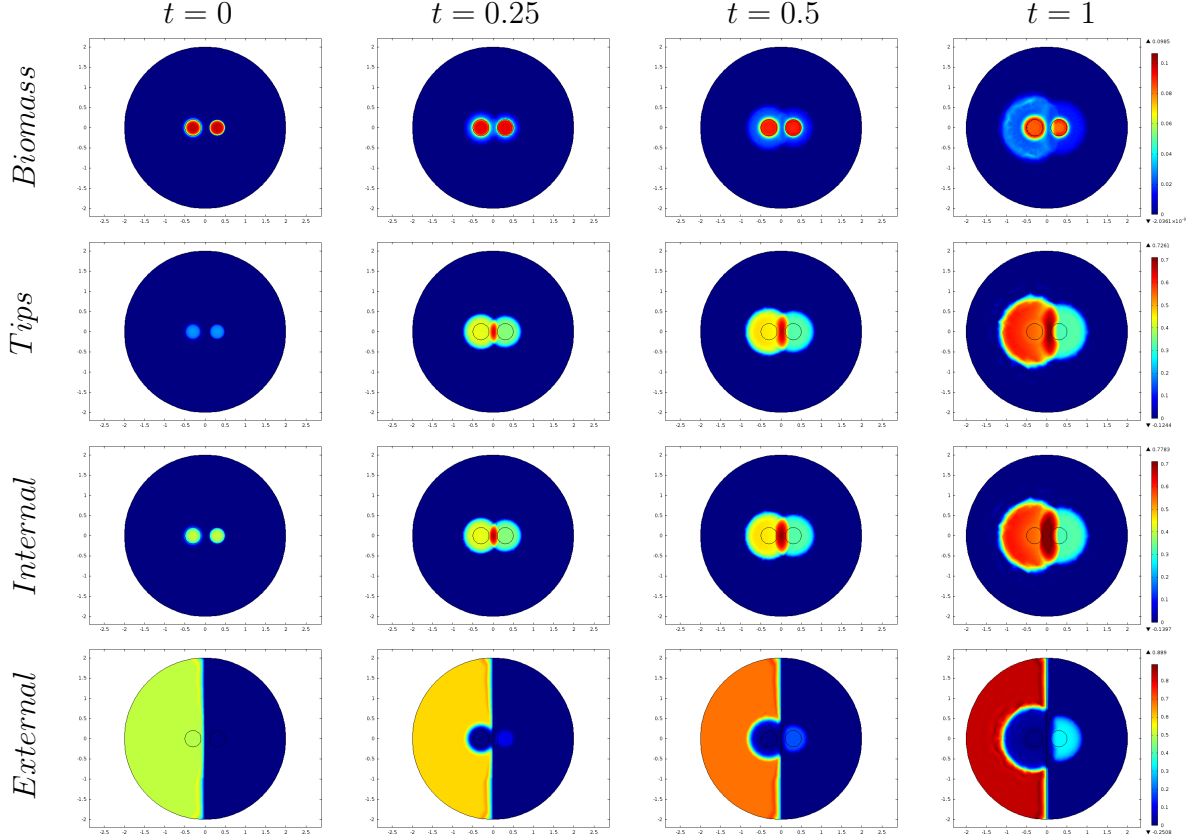


**Figure 5.11:** 2d representation of the solutions to equations (5.10) with initial data (5.11), (5.13) and parameter values from Table 5.2. The parameters  $s_{e10} = s_{e20} = 0.5$ ,  $A = B = 1000$ ,  $G_0 = 0.3$  and  $H = 0$ . Biomass on the left is displacing the biomass on the right. [For a movie of these plots please see external folder labelled:- Comsol - Movie\_files - Fig.5.11]

Figure 5.11 illustrates how the biomass, tip, internal and external substrate densities on the left increase with time (depicted via the colour change within the plots). Figure 5.11 shows the same outcome as the previous case; having access to greater resources provides dominance over a competitor. For example the biomass on the left hand side is able to dominate and displace the biomass on the right hand side. This is the result of continual replenishment being supplied to the biomass on the left (also see movie files *Fig.5.11* and *Fig.5.12*). Although the behaviour is clear from the 2D plots in Figure 5.11, we can take the cross section

of the domain to observe the dynamics of the biomass and tips at the interaction zone (Figure 5.12).

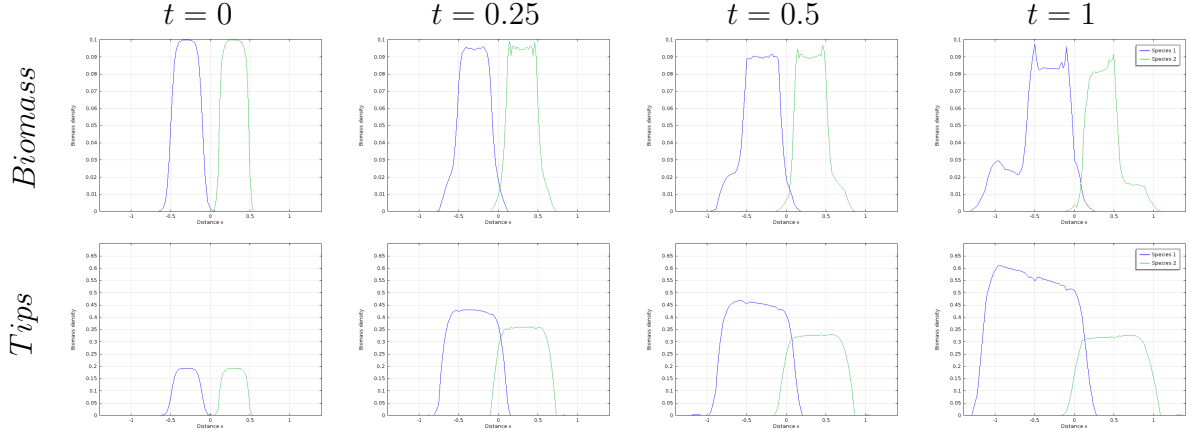


**Figure 5.12:** *Cross section of the solutions to equations (5.10) with initial data (5.11), (5.13) and parameter values from Table 5.2. The parameters  $s_{e1_0} = s_{e2_0} = 0.5$ ,  $A = B = 1000$ ,  $G_0 = 0.3$  and  $H = 0$ . Clearly displacement can be observed (left biomass is displacing the right). [For a movie of these plots please see external folder labelled:- Comsol - Movie\_files - Fig\_5.12]*

### 5.2.2.2 Nutrient replenishment in an uneven domain

The effect of the continual replenishment of external substrate to one biomass may be influenced by the substrate available to its rival, in much the same way as seen in Section 5.2.1. To this end we repeat the simulation in Section 5.2.2.1 except the initial substrate available to the non-replenished biomass is greater. Essentially this corresponds to the model equations (5.10) with initial data (5.11) being solved as previously described with parameter values in Table 5.2 except  $s_{e2_0} = 1$  to create initial nutrient heterogeneity (Figures 5.13 and 5.14).



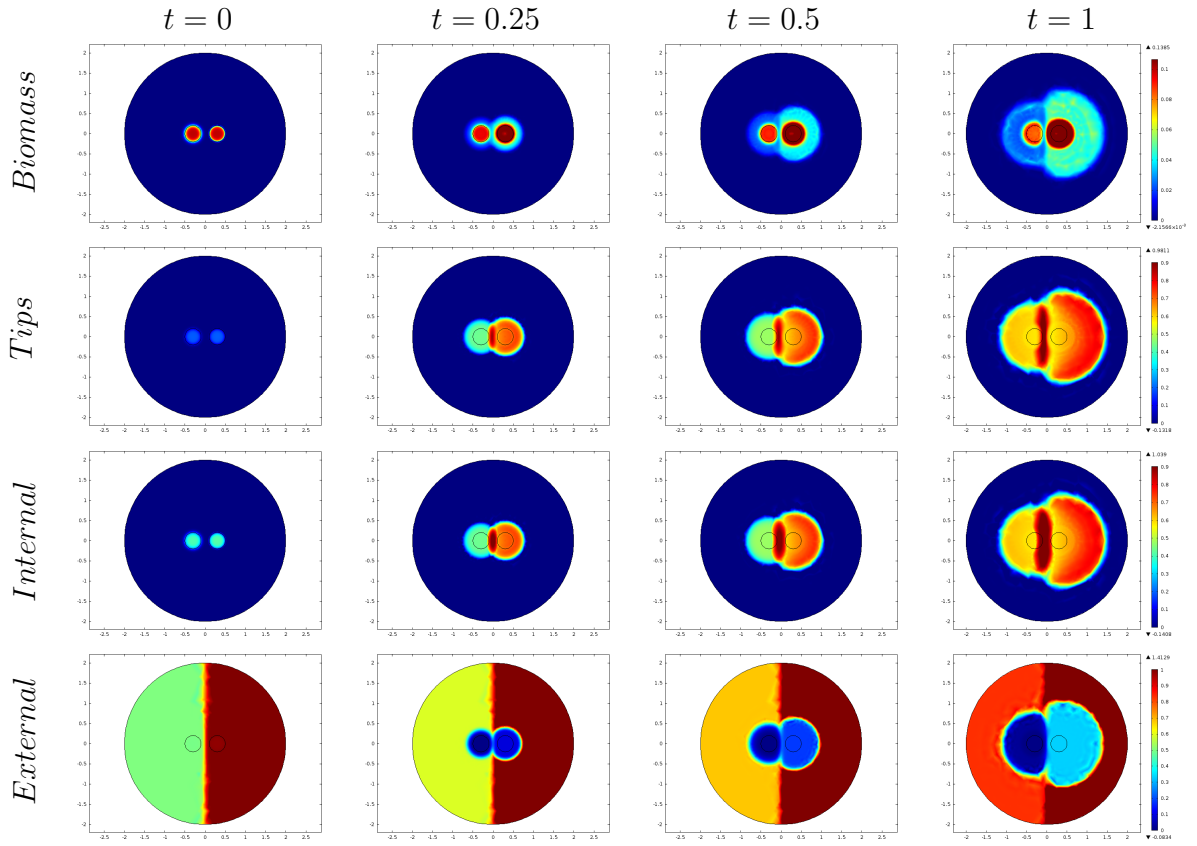


**Figure 5.13:** *2d representation of the solutions to equations (5.10) with initial data (5.11), (5.13) and parameter values from Table 5.2 with  $s_{e1_0} = 0.5$ ,  $s_{e2_0} = 1$ ,  $A = B = 1000$ ,  $G_0 = 0.3$  and  $H = 0$  (species on the right has limited resources and species on the left has continuous resources). Displacement of left biomass by the right biomass is observed. [For a movie of these plots please see external folder labelled:- Cmsol - Movie\_files - Fig.5.13]*

Initially the biomass starting on the right seems to displace that on the left due to it having access to a greater resource. However, as the resources on the right deplete, the biomass on the left displaces that on the right as it has access to continually replenishing resources (see movie files *Fig.5.13* and *Fig.5.14*).

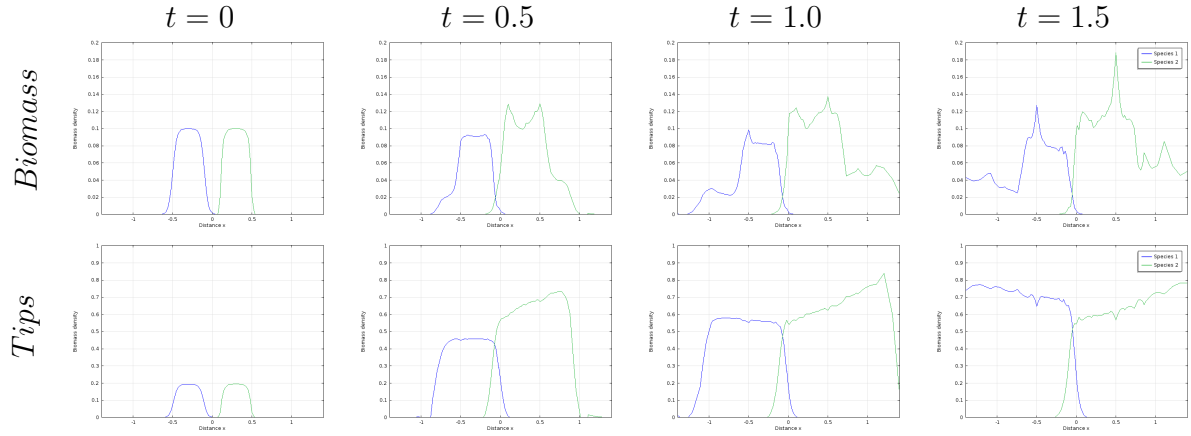


**Figure 5.14:** Cross section of the solutions to equations (5.10) with initial data (5.11), (5.13) and parameter values from Table 5.2 with  $s_{e10} = 0.5$ ,  $s_{e20} = 1$ ,  $A = B = 1000$ ,  $G_0 = 0.3$  and  $H = 0$  (species on the right has limited resources and species on the left has continuous resources). Initially the right biomass is seen to displace the left but then the left biomass displaces the right. [For a movie of these plots please see external folder labelled:- Comsol - Movie\_files - Fig-5.14]

Thus, even if two fungi have access to very different types and amounts of nutrients, the longer term fate of each can be controlled through the supply of additional nutrients. Clearly, this has great potential in the field of bio-remediation and biological control.

### 5.2.2.3 Nutrient replenishment with competitive variability

It was shown above that the continual replenishment of nutrients to a biomass could overcome any initial disparity in nutrient conditions. However, those simulations neglected to account for any disparity in how the biomass was able to use resources when in competition. To this end, we here consider the instance where one biomass is naturally a superior competitor and continually supply the inferior competitor with additional nutrients. Hence using the same approach as before we solve equation (5.10) with the same initial data (5.11) as in the previous section but with  $s_{e10} = s_{e20} = 0.5$ ,  $G_0 = 0.2$ ,  $A = 1000$  and  $B = 300$  (see Figures 5.15 and 5.16).

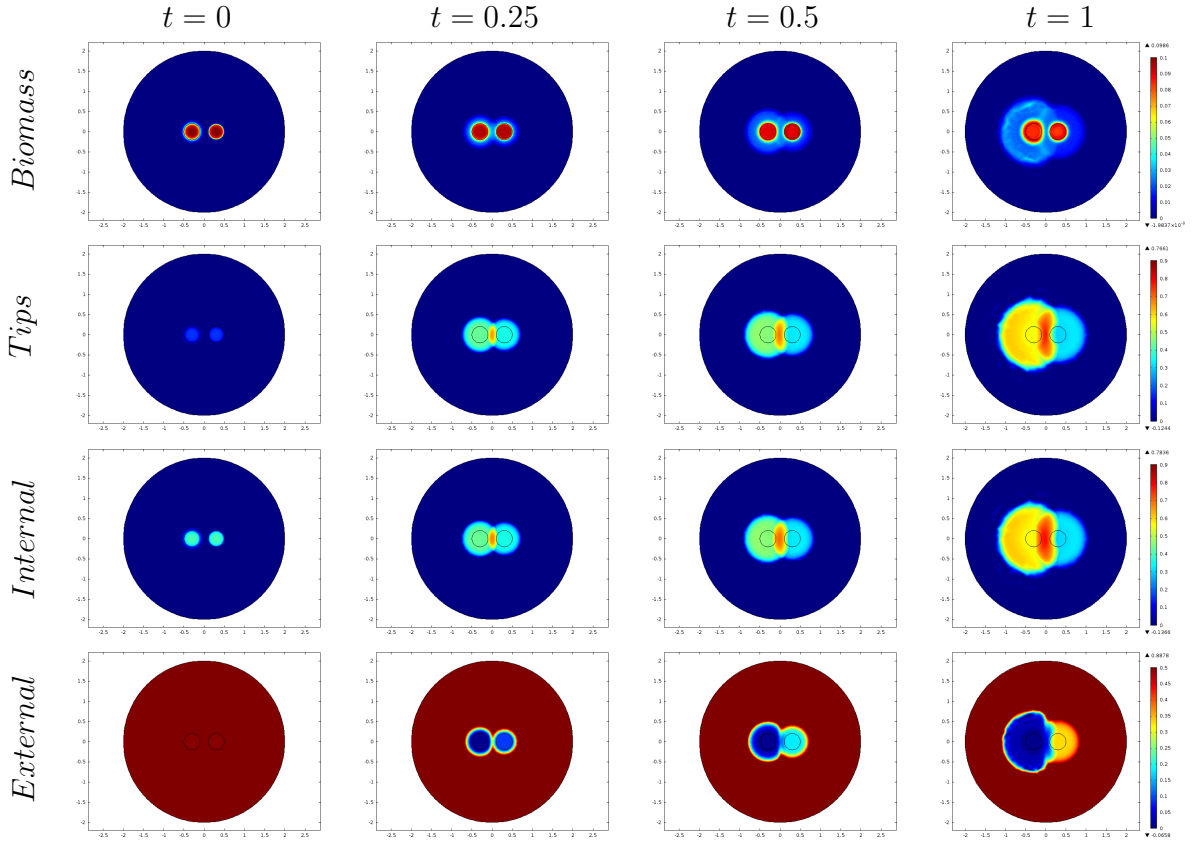


**Figure 5.15:** 2d representation of the solutions to equations (5.10) with initial data (5.11), (5.13) and parameter values from Table 5.2 with  $s_{e1_0} = s_{e2_0} = 0.5$ ,  $G_0 = 0.2$ ,  $H = 0$ ,  $A = 1000$  and  $B = 300$ . The right species can be seen to displace the left species for a very short period and then the left species displaces the right). [For a movie of these plots please see external folder labelled:- Comsol - Movie\_files - Fig.5.15]

Under equally distributed resources, the biomass starting on the right is initially able to displace the biomass starting on the left. However, as the additional supply of substrate is absorbed by the biomass on the left it is better able to defend its territory and propel outwards, eventually dominating and displacing the right biomass (see movie files *Fig.5.15* and *Fig.5.16*). Figure 5.16 more closely shows the development of the biomass and tip densities along the line  $y = 0$ .

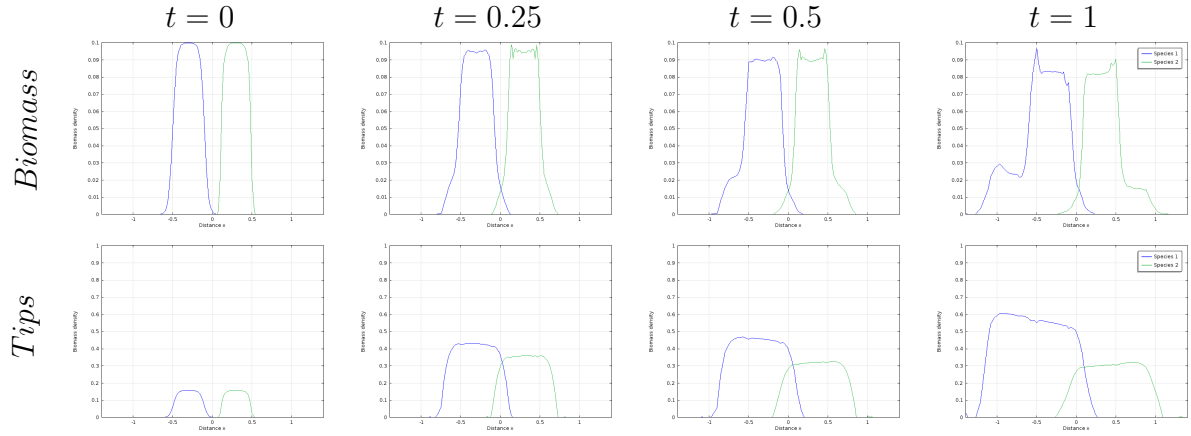


**Figure 5.16:** *Cross section of the solutions to equations (5.10) with initial data (5.11), (5.13) and parameter values from Table 5.2 with  $s_{e10} = s_{e20} = 0.5$ ,  $G_0 = 0.2$ ,  $H_0 = 0$ ,  $A = 1000$  and  $B = 300$ . Right biomass is displacing the left initially but then left biomass displaces the right. [For a movie of these plots please see external folder labelled:- Comsol - Movie\_files - Fig-5.16]*

### 5.2.3 Pulsed nutrient replenishment

In the terrestrial environment when additional resources are made available they are inherently heterogeneous in both space and time. For example, a leaf falling onto the ground provides nutrients to a small spatial region and is not replaced once used up until the next leaf falls. Similarly rainfall may be short lived and localised. Such situations could be mimicked in laboratory settings. For example, resources could be supplied to the respective fungal colonies using a ‘pipette’ at regular intervals. We can easily simulate the impact of using such technique with our model equations by adapting our external resource terms  $G$  and  $H$ , e.g.

$$\begin{aligned} G(x, y, t) &= \begin{cases} G_0 (1 + \sin(Kt)), & \text{if } r < R, \\ 0, & \text{otherwise} \end{cases} \\ H(x, y, t) &= \begin{cases} H_0 (1 + \sin(Kt)), & \text{if } \bar{r} < R, \\ 0, & \text{otherwise} \end{cases} \end{aligned} \quad (5.14)$$

where  $r$  and  $\bar{r}$  have been previously defined in equation (5.12). Recall  $G(x, y, t)$  is a function representing the addition of substrate to the biomass on the left and  $H(x, y, t)$  is a function representing the addition of substrate to the biomass on the right. The constant  $K$  (hereafter taken to be 10) denotes the frequency of

nutrient addition, so that the expression  $1 + \sin(Kt)$  represents the concentration of nutrients supplemented to each biomass over time.

### 5.2.3.1 Competition under equality

Consider two biomasses with equal capabilities growing on a Petri dish. In Section 5.2 and in the absence of any additional substrate the biomasses were seen to reach a state of deadlock at the interaction zone. In this section, both biomasses are continually supplied with oscillating resources at frequency  $K$ . Hence equation (5.10) is solved with initial conditions (5.11) and parameter values from Table 5.2 with  $G_0 = H_0 = 1$  where  $G$  and  $H$  were defined in equation (5.14) (Figures 5.17 and 5.18).

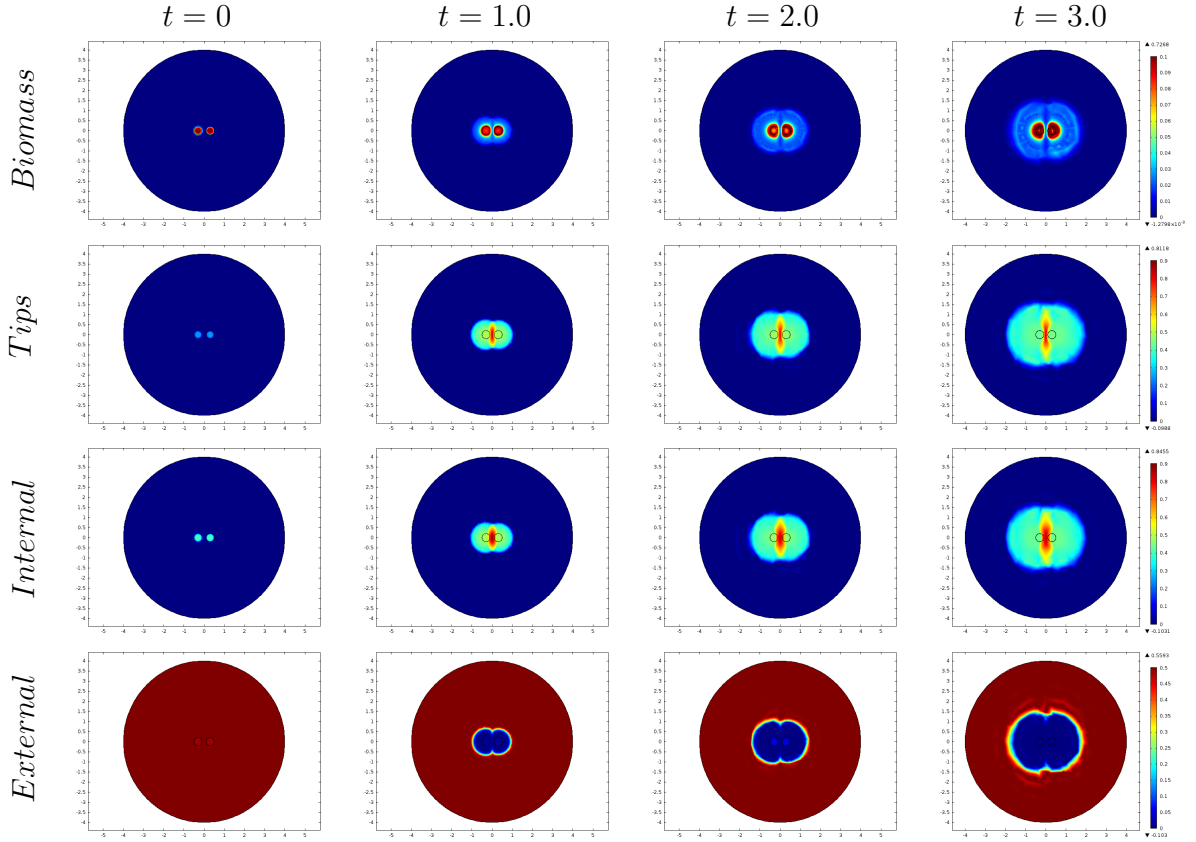


**Figure 5.17:** 2d representation of the solutions to equations (5.10) with initial data (5.11), (5.14) and parameter values from Table 5.2 with  $s_{e1_0} = s_{e2_0} = 0.5$ ,  $G = H = 1 + \sin(10t)$  and  $A = B = 1000$ . A state of deadlock can be seen to form. [For a movie of these plots please see external folder labelled:- Comsol - Movie\_files - Fig-5.17]

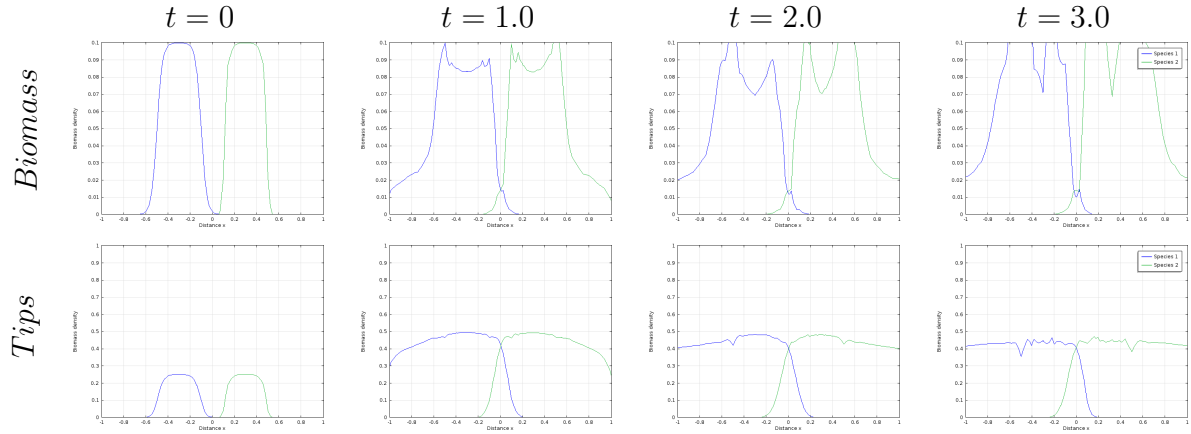


**Figure 5.18:** *Cross section of the solutions to equations (5.10) with initial data (5.11), (5.14) and parameter values from Table 5.2 with  $s_{e10} = s_{e20} = 0.5$ ,  $A = B = 1000$  and  $G = H = 1 + \sin(10t)$ . The graphs are focussed around the interaction zone to illustrate the behaviour of deadlock between both species biomasses. [For a movie of these plots please see external folder labelled:- Comsol - Movie\_files - Fig-5.18]*

Under equally distributed resources and combative abilities, the biomasses collide at the interaction zone producing stalemate behaviour seen in earlier sections. However, due to the continuous nutrient replenishment supplied to the site of the inoculum, the densities at the interaction zone fluctuates but the stalemate state does not alter. Figures 5.17 and 5.18 demonstrates this phenomena. Notice that the region where the resources are being supplied are shown via the colour change (this is clearer to see in the movie files *Fig\_5.17* and *Fig\_5.18*).

### 5.2.3.2 Additional resource impact on competition

It was demonstrated above that the pulsative addition of equal concentrations of substrate did not alter the outcome of competition between two equally comparable biomasses. Previously in Section 5.2.1.4, it was shown that nutritional variability can alter the outcome of competition and hence it is of interest to consider the case where one biomass is provided with additional substrate during each supplementation. In the terrestrial environment this could correspond to additional leaf litter being made available to one fungus at its location. We therefore solve the model equations with parameter values and initial data as stated in Section 5.2.3 except  $G_0 = 2H_0$  corresponding to the biomass on the left receiving twice the substrate as that on the right. The simulated output is shown in Figure

5.19.

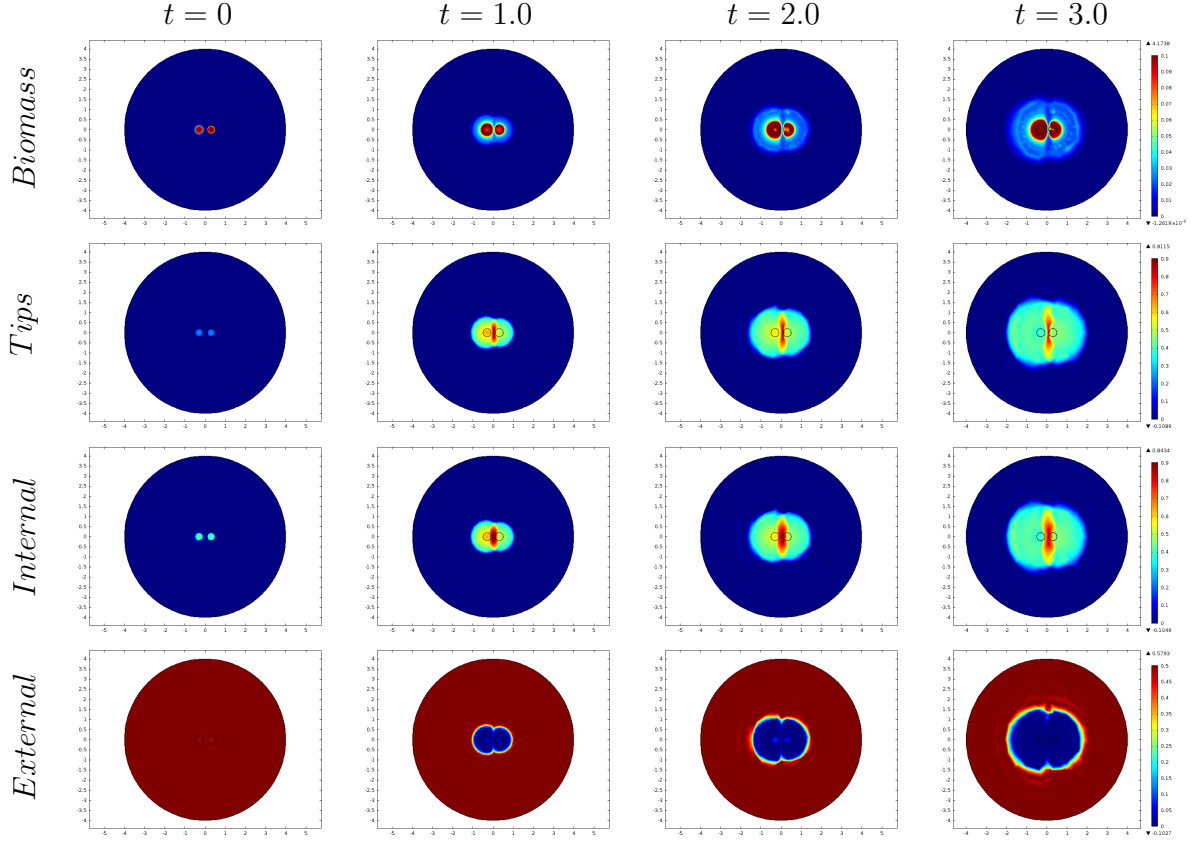


**Figure 5.19:** *2d representation of the solutions to equations (5.10) with initial data (5.11), (5.14) and parameter values from Table 5.2 with  $s_{e10} = s_{e20} = 0.5$ ,  $G = 2(1 + \sin(10t))$ ,  $H = 1 + \sin(10t)$ ,  $A = B = 1000$ . The left biomass can be seen to displace the right biomass. [For a movie of these plots see external folder labelled:- Comsol - Movie\_files - Fig\_5.19]*

When greater resources are supplied to one biomass it is able to displace its competitor. The biomass starting on the left is displacing the species starting on the right but in a pulsed manner. Although the pulsed behaviour is not absolutely clear from Figure 5.19, a cross sectional plot of the domain focussing on the interaction site displays this feature more clearly (see Figure 5.20) while the movie files *Fig\_5.19* and *Fig\_5.20* provide the best illustration of this behaviour.

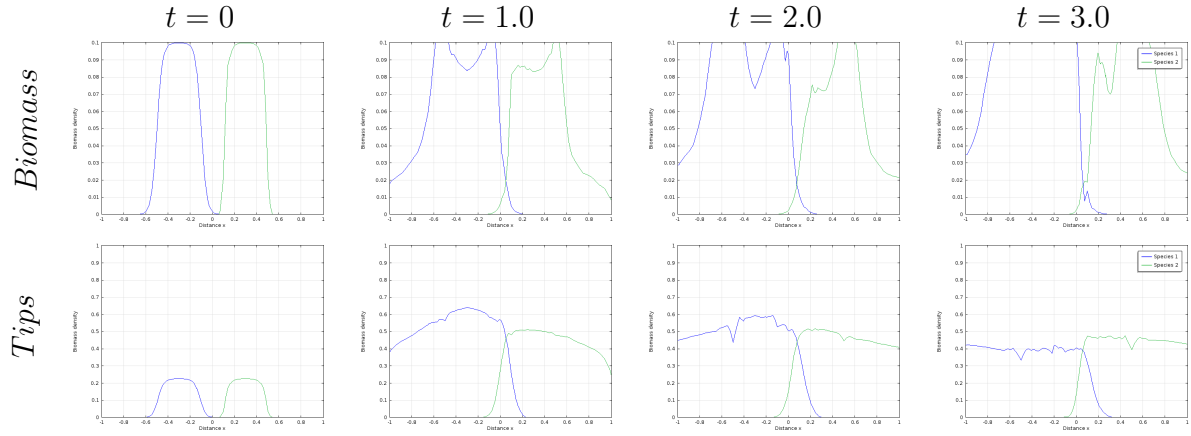


**Figure 5.20:** *Cross section of the solutions to equations (5.10) with initial data (5.11), (5.14) and parameter values from Table 5.2 with  $s_{e10} = s_{e20} = 0.5$ ,  $G = 2(1 + \sin(10t))$ ,  $H = 1 + \sin(10t)$ ,  $A = B = 1000$ . The interaction zone has been zoomed in to illustrate more clearly the behaviour of the left biomass displacing the right. [For a movie of these plots please see external folder labelled:- Comsol - Movie\_files - Fig-5.20]*

### 5.2.3.3 Combative variability and resources

In the terrestrial environment fungi evolve with various capabilities. Some fungi develop better competing abilities compared to their competitors. If a less dominant species were to access resources greater than its competitor, then it could have the energy to overcome, or at least withstand, the attacks of its rival. To investigate such intricacies we solve the model equations (5.10) with parameter values and initial data as stated in Section 5.2.3 except  $G_0 = 2H_0$  corresponding to the biomass on the left receiving twice the substrate as that on the right and  $A = 500$  and  $B = 1000$  to denote the biomass on the left hand side's ability to attack being half of the biomass on the right. The corresponding results are shown in Figure 5.21.



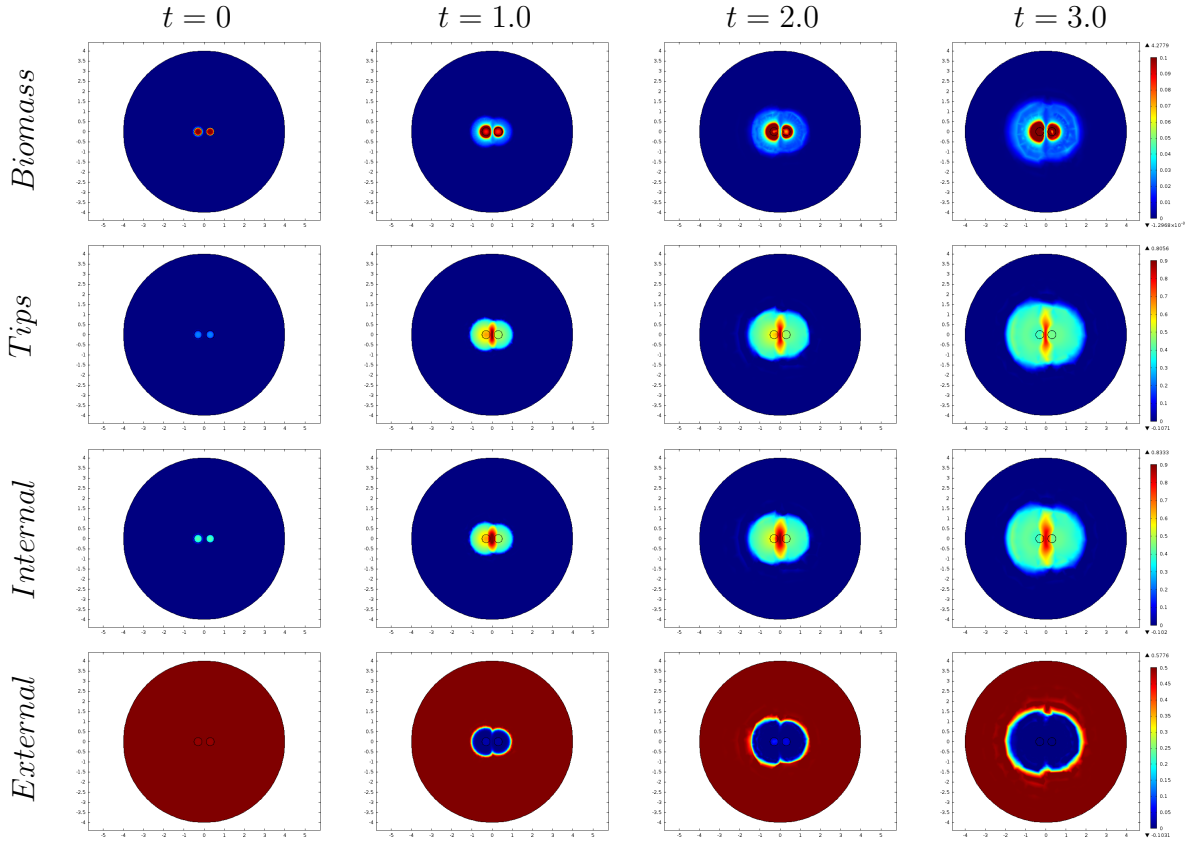


**Figure 5.21:** 2d representation of the solutions to equations (5.10) with initial data (5.11), (5.14) and parameter values from Table 5.2 with  $s_{e1_0} = s_{e2_0} = 0.5$ ,  $G = 2(1 + \sin(10t))$ ,  $H = 1 + \sin(10t)$ ,  $A = 500$  and  $B = 1000$ . There is a subtle oscillatory behaviour between the species. [For a movie of these plots please see external folder labelled:- Comsol - Movie\_files - Fig.5.21]

While not particularly clear from Figure 5.21, the biomass peripheries actually show subtle oscillatory behaviour. The biomass on the left seems to displace the biomass on the right for a short period then halt. The right biomass cannot seem to displace the biomass on the left but does seem to invade its space (at low densities). This consequence of additional resources being pumped to the left biomass results in the less dominant species holding its ground and thus not being displaced by a dominant antagonist (see movie files *Fig.5.21* and *Fig.5.22* for a clearer illustration of this phenomena). A cross sectional plot of the domain captured this phenomenon better than the 2D views above (see Figure 5.22).

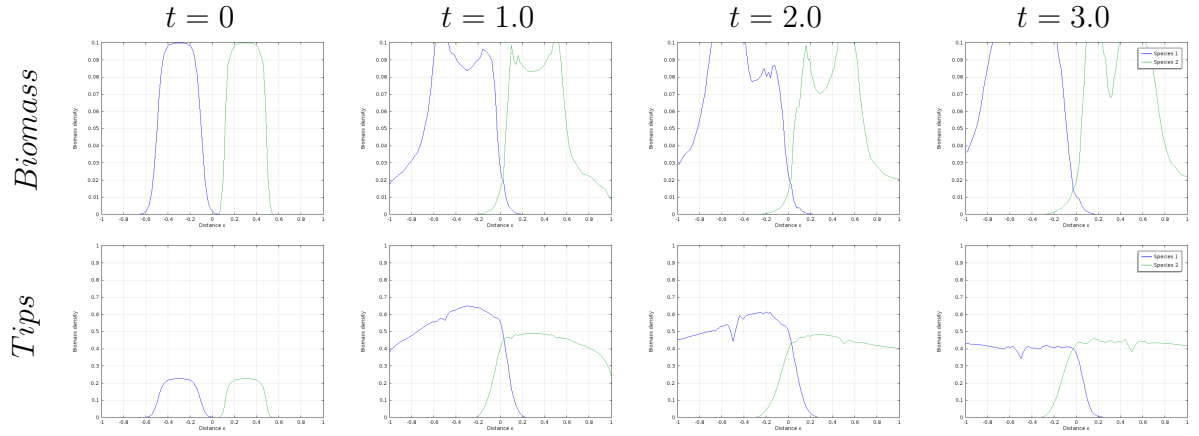


**Figure 5.22:** *Cross section of the solutions to equations (5.10) with initial data (5.11), (5.14) and parameter values from Table 5.2 with  $s_{e10} = s_{e20} = 0.5$ ,  $G = 2(1 + \sin(10t))$ ,  $H = 1 + \sin(10t)$ ,  $A = 1000$  and  $B = 500$ . There is subtle oscillatory behaviour between the species. [For a movie of these plots please see external folder labelled:- Comsol - Movie\_files - Fig.5.22]*

The subtle oscillatory behaviour seen in Figures 5.21 and 5.22 might not easily be observable in experiments where the fungi is monitored in a period of days due to the time and spatial scales involved in the oscillations. However, calibrating experiments using the techniques specified in this section could lead to determine critical nutrient concentrations required to control various fungal pathogens.

There are a vast number of scenarios that can be tested with the models presented in this section. For example varying the phase parameter ‘ $K$ ’ would result in asynchronous delivery of resources depicted by different phases of the functions  $G$  and  $H$  potentially representing an instance where droplets of water are continuously supplied to a hydrophilic fungal mycelium competing for space with another species that obtains water from the rain. In such an instance it is reasonable to hypothesize the possible existence of cyclic displacements of one biomass by another at rates dictated by the periodicity of additionally supplied substrate. However, this would require further extensive numerical investigation to confirm. To avoid repetition many observations have been omitted from this thesis and only the scenarios that add qualitative value to the investigation are included.

### 5.2.4 Initial homogeneous resources

We have explored the behaviour of fungal competition where two species have access to independent and spatially separated resources. Typically in the terrestrial environment, fungal species have to search for resources beyond their immediate vicinity. In laboratory settings this is achieved by filling a Petri dish with a single type of resource throughout, mixed with agar solution at different concentrations on which the fungal mycelium is placed and monitored for growth and reaction. Essentially, with respect to our model equations, the different types of external substrate will be present across the entire domain and not just confined to one half. In this section we will use our model equation (5.10) to simulate the outcome of such implications and thus a slight adjustment to the initial conditions (5.11) is made, specifically

$$\begin{aligned}
\frac{\rho_1(x, y, 0)}{\rho_{1_0}} &= \frac{n_1(x, y, 0)}{n_{1_0}} = \frac{s_{i1}(x, y, 0)}{s_{i1_0}} = \frac{1 - \tanh(\phi(r - R))}{2} \\
\rho'_1(x, y, 0) &= 0, \quad s_{e1}(x, y, 0) = s_{e1_0} \\
\frac{\rho_2(x, y, 0)}{\rho_{2_0}} &= \frac{n_2(x, y, 0)}{n_{2_0}} = \frac{s_{i2}(x, y, 0)}{s_{i2_0}} = \frac{1 - \tanh(\theta(\bar{r} - R))}{2} \\
\rho'_2(x, y, 0) &= 0, \quad s_{e2}(x, y, 0) = s_{e2_0}
\end{aligned} \tag{5.15}$$

where all the variables are the same as previously described.

#### 5.2.4.1 Combative variability in an exhaustive nutrient domain

The simulations for fungi with equal competing ability (i.e.  $A = B$ ) but no nutrient replenishment provided results identical to Figures in 5.3 and 5.4, i.e. deadlock. The case when one fungal species is more dominant than the other (i.e.  $A \neq B$ ) will be considered here. Thus equations (5.10) will be numerically integrated with initial conditions (5.15) and using parameters values in Table 5.2 but with the following changes:  $A = 200$ ,  $B = 1000$  and  $s_{e1_0} = s_{e2_0} = 1$ . Typical results are shown in Figure 5.23.

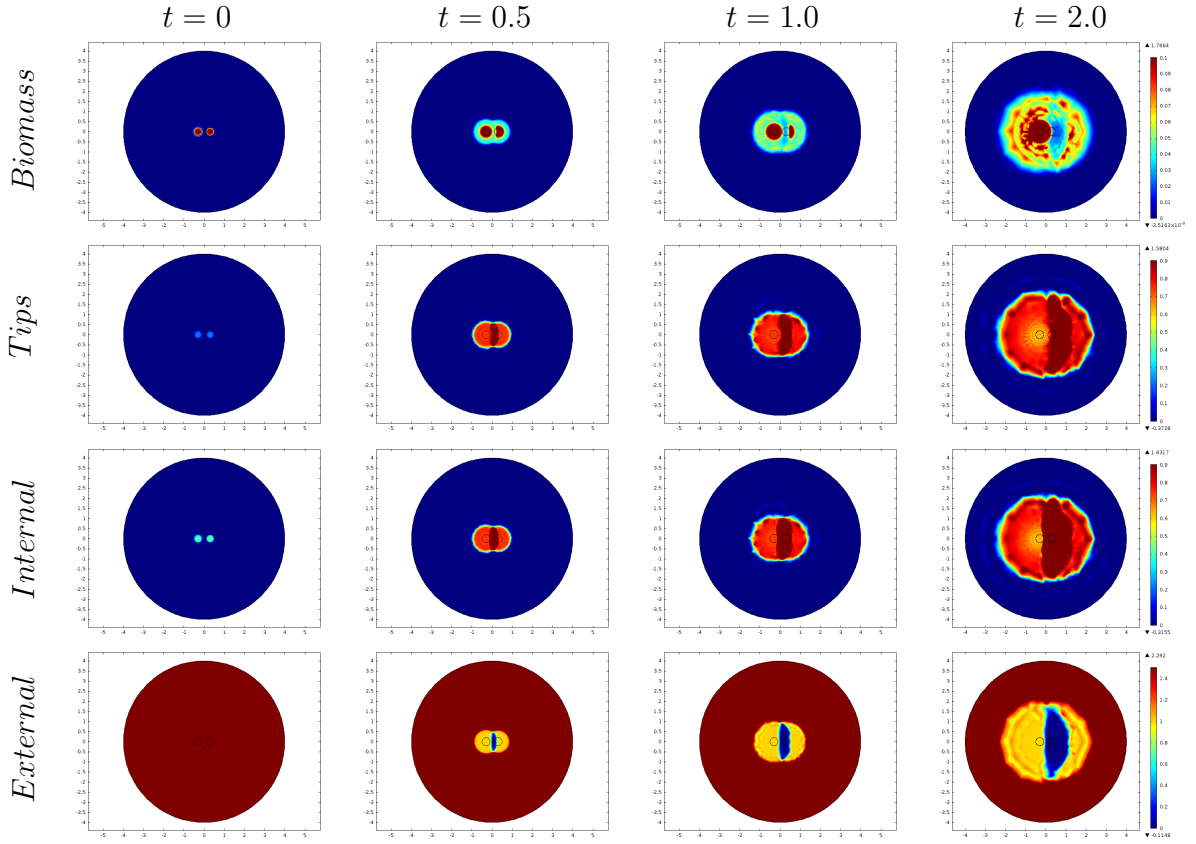


**Figure 5.23:** 2d representation of the solutions to equations (5.10) with initial data (5.15) and parameter values from Table 5.2 with  $s_{e1_0} = s_{e2_0} = 1$ ,  $G = H = 0$ ,  $A = 200$  and  $B = 1000$ . The left biomass can be seen to displace the right biomass very quickly. [For a movie of these plots please see external folder labelled:- Cmsol - Movie\_files - Fig-5.23]

Figure 5.23 demonstrates that when the finite resource is initially distributed across the entire domain, the biomass on the left is able to displace the biomass on the right. It is worth noticing the similarities between Figure 5.23 and Figure 5.7 but the biomass on the left displaces the biomass on the right at a faster rate due to the difference in magnitude of the proportionality constant ( $A = 200$  and  $B = 1000$ ). Figure 5.24 shows a cross sectional plot of the hyphae and tip densities (see also movie files *Fig-5.23* and *Fig-5.24*).

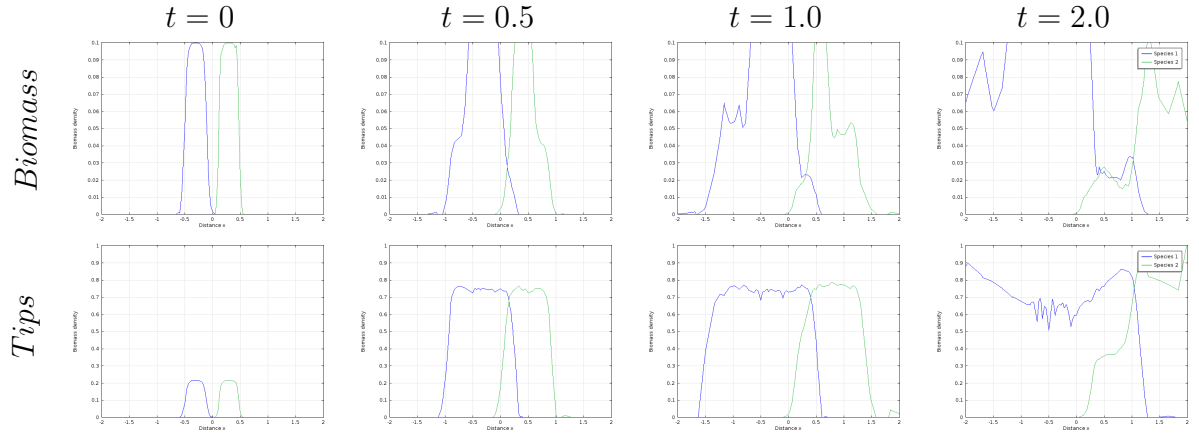


**Figure 5.24:** *Cross section of the solutions to equations (5.10) with initial data (5.15) and parameter values from Table 5.2 with  $s_{e1_0} = s_{e2_0} = 1$ ,  $A = 200$ ,  $B = 1000$  and  $G = H = 0$ . Left biomass is displacing the right. [For a movie of these plots please see external folder labelled:- Comsol - Movie\_files - Fig\_5.24]*

#### 5.2.4.2 Combative variability in a biased nutrient domain

In the previous section the dominant biomass was seen to displace the less dominant species due to ample resources available within the domain. Here we consider the case where the naturally inferior competitor has access to greater resources than its rival. This scenario is simulated using the same protocol except  $s_{e1_0} = 0.5$  and  $s_{e2_0} = 1$  with the results shown in Figure 5.25.

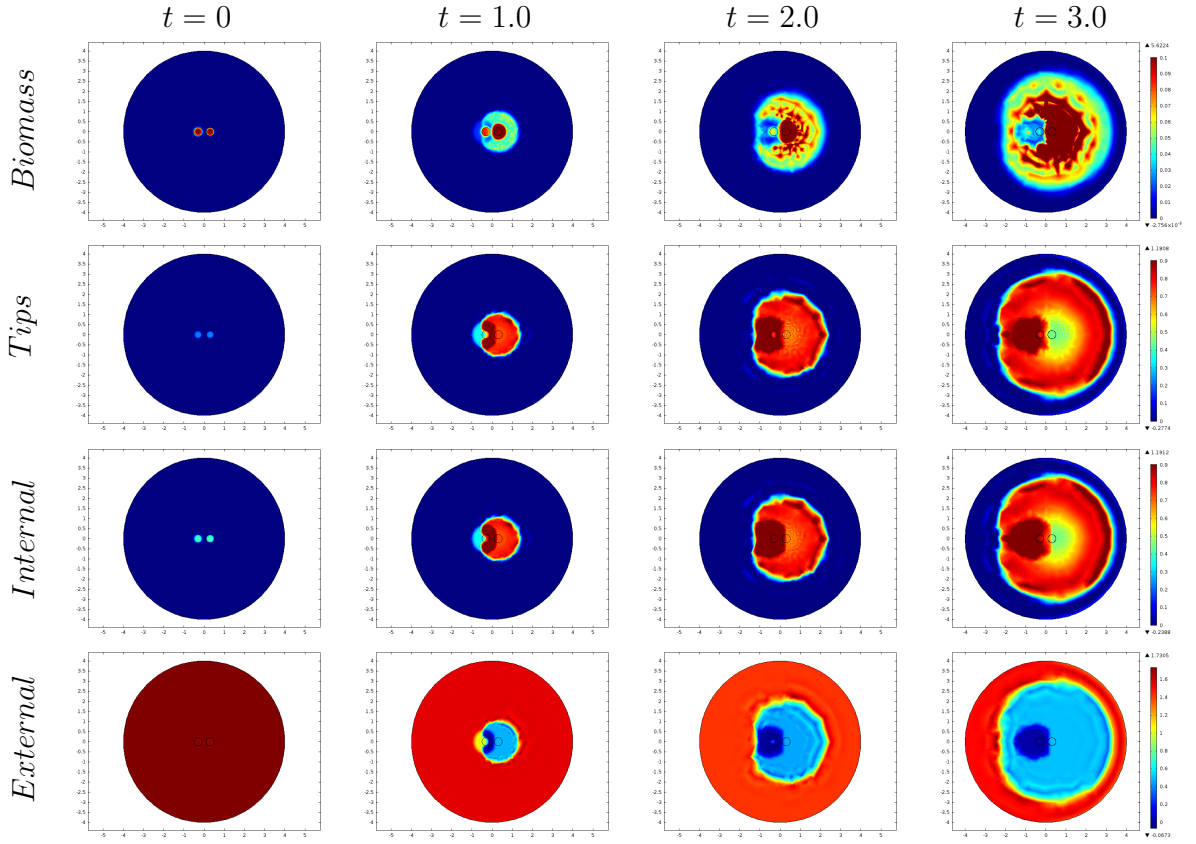


**Figure 5.25:** 2d representation of the solutions to equations (5.10) with initial data (5.15) and parameter values from Table 5.2 with  $s_{e1_0} = 0.5$ ,  $s_{e2_0} = 1$ ,  $G = H = 0$ ,  $A = 200$  and  $B = 1000$ . The right biomass can be seen to displace the left biomass and grow around it. [For a movie of these plots please see external folder labelled:- Cmsol - Movie\_files - Fig\_5.25]

Figure 5.25 depicts a surprising result. Although the biomass on the right is less dominant, it is not only able to initially displace the biomass on the left at a fast rate but also grow around it and eventually engulf it (see movie files *Fig\_5.25* and *Fig\_5.26*). The tip density seem to show a possible case of displacement followed by coexistence; Figure 5.26 shows this clearly.

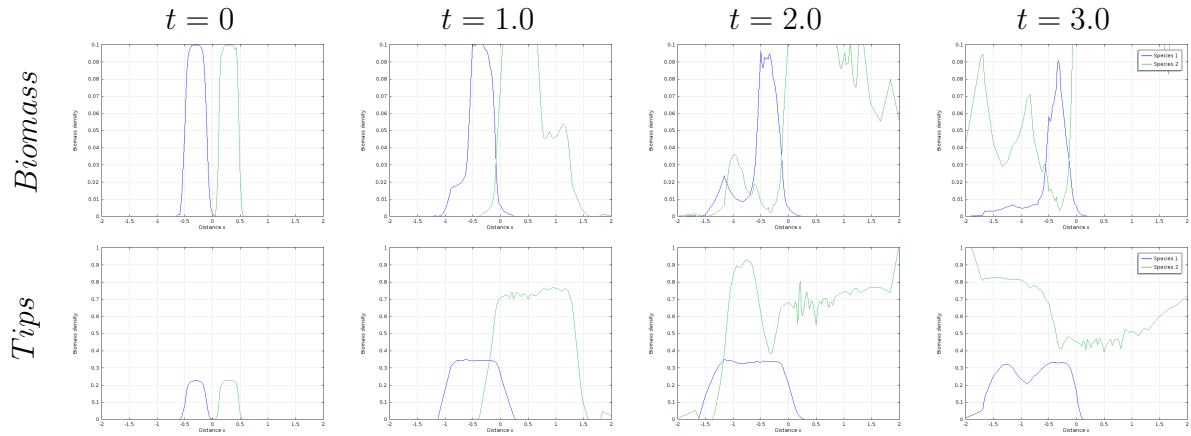


**Figure 5.26:** Cross section of the solutions to equations (5.10) with initial data (5.15) and parameter values from Table 5.2 with  $s_{e10} = 0.5$ ,  $s_{e20} = 1$ ,  $A = 200$ ,  $B = 1000$  and  $G = H = 0$ . Right biomass is displacing the left. [For a movie of these plots please see external folder labelled:- Comsol - Movie\_files - Fig\_5.26]

Figures 5.25 and 5.26 demonstrates that if a fungus has access to enough resources (i.e. energy), a less dominant species can overpower a dominant species. Another interpretation of the results is that by reducing the resource available to a dominant species, an inferior competitor can coexist. This result can potentially be of use in bio-remediation (myco-remediation) and agriculture where fungi are used to reduce the adverse effect of other pathogenic fungi. It may not always be the best option to completely rid an adverse competitor especially if it has mutual benefits. For example, an antagonist fungi could be favourable to an animal which keep other more dangerous species away from causing greater damage to the yield. Thus, determining and controlling the levels of the resource which the rival species of fungi seek can provide more benefit than to completely eradicating the species.

### 5.3 Single common resource

In the previous sections, an independent nutrient source for each respective fungi was assumed. In the terrestrial environments, fungal species often have to compete for a common resource. Indeed, in typical laboratory experimental settings, a Petri dish is laced with a resource mixed with other chemical compounds in the form of an agar solution accessible to both competing fungi. To represent this scenario we need to modify our original model equations. The corresponding updated coupled

partial differential equations are

$$\begin{aligned}
\frac{\partial \rho_1}{\partial t} &= |v_1 s_{i1} n_1 \nabla \rho_1 + D_{n1} s_{i1} \nabla n_1| - d_{\rho_1} \rho_1 - E s_{i2} \rho_2 \rho_1 \\
\frac{\partial \rho'_1}{\partial t} &= d_{\rho_1} \rho_1 - d_{i1} \rho'_1 \\
\frac{\partial n_1}{\partial t} &= \nabla \cdot (v_1 s_{i1} n_1 \nabla \rho_1 + D_{n1} s_{i1} \nabla n_1) + \alpha_1 s_{i1} \rho_1 - \beta_1 n_1 \rho_1 - A s_{i2} \rho_2 n_1 \\
\frac{\partial s_{i1}}{\partial t} &= \nabla \cdot (D_{i1} \rho_1 \nabla s_{i1} - D_{a1} \rho_1 s_{i1} \nabla n_1) + c_1 s_{i1} \rho_1 s_e \\
&\quad - c_2 |v_1 s_{i1} n_1 \nabla \rho_1 + D_{n1} s_{i1} \nabla n_1| - c_4 |D_{a1} \rho_1 s_{i1} \nabla n_1| \\
\frac{\partial \rho_2}{\partial t} &= |v_2 s_{i2} n_2 \nabla \rho_2 + D_{n2} s_{i2} \nabla n_2| - d_{\rho_2} \rho_2 - F s_{i1} \rho_1 \rho_2 \\
\frac{\partial \rho'_2}{\partial t} &= d_{\rho_2} \rho_2 - d_{i2} \rho'_2 \\
\frac{\partial n_2}{\partial t} &= \nabla \cdot (v_2 s_{i2} n_2 \nabla \rho_2 + D_{n2} s_{i2} \nabla n_2) + \alpha_2 s_{i2} \rho_2 - \beta_2 n_2 \rho_2 - B s_{i1} \rho_1 n_2 \\
\frac{\partial s_{i2}}{\partial t} &= \nabla \cdot (D_{i2} \rho_2 \nabla s_{i2} - D_{a2} \rho_2 s_{i2} \nabla n_2) + \bar{c}_1 s_{i2} \rho_2 s_e \\
&\quad - \bar{c}_2 |v_2 s_{i2} n_2 \nabla \rho_2 + D_{n2} s_{i2} \nabla n_2| - \bar{c}_4 |D_{a2} \rho_2 s_{i2} \nabla n_2| \\
\frac{\partial s_e}{\partial t} &= D_{e2} \nabla^2 s_e - c_3 s_{i1} \rho_1 s_e - \bar{c}_3 s_{i2} \rho_2 s_e
\end{aligned} \tag{5.16}$$

where there is now only one equation representing the external substrate concentration denoted by  $s_e$  with two uptake terms for both biomasses. Following earlier work, the initial conditions are

$$\begin{aligned}
\frac{\rho_1(x, y, 0)}{\rho_{10}} &= \frac{n_1(x, y, 0)}{n_{10}} = \frac{s_{i1}(x, y, 0)}{s_{i10}} = \frac{1 - \tanh(\phi(r - R))}{2} \\
\rho'_1(x, y, 0) &= 0 \\
\frac{\rho_2(x, y, 0)}{\rho_{20}} &= \frac{n_2(x, y, 0)}{n_{20}} = \frac{s_{i2}(x, y, 0)}{s_{i20}} = \frac{1 - \tanh(\theta(\bar{r} - R))}{2} \\
\rho'_2(x, y, 0) &= 0 \\
s_e(x, y, 0) &= s_{e0}
\end{aligned} \tag{5.17}$$

where  $r$ ,  $\bar{r}$ ,  $R$  and  $M$  have been previously defined which corresponds to the inoculation at a uniform growth medium with two rival fungi. The parameter values used are from Table 5.2 unless stated otherwise.

Equations (5.16) will be solved for competing fungi with different combat



abilities below. Fungal competition for equal abilities form deadlock similar to that seen in Figures 5.3 and 5.4 hence will not be explored here.

### 5.3.1 Competitive variability in a nutrient scarce domain

The impact of two fungal species with varying combat ability competing for a scarce resource in a shared environment will be explored in this section. Limited nutrient sources phenomena is a common occurrence in terrestrial landscapes and thus a worthy target of investigation. Solving equation (5.16) with initial conditions (5.17) and parameter values in Table 5.2 except  $A = 1000$ ,  $B = 300$  and  $s_{e0} = 0.5$  we obtain the plots shown in Figure 5.27.

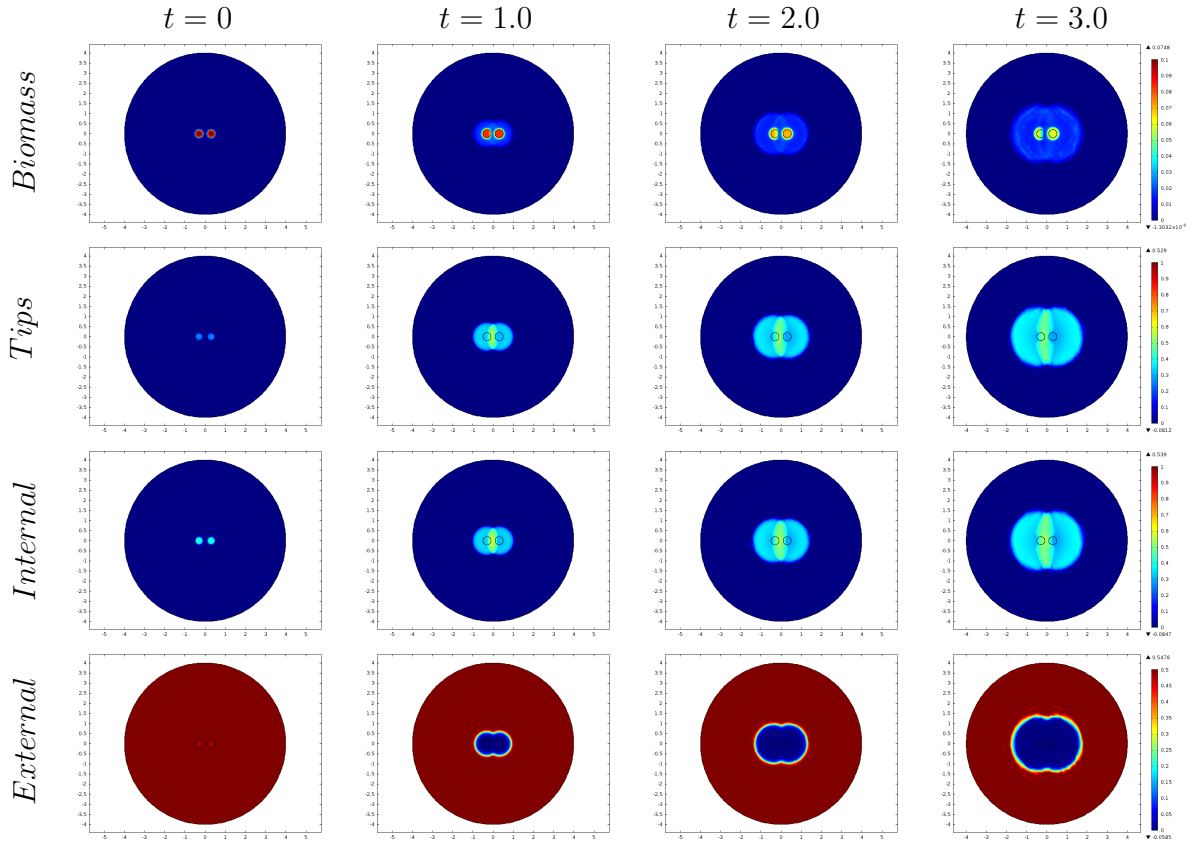


**Figure 5.27:** *2d representation of the solutions to equations (5.16) with initial data (5.17) and parameter values from Table 5.2 with  $s_{e0} = 0.5$ ,  $A = 1000$  and  $B = 300$ . The right biomass can be seen to displace the left. [For a movie of these plots please see external folder labelled:- Comsol - Movie\_files - Fig.5.27]*

Figure 5.27 demonstrates the dominant biomass on the right is displacing

the biomass on the left. Due to the limited resource present in the domain and the aggressive nature of its competitor the less dominant biomass is not able to defend its territory and succumbs to being overpowered. Figure 5.28 shows this clearly by illustrating the model densities along the line  $y = 0$ .

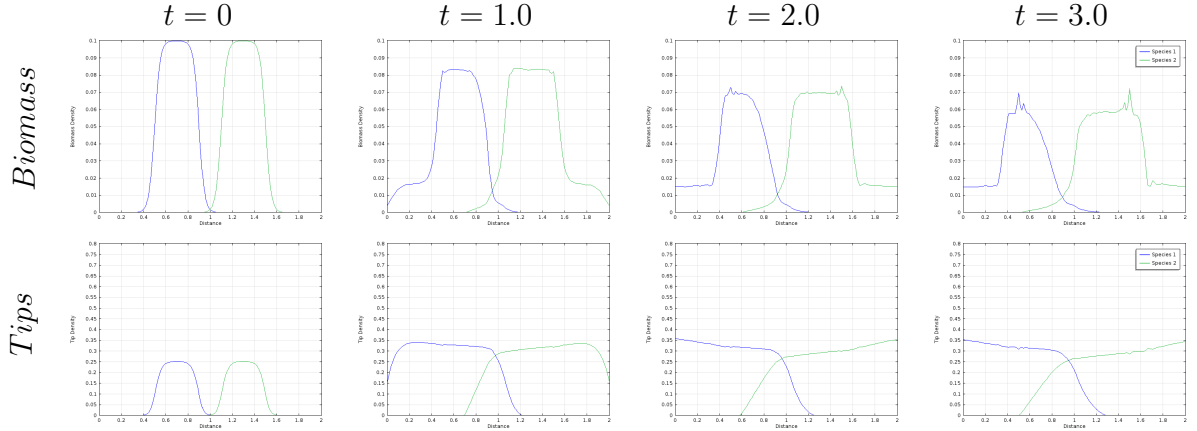


**Figure 5.28:** Cross sectional representation of the solutions to equations (5.16) with initial data (5.17) and parameter values from Table 5.2 with  $s_{e0} = 0.5$ ,  $A = 1000$  and  $B = 300$ . The right biomass can be seen to gradually displace the left. [For a movie of these plots please see external folder labelled:- Comsol - Movie\_files - Fig\_5.28]

Figure 5.28 shows that in a low nutrient environment the dominant species is able to dominate its competitor. Interestingly there seems to be coexistence at lower levels seen in the biomass plot (see movie files *Fig\_5.27* and *Fig\_5.28*). This result corresponds to that determined in Chapter 4.

### 5.3.2 Competitive variability in a nutrient rich domain

In the previous section we explored the behaviour of two biomasses with varying combative capabilities competing for space in a nutrient scarce domain. In this section will observe how the biomasses behave in a nutrient rich environment. Using the same protocol as in the previous section except with  $s_{e0} = 1$ , typical results are shown in Figure 5.29.

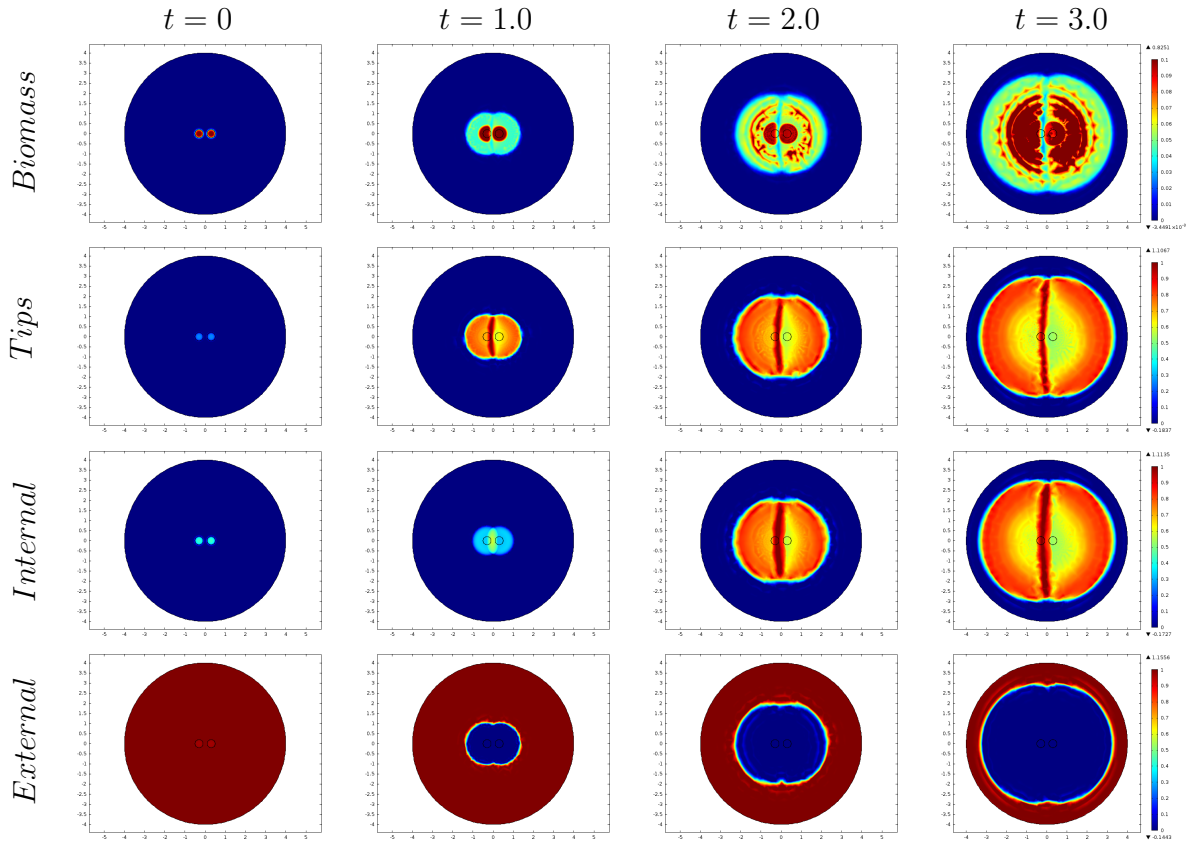


**Figure 5.29:** *2d representation of the solutions to equations (5.16) with initial data (5.17) and parameter values from Table 5.2 with  $s_{e0} = 1$ ,  $A = 1000$  and  $B = 300$ . The right biomass can be seen to displace the left biomass at a fast pace. [For a movie of these plots please see external folder labelled:- Comsol - Movie\_files - Fig\_5.29]*

Figure 5.29 demonstrates that the biomass on the right displaces the biomass on the left much faster than in Figure 5.27. Figure 5.30 shows a cross sectional plot of this where the displacement is more easily observed.

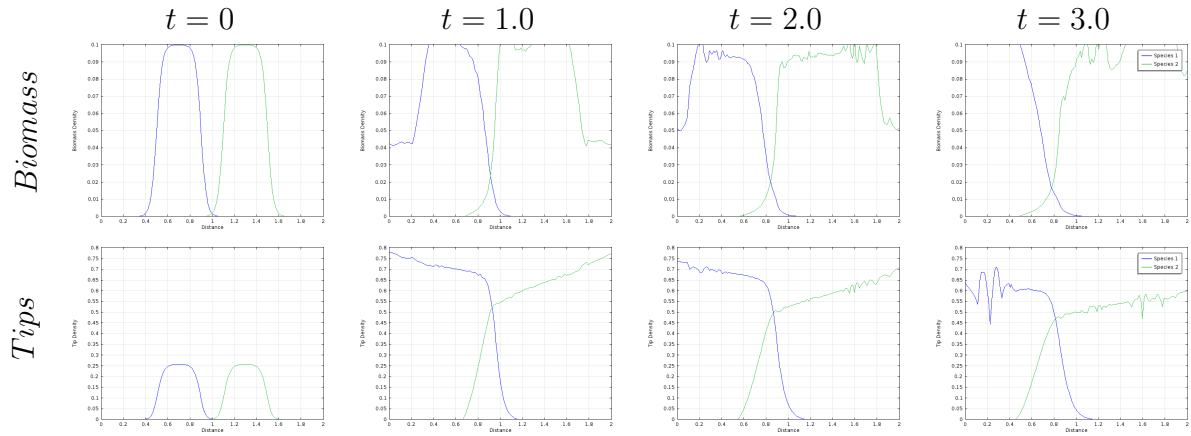


**Figure 5.30:** Cross section of the solutions to equations (5.16) with initial data (5.17) and parameter values from Table 5.2 with  $s_{e0} = 1$ ,  $A = 1000$  and  $B = 300$ . The right biomass can be seen to displace the left biomass at a faster rate. [For a movie of these plots please see external folder labelled:- Comsol - Movie\_files - Fig-5.30]

Figure 5.30 shows that in a nutrient rich environment the dominant species is able to dominate its competitor at a faster speed than in a nutrient scarce environment. Interestingly, displacement can be seen to occur initially then coexistence seems to form on the hyphae plot (see movie files *Fig-5.29* and *Fig-5.30*). This type of behaviour (i.e. changes in state) was represented in the parameter space diagram (Figure 4.11 in Chapter 4) where it was predicted that varying substrate concentrations alters the outcome of competition. Thus, here we observe that as the substrate concentration depletes the states also change i.e. coexistence to displacement.

### 5.3.3 Competitive and block nutrient

In the previous sections it was assumed that resources were well mixed in the domain. In fungal habitats the resources are often not homogeneously distributed. While in experimental studies care is taken to mix the substrate, there could arise a situation where the nutrients are not well mixed or over time form amalgamations in certain regions of the Petri dish or even be deliberately introduced. In this section we will investigate a scenario where the less dominant fungal species grows on a highly concentrated region of the Petri dish. To represent this we will use

the following

$$s_e(x, y, 0) = \begin{cases} \hat{s}_{e0} \frac{(1 - \tanh(\phi(r-R)))}{2}, & \text{if } r < R, \\ s_{e0}, & \text{otherwise,} \end{cases} \quad (5.18)$$

where  $r$ ,  $R$  and  $M$  have been previously defined. Here the parameter  $\hat{s}_{e0}$  represents the concentration of external substrate in the domain at the biomass on the left hand side where  $s_{e0}$  is the concentration elsewhere. The parameter values used are from Table 5.2 unless stated otherwise. Thus, we will solve equations (5.16) with initial conditions in (5.17) using parameter values from Table 5.2 and initial data (5.18) by setting  $\hat{s}_{e0} = 1$  and  $s_{e0} = 0.5$ ,  $A = 1000$  and  $B = 300$  (Figure 5.31).

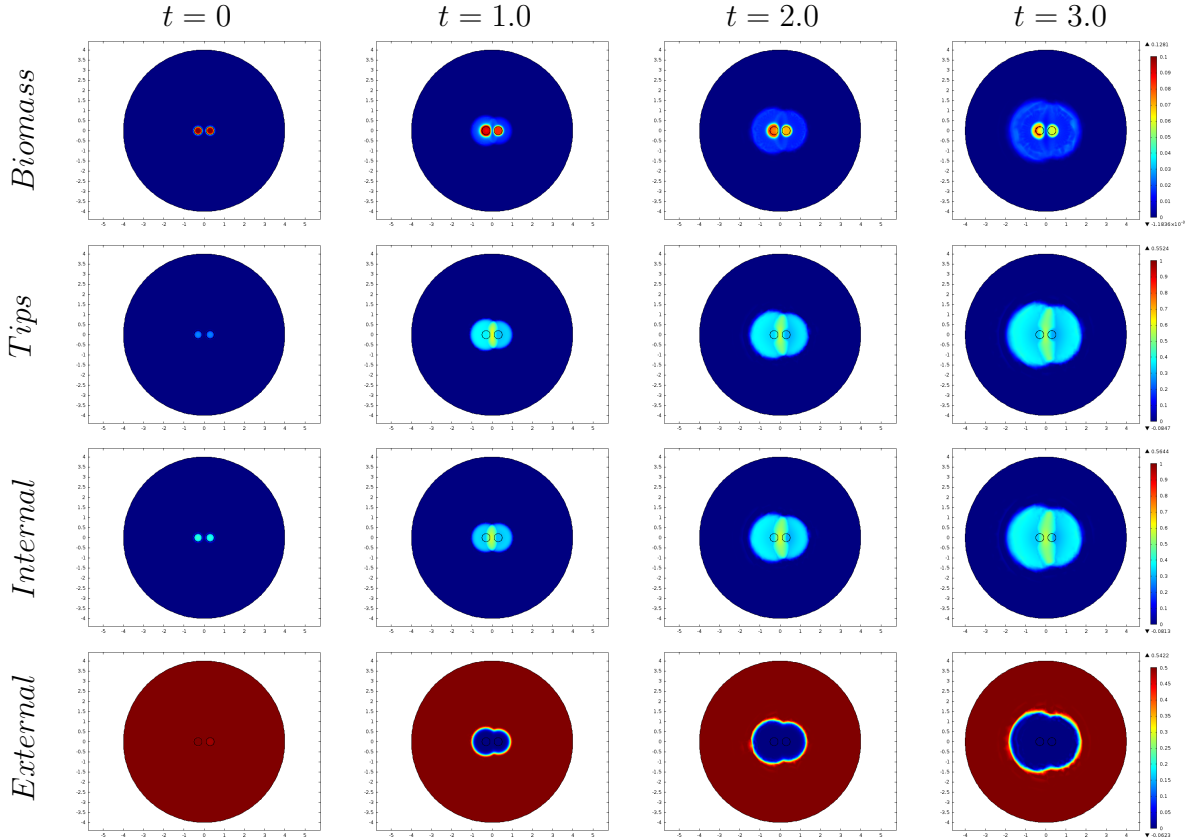


**Figure 5.31:** 2d representation of the solutions to equations (5.16) with initial data (5.17) and (5.18) and parameter values from Table 5.2 with  $\hat{s}_{e0} = 1$ ,  $s_{e0} = 0.5$ ,  $A = 1000$  and  $B = 300$ . The fungi seem to be in a state of deadlock. [For a movie of these plots please see external folder labelled:- Comsol - Movie\_files - Fig\_5.31]

Figure 5.31 shows that despite the biomass on the left being less dominant,

having access to a nutrient-rich patch provides it with the ability to defend its territory and resist displacement by the superior competitor starting on the right (see movie files *Fig\_5.31* and *Fig\_5.32*). However, as the resources deplete biomass on the right starts to displace the biomass on the left. Figure 5.32 shows a cross sectional plot of this more clearly illustrating the delayed displacement.

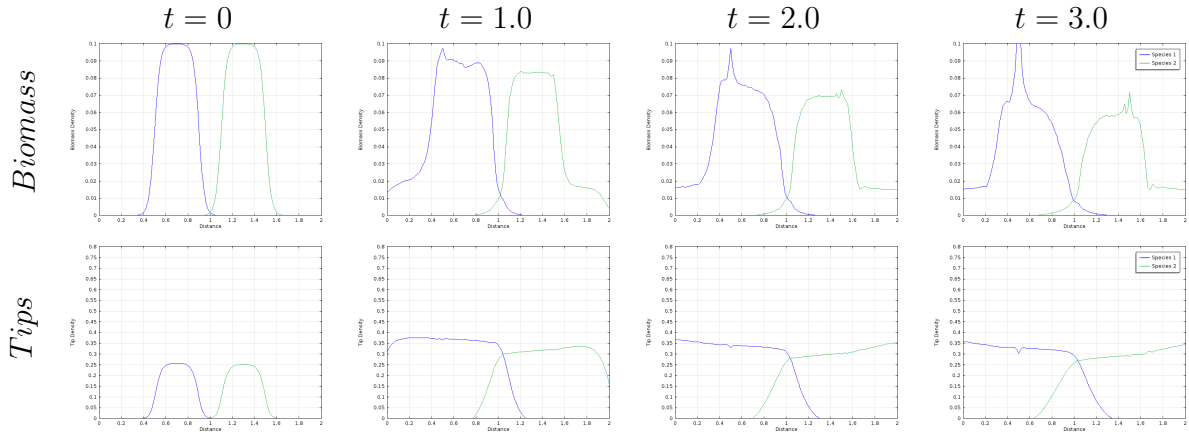


**Figure 5.32:** *Cross sectional representation of the solutions to equations (5.16) with initial data (5.17) and (5.18) and parameter values from Table 5.2 with  $\hat{s}_{e0} = 1$ ,  $s_{e0} = 0.5$ ,  $A = 1000$  and  $B = 300$ . The fungi seem to be in a state of deadlock. [For a movie of these plots please see external folder labelled:- Comsol - Movie\_files - Fig\_5.32]*

The observations in this section are consistent with the observations seen earlier; having access to nutrients can determine the outcome of competition. In the context of agriculture, manipulating the resource location may provide an alternative way to deal with an antagonist. Allocating different patches of suitable resources around the perimeter of an antagonist's colony may lead to hindering its growth and render it less effective or at least suppress its adverse effects. Even if the biomass does not have a competitive advantage over its rival, the techniques shown in this section may still optimise its utilisation.

## 5.4 Conclusion

The mathematical models explored in this chapter resulted in interesting simulations capturing complex intermingling behaviours often observed in the experimental study of fungal interactions. The analysis has suggested many potential applications discussed above.

The results of the simulations here are consistent with the one dimensional analysis carried out in Chapter 4. However, the two dimensional models developed have shown to be very effective in depicting the spatial component of fungal growth observed in laboratory experiments, which was lacking in the one-dimensional models; for example the complete surrounding of one biomass by a rival (Figure 5.25). The primary observation obtained from the analysis in this chapter was that the variation of resources accessible to fungal species have a significant influence on the outcome of competition. The model equations formulated were used to investigate various scenarios involving resource distributions; namely, the outcome of competition with distinct resources, perpetual availability of distinct resources, resource availability at intervals, distinct resources spread across the domain and a single resource on a unified domain. The prevailing findings of the analysis was that access to greater concentration of resources is sufficient to gain advantage in fungal interactions.

Fungi are abundantly used in the field of agriculture, bio-remediation and bio-technology. Thus the techniques and the analysis seen here can provide benefits to the respective fields. Primarily, by determining the critical nutrient concentrations required to obtain a sought after outcome will provide greater control over the desired outcome.

The set of equations formulated in this work are highly versatile in modelling various fungal behaviours and have not been fully exploited. For example the model can easily incorporate the effects that *collembola* (an insect species that graze on hyphae) have on fungal competition. The simulations will be of the form observed in experiments similar to Rotheray et al. (2010). This feature can be incorporated in our model via changing the proportionality constant term  $E$  and  $F$  to a function related to the damage collembola is causing to the host fungal species. This would be a starting point which can then be extended further by incorporating another simple equation modelling the population dynamics of the insects.

Also, only competition between two fungal species of the same kind was explored. The model can be used to simulate other fungal morphologies stated in Chapter 2 that will require using different diffusion rates, uptake costs and tip velocities. The model equations can be converted easily to higher dimensional analysis for a three-dimensional model if desired. Another interesting feature would be to model multiple species in a single domain as seen in experimental

studies referenced in Chapter 4. This would open the door for new research exploring interactions between multiple species and could extend the interesting work by Halley et al. (1994), Davidson et al. (1996) and Falconer et al. (2011).

In the following chapter we will apply the above modelling techniques to consider the interaction between a fungus and a toxin.



## Chapter 6

# Fungal Growth in Toxic Environments

The industrial past has left a legacy of landscapes polluted by various heavy metals and toxins that have resulted in vast swathes of barren land unsuitable for agricultural or habitable conditions. Certain fungi have the ability to extract various toxic materials such as mercury, arsenic, copper and cadmium from the environment and thus remediate such landscapes. For example studies such as Gadd (1993); Fomina et al. (2000, 2003); Srivastava et al. (2011); Ho-Man et al. (2013); Kurniati et al. (2014) and Stamets (2014) have shown great potential of using fungi for bioremediation purposes. Furthermore mycoremediation studies have also demonstrated the applicability of mushrooms to remove oil spillage from lakes and sea water (Stamets, 2014). In this chapter we will investigate, through mathematical modelling, how a fungus behaves in response to toxic metals, which is crucial in such applications.

### 6.1 Motivation

The behaviour of fungi reacting to adverse conditions in a heterogeneous environment has been investigated both through experiments (Gadd, 1993; Fomina et al., 2000, 2003; Gadd, 2010) and mathematical modelling (Boswell et al., 2007; Orlishevskya and Zhdanova, 2009). In the area of bio-remediation, fungi have been introduced to assist in the removal of toxic materials as an alternative and in addition to traditional methods (Gupta and Shrivastava, 2014). There have been various studies and observations of fungal colonies interacting with toxic sub-

stances but we will primarily focus our attention on work published by Fomina et al. (2000, 2003).

Fomina et al. (2000) investigated the strong tropic behaviour of fungal hyphae. In particular, hyphae show negative chemotropic responses to some toxic metals (by moving away from regions augmented with Copper (Cu) and Cadmium (Cd)). These experiments were carried out in a simple agar tile system. Two square tiles ( $10 \times 10 \times 3$  mm) of agar were placed in a sterile 9 cm diameter Petri dish with a 2 cm gap between the tiles. The control tile (metal free) contained  $30 \text{ g l}^{-1}$  of sucrose along with other chemicals. The control tile was inoculated by the fungal species. The metal containing tile had varying levels of sucrose between ( $1 - 30 \text{ g l}^{-1}$ ) and either Cu or Cd chloride at concentrations of 0 or 5 mM.

The initial experiments consisted of both the agar tiles containing equal amounts of sucrose concentrations ( $30 \text{ g l}^{-1}$ ) and varying levels of toxic metal chloride between (2 and 5 mM). The key observation of the study was the behaviour of leading hyphae of the colony turning away from the toxic source and the greater the toxicity levels, the more pronounced was the chemotropic response.

The latter experiments consisted of varying the levels of sucrose between ( $1$  and  $15 \text{ g l}^{-1}$ ) and the metal chloride (0 to 2 mM) in the toxic domain. The key observation was that the differing levels of sucrose affected the degree of the negative chemotropic behaviour of the fungal hyphae. When the nutrient concentration was low and the toxic concentration high, there was a greater negative chemotropic behaviour and as the nutrient was increased the magnitude of the chemotropic behaviour reduced.

The key finding of Fomina et al. (2003) was the ability of fungi to penetrate through a toxic domain of various concentrations with varying amounts of nutrients. The experiments were carried out on a Petri dish but this time with three agar tiles. The first (control) and the third (target) tile contained  $30 \text{ g l}^{-1}$  of sucrose at the start of each realisation and the second (toxic metal) tile contained varying levels of metal concentration between (0 and 2 mM) and sucrose between ( $1$  and  $30 \text{ g l}^{-1}$ ).

The main findings of the study related to fungal morphology, chemotropic behaviour and penetration in adverse conditions. Our focus will solely be on the penetration of the toxic domain aspect of the study.

In Figure 6.1 it can be seen that the penetration of hyphae into the metal domain was followed by the formation of very dense mycelial bush on the border

between the gap and the toxic metal tile. This was common for nutrient concentrations up to  $30 \text{ g l}^{-1}$ . The density of the hyphae at the edge of the tiles increased with both the nutrient concentration and the amount of toxin. This may be due to the larger quantity of toxic chloride diffusing faster to the edge of the tile and thus as more chloride is added the further the hyphae is pushed back. It was also found that the fungi were able to penetrate the metal tile at low toxic levels and reach the target tile.

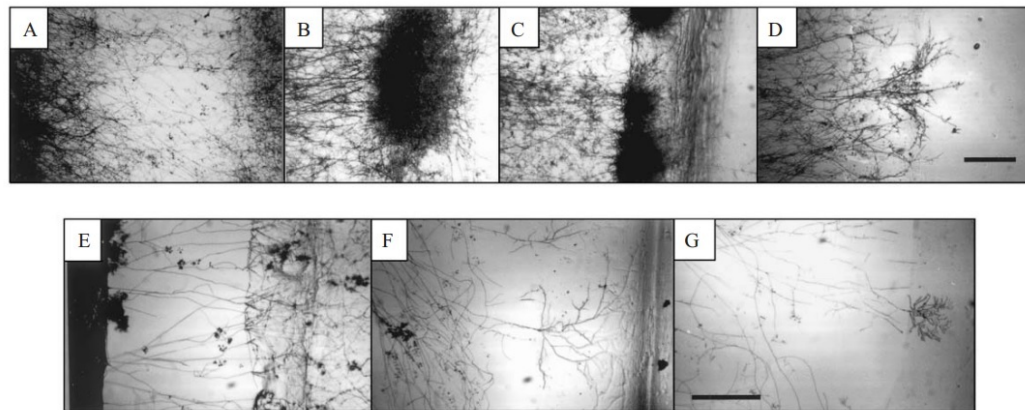


**Figure 6.1:** (A - D) show *Clonostachys rosea* growing from the left tile to the metal tile which contain  $5 \text{ g l}^{-1}$  of sucrose and the following quantity of toxic metal; A) Control no toxic, B)  $0.5 \text{ mM}$ , C)  $1 \text{ mM}$  and D)  $2 \text{ mM}$ . (E - G) show *Trichoderma virens* growing from the left tile to the metal tile which contain  $1 \text{ g l}^{-1}$  of sucrose and the following quantity of toxic metal; E) Control no toxic, F)  $1 \text{ mM}$  and G)  $2 \text{ mM}$  (Fomina et al., 2003).

In Figure 6.2 the fungal species *T. virens* can be seen to be growing on a toxic domain at low sucrose concentration between ( $1$  and  $5 \text{ g l}^{-1}$ ). The authors' comments on this aspect was, 'Fungal mycelia can vary the balance between processes of exploration and assimilation, conservation and redistribution of resources and so respond efficiently to changes in local circumstances'. However, it is still unclear why local circumstances happen in some regions of the toxic domains and not others and why they do not arise when the toxic concentration is high. One possible explanation we conjecture in this thesis is that the local circumstance could refer to the non-uniform mixing of the nutrient with the toxic chloride or diffusion altering the concentrations of the ratio of nutrient and toxic, specifically the plethora of branching could correspond to a region where, through chance alone, there is little or no toxin. As fungi respond to their environment, some tips

diffuse through the high toxic area of the tile might approach a patch where the toxicity is low and nutrient content high, thus branching and exploring may take place in this new area. This could be a possible explanation of the behaviour seen in Figure 6.2.

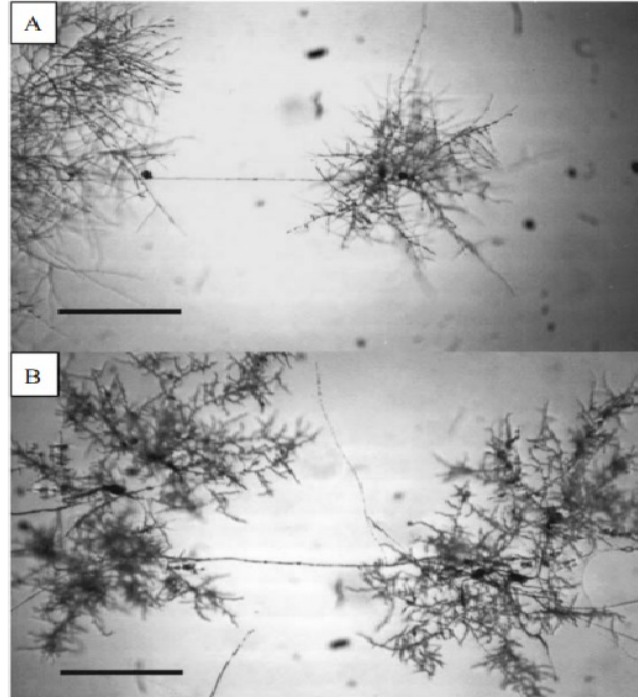


**Figure 6.2:** (A and B) show *T.virens* growing from the left tile and inoculating on the metal tile. The behaviour was also observed with varying levels of sucrose ( $1 - 5 \text{ g l}^{-1}$ ) and copper ( $1 - 5 \text{ mM}$ ) on the metal tile (Fomina et al., 2003).

Thus we aim to investigate and provide some insights into the behaviours observed by Fomina et al. (2000, 2003) using numerical simulations.

We begin by extending our system of equations (3.48) from Chapter 3 (Section 3.1.5) to depict the effects of toxicity on the hyphal density at the periphery of a fungal colony across a one dimensional geometry and carry out some basic analysis. A one dimensional representation is a reasonable approach to modelling the dynamics of biomass and toxic interaction, due to its ability to capture the sought behaviour that occur at the periphery without the need for an over complicated model. We then further extend the model into two dimensions to capture typical behaviour obtained from experimental observations and thus carry out some analysis similar to that of Fomina et al. (2000, 2003).

## 6.2 One dimensional model of fungal toxic interaction

In this section a simple model is formulated to represent a species of fungi interacting with toxic material. Our default choice of the specific phenotype is that of the FHD phenotype in equations (3.48), which is repeated here for convenience where  $\rho$  denotes the hyphal density and  $n$  represents the hyphal tip density:

$$\begin{aligned}\frac{\partial \rho}{\partial t} &= nv - \gamma \rho, \\ \frac{\partial n}{\partial t} &= -\frac{\partial(nv)}{\partial x} + \rho(\alpha - \beta n).\end{aligned}$$

Suppose there is a toxic material whose density at position  $x$  is denoted by  $T = T(x)$  and does not change over time (for example, the toxic compound considered in Fomina et al. (2000, 2003) only existed on the metal tile, thus on a one dimensional plane it is sufficient to assume it is stationary). Since hyphal tips divert away from toxic materials (Fomina et al., 2003) we introduce a corresponding flux  $-n\kappa \frac{\partial T}{\partial x}$  into the model equations where  $\kappa$  represents the strength of the repulsion. Thus our system of equations becomes

$$\begin{aligned}\frac{\partial \rho}{\partial t} &= \left| nv - n\kappa \frac{\partial T}{\partial x} \right| - \gamma \rho, \\ \frac{\partial n}{\partial t} &= -\frac{\partial}{\partial x} \left( nv - n\kappa \frac{\partial T}{\partial x} \right) + \rho(\alpha - \beta n),\end{aligned}\tag{6.1}$$

where the total hyphal length created per unit time is the absolute value of the tip flux (consistent with that seen for the model in Chapter 5). Notice that these equations do not explicitly model the long term remediation of the toxic materials but instead the short-term response of the biomass to the toxins.

### 6.2.1 Numerical simulation

Before constructing algebraic solutions to equations (6.1), we numerically integrate the system in COMSOL using a ‘1d time dependent model’ for a ‘coefficient form’ type PDE over a spatial domain  $[0, 25]$ . Zero flux boundary conditions have been assumed. We have used similar initial conditions mentioned in previous

analysis from equation (3.34) for  $\rho$  and  $n$ , respectively i.e.

$$\rho(x, 0) = \frac{1}{2}(1 - \tanh(\theta x)), \quad n(x, 0) = \frac{1}{2}(1 - \tanh(\phi x)),$$

to ensure their derivatives are defined everywhere and can be easily computed. For convenience we set  $\alpha = \beta = \gamma = \theta = \phi = v = 1$  and for illustration take  $T(x) = \frac{x^2}{100}$  for a variable spatial gradient and  $\kappa = 2$ .

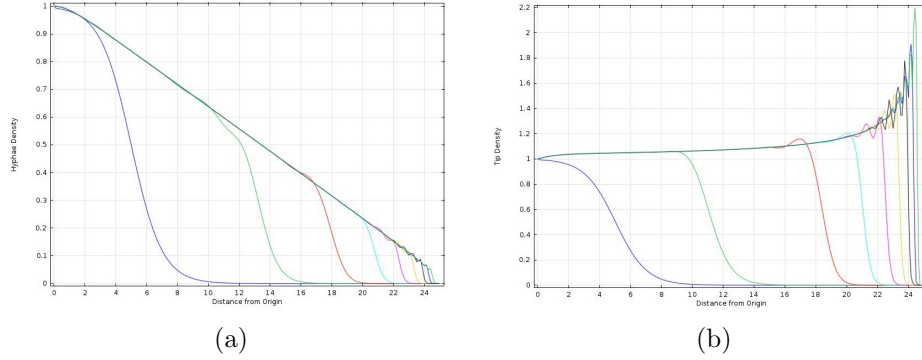


**Figure 6.3:** (a) Depicts the hyphal density obtained from (6.1) and (b) depicts the tip density increasing around  $x=25$  (critical value) due to the presence of toxic substances shown at times  $t=0, 10, 20, 30, 40, 50, 60$  and  $80$  represented via different colours and propagating from left to right.

From Figures 6.3(a) and 6.3(b) there is a propagating wave of biomass and tips that reduces its speed as it approaches a critical value of  $x = \frac{50v}{\kappa}$  since the corresponding flux is zero. The hyphal density declines to zero at this critical value and the hyphal tips cease to propagate.

### 6.2.2 Analysis of immobile toxicity

If we assume the toxic substrate is immobile (or at least changes more slowly than the growth of the model biomass), the system of equations (6.1) has a closed form solution for certain forms of  $T$ . Thus the stationary distribution satisfies

$$0 = |nv - n\kappa T_x| - \gamma\rho \quad (6.2)$$

$$0 = -\frac{\partial}{\partial x}(nv - n\kappa T_x) + \rho(\alpha - \beta n). \quad (6.3)$$

From the first equation (6.2) we obtain two solutions

$$n = \pm \frac{\gamma \rho}{v - \kappa T_x}. \quad (6.4)$$

We take the positive solution from equation (6.4) when referred henceforth. Substituting the solution into equation (6.3) and rearranging we obtain

$$\gamma \frac{\partial \rho}{\partial x} - \alpha \rho = -\frac{\beta \gamma \rho^2}{v - \kappa T_x}. \quad (6.5)$$

Equation (6.5) is a first order Bernoulli equation. Thus upon setting  $w = \rho^{-1}$  we obtain

$$\frac{dw}{dx} + \frac{\alpha}{\gamma} w = \frac{\beta}{v - \kappa T_x} \implies \frac{d}{dx} (e^{\frac{\alpha}{\gamma} x} w) = \frac{\beta e^{\frac{\alpha}{\gamma} x}}{v - \kappa T_x}. \quad (6.6)$$

Integrating both sides, we obtain

$$w = \beta e^{-\frac{\alpha}{\gamma} x} \int \frac{e^{\frac{\alpha}{\gamma} x}}{v - \kappa T_x} dx + c e^{-\frac{\alpha}{\gamma} x}, \quad (6.7)$$

where  $c$  is a constant of integration. Some particularly nice solutions can be obtained for certain functional forms of  $T(x)$ . Some examples are shown below

$$T_1(x) = x \text{ then } u_1 = v - \kappa \implies \rho^{-1} = c e^{-\frac{\alpha}{\gamma} x} + \frac{\beta \gamma}{\alpha(v - \kappa)}, \quad (6.8)$$

$$\begin{aligned} T_2(x) &= \frac{x^2}{2} \text{ then } u_2 = v - \kappa x \implies \\ \rho^{-1} &= c e^{-\frac{\alpha}{\gamma} x} + \frac{\beta}{\kappa} e^{\left(\frac{\alpha u_2}{\kappa \gamma}\right)} \text{Ei} \left( \frac{\alpha}{\gamma \kappa} u_2 \right), \end{aligned} \quad (6.9)$$

$$\begin{aligned} T_3(x) &= e^{\frac{\alpha x}{\gamma}} \text{ then } u_3 = v - \frac{\alpha \kappa}{\gamma} e^{\frac{\alpha x}{\gamma}} \implies \\ \rho^{-1} &= c e^{-\frac{\alpha}{\gamma} x} - \frac{\beta \gamma^2}{\alpha^2 \kappa} e^{(-\frac{\alpha}{\gamma} x)} \ln(u_3), \end{aligned} \quad (6.10)$$

where Ei is the exponential integral function ( $\text{Ei}(x) = \int_{-\infty}^x \frac{e^u}{u} du$  for  $x > 0$ ).

Illustrative solutions of equations (6.4) and (6.9) using parameter values  $\alpha = \beta = \gamma = v = 1$  and  $\kappa = \frac{1}{25}$  are shown in Figures 6.4(a) and 6.4(b).

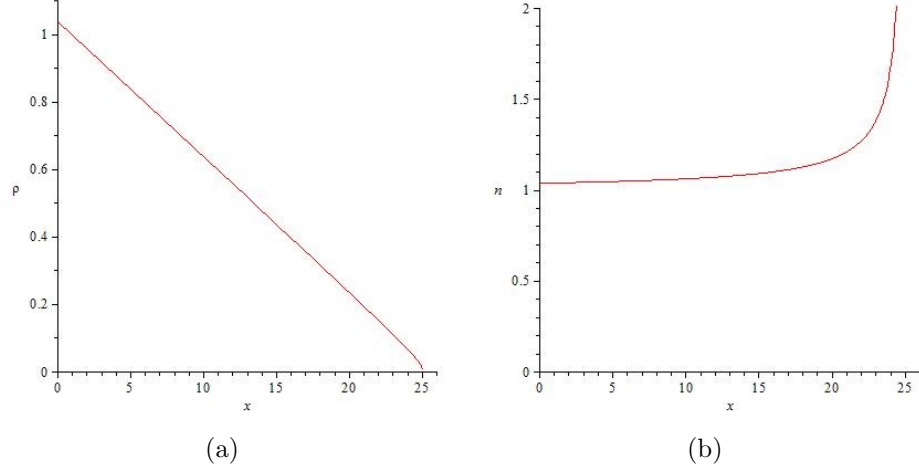


**Figure 6.4:** (a) Depicts steady state hyphal density from (6.9) and (b) depicts the steady state of tip density from (6.4) which blows up at  $T_x = \frac{v}{\kappa}$  for parameters  $\alpha = \beta = \gamma = v = 1$ ,  $\kappa = \frac{1}{25}$  and  $T = \frac{x^2}{2}$ .

The steady state distributions predicted by the above analysis is in accordance with experimental observations and numerical integration of equations (6.1) (Figure 6.3(a)). From Figure 6.4(a) we see that the solutions approach a critical value of  $T_x = \frac{v}{\kappa}$  beyond which the solution is not defined (further growth is impossible). The hyphal density declines to zero at this critical value whereas the hyphal tip density increases due to the singularity in equation (6.3). The solutions capture the general behaviour observed in experiments as described in the previous section i.e. a cessation of colony expansion. However the tip density in reality will eventually die in a nutrient limited environment and will not continue to grow to infinity. The build up of tips and decline in hyphal densities are types of behaviour observed when a species of fungi interacts with an antagonistic competitor or if it encounters an adverse material in the environment (i.e. toxic substance); there is a build up of hyphal tips (sclerotium) on the periphery of the colony to form a barrage to protect the colony (see Figure 4.1).

### 6.2.3 Conclusion from basic modelling

Our model captures the intrinsic behaviour of a fungal colony exploring new space until it reaches a critical toxic concentration gradient that it cannot penetrate. This leads to the accumulation of tips forming near the critical toxic gradient of



fungi (i.e.  $\frac{v}{k}$ ) and the steady depletion of hyphal density. This model may be an oversimplification of the actual biological characteristics of fungi, but it captures the behaviour seen in experiments (Fomina et al. (2003) and references therein): with a low nutrient concentration and high metal toxicity concentrations, the fungi *Trichoderma virens* produced negative chemotaxis behaviour and high tip accumulation in the vicinity of the toxic metals and the density of its mycelium became less dense. A similar behaviour was observed for the fungi *Clonostachys rosea*.

In experiments, nutrients play a key role in the functionality of fungi (Fomina et al., 2003; Goyal et al., 2013). It was found in the study carried out by Fomina et al. (2003) that by adjusting the nutrient levels with varying levels of toxicity of metals fungi were able to move away from the hostile zone and continue to propagate. The model we have proposed above captures some aspects of that experiment. One is the mobility of hyphal tips of a fungal species moving towards an immobile toxic metal source and the other is the decrease in the hyphal density of the fungi as its tips approach the hostile material (see Fomina et al. (2003) and Figure 6.4(a)). We can also see the accumulation of hyphal tips (representing sclerotia) at the interaction zone which can be compared to Figure 6.4(b) but whether they continue to accumulate and form a barrier to protect the colony from contamination, we cannot infer from the given experimental data. These barriers were also observed by Boddy (2000) where fungi formed ‘barrages’ to protect the colony from invasive species.

The investigations seen in this chapter thus far have been restricted to a one dimensional setting. A one dimensional model cannot fully capture the spatial dynamics or the impact toxic materials have on the fungal mycelium, seen in laboratory studies. The influence of resources has also not been explicitly modelled to avoid formulating a complex model. It was seen in previous chapters that resources have a crucial role on fungal competition and their influence on fungi’s ability to deal with adverse conditions was stressed by Fomina et al. (2003).

Thus we now formulate a two dimensional model to incorporate the aforementioned fungal interaction with toxic substance via using the system of equations (5.4) introduced in Chapter 5. The model will be used to simulate complex interactions between fungi and toxic contaminated sources in planar environments, thus providing comparisons between laboratory experiments.

## 6.3 Two dimensional model of fungal growth in toxic environments

The study by Fomina et al. (2000) explored negative chemotropic behaviour of individual hyphae. In our study we will not be observing the behaviour of individual hyphae but rather the density of the biomass as a whole. In particular, we simulate the different densities of hyphae and tips in response to toxic metals. Nonetheless, the negative chemotropic behaviour of hyphal tips is incorporated in the model equations by a suitable revision to the corresponding flux term.

In order to simulate the studies we will use the mixed hyperbolic-parabolic type equations (5.4) tailored with the toxicity component to take into account the interaction of fungi and toxic metals, i.e.

$$\begin{aligned}
\frac{\partial \rho}{\partial t} &= |vs_i n \nabla \rho + D_n s_i \nabla n + \kappa s_i n \nabla T| - d_\rho \rho, \\
\frac{\partial \rho'}{\partial t} &= d_\rho \rho - d_i \rho', \\
\frac{\partial n}{\partial t} &= \nabla \cdot (vs_i n \nabla \rho + D_n s_i \nabla n + \kappa s_i n \nabla T) + \alpha s_i \rho - \beta n \rho, \\
\frac{\partial s_i}{\partial t} &= \nabla \cdot (D_i \rho \nabla s_i - D_a \rho s_i \nabla n) + c_1 s_i \rho s_e - c_2 |vs_i n \nabla \rho + D_n s_i \nabla n + \kappa s_i n \nabla T| \\
&\quad - c_4 |D_a \rho s_i \nabla n|, \\
\frac{\partial s_e}{\partial t} &= D_e \nabla^2 s_e - c_3 s_i \rho s_e, \\
\frac{\partial T}{\partial t} &= D_T \nabla^2 T,
\end{aligned} \tag{6.11}$$

where  $T$  represents the toxic compound concentration (not to be confused with the standard symbol used for dimensions representing time  $T$  (see Table 6.1) and  $D_T$  the coefficient of diffusion of the substance. The  $\kappa$  parameter is a simple representation of the sensitivity to the toxicity or the repeller term for the fungi. Thus the term  $-\kappa s_i n \nabla T$  represents the movement of the tips in respect to (the gradient of) the toxic substance.

The system of equations (6.11) is solved numerically on a domain satisfying zero flux boundary conditions using various initial conditions that will be shown accordingly prior to each simulation.

### 6.3.1 Fomina *et al.* (2000) revisited

In this section we will simulate the experiments seen in Fomina et al. (2000) via numerically integrating model equations (6.11) in COMSOL. The initial data is chosen to resemble the experimental setup of Fomina et al. (2000). For the purpose of focusing on the key interactions occurring between fungal biomass and toxic materials, we will rescale the dimensions of the boundaries for the simulation to that used in Chapter 5. The square tiles will be depicted as  $0.2 \times 0.2$  cm dimensions instead of  $1 \times 1$  cm. Hence the domain comprises of one circular region of radius 2 cm representing a Petri dish containing two ‘square’ tiles; one “tile” labelled ‘Source’ ( $u_S$ ) laced with nutrients, on which an initial inoculum is placed and the other “tile” labelled ‘Pollutant’ ( $u_P$ ) with initially only nutrient and toxic compounds (schematic representation is shown in Figure 6.5).

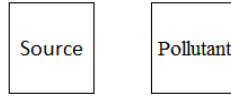


**Figure 6.5:** *Initial configuration used for the simulations.*

The parameter values used are given in Table 6.1. All parameters will be kept constant throughout the simulations and only the initial data for the external resources and toxic concentration will be adjusted according to the experiments.

| Initial data/Parameters | Rescaled Value | Dimensions                 | Description                              |
|-------------------------|----------------|----------------------------|--|
| $v$                     | 0.5            | $L^5 T^{-1} N^{-1}$        | Directed tip velocity                    |
| $d_\rho$                | 0.5            | $T^{-1}$                   | Hyphal inactivation rate                 |
| $d_i$                   | 0              | $T^{-1}$                   | Inactive hyphae loss rate                |
| $\alpha$                | $10^3$         | $L^{-1} T^{-1} N^{-1}$     | Branching rate                           |
| $\beta$                 | $10^4$         | $LT^{-1}$                  | Anastomosis rate                         |
| $c_1$                   | 900            | $L^3 T^{-1} N^{-1}$        | Uptake rate of external substrate        |
| $c_2$                   | 1              | $NL^{-1}$                  | Growth cost                              |
| $c_3$                   | $10^3$         | $L^3 T^{-1} N^{-1}$        | Uptake of external substrate             |
| $c_4$                   | $10^{-8}$      | $L^{-1}$                   | Active translocation cost                |
| $D_n$                   | 0.1            | $L^4 T^{-1} N^{-1}$        | Tip avoidance cost                       |
| $D_i$                   | 10             | $L^3 T^{-1}$               | Internal substrate diffusion coefficient |
| $D_a$                   | 10             | $L^5 T^{-1}$               | Active translocation rate                |
| $D_e$                   | $10^{-4}$      | $L^2 T^{-1}$               | External substrate diffusion coefficient |
| $D_T$                   | $10^{-4}$      | $L^2 T^{-1}$               | Toxic substance diffusion coefficient    |
| $R$                     | 0.1            | $L$                        | Radius of active hyphal plug             |
| $\kappa$                | 1              | $L^6 T^{-1} N^{-1} M^{-1}$ | Repellor strength                        |
| $\phi$                  | 20             | -                          | Scalar constant of initial data          |
| $\rho_0$                | 0.1            | $L^{-1}$                   | Initial active hyphal density            |
| $\rho'_0$               | 0              | $L^{-1}$                   | Initial inactive hyphal density          |
| $n_0$                   | 0.1            | $L^{-2}$                   | Initial tip density                      |
| $s_{i0}$                | 0.4            | $NL^{-2}$                  | Initial internal substrate               |
| $s_{e0}$                | 0.5            | $NL^{-2}$                  | External substrate                       |
| $T_0$                   | 0              | $ML^{-2}$                  | Toxic concentration                      |

**Table 6.1:** *The initial data and default parameter values used to solve model equations (6.11). The parameter values used for fungal growth are from the calibration experiments carried out by Boswell et al. (2003b) where known, while reasonable assumed values have been adopted elsewhere based on known similar processes.*

### 6.3.1.1 Biomass expansion in a toxic free environment

We begin with simulating a default case where it is assumed that there is no toxic material on the Pollutant “tile”. This case can be thought of as a control run. Prior to investigation the initial conditions must be defined. For the Source “tile”, the following initial data are taken

$$\begin{aligned}
\frac{\rho(x, y, 0)}{\rho_0} &= \frac{n(x, y, 0)}{n_0} = \frac{s_i(x, y, 0)}{s_{i0}} = \frac{s_e(x, y, 0)}{s_{e0}} = \frac{1 - \tanh(\phi(r - R))}{2}, \\
\rho'(x, y, 0) &= \rho'_0, \\
T(x, y, 0) &= 0,
\end{aligned} \tag{6.12}$$

where  $\phi$  is a scalar constant,  $R = 0.1$  corresponds to the radius of the fungal inoculum where we have assumed they are circular in shape and

$$r = \sqrt{(x + M)^2 + y^2}. \quad (6.13)$$

We set  $M = 0.2$ , where  $(-M, 0)$  is the centre of the initial mycelium. For the Pollutant “tile”,

$$\begin{aligned} \rho(x, y, 0) &= \rho'(x, y, 0) = n(x, y, 0) = s_i(x, y, 0) = 0, \\ s_e(x, y, 0) &= s_{e0}, \\ T(x, y, 0) &= T_0. \end{aligned} \quad (6.14)$$

Thus the initial profiles are identical to that seen in previous chapters. These initial conditions for hyphae, tips and internal substrate therefore correspond to the initial plug of mycelium placed on the Petri dish at  $(-M, 0)$  of radius  $R$  respectively which includes the Source “tile” ( $u_S$ ). Henceforth, for convenience, initial data in each simulation (Table 6.1) for each “tile” will be denoted using the notation,  $u_{\text{tile}} = (s_{e0}, T_0)$

The model equations (6.11) were solved in COMSOL with initial data in equations (6.12), (6.14) and zero flux boundary conditions using the default parameters in Table 6.1 ( $u_S = (0.5, 0)$  and  $u_P = (0.5, 0)$ ). Using similar techniques to those in Chapter 5, typical results are shown in Figure 6.6.

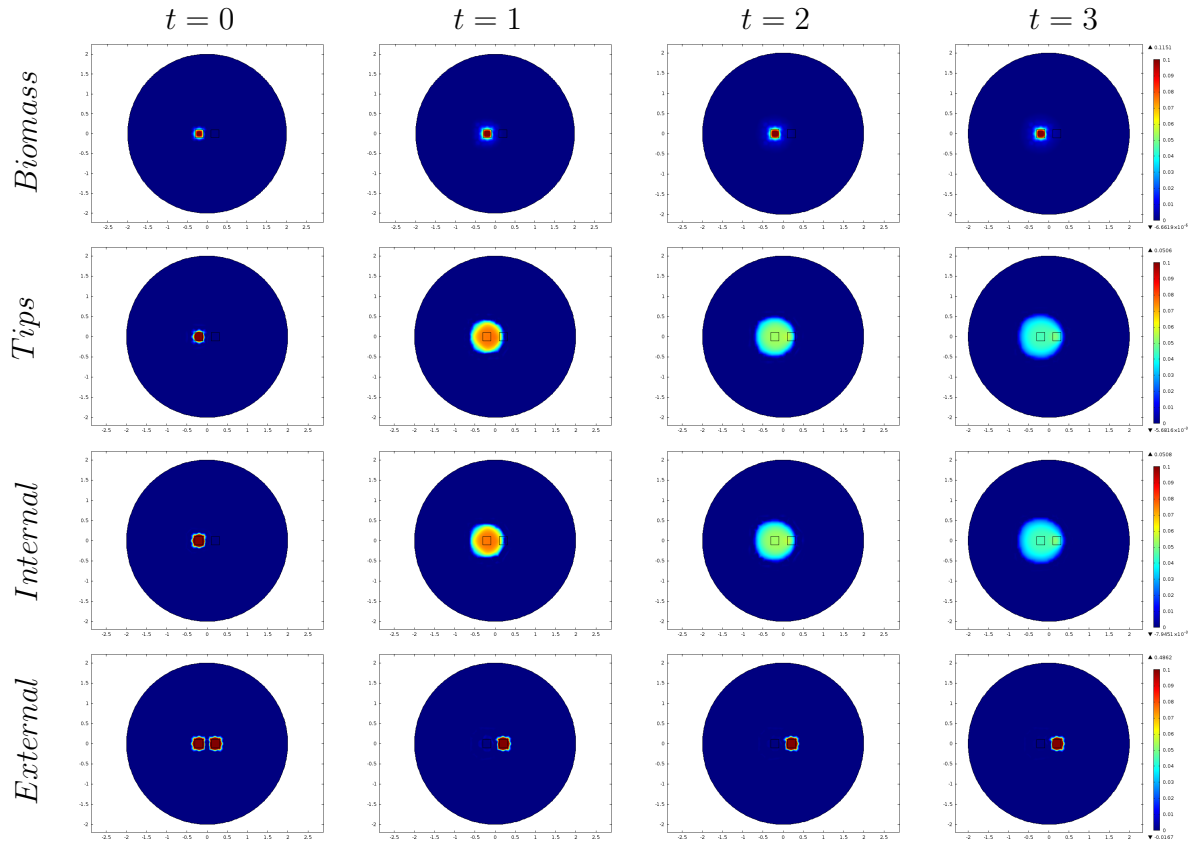


**Figure 6.6:** *2d representation of the solutions to equations (6.11) with initial data (6.12) and (6.14) using parameter values from Table 6.1 with  $u_s = (0.5, 0)$  and  $u_p = (0.5, 0)$ . A uniform proliferation can be observed. [For a movie of these plots please see external Folder labelled: Comsol - Movie\_files - Toxic - 2Tile - Fig\_6.6]*

In the absence of any toxic material the biomass proliferates in a radially symmetric manner until it finds a new source of nutrients where it begins to colonise and thus expand further. The biomass expands until all of the substrate is depleted and eventually dies out (data not shown). For improved exposition, Figure 6.7 displays a cross sectional plot of the total hyphal biomass, tip density and external resource as introduced in previous chapters.

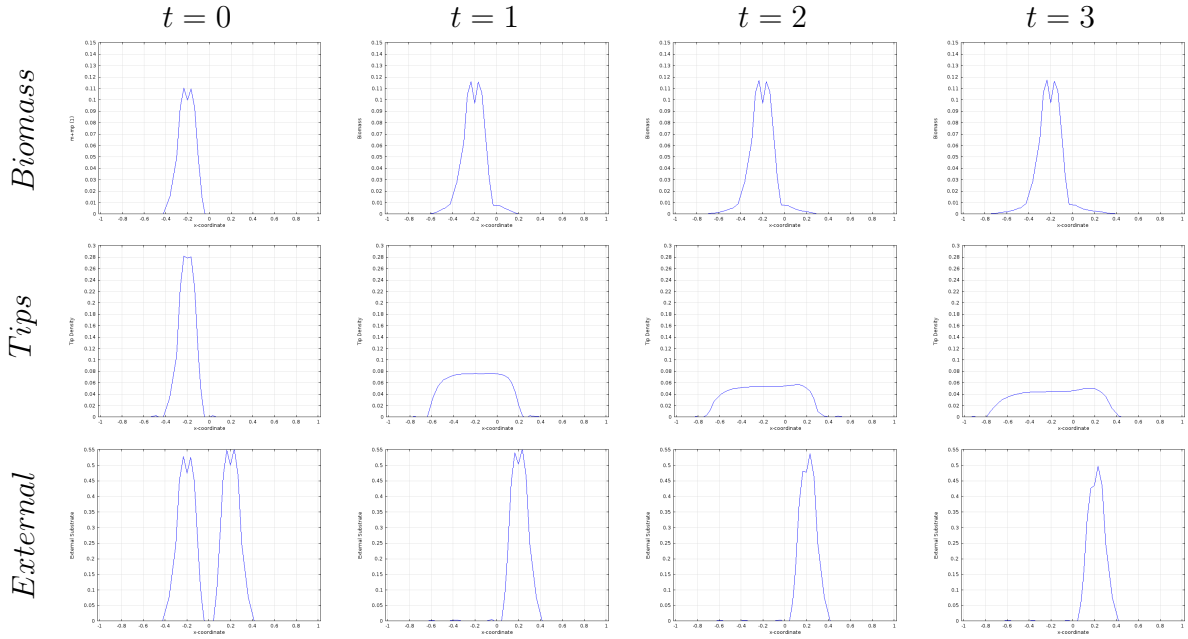


**Figure 6.7:** *Cross section of the solutions to equations (6.11) with initial data (6.12) and (6.14) using parameter values from Table 6.1 with  $u_S = (0.5, 0)$  and  $u_P = (0.5, 0)$ . Clearly a steady proliferation is observed. [For a movie of these plots please see external Folder labelled:- Comsol - Movie\_files - Toxic - 2Tile - Fig\_6.7]*

From Figure 6.7 we can indeed see the growth of the biomass. The active hyphae is seen to expand radially from its initial location and subsequently encountering the new substrate location (see also movie file *Fig\_6.6* and *Fig\_6.7*). The total hyphal biomass that exists for a longer period of time eventually also deteriorates once the substrate is depleted.

For the forthcoming analyses, the two dimensional plots will depict the region magnified around the “tiles” to display the behaviour more clearly. The plots for the toxic component are not included due to the low diffusion coefficient.

### 6.3.1.2 Biomass expansion in low toxic domain with scarce resources

In this section we introduce a small amount of toxicity to the right “tile” and observe the affect it has on the expansion of biomass. Hence solving model equations (6.11) with initial data equation (6.12) and (6.14) using default parameters in Table 6.1 with  $u_S = (0.5, 0)$  and  $u_P = (0.5, 0.1)$  results in the outcome depicted in Figure 6.8.

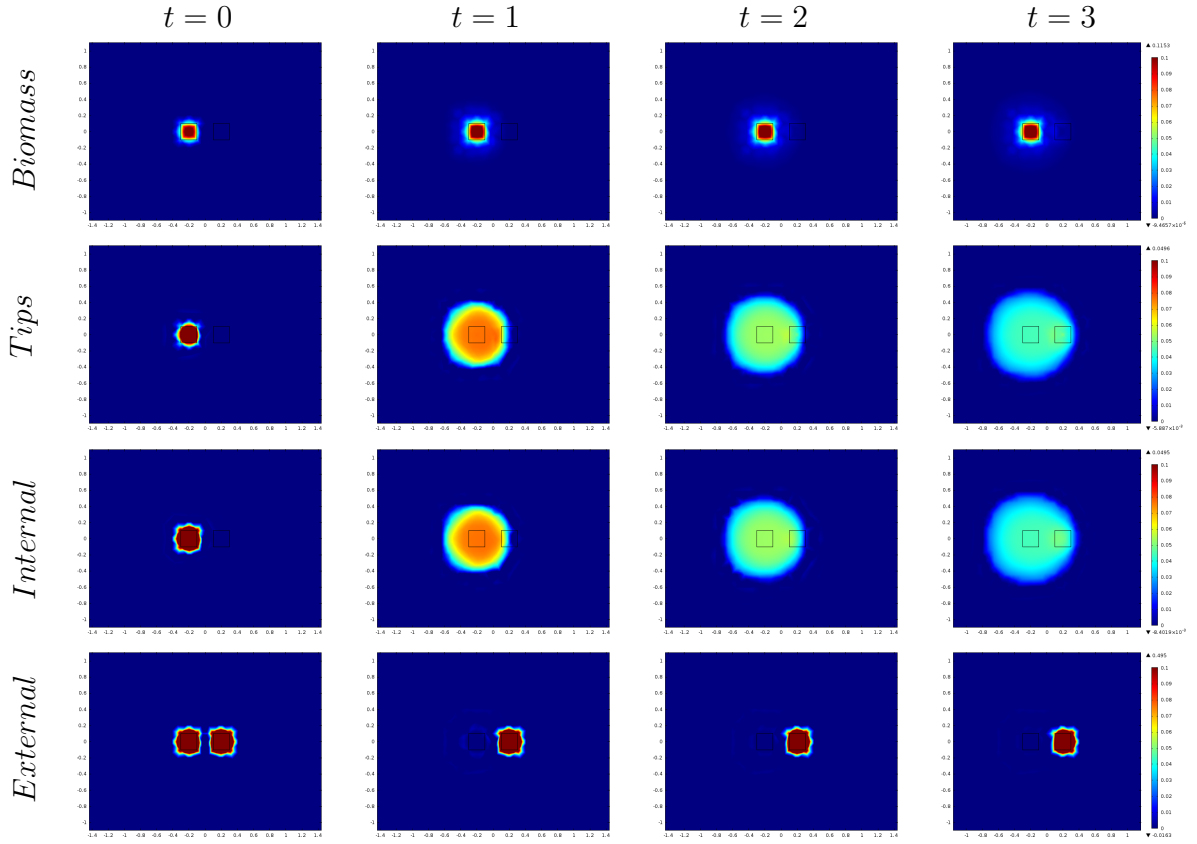


**Figure 6.8:** *2d representation of the solutions to equations (6.11) with initial data (6.12) and (6.14) using parameter values from Table 6.1 with  $u_S = (0.5, 0)$  and  $u_P = (0.5, 0.1)$ . A small accumulation is observed on the periphery of the right hand side “tile”. [For a movie of these plots please see external Folder labelled: Comsol - Movie\_files - Toxic - 2Tile- Fig.6.8]*

It is evident from Figure 6.8 that in the presence of any toxic material the biomass proliferation ceases to be radially symmetric. The colony grows until it reaches the right domain where a small quantity of biomass accumulates on the periphery (see movie file *Fig.6.8* and *Fig.6.9*). Also notice the distribution of tip density and internal substrate as time progresses is of an oval shape as a result of modelled toxicity. The intricate details can be observed on the following cross sectional plot (see Figure 6.9).



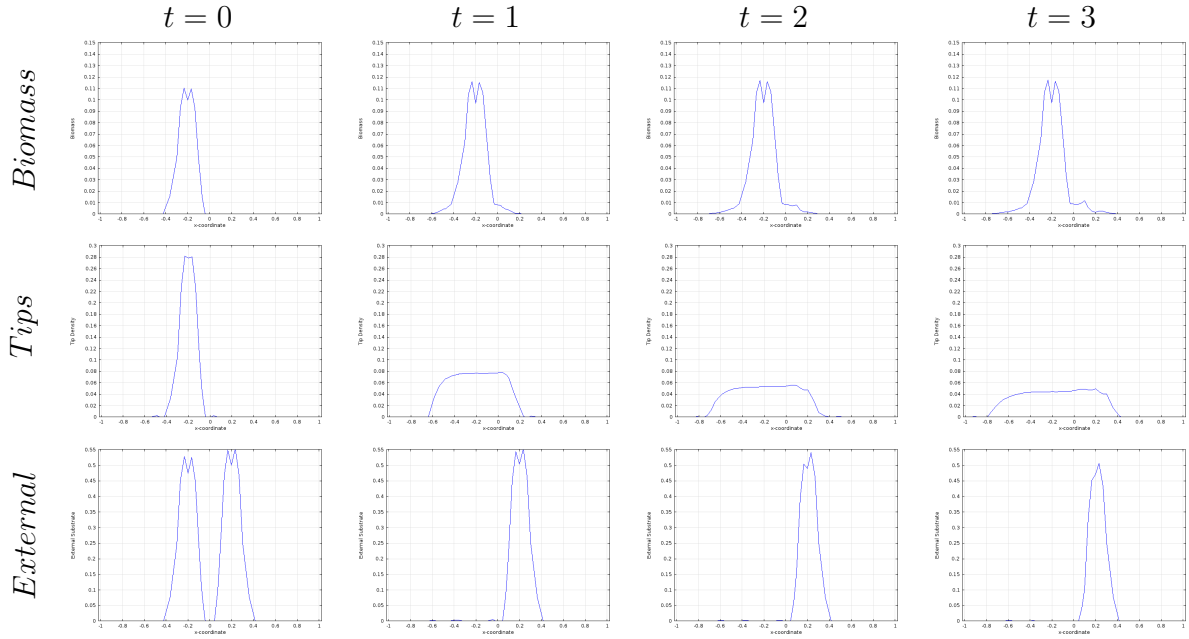
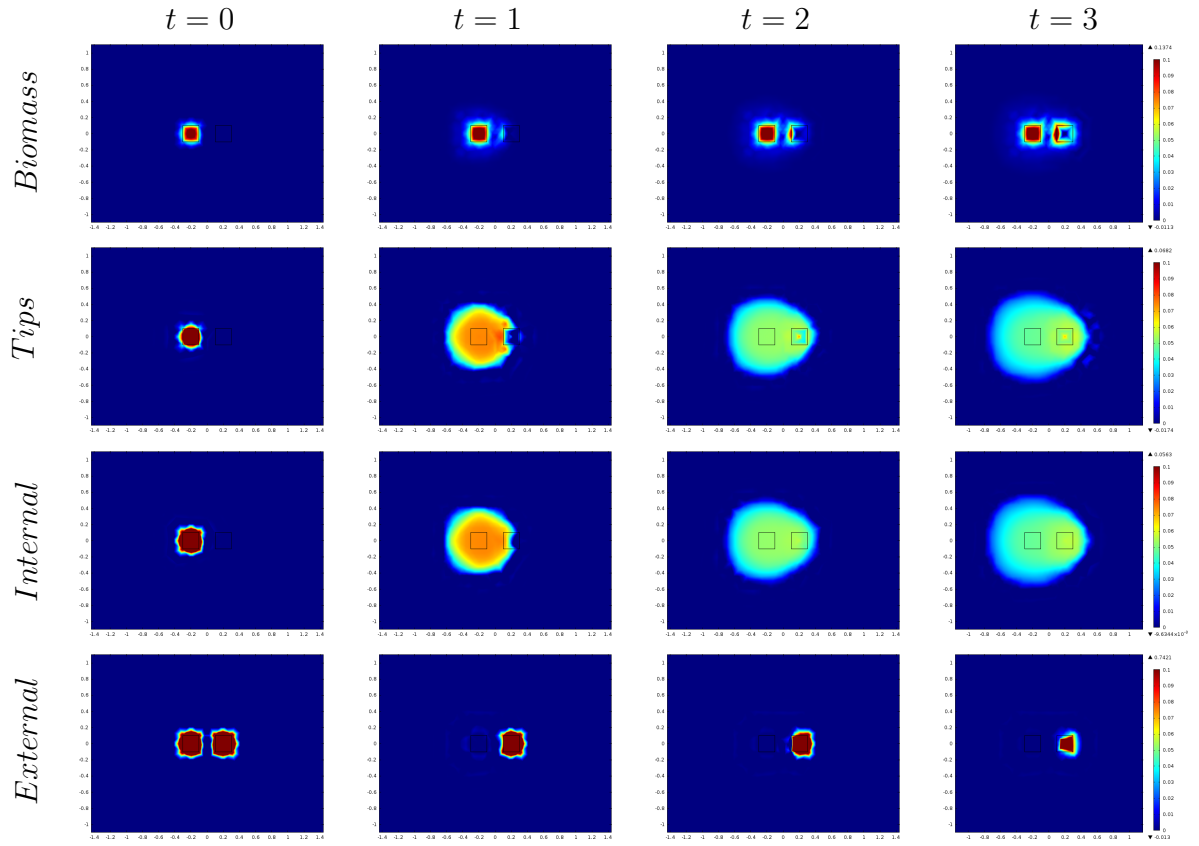


**Figure 6.9:** *Cross section of the solutions to equations (6.11) with initial data (6.12) and (6.14) using parameter values from Table 6.1 with  $u_S = (0.5, 0)$  and  $u_P = (0.5, 0.1)$ . An accumulation is prominent on the periphery of the right hand side “tile”. [For a movie of these plots please see external Folder labelled:- Comsol - Movie\_files - Toxic - 2Tile - Fig-6.9]*

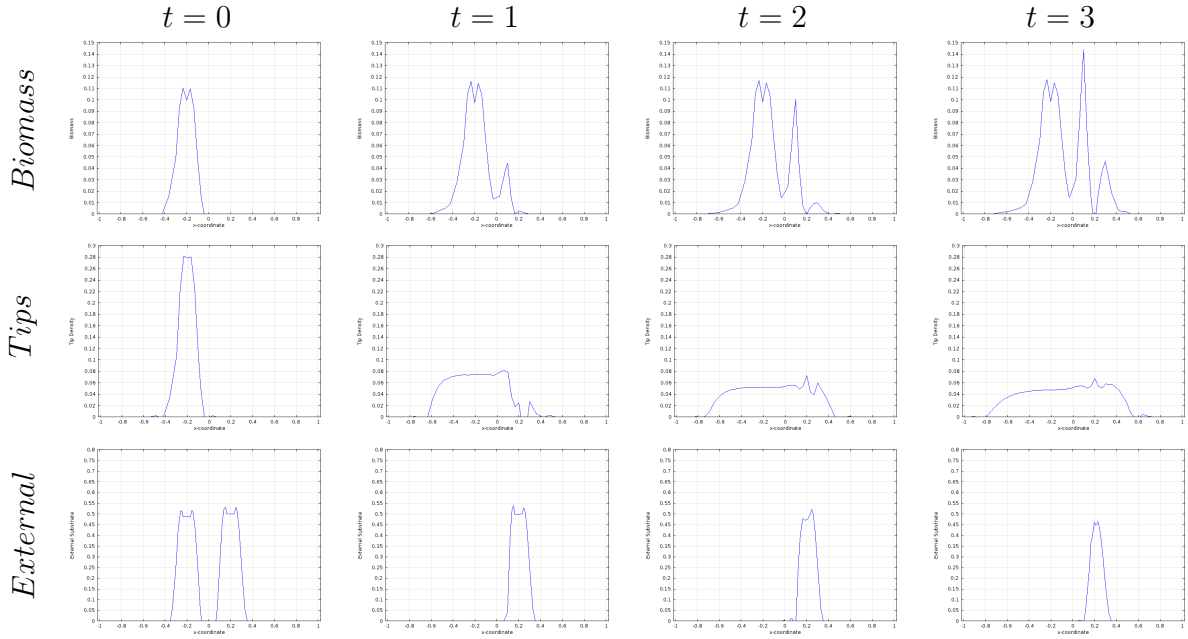
Notice, the accumulation of biomass near  $x = 0.1$  in Figure 6.9 whereas this is absent in Figure 6.7. Also notice the reduction in external substrate consumption in Figure 6.9 compared to that in Figure 6.7; an outcome obtained due to less biomass penetrating the right “tile”.

### 6.3.1.3 Biomass expansion in high toxic domain with scarce resources

A greater concentration of toxic substance is now added on the same “tile” containing reduced nutrients, to mimic the experiments in Fomina et al. (2000). The model equations (6.11) were solved with initial data (6.12) and (6.14) using default parameters in Table 6.1 with  $u_S = (0.5, 0)$  and  $u_P = (0.1, 1)$  (Figure 6.10 and 6.11).



**Figure 6.10:** 2d representation of the solutions to equations (6.11) with initial data (6.12) and (6.14) using parameter values from Table 6.1 i.e.  $u_S = (0.5, 0)$  and  $u_P = (0.5, 1)$ . A high accumulation of biomass is observed on the periphery of the right domain. [For a movie of these plots please see external Folder labelled: *Comsol - Movie\_files - Toxic - 2Tile - Fig.6.10*]



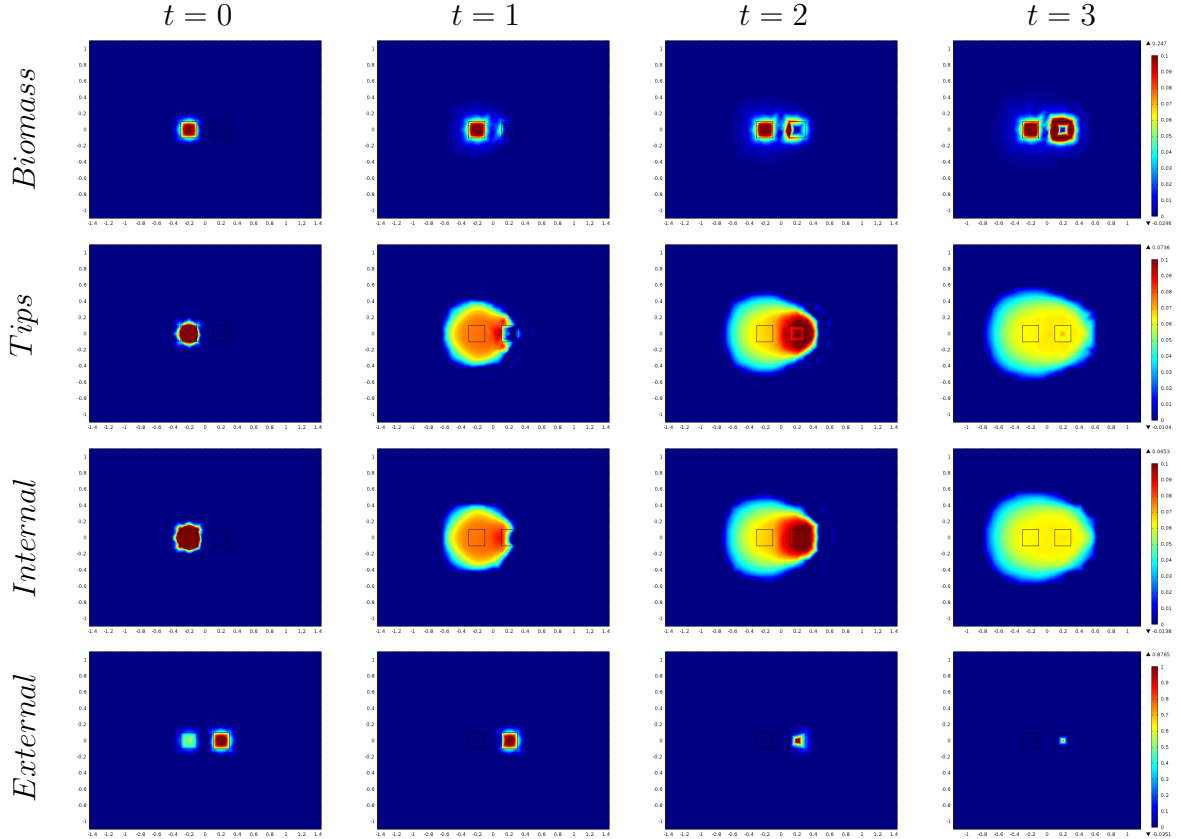
**Figure 6.11:** Cross section of the solutions to equations (6.11) with initial data (6.12) and (6.14) using parameter values from Table 6.1 with  $u_S = (0.5, 0)$  and  $u_P = (0.5, 1)$ . A high accumulation of biomass is prominent on the periphery of the right hand side “tile”. [For a movie of these plots please see external Folder labelled:- Comsol - Movie\_files - Toxic - 2Tile - Fig.6.11]

Figure 6.10 and 6.11 demonstrate that increasing the toxic concentration on the pollutant “tile” and lowering the nutrient concentration results in the biomass from the left “tile” being unable to penetrate the right hand “tile” and thus accumulate outside the boundary of the toxic “tile” (see also movie files *Fig.6.10* and *Fig.6.11*). Notice also that the majority of biomass expands around the toxic “tile” without penetrating the “tile”. Similar behaviour was observed by Fomina et al. (2000).

Interestingly, some biomass can be seen to accumulate on the right hand side of the right “tile” (i.e. close to  $x = 0.4$ ). This phenomenon has occurred due to the modelling of the flux of tips, namely the diffusion term. The diffusion of tips is modelled using a random process unaffected by the pollutant which results in a small quantity of tips penetrating the right “tile” and once across they begin to consume the resources from the other side, thus the accumulation of biomass.

### 6.3.1.4 Biomass expansion from a nutrient scarce domain to a highly toxic domain with abundant resources

As mentioned earlier, Fomina et al. (2000) demonstrated that fungi were able to penetrate and react positively to the toxic material via the increase of nutrients on the shared “tile”. Thus here we increase the nutrients on the right “tile” only and solve the model equations (6.11) with initial data (6.12) and (6.14) using default parameters in Table 6.1 with  $u_S = (0.5, 0)$  and  $u_P = (1, 1)$ . The results are shown in Figure 6.12.



**Figure 6.12:** 2d representation of the solutions to equations (6.11) with initial data (6.12) and (6.14) using parameter values from Table 6.1 with  $u_S = (0.5, 0)$  and  $u_P = (1, 1)$ . Biomass can be seen to grow on the toxic domain. [For a movie of these plots please see external Folder labelled: Comsol - Movie\_files - Toxic - 2Tile - Fig.6.12]

Figure 6.12 shows the presence of a greater nutrient concentration on the toxic “tile” enabled the model biomass to penetrate the toxic “tile” and consume

the resources present, consistent with the experimental analysis of Fomina et al. (2000).

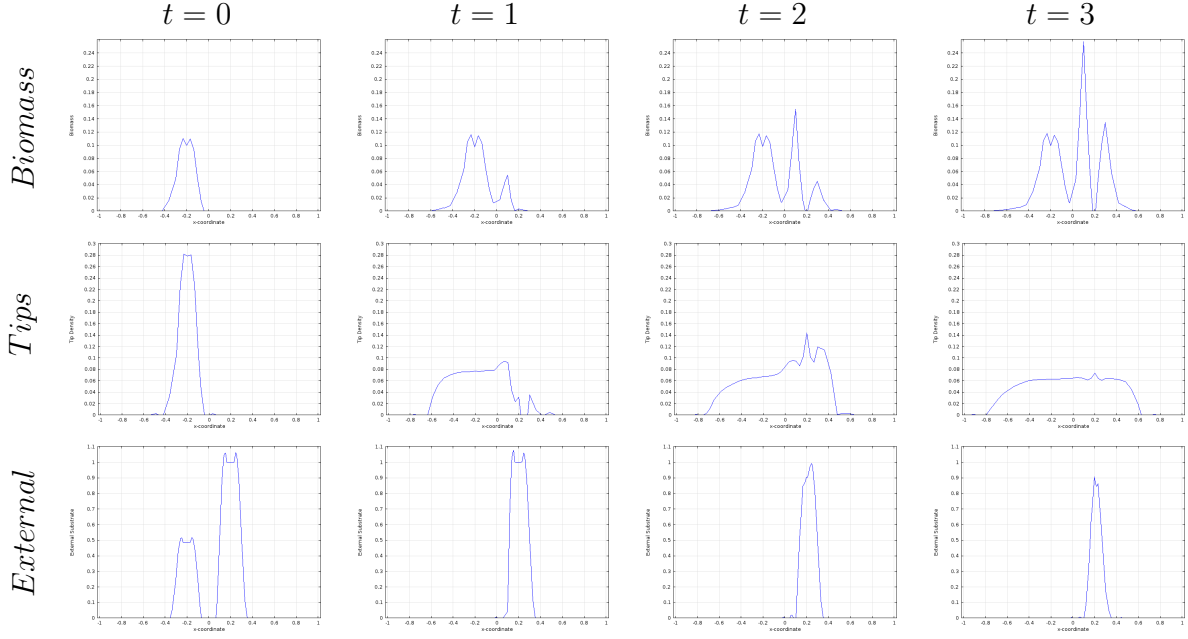


**Figure 6.13:** Cross section of the solutions to equations (6.11) with initial data (6.12) and (6.14) using parameter values from Table 6.1 with  $u_S = (0.5, 0)$  and  $u_P = (1, 1)$ . Lower initial biomass resulted in lower depletion of external resources. [For a movie of these plots please see external Folder labelled:- Comsol - Movie\_files - Toxic - 2Tile - Fig\_6.13]

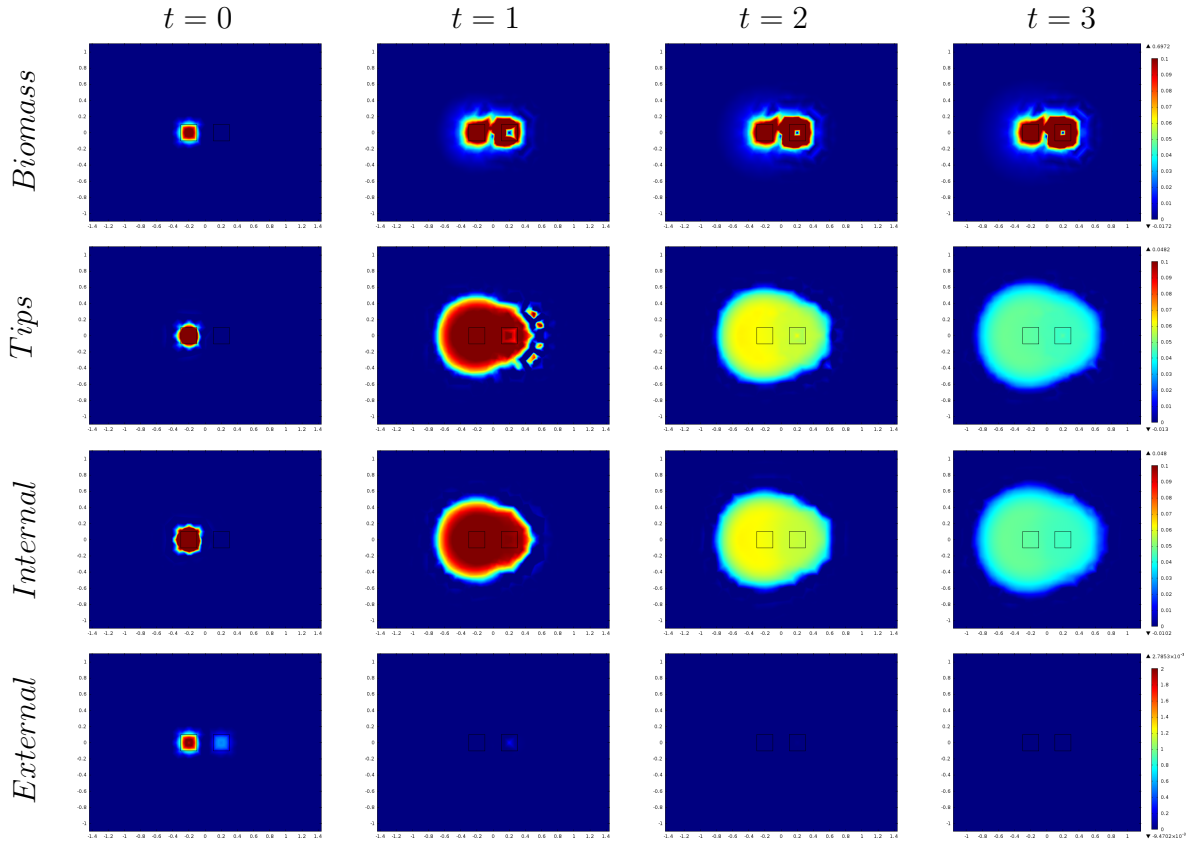
Figure 6.13 demonstrate that the impact of increasing the resources on the polluted “tile” resulted in the biomass penetrating and consuming the resources (see movie file *Fig\_6.12* and *Fig\_6.13*). Comparing Figure 6.13 to Figure 6.11, it can be seen that a greater density of biomass is accumulated on the periphery (i.e. close to  $x = 0.1$ ). Notice that this resulted in the increased consumption of the resources of the right domain however this was significantly less compared to the case where the biomass has access to higher resources initially (see Figure 6.15).

### 6.3.1.5 Biomass expansion from a nutrient rich domain to a highly toxic domain with scarce resources

Somewhat surprisingly, the impact of increasing the initial nutrients available to the fungi (i.e. that on the left “tile”) was not addressed in Fomina et al. (2000) and thus the study did not consider how the initially supplied nutrients affected the

ability of fungi to penetrate a hostile zone. Chapters 4 and 5 demonstrated that the outcome of fungal interactions could be controlled by manipulating nutrient levels and so this is clearly an interesting scenario to investigate. Thus we consider the instance where the right “tile” was not previously penetrated by biomass (see Section 6.3.1.3) but increase the external substrate concentration on the left “tile”.

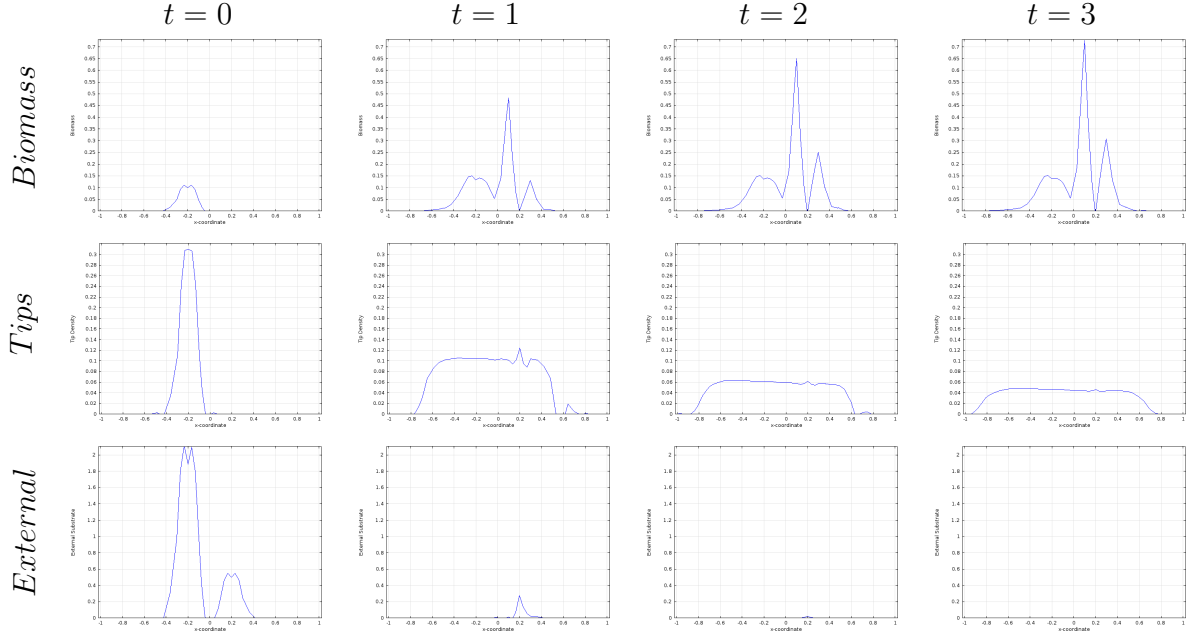
The model equations (6.11) were solved with initial data in equations (6.12) and (6.14) using the default parameters in Table 6.1 with  $u_S = (2, 0)$  and  $u_P = (0.5, 1)$  and the results are shown in Figure 6.14.



**Figure 6.14:** 2d representation of the solutions to equations (6.11) with initial data (6.12) and (6.14) using parameter values from Table 6.1 with  $u_S = (2, 0)$  and  $u_P = (0.5, 1)$ . A high accumulation of biomass is prominent around the periphery of the pollutant “tile” resulting in depletion of external resources. [For a movie of these plots please see external Folder labelled: Comsol - Movie\_files - Toxic - 2Tile - Fig\_6.14]

Figure 6.14 clearly demonstrates that provided the biomass has access to sufficient external substrate in its immediate vicinity, it is better able to deal with

adverse conditions, even expanding through toxic regions since it has sufficient energy supplied to the tips to overcome the negative chemotaxis (see movie file *Fig\_6.14* and *Fig\_6.15*).



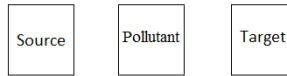
**Figure 6.15:** Cross section of the solutions to equations (6.11) with initial data (6.12) and (6.14) using parameter values from Table 6.1 with  $u_S = (2, 0)$  and  $u_P = (0.5, 1)$ . An increased density is observed in biomass and tips, resulting in the absorption of external substrate. [For a movie of these plots please see external Folder labelled:- Cmsol - Movie\_files - Toxic - 2Tile - Fig.6.15]

Figure 6.15 demonstrates the impact of increasing the resources available to the biomass in its immediate vicinity on a one dimensional plot. Comparing the results to Figure 6.11, it can be seen that a greater density of biomass is accumulated on the periphery ( $x = 0.1$ ). Notice that this resulted in the increased consumption of resources from the right domain. Therefore we can infer from these results that having access to an initial nutrient rich source, biomass is better able to deal with adverse conditions.

The results produced in this section are in accordance with the findings of Fomina et al. (2000), i.e. when provided with sufficient resources, fungi are able to invade toxic landscapes and the simulations described above represent a first attempt to quantify the amount of resources required. Clearly these results have significant relevance to applications in bioremediation.

### 6.3.2 Fomina *et al.* (2003) revisited

In this section key experiments from Fomina et al. (2003) are considered and extended using model equations (6.11) with default parameter values in Table 6.1. The extended results aim to generate a better understanding of the key processes involved in fungal growth in toxic environments. As before, certain initial data will be adjusted according to the experiments. The initial data is chosen to resemble the experimental setup of Fomina et al. (2003) (see Figure 6.16 for a schematic illustration) namely an initial inoculum is placed onto an agar based ‘square’ “tile” (denoted by ‘Source’) alongside a second “tile” (‘Pollutant’) that is laced with both nutrient and toxic compounds and followed by a third “tile” only containing nutrients (‘Target’).



**Figure 6.16:** *Initial experimental configuration used in the simulations.*

Thus the primary objective of this layout is to explore the behaviour of hyphal biomass with a toxic substance and whether it can reach the target “tile” when provided with a range of nutrients.

#### 6.3.2.1 Biomass expansion in a toxic free environment

The initial data for the Source and Pollutant “tile” are taken to be the same as before. The Target “tile” has the following conditions

$$\begin{aligned} \rho(x, y, 0) &= \rho'(x, y, 0) = n(x, y, 0) = s_i(x, y, 0) = T(x, y, 0) = 0, \\ s_e(x, y, 0) &= s_{e0}, \end{aligned} \tag{6.15}$$

where all parameters and variables are the same as before (see section 6.3.1.1). The initial model biomass is placed on the Source “tile”. For convenience, initial parameter values that change in each simulation for each “tile” will be denoted using the same notation used in previous sections.

The model equations (6.11) with initial data in equations (6.12), (6.14) and (6.15) using the default parameters in Table 6.1 with  $u_S = (0.5, 0)$ ,  $u_P = (1, 0)$  and



$u_T = (1, 0)$  are solved using similar techniques to those in the previous sections (Figure 6.17).

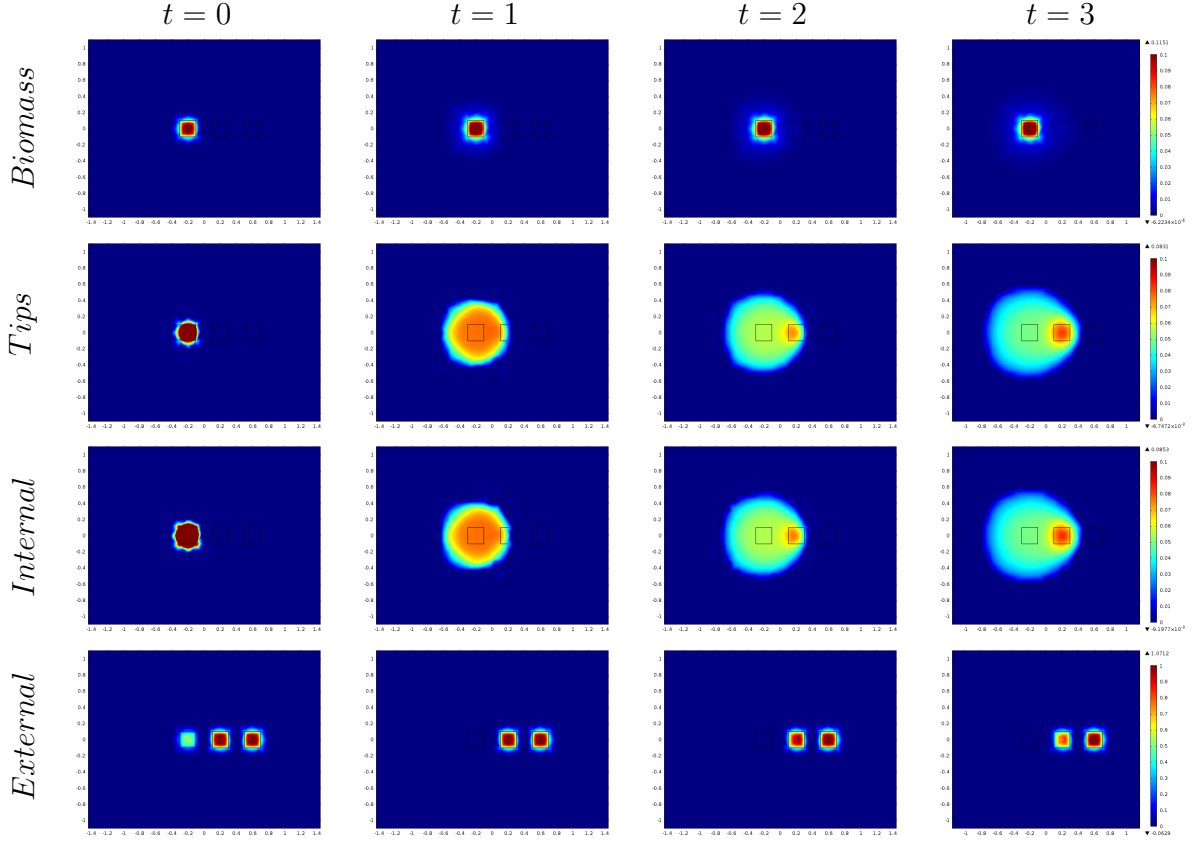


**Figure 6.17:** *2d representation of the solutions to equations (6.11) with initial data (6.12), (6.14) and (6.15) using parameter values from Table 6.1 with  $u_S = (0.5, 0)$ ,  $u_P = (1, 0)$  and  $u_T = (1, 0)$ . Corresponding to biomass proliferation in the absence of pollutant. [For a movie of these plots please see external Folder labelled: Comsol - Movie\_files - Toxic - 3Tile - Fig-6.17]*

It can be seen from Figure 6.17 that the expansion of the biomass is radially symmetric until it encounters the pollutant and target “tile” where upon encountering new resources the shape of the initial profile changes. This behaviour can be compared to the observations made by Jacobs et al. (2002) and Boswell et al. (2003a) where biomass was found to expand and bridge the narrow gaps between the source and new substrate rich location. Upon reaching the new resource, the sudden increase in internal substrate caused a burst of branching and a marked increase of biomass density that lead to the colonisation of the newer location by the biomass.

For clarity, Figure 6.18 shows a cross sectional plot of the total model biomass, tip density and external resource.

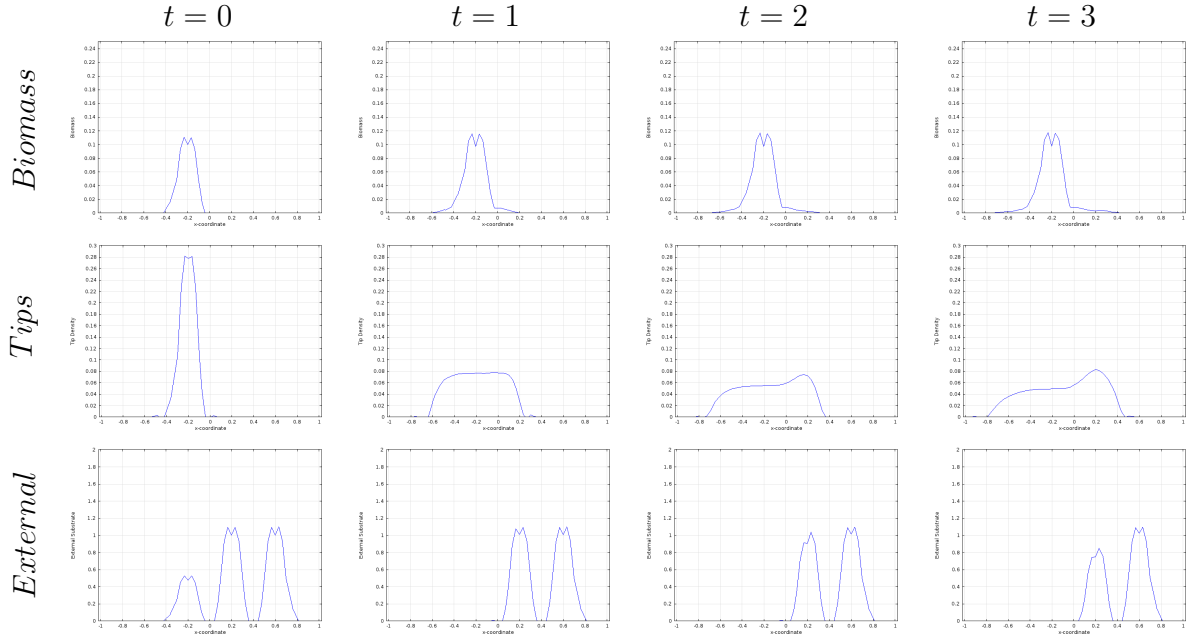


**Figure 6.18:** Cross section of the solutions to equations (6.11) with initial data (6.12), (6.14) and (6.15) using parameter values from Table 6.1 with  $u_S = (0.5, 0)$ ,  $u_P = (1, 0)$  and  $u_T = (1, 0)$ . Tip density can be seen to growing on the pollutant region. [For a movie of these plots please see external Folder labelled:- Comsol - Movie\_files - Toxic - 3Tile - Fig\_6.18]

From Figure 6.18 we can indeed see the expansion of biomass, tips and the depletion of resources. The biomass is seen to expand radially from its initial location and subsequently encountering the new substrate location (see movie files *Fig\_6.17* and *Fig\_6.18*). The total model biomass eventually deteriorates once the substrates are depleted (results not shown).

### 6.3.2.2 Biomass expansion in a low toxicity environment

In this section we explore the effects of adding a small quantity of toxicity to the middle “tile” on the expansion of the biomass. The model equations (6.11) with initial data in equations (6.12), (6.14) and (6.15) are solved using the default parameters in Table 6.1 with  $u_S = (0.5, 0)$ ,  $u_P = (1, 0.1)$  and  $u_T = (1, 0)$  are solved and results are shown in Figure 6.19.

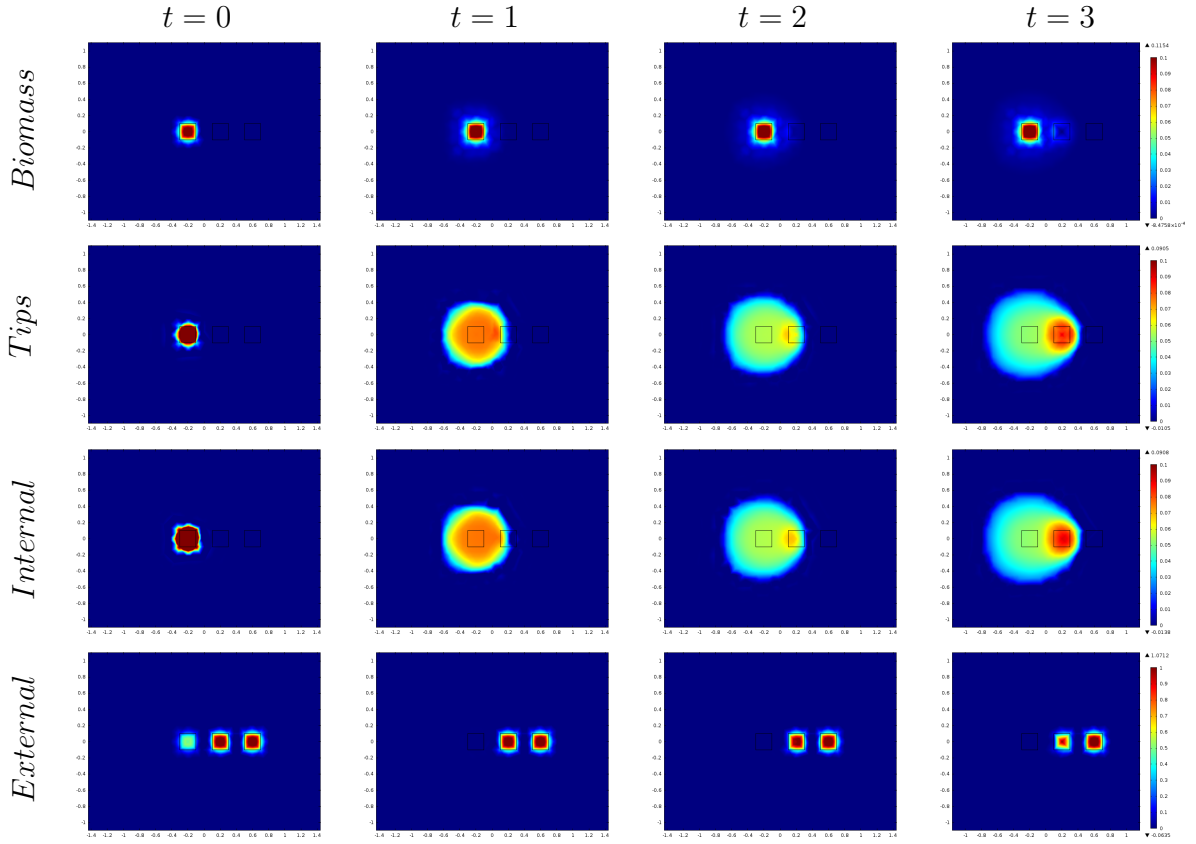


**Figure 6.19:** 2d representation of the solutions to equations (6.11) with initial data (6.12), (6.14) and (6.15) using parameter values from Table 6.1 with  $u_S = (0.5, 0)$ ,  $u_P = (1, 0.1)$  and  $u_T = (1, 0)$ . The presence of a pollutant on the central “tile” limits the expansion of the biomass. [For a movie of these plots please see external Folder labelled: Comsol - Movie\_files - Toxic - 3Tile - Fig-6.19]

It is clear from Figure 6.19 that the presence of toxicity in the central “tile” hindered the expansion of the model biomass when compared to the control simulation in Figure 6.17. This difference is not obvious through the accumulation of biomass along the periphery of the toxic “tile”. We also see that as time progresses, the biomass is expanding around the hostile zone. Also due to the low toxicity level in this realisation, the biomass was able to penetrate and even take up the nutrient from the middle “tile” shown clearly on the cross sectional plot in Figure 6.20. This phenomenon was observed by Fomina et al. (2003) for the fungal species *T. virens*.

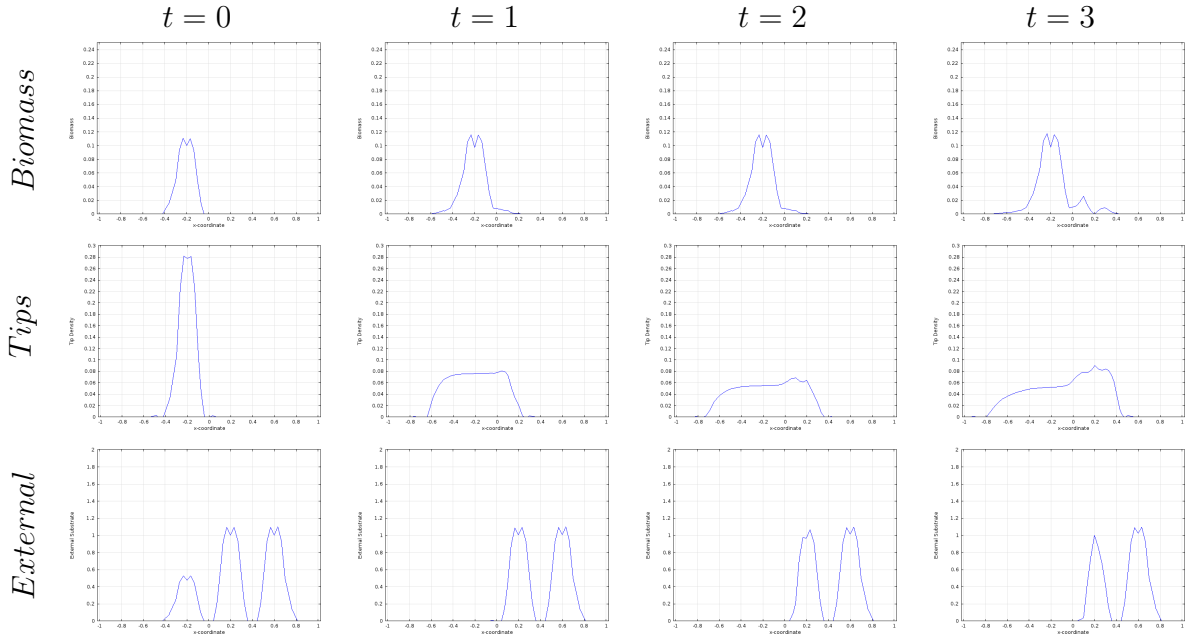


**Figure 6.20:** Cross sectional representation of the solutions to equations (6.11) with initial data (6.12), (6.14) and (6.15) using parameter values from Table 6.1 with  $u_S = (0.5, 0)$ ,  $u_P = (1, 0.1)$  and  $u_T = (1, 0)$ . Biomass accumulation on each side of the pollutant “tile” is depicted. [For a movie of these plots please see external Folder labelled:- Comsol - Movie\_files - Toxic - 3Tile - Fig-6.20]

From Figure 6.20 we can indeed see the adverse effects of pollutants on the biomass. The biomass density is seen to increase on the border of the pollutant “tile” (i.e. close to  $x = 0.1$ ), which is seen clearly at time  $t = 3$  (see also movie files *Fig\_6.19* and *Fig\_6.20*). Notice the higher density of biomass, tips and uptake of substrate around the pollutant “tile” when compared with that of Figure 6.18.

### 6.3.2.3 Biomass expansion in a highly toxic domain.

Here we investigate the impact on the model biomass of increasing the toxicity of the pollutant “tile”. Figure 6.21 displays the solutions of the model equations (6.11) with initial data (6.12), (6.14) and (6.15) using the default parameters in Table 6.1 with  $u_S = (0.5, 0)$ ,  $u_P = (1, 1)$  and  $u_T = (1, 0)$ .

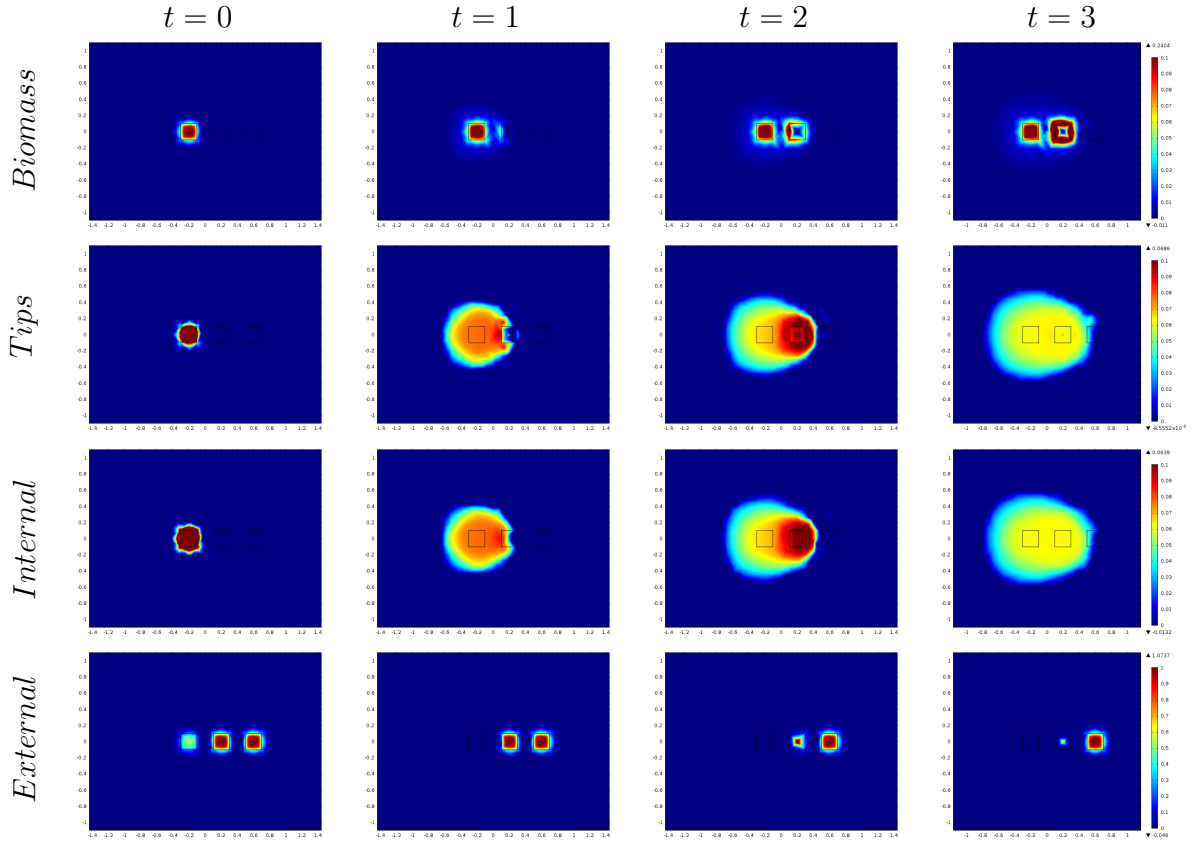


**Figure 6.21:** *2d representation of the solutions to equations (6.11) with initial data (6.12), (6.14) and (6.15) using parameter values from Table 6.1 with  $u_S = (0.5, 0)$ ,  $u_P = (1, 1)$  and  $u_T = (1, 0)$ . The presence of increased pollutant significantly hinders biomass growth across the central “tile”. [For a movie of these plots please see external Folder labelled: Comsol - Movie\_files - Toxic - 3Tile - Fig.6.21]*

When the toxicity level in the central “tile” was further increased (Figure 6.21) the biomass density also increased in the gap between the “tiles”. The greater substrate concentration within the toxic “tile” resulted in biomass accumulating around the periphery of this hostile zone. This is shown clearly on the cross sectional plot in Figure 6.22. The tip density and internal substrate are significantly less at time  $t = 3$  compared to that observed in previous sections (e.g. Figures 6.17 and 6.19). Also notice the sparse shape of the area depicted by the tips and internal substrate in Figure 6.21 whereas in prior sections the area was more compact (see Figure 6.17). This is due to the disfigurement of the biomass (and associated tip density and internal substrate) that occurred close to time  $t = 1$  corresponding to the biomass first encountering the high concentration of

pollutant on the central “tile” forcing its expansion around this hostile zone and reforming on the other side.

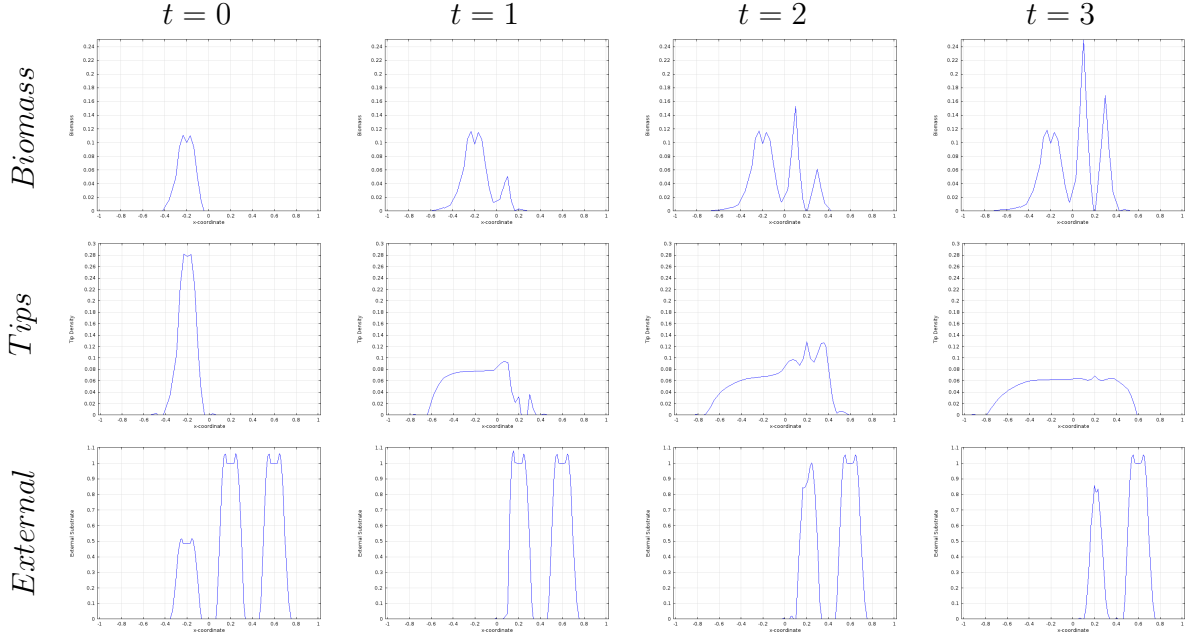


**Figure 6.22:** *Cross sectional representation of biomass, tip density and external substrate along  $y = 0$  obtained from the solutions to equations (6.11) with initial data (6.12), (6.14) and (6.15) with parameter values from Table 6.1 with  $u_S = (0.5, 0)$ ,  $u_P = (1, 1)$  and  $u_T = (1, 0)$ . An increase of biomass is observed around the periphery of the central “tile”. [For a movie of these plots please see external Folder labelled:- Comsol - Movie\_files - Toxic - 3Tile - Fig.6.22]*

Figure 6.22 clearly illustrates the adverse effects of pollutants on the model biomass. The biomass density is seen to increase on each side of the borders of the pollutant “tile” (i.e. close to  $x = 0.1$  and  $x = 0.3$ ). As mentioned earlier, the expansion of the biomass around the pollutant “tile” and consuming substrate along its border where the toxic concentration is low can be seen (see movie files *Fig\_6.21* and *Fig\_6.22* for an animation of the solutions). The outcome obtained in this section is very similar to that seen for the corresponding two “tile” case (see Figures 6.12 and 6.13).

### 6.3.2.4 Biomass expansion in a highly toxic domain with scarce resources.

In this section we explore if similar behaviour to that seen previously occurs if the substrate concentration on the pollutant domain is lowered. Thus model equations (6.11) with initial data in equations (6.12), (6.14) and (6.15) using the default parameters in Table 6.1 with  $u_S = (0.5, 0)$ ,  $u_P = (0.1, 1)$  and  $u_T = (1, 0)$  are solved (Figure 6.23).

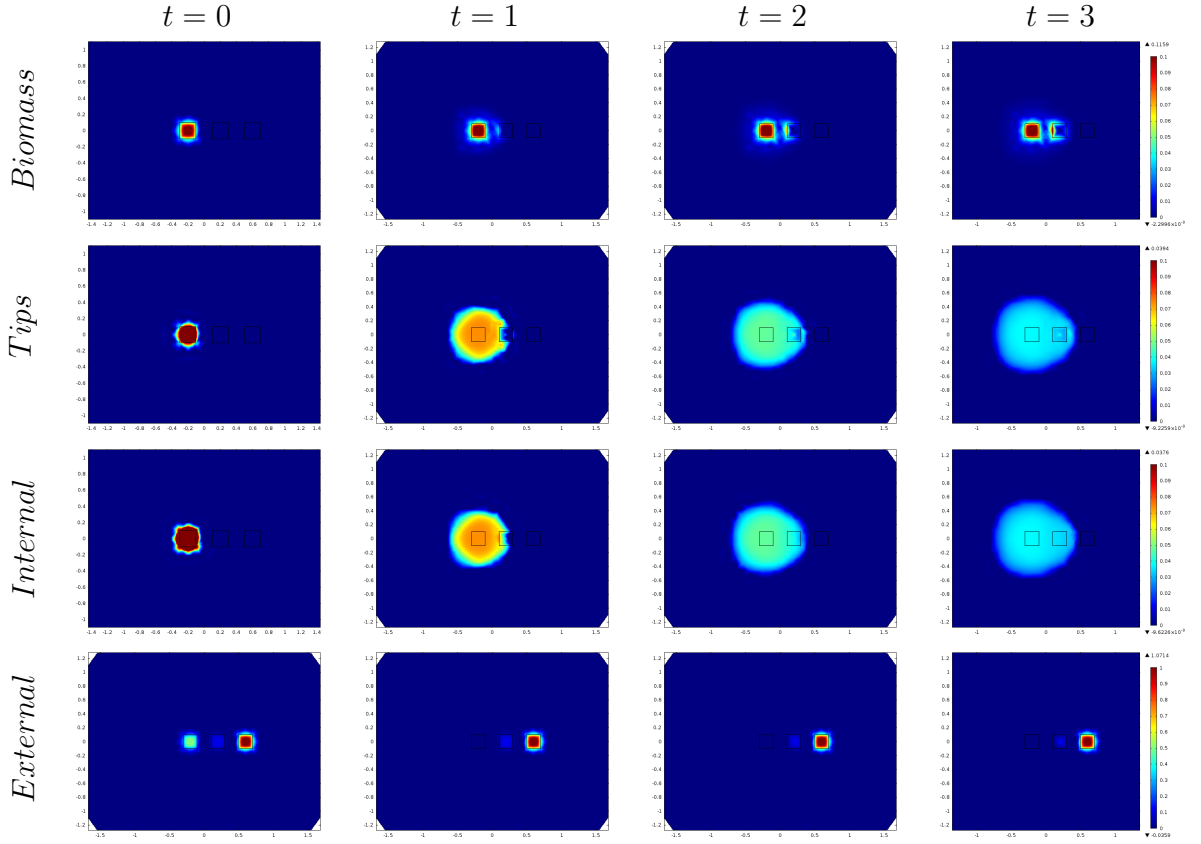


**Figure 6.23:** *2d representation of the solutions to equations (6.11) with initial data (6.12), (6.14) and (6.15) using parameter values from Table 6.1 with  $u_S = (0.5, 0)$ ,  $u_P = (0.1, 1)$  and  $u_T = (1, 0)$ . The reduced substrate on the pollutant “tile” significantly reduced biomass growth compared to Figure 6.21. [For a movie of these plots please see external Folder labelled: Comsol - Movie\_files - Toxic - 3Tile - Fig\_6.23]*

Figure 6.23 demonstrates the effect of reducing the substrate in the central “tile” while retaining the same amount of toxic compound compared to Section 6.3.2.3. The lack of substrate hinders the expansion of biomass in reaching the

target “tile” as expected. Furthermore, the tip density and internal substrate can be seen to diminish at a faster rate than before. Figure 6.24 depicts the cross sectional plot of the biomass, tips density and external substrate.

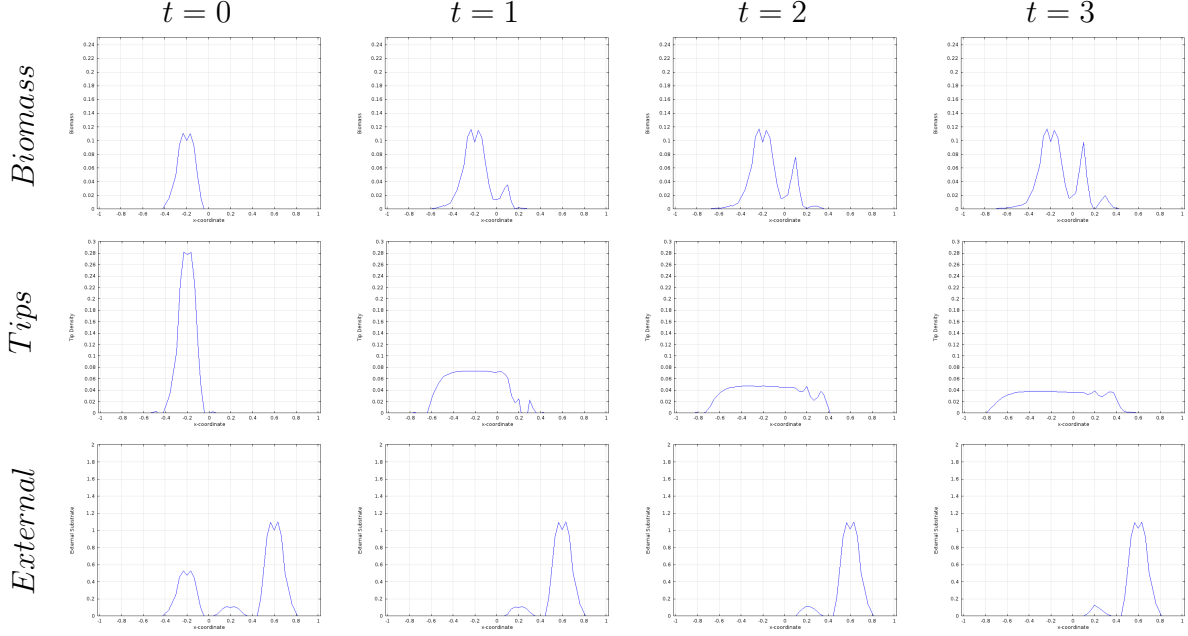


**Figure 6.24:** Cross sectional representation of biomass, tip density and external substrate obtained from solutions to equations (6.11) with initial data (6.12), (6.14) and (6.15) using parameter values from Table 6.1 with  $u_S = (0.5, 0)$ ,  $u_P = (0.1, 1)$  and  $u_T = (1, 0)$ . Biomass is seen to accumulate at the pollutant periphery. [For a movie of these plots please see external Folder labelled:- Comsol - Movie\_files - Toxic - 3Tile - Fig.6.24]

We can clearly see the adverse effects of pollutants on the biomass (Figure 6.24) (see also movie files *Fig.6.23* and *Fig.6.24* for an animation of the solutions). All of the model results seen in this section thus far, compare accordingly with the experimental observations of Fomina et al. (2003).

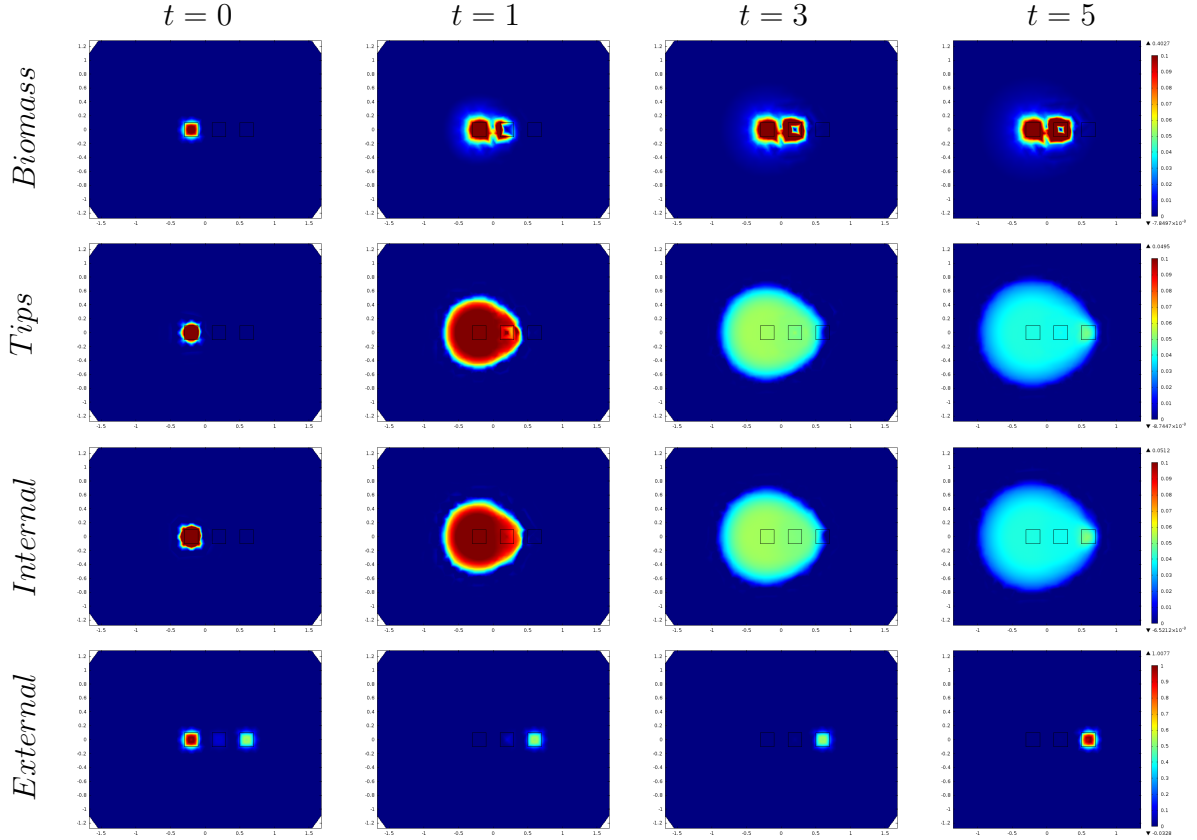
### 6.3.2.5 Biomass expansion from a nutrient rich region to a highly toxic region with scarce resources

In Section 6.3.1.5 a scenario not explored by Fomina et al. (2000) was considered where the impact of increasing the initial substrate immediately available to the biomass was investigated. Similarly in this section we investigate how the system would behave if the initial inoculum (i.e. the source “tile”) had a greater local



substrate concentration.

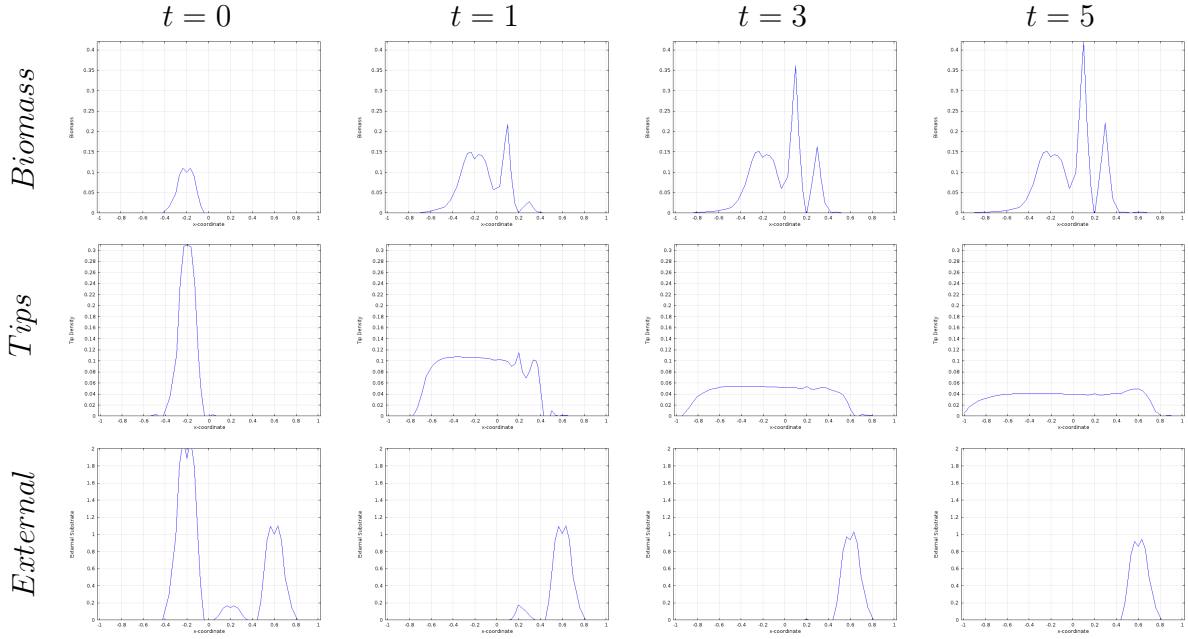
Solving model equations (6.11) with initial data in equations (6.12), (6.14) and (6.15) using default parameters specified in Table 6.1 with  $u_S = (2, 0)$ ,  $u_P = (0.1, 1)$  and  $u_T = (1, 0)$  produces the resulting Figure 6.25.



**Figure 6.25:** 2d representation of the solutions to equations (6.11) with initial data (6.12), (6.14) and (6.15) using parameter values from Table 6.1 with  $u_S = (2, 0)$ ,  $u_P = (0.1, 1)$  and  $u_T = (1, 0)$ . The model biomass accumulates around the pollutant “tile” and reaches the target “tile”. [For a movie of these plots please see external Folder labelled: Comsol - Movie\_files - Toxic - 3Tile - Fig-6.25]

The first three columns in Figure 6.25 depict results similar to those shown in Figures 6.21 and 6.23. Notice the greater quantity of model biomass around the pollutant “tile” resulting from the increased quantity of substrate in the source domain compared to Figures 6.21 and 6.23. Thus increasing the substrate in the source “tile” has provided the biomass with the ability to penetrate the pollutant “tile” and reach the newer target “tile” (shown at time  $t = 5$ ). In the previous in-

stances where the initial external substrates were low, the biomass failed to reach the target domain, even when the simulation was run for longer times (results not shown). Also the pollutant presence forced growth around the periphery of the domain causing deformation of the range of tip density and the internal substrate (Figures 6.21 and 6.23). However due to the increased resources around its immediate vicinity, the model biomass and tips in the current scenario can be seen to penetrate through the hostile “tile” with minimal changes to its distribution (see Figure 6.25). A cross sectional representation is shown in Figure 6.26.



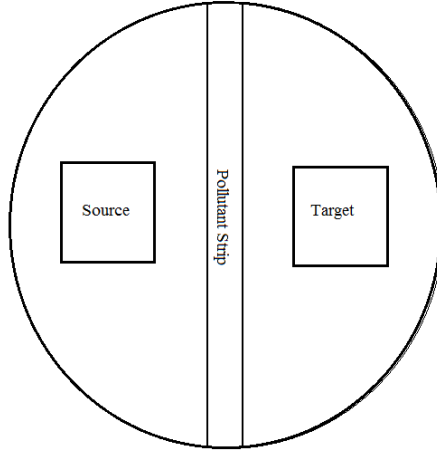
**Figure 6.26:** *Cross sectional representation of biomass, tip density and external substrate obtained from solutions to equations (6.11) with initial data (6.12), (6.14) and (6.15) using parameter values from Table 6.1 with  $u_S = (2, 0)$ ,  $u_P = (0.1, 1)$  and  $u_T = (1, 0)$ . External resources are shown to deplete on the target “tile”. [For a movie of these plots please see external Folder labelled:- Comsol - Movie\_files - Toxic - 3Tile - Fig\_6.26]*

Figure 6.26 shows that the density of biomass is greater around the pollutant “tile” than that observed from Figures 6.22 and 6.24 (see also movie files *Fig\_6.25* and *Fig\_6.26*). Notice that the biomass has reached the target “tile” as evidenced by the depletion of external substrate at time  $t = 5$ . The representation in Figure 6.25 also depicts the increased density of tips and internal substrate on the target “tile” compared to previous case (e.g. Figure 6.23).

It was mentioned earlier that Fomina et al. (2003) showed the presence of toxic metals caused an accumulation of hyphae in the border of the toxic “tile” but a small amount of hyphae were able to penetrate the toxic region. The increase of toxicity in the pollutant region made the accumulation of hyphae more dense around its border but small increments of hyphae were still able to reach the target domain. This has been replicated in the above modelling. In the current investigation a scenario not explored by Fomina et al. (2003) was considered, namely the effects of altering the nutrient on the source “tile”. In our simulations it was seen that the model biomass is better placed to deal with the hostility of the toxic region provided sufficient nutrients were readily available elsewhere. Furthermore, by increasing the amount of substrate in the toxic region, a greater quantity of biomass was able to penetrate and reach the target “tile”. Crucially, in all these experimental configurations the biomass was able to expand around the toxic material in the central “tile”, which was not discussed in Fomina et al. (2003) although observed in their published images. Therefore in the next section we aim to investigate this issue by altering the domain to avoid such behaviour.

### **6.3.3 Biomass expansion across a pollutant strip**

In order to avoid situations where the biomass expands around a hostile region, we now make the shape of the middle “tile” rectangular and extending across the middle of the simulated Petri dish (see schematic representation in Figure 6.27). This will prevent the biomass expanding around the “tile” to access additional resources.



**Figure 6.27:** *Initial experimental configuration depicting a toxic strip domain.*

The initial conditions are identical to that used in the previous section i.e. (6.12), (6.14) and (6.15) respectively.

#### **6.3.3.1 Biomass expansion from a rich nutrient source across a highly toxic domain abundant in resources**

We will solve model equations (6.11) with initial data (6.12), (6.14) and (6.15) using the same set of parameters in Table 6.1 with  $u_S = (1, 0)$ ,  $u_P = (1, 1)$  and  $u_T = (1, 0)$  using zero flux boundary conditions. The domain is similar to that of the previous section apart from the middle “tile” (i.e. pollutant strip) that now extends across a diameter of the “Petri dish”. Results are shown in Figure 6.28.

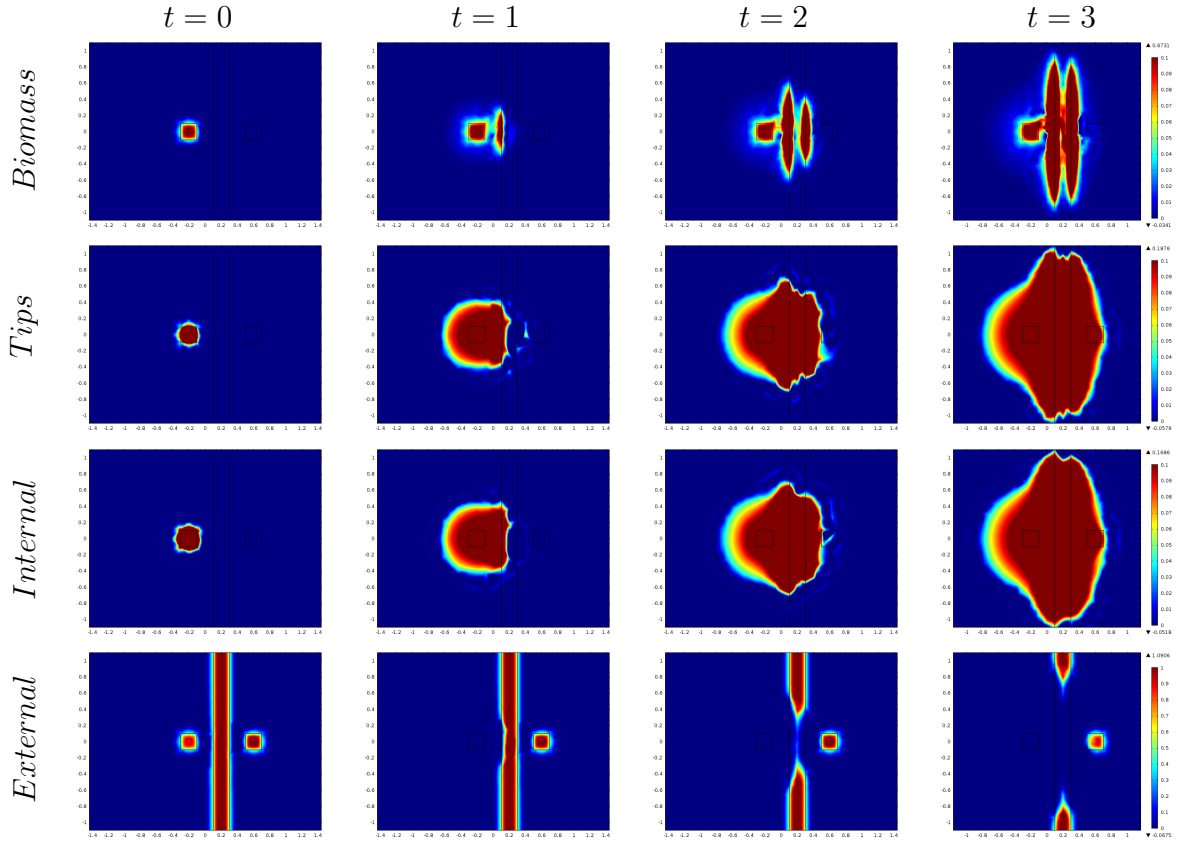


**Figure 6.28:** 2d representation of the solutions to equations (6.11) with initial data (6.12), (6.14) and (6.15) using parameter values from Table 6.1 with  $u_S = (1, 0)$ ,  $u_P = (1, 1)$  and  $u_T = (1, 0)$ . Biomass accumulates on the boundary and penetrates the pollutant strip and some reaches the target “tile”. [For a movie of these plots please see external Folder labelled: Comsol - Movie\_files - Toxic - 3Tile - Fig-6.28]

In Figure 6.28 a build up of model biomass is observed at the edge of the toxic strip but some biomass was able to cross the strip, take up substrate en route and reach the target “tile”. Interestingly a build up of biomass on the right hand side of the toxic strip is observed. This is due to the low levels of toxicity present on the borders of the pollutant “tile” causing the tip velocity to slow down when leaving the toxic strip resulting in a build up of biomass and which is supplemented by the extra substrate present due to the increased size of the pollutant “tile”. A cross sectional representation is shown in Figure 6.29.

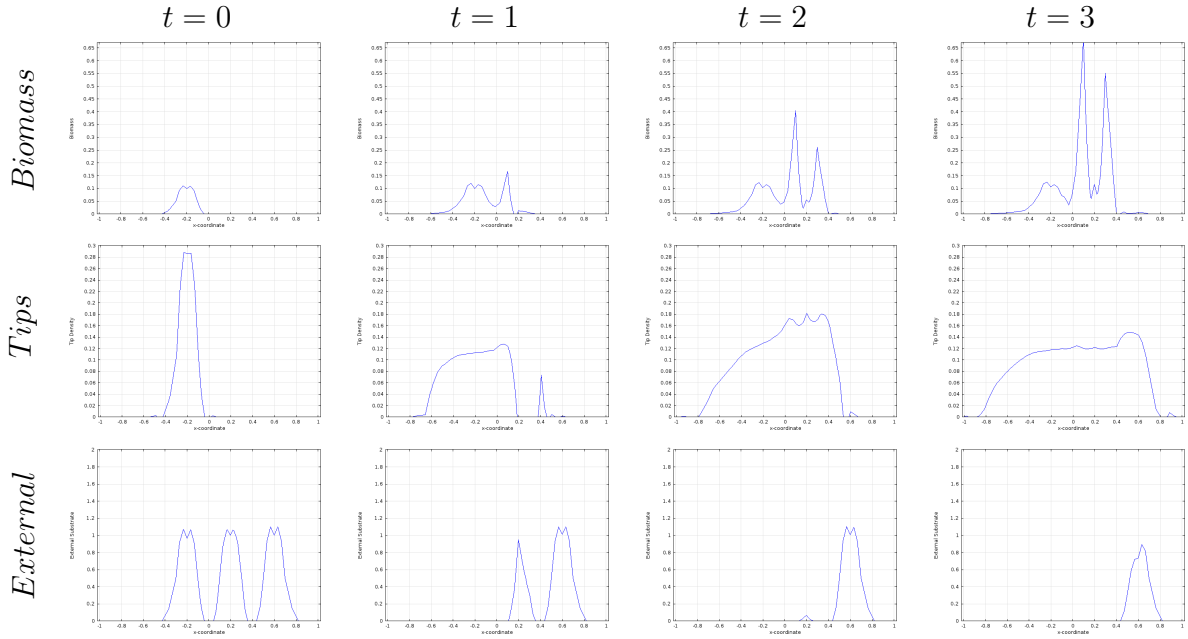


**Figure 6.29:** Cross sectional representation along  $y = 0$  of biomass, tip density and external substrate obtained from solutions to equations (6.11) with initial data (6.12), (6.14) and (6.15) using parameter values from Table 6.1 with  $u_S = (1, 0)$ ,  $u_P = (1, 1)$  and  $u_T = (1, 0)$ . Biomass penetrates the pollutant strip and tips grow rapidly on the target “tile”. The external substrate depletes on all “tiles”. [For a movie of these plots please see external Folder labelled:- Comsol - Movie\_files - Toxic - 3Tile - Fig.6.29]

The behaviour of the model biomass in Figure 6.29 resembles that observed in Figure 6.22. The adverse effects of pollutants on the biomass are seen via its accumulation on the borders of the pollutant strip (i.e. around  $x = 0.1$  and  $x = 0.3$ ) at time  $t = 3$ . As mentioned earlier, the result of biomass penetrating the pollutant strip and accumulating on the right hand side provides the biomass with sufficient energy to propel and acquire new resources from the target “tile”, which is indicated by the depletion of external substrate (Figure 6.29) (see also movie files *Fig.6.28* and *Fig.6.29*).

### 6.3.3.2 Biomass expansion from a limited nutrient domain across a highly toxic region abundant in resources

We further explore the effects of reducing the substrate level in the initial growth zone of the fungi (source “tile”) and keep all the other conditions the same as above to observe the impact of initial resources. We solve the model equations

(6.11) with initial data (6.12), (6.14) and (6.15) using the parameters specified in Table 6.1 with  $u_S = (0.5, 0)$ ,  $u_P = (1, 1)$  and  $u_T = (1, 0)$  using zero flux boundary conditions and generate results shown in Figure 6.30.

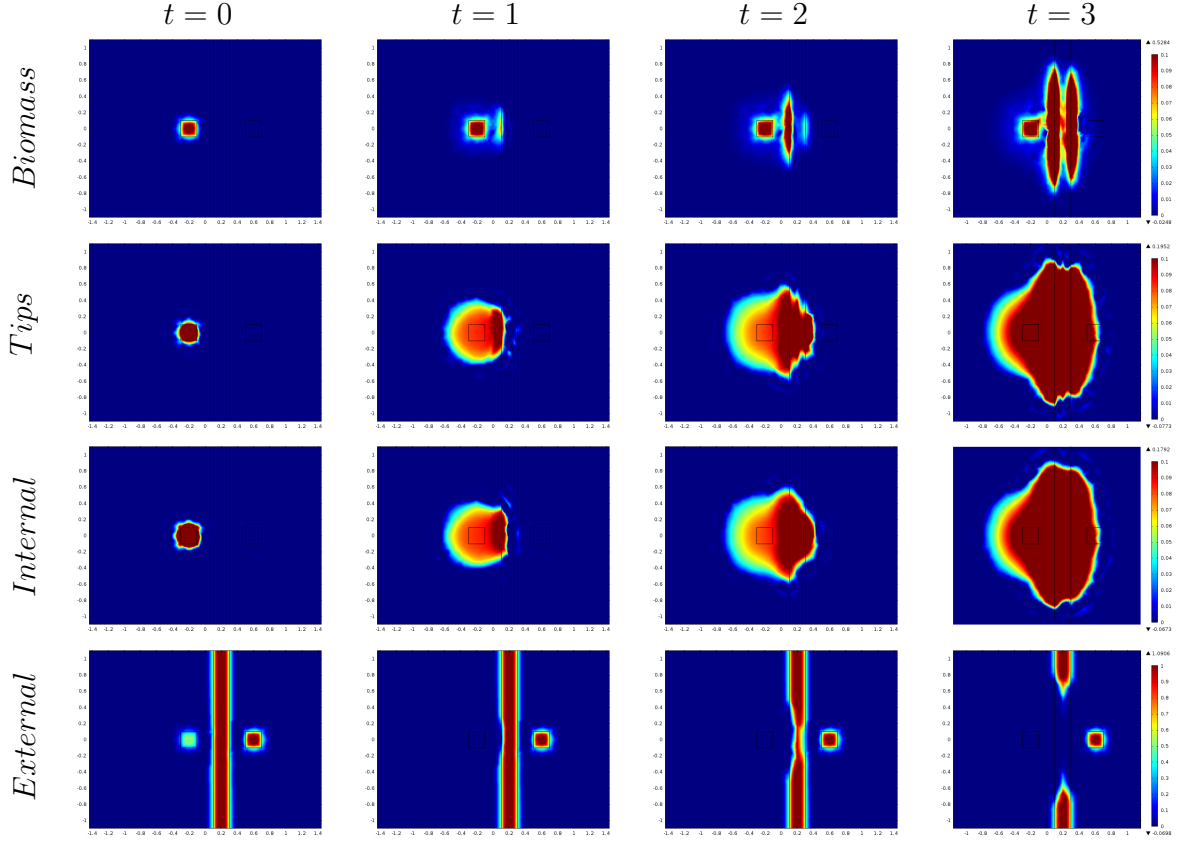


**Figure 6.30:** 2d representation of the solutions to equations (6.11) with initial data (6.12), (6.14) and (6.15) using parameter values from Table 6.1 with  $u_S = (0.5, 0)$ ,  $u_P = (1, 1)$  and  $u_T = (1, 0)$ . Biomass can be seen to accumulate on the left and right hand side of the pollutant strip. [For a movie of these plots please see external Folder labelled: Comsol - Movie\_files - Toxic - 3Tile - Fig-6.30]

In Figure 6.30 it is shown that the amount of biomass penetrating the pollutant strip decreased when the substrate in the source “tile” was reduced. There was a build up of biomass on the left hand side of the pollutant strip but at a lower density than before (see Figure 6.28). This result is due to the biomass having less energy to penetrate the hostile zone. The biomass can be seen to grow rapidly once some tips cross the pollutant strip (see movie files Fig-6.30). This phenomenon has been explained previously. A cross sectional representation is

shown in Figure 6.31.

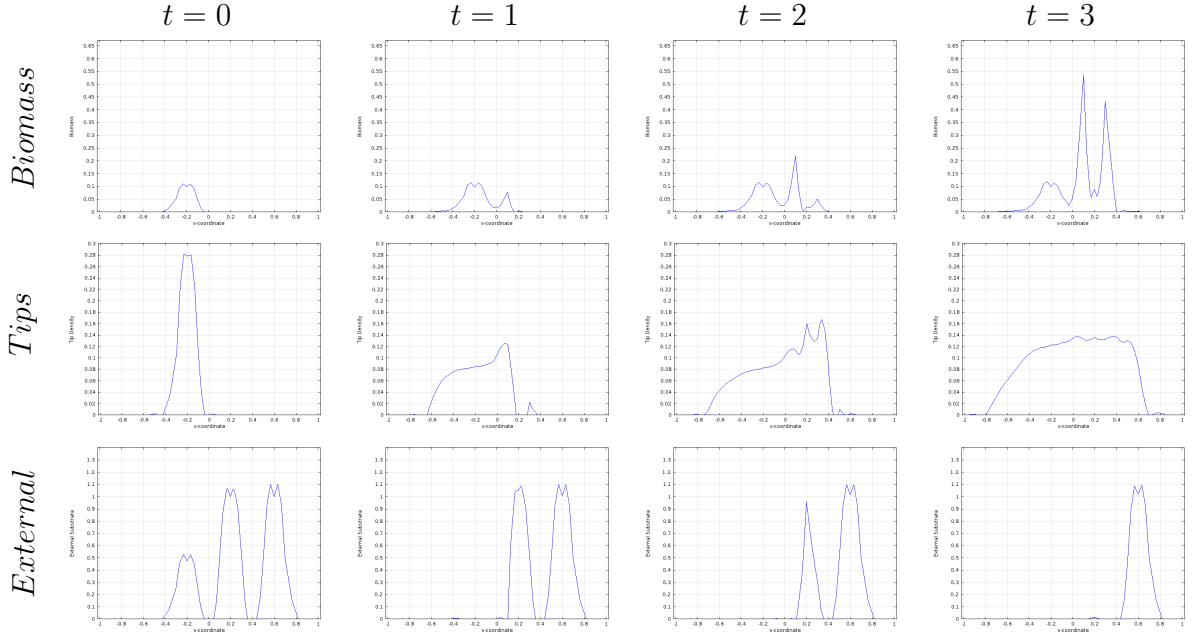


**Figure 6.31:** *Cross sectional representation of biomass, tip density and external substrate obtained from solutions to equations (6.11) with initial data (6.12), (6.14) and (6.15) using parameter values from Table 6.1 with  $u_S = (0.5, 0)$ ,  $u_P = (1, 1)$  and  $u_T = (1, 0)$ . Biomass has lower density, consumed substrate from the pollutant strip but has not from the target domain. [For a movie of these plots please see external Folder labelled:- Comsol - Movie\_files - Toxic - 3Tile - Fig-6.31]*

The key observations from Figure 6.31 is that the biomass has a lower density than the previous case in Figure 6.29 and the external substrate on the target “tile” has not been altered, thus signifying the lack of biomass present in the location (see movie file *Fig.6.31*). This reduction in biomass expansion is solely due to the reduction in initial resources.

### 6.3.3.3 Biomass expansion from a scarce nutrient source across a highly toxic region with limited resources

We will now explore the effects of lowering the nutrient levels in the toxic strip. Model equations (6.11) are solved with initial data (6.12), (6.14) and (6.15) using the same set of parameters in Table 6.1 with  $u_S = (0.5, 0)$ ,  $u_P = (0.1, 1)$  and  $u_T = (1, 0)$  generating results in Figure 6.32.



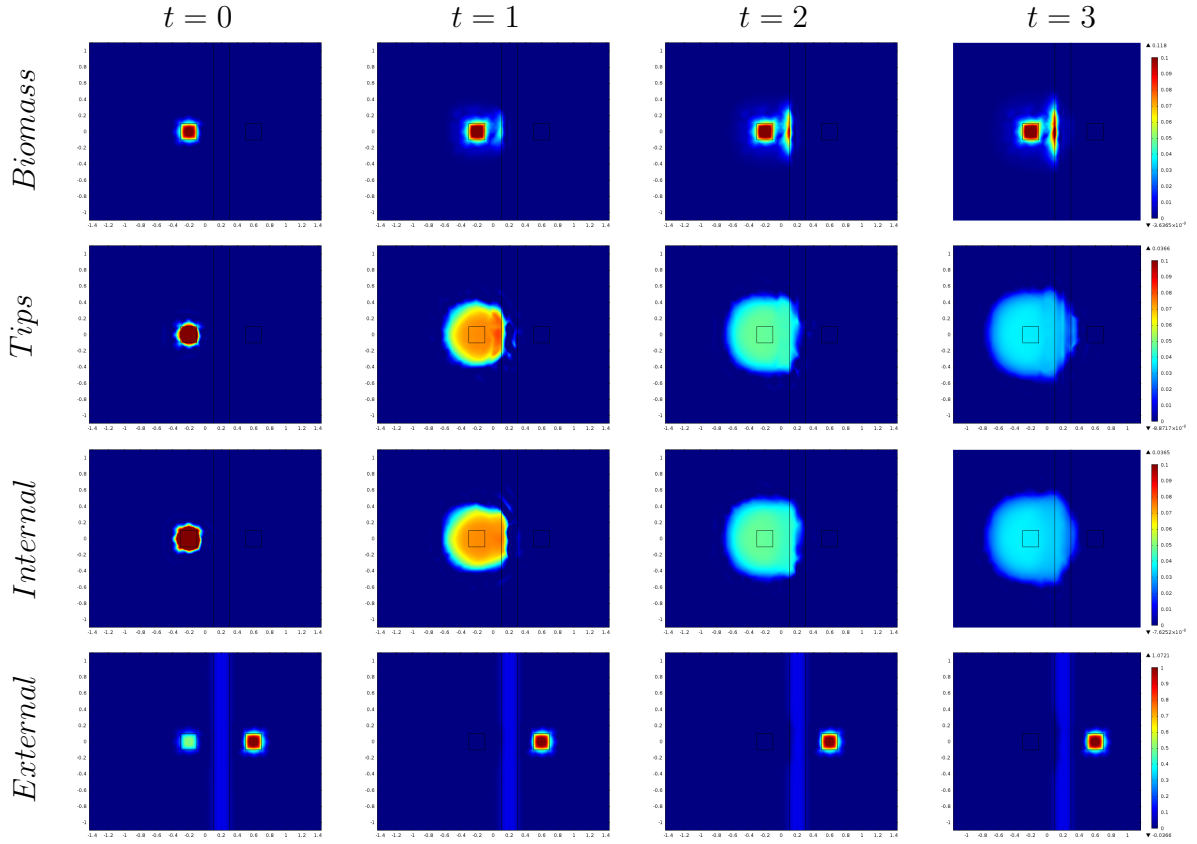


**Figure 6.32:** *2d representation of the solutions to equations (6.11) with initial data (6.12), (6.14) and (6.15) using parameter values from Table 6.1 with  $u_S = (0.5, 0)$ ,  $u_P = (0.1, 1)$  and  $u_T = (1, 0)$ . Biomass can be seen to accumulate on the boundary and fail to penetrate the pollutant strip. [For a movie of these plots please see external Folder labelled: Comsol - Movie\_files - Toxic - 3Tile - Fig-6.32]*

We see from Figure 6.32 that the biomass does not penetrate the pollutant strip in the same way as before when the amount of substrate in this region is reduced. We do see that while some tips are able to penetrate due to diffusion, their density is not sufficient for them to form a significant concentration of biomass. The one dimensional plot in Figure 6.33 shows a clearer picture of the behaviour of biomass, tip density and external substrate.

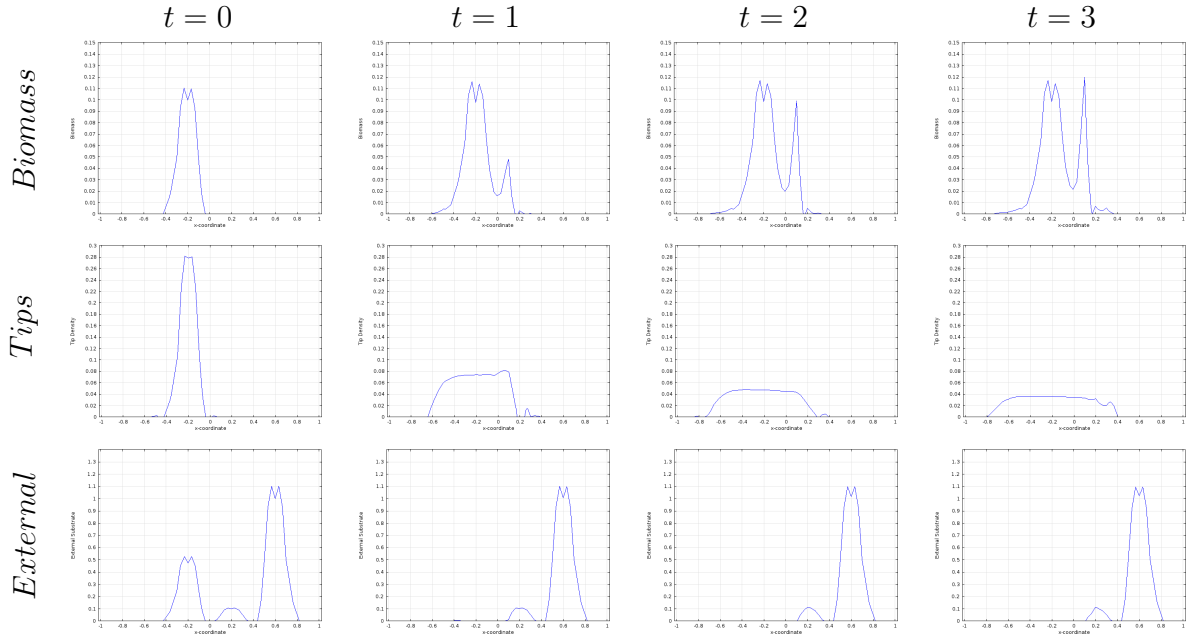


**Figure 6.33:** *Cross sectional representation of biomass, tip density and external substrate obtained from solutions to equations (6.11) with initial data (6.12), (6.14) and (6.15) using parameter values from Table 6.1 with  $u_S = (0.5, 0)$ ,  $u_P = (0.1, 1)$  and  $u_T = (1, 0)$ . Biomass can be seen failing to penetrate the pollutant strip and reach the target domain. [For a movie of these plots please see external Folder labelled:- Comsol - Movie\_files - Toxic - 3Tile - Fig\_6.33]*

It is seen in Figure 6.33 that the majority of the biomass has halted at the periphery of the pollutant strip resulting in an accumulation within the gap between the “tiles”. The external substrate on the source “tile” depletes which results in the demise of the biomass (see movie file *Fig\_6.33*).

### 6.3.4 Biomass expansion on toxic domain

As mentioned previously, an interesting observation made by Fomina et al. (2003) was that a species of fungi was seen to accumulate hyphae on the border of the toxic domain (see Figure 6.2) and then penetrate and form a small colony on toxic “tiles” at low toxic concentrations and at varying nutrient levels. No possible explanation was given for this phenomenon. However, we conjecture that non-uniform mixing of the metal chloride with the nutrient in the formation of the agar or due to natural diffusion is sufficient to create such structures. We will here use our model to test this hypothesis.

The region of interest is the middle strip and hence we will consider a circular region within the pollutant strip to represent a location (or patch) where a high concentration of substrate is clustered. Figure 6.34 shows a schematic diagram of the domain.

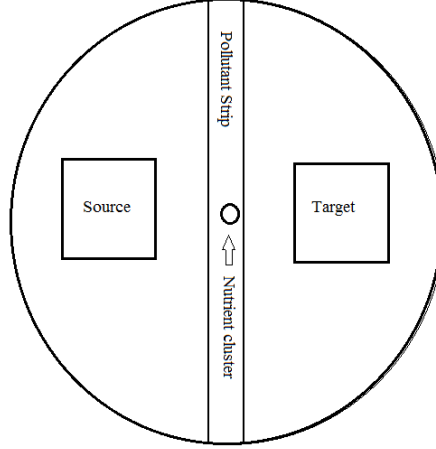


**Figure 6.34:** *Schematic representation depicting the formation of cluster of nutrients on a toxic strip domain.*

The initial data for the Source, Pollutant, and Target “tiles” are taken to be the same as before. The Patch on the pollutant “tile” has identical conditions to the Target “tile” i.e.

$$\begin{aligned} \rho(x, y, 0) &= \rho'(x, y, 0) = n(x, y, 0) = s_i(x, y, 0) = 0, \\ T(x, y, 0) &= T_0, \\ s_e(x, y, 0) &= \begin{cases} s_{e0}^{high}, & \text{if } \sqrt{(x - 0.23)^2 + y^2} \leq 0.03, \\ s_{e0}, & \text{otherwise,} \end{cases} \end{aligned} \quad (6.16)$$

where all parameters are the same as before (see Section 6.3.1.1) except the pollutant strip now contains a patch with high substrate denoted by  $s_{e0}^{high}$ . For convenience, initial data for the patch will be denoted using the notation,  $u_H = (s_{e0}, T_0)$  representing external substrate and toxicity levels respectively.

The model equations (6.11) with initial data (6.12), (6.15) and (6.16) using default parameters in Table 6.1 with  $u_S = (0.5, 0)$ ,  $u_P = (0.1, 1)$ ,  $u_T = (2, 0)$  and  $u_H = (1, 0)$  were solved using similar techniques to those in the previous sections. The following simulation depicts the growth of biomass in the presence of

a pollutant strip containing a region where a cluster of substrate has accumulated (Figure 6.35).

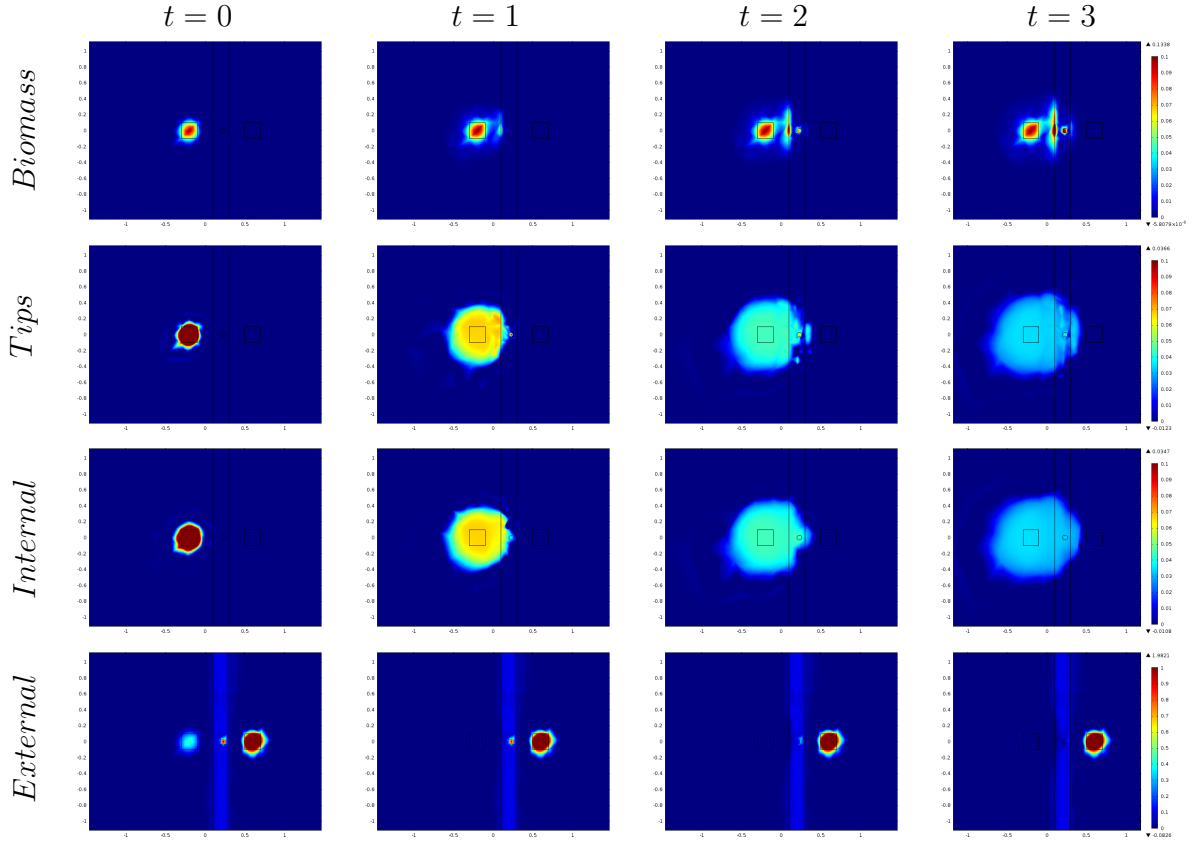


**Figure 6.35:** *2d representation of the solutions to equations (6.11) with initial data (6.12), (6.14), (6.15) and (6.16) using parameter values from Table 6.1 with  $u_S = (0.5, 0)$ ,  $u_P = (0.1, 1)$ ,  $u_T = (2, 0)$  and  $u_H = (1, 0)$ . Biomass accumulates on the pollutant strip around the circular patch. [For a movie of these plots please see external Folder labelled: Comsol - Movie\_files - Toxic - 3Tile - Fig-6.35]*

We see from Figure 6.35 that our hypothesis has successfully captured the phenomena observed by Fomina et al. (2003) regarding concentrated biomass growth in toxic regions (see movie file *Fig-6.35*).

When the same model equations are solved over a larger period of time the biomass developing within the central region can extend across the pollutant “tile” and ultimately reach the target “tile” (see Figure 6.36).

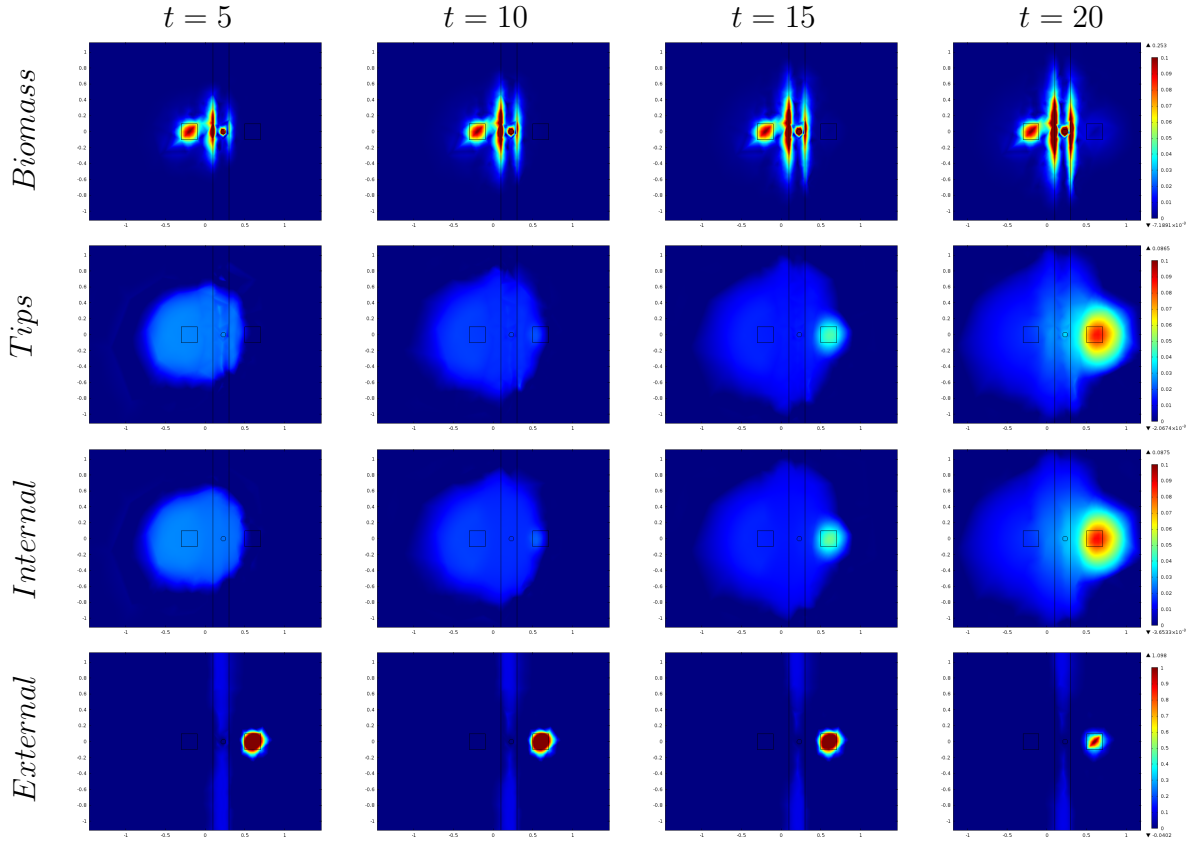


**Figure 6.36:** *2d representation of the solutions to equations (6.11) with initial data (6.12), (6.14), (6.15) and (6.16) using parameter values from Table 6.1 with  $u_S = (0.5, 0)$ ,  $u_P = (0.1, 1)$ ,  $u_T = (2, 0)$  and  $u_H = (1, 0)$  run for longer times. Biomass can be seen to accumulate on the pollutant strip on the circular patch and reach the target domain. [For a movie of these plots please see external Folder labelled: Comsol - Movie\_files - Toxic - 3Tile - Fig.6.36]*

Figure 6.36 shows that the biomass can penetrate the toxic strip and colonise the patch of nutrients within the toxic region. After absorbing the substrate, the biomass can move out of the toxic region and start to colonize the outer parts of the toxic region. We also observe that the biomass has reached the newer resource “tile” and increased its density accordingly.

## 6.4 Conclusion

In this chapter we have primarily used the work of Fomina et al. (2000, 2003) as a template to construct and apply the model equations to predicting the response

of fungi to polluted landscapes. We have tested various cases from these papers and successfully replicated some observations with the aid of numerical simulations. Typically fungal experiments take a significant amount of time (between days and weeks) to obtain results and numerous replicates are needed. With our model we can simulate several observations within the space of a few minutes and provide useful insights about the biology otherwise not obvious from experimental observations alone.

One such case is the formation of biomass on the toxic domain, a phenomenon which until now has been unexplained. Our hypothesis, namely that non-uniform mixing of the metal chloride with the nutrient in the formation of the agar or due to natural diffusion, is sufficient to create structures seen in Fomina et al. (2003) is certainly plausible considering the unlikeliness of performing perfectly uniform mixing of substrate onto a fine medium (tiles are of size  $10 \times 10 \times 3$  mm). Thus some patches may contain higher nutrient concentrations allowing the hyphae to colonise and provide additional energy to the leading tips so they can move out of the toxic region and scour for newer resources.

Another aspect explored using the model was the impact of inoculating biomass on a substrate rich domain to observe how it reacts with adverse conditions. It was shown that provided the biomass had access to significant amounts of resources in its immediate vicinity, it is better able to react and even penetrate polluted regions (i.e. more “energy” is available to overcome the effects of the toxicity). This aspect was not explored in Fomina et al. (2000, 2003). While further different scenarios could have been explored by applying different combinations of the parameter variables and initial data, we have only focused on a handful of cases that were similar to the experiments of Fomina et al. (2000, 2003).

It was stated by Olishkevskya and Zhdanova (2009) that in a toxic metal-containing domain, aggregated mycelia could produce high local concentrations of many extracellular products, such as chelating and sequestering agents (e.g. siderophores) with metal-binding abilities (Gadd, 1993; Morley et al., 1996; Baldrian, 2003; Olishkevskya and Zhdanova, 2009). Surprisingly, no previous modelling study, at least to the author’s knowledge, has investigated the production of such agents. Hence, in the following chapter we will investigate such phenomena by developing a suitable mathematical framework.

## Chapter 7

# Iron in Fungi: Modelling the Role of Siderophores in Iron Acquisition

Iron is an essential element for nearly all life forms on earth. Iron deficiency can lead to several chronic medical conditions in humans such as anemia (Zimmermann and Hurrell, 2007; Beard, 2008). In plants, iron deficiency can severely hinder growth. One third of the world's soils are considered to be iron deficient due to the insolubility of ferric iron present in the environment (Marschner, 1995). Eukaryotic cells contain a large number of iron-dependent proteins, responsible for major cellular activity. Nutritional iron is not readily available in terrestrial environment thus various microorganisms have evolved mechanisms to cope with iron scarcity. These mechanisms have been studied at the molecular level for various microscopic eukaryotes such as bacteria and pathogenic fungi (Philpott et al., 2012). In fungi, four different mechanisms for the acquisition of iron have been identified (Helm and Winkelmann, 1994; Renshaw et al., 2002, and references therein) (i) Shuttle mechanism: ferric iron uptake mediated by ferric iron specific chelators (siderophores), (ii) Direct-transfer mechanism: reductive iron assimilation, (iii) Esterase-reductase mechanism: low-affinity ferrous iron uptake and (iv) Reductive mechanism: heme uptake and degradation (Haas, 2014). We will focus our attention on the first of these mechanisms. Under iron-limited conditions, microorganisms produce and secrete small organic molecules called siderophores to enhance the uptake of iron (Schwyn and Neilands, 1987; Saha et al., 2016). Siderophores are typically produced by bacteria, fungi and mono-

cotyledonous plants (Ratledge and Dover, 2000). Siderophore functions comprise uptake, intracellular transport and storage of iron.

Siderophores have drawn much attention in recent times due to their potential roles and applications in various bio-technologies including agriculture, ecology, bio-remediation, bio-control, bio-sensor and medicine (Saha et al., 2016). Siderophores (Greek *sideros* meaning iron and *phores* meaning bearers) are low molecular weight iron chelating compounds that have a high affinity for ferric iron. Generally once the siderophores are attached to the ferric iron, the iron-siderophore complexes are transported (Srivastava et al., 2013) and can be acquired by the organism, where the iron is internalised and used to support further biomass growth and function. Their significance in applications are mainly due to siderophores having the ability to bind to a variety of metals in addition to iron (Bellenger et al., 2008; Braud et al., 2009; Sasirekha and Srividya, 2016). For example, siderophores play a crucial role in mobilising metals from metal-contaminated soils (Ahmed and Holmström, 2014, and references therein). Additionally in bio-control, microorganisms that produce certain siderophores can take up iron from around their immediate vicinity and invade a competitor's space in search for iron, which leads to the suppression of growth of several fungal pathogens (McLoughlin et al., 1992; Verma et al., 2011).

In Chapter 6 the work of Fomina et al. (2000, 2003) was explored which involved investigating the interactions between some strains of fungi (*T. Viride* and *C. Rosea*) with toxic metals (principally cadmium and copper). A key observation made from the experiments was the ability of hyphae to penetrate the polluted domain in response to varying levels of nutrient and metal concentration; for example under low levels of toxic metals, hyphae were able to penetrate and even cultivate the pollutant tile but this ability declined with greater metal concentration. Siderophores released by the respective fungi could be a possible explanation for this phenomena since too much metal can be lethal to the organism, also less siderophores are released and taken up in the presence of high metal concentration.



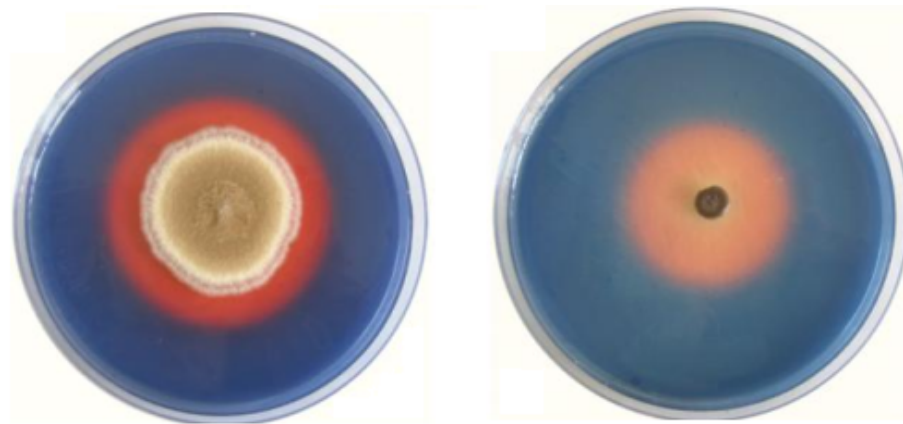
## 7.1 Siderophore detection in laboratory experiments

Siderophores exist throughout all hyphae in fungal mycelia. An internal mechanism within the organism is responsible for monitoring iron levels and when it detects a critical level of iron depletion, siderophores are released to the external environment in search of an iron source (Miethke and Marahiel, 2007). The amount of siderophores released depend on the species of microorganism under investigation and the internal concentration of iron. Species of fungi vary in their requirement of iron; some have an extreme affinity for iron and thus require greater quantities while others require less for colony functionality. Also siderophores are not always continuously released and iron is not always constantly taken up since too much iron can be harmful to the organism. Thus, once a threshold has been reached (for bacteria this is of the order  $10^{-5}$  mol/l, Neilands, 1995; Cabaj and Kosakowska, 2009), the release of siderophores is reduced or stopped altogether (Oberegger et al., 2001; Eisendle et al., 2006).

Siderophores are classified by the ligands (an ion, molecule, or molecular group that binds to another chemical entity to form a larger complex) used to chelate the ferric iron that can be categorised as catecholates, hydroxamates, and carboxylates (types of siderophore) (Winkelmann, 1991, 2002; Ahmed and Holmström, 2014). Fungi mostly produce siderophores that fall in the “hydroxamates” category and most species of fungi make more than one type of siderophore, possibly to adapt to different environmental conditions (Renshaw et al., 2002; Perez-Miranda et al., 2007; Johnson, 2008). Thus various assays have been developed to detect the different phenotypes of siderophores. While these assays are useful for identifying various siderophores, numerous assays would have to be formed independently to detect all possible forms of siderophores of which there are more than 500 known distinct types (Boukhalfa et al., 2003; Kraemer et al., 2005).

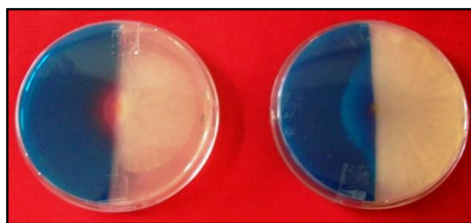
Schwyn and Neilands (1987) developed a universal siderophore detection assay using chrome azurol S(CAS) and hexadecyltrimethylammonium bromide (HDTMA) as indicators. The CAS/HDTMA complexes tightly bond with ferric iron to produce a blue colour. When a strong iron chelator, such as a siderophore, removes iron from the dye complex, the colour typically changes from blue to either orange, magenta or purple (see Figures 7.1 and 7.2). Siderophore production by microorganisms in solid medium can thus be measured by azurol S (CAS)-agar

plate assay. Typically the CAS complex is prepared and distributed uniformly on to a Petri dish. A fungal strain from a species of interest is grown on a Petri dish and a small segment is carefully sliced and placed on the centre of the uniform domain containing the CAS complex see Figure 7.1 (in some experiments a sterile toothpick is used to transfer the fungi, Andrews et al., 2016a,b). However, the high toxicity of CAS-blue agar medium caused by the detergent (HDTMA) impedes its utilisation with many varieties of fungi and bacteria. A modification of the CAS-agar plate assay was made by Milagres et al. (1999) incorporating the CAS-blue dye in a medium with no contact with the microorganisms, e.g. on a partitioned Petri dish. Half of each plate used in the experiments were filled with the most appropriate culture medium for each type of microorganism and the other half with CAS-blue agar (see Figures 7.2 and 7.3). This modification paved the way to study several strains of fungi (basidiomycetes, deuteromycetes, ascomycetes and zygomycetes) and bacteria (Gram positive and negative). All the microorganisms grew without interference from the CAS-blue agar and reacted in different manners to the CAS assay upon contact. Some strains of wood-decaying basidiomycetes (mainly white-rot fungi) and *Aspergillus* species produced the fastest colour-change reactions in the CAS-blue agar (Milagres et al., 1999). This modified method facilitated optimisation of culture conditions, since both CAS-blue agar and growth medium were prepared and added in the Petri dish separately.



**Figure 7.1:** *Experimental observation by Bertrand et al. (2010) on the production of siderophores. The pink halo around the fungal colony signifies the presence of siderophores.*

In summary, according to Milagres et al. (1999) a fungal strain is typically cultivated on an independent Petri dish laced with some form of substrate



**Figure 7.2:** *Experimental observation by Srivastava et al. (2013) on the production of siderophores observed via colour change occurring at the centre of the Petri dish.*

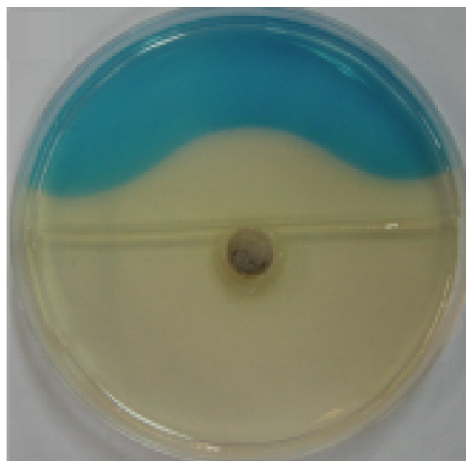


**Figure 7.3:** *Experimental observation by Indiragandhi et al. (2008) on the production of siderophores determined via colour change from blue to clear.*

(typically malt agar) and the CAS/HDTMA-iron (iron-complex) is prepared on a separate Petri dish. Once the iron-complex solidifies, it is cut in half and placed onto a new Petri dish, leaving one half empty. The other half is then laced with some nutrient such as potato agar extract (PAE), malt agar extract (MAE) or yeast morphology agar (YMA) upon which a small block of the cultivated fungal mycelium is firmly placed, making sure no interaction is made with the iron-complex. The Petri dish is then observed over a period of a few days. The fungal mycelium grows from its initial inoculum site and upon reaching the iron-complex an immediate colour change can be observed indicating the release of siderophores from the fungi that start to chelate the iron from the CAS-iron complex resulting in the colour change.

These types of experiments are primarily focused on the detection of siderophores, rather than the uptake process of the siderophore-iron complex by the fungal mycelium as it occurs in actual external habitats. As siderophores are considered to be organic compounds which are not currently detectable in standard experiments (i.e. without CAS agar), they can easily be mistaken to be part of the volatile organic compounds produced and used by some fungi in competition. The actual process of siderophore-iron complex uptake by fungi involves much more complexities including various cell activity such as transport, storing and release (see Haas, 2014, for a more complete description). We will not focus our attention to such intricacies but rather focus on the laboratory experiments

involving the detection of siderophores.

There is currently extremely limited literature on the mathematical modelling of siderophore study in fungi. The mathematical models that are available have limited use such as to quantify the siderophore via using simple ad-hoc approaches such as measuring the physical distance of the colour change on a Petri dish or placing square paper underneath the Petri dish and recording the change over a time period (in experiments involving solid medium) (Machuca and Milagres, 2003; Bogumił et al., 2013; Ghosh et al., 2015; Andrews et al., 2016a,b). These models tend to be linear. Siderophore study involving bacteria contain some publications on continuous approaches to modelling siderophore behaviour (Eberi and Collinson, 2009; Leventhal et al., 2016; Niehus et al., 2017). The models are typically a set of ODEs that are solved numerically. Leventhal et al. (2016, 2019) proposed a simple model representing siderophores produced by an isolated bacteria cell and subsequently interacting with iron to form siderophore-iron complexes. The focus of the study was primarily on the biology of the process but the supplementary materials shed some light on to the mathematical analysis. In particular, to this author's knowledge, there is no mathematical model of siderophore function applied to any organism more complicated than a single cell bacteria hence a novel approach is developed here in this chapter.

We will develop our previous mathematical models and extend them to capture known siderophore behaviours seen in experimental studies (Schwyn and Neilands, 1987; Milagres et al., 1999). Since the only visual clues relate to the colour change of the agar medium once the iron has been extracted from it, the initial model will focus exclusively up to the point when the iron is extracted from the external environment but not how the siderophore-iron complexes behave after that. Later analysis in Chapter 8 will consider simplified systems where the complexes are included and analytical treatments are possible.

## 7.2 Mathematical model and numerical simulation

The model equations (6.11) used to model the experimental work of Fomina et al. (2000, 2003) were adapted to represent the growth of a mycelium and the release of siderophores in a two-dimensional domain corresponding to a Petri dish.

The revised mathematical model to investigate the activity of siderophores

is therefore represented as

$$\begin{aligned}
\frac{\partial \rho}{\partial t} &= |vs_i n \nabla \rho + D_n s_i \nabla n + \kappa s_i n \nabla T| - d_\rho \rho, \\
\frac{\partial \rho'}{\partial t} &= d_\rho \rho - d_i \rho', \\
\frac{\partial n}{\partial t} &= \nabla \cdot (vs_i n \nabla \rho + D_n s_i \nabla n + \kappa s_i n \nabla T) + \alpha s_i \rho - \beta n \rho, \\
\frac{\partial s_i}{\partial t} &= \nabla \cdot (D_i \rho \nabla s_i - D_a \rho s_i \nabla n) + c_1 s_i \rho s_e \\
&\quad - c_2 |vs_i n \nabla \rho + D_n s_i \nabla n + \kappa s_i n \nabla T| - c_4 |D_a \rho s_i \nabla n| - c_5 g(s_i), \\
\frac{\partial s_e}{\partial t} &= D_e \nabla^2 s_e - c_3 s_i \rho s_e, \\
\frac{\partial C}{\partial t} &= D_C \nabla^2 C + g(s_i) - r_1 C I, \\
\frac{\partial I}{\partial t} &= D_I \nabla^2 I - r_2 C I, \\
\frac{\partial T}{\partial t} &= D_T \nabla^2 T,
\end{aligned} \tag{7.1}$$

using similar notation as before and where  $C$  denotes the concentration of siderophores,  $I$  denotes the iron concentration in the CAS agar and  $T$  denotes the toxic compound concentration in the CAS agar, e.g. HDTMA.  $D_C$  and  $D_I$  are the diffusion coefficients of siderophores and iron respectively,  $r_1$  and  $r_2$  are reaction constants associated with the loss of free iron and siderophores that have bonded to form siderophore-iron complexes. (The complexes themselves will not be modelled here but will be considered in Chapter 8). The parameter  $c_5$  is a constant associated with the energy used for the siderophores to be produced and released. Finally,  $g(s_i)$  is a function representing the production of siderophores which depends upon the internal substrate concentration  $s_i$ . For simplicity we will take

$$g(s_i) = g_0 s_i. \tag{7.2}$$

The function  $g(s_i)$  is an oversimplification of the production of siderophores but it does capture the key quality of siderophore production; in particular that the creation of siderophores is associated with the internal substrate concentrations within a hyphae; if the internal substrate level is zero there will be no siderophores produced. In our investigations we will assume that the type of fungi under observation is in an iron-depleted state and siderophores are continually being

released into the environment at a rate dependent upon internal resources. Thus we have neglected to include a process that reduces siderophore production when the internal concentration of iron is plentiful and hence note that this model may not be suitable for large time simulations in iron-rich settings.

We solve the system of PDEs (7.1) numerically in a circular domain, representing a Petri dish, with initial data representing experimental protocol. A zero flux boundary condition is assumed since in laboratory experiments there are no external addition or loss of biomass, nutrient or iron at the boundaries.

### 7.2.1 Siderophore detection on a partitioned domain

In this section we will investigate siderophore detection on a split domain similar to that observed in experiments proposed by Milagres et al. (1999).

We numerically integrate equations (7.1) in COMSOL. The domain comprises of two semi-circular regions with radius representing 2 cm joined together, one of which (left hand side) is inoculated by a model fungus and the other (right hand side) represents iron and HDTMA and where the origin corresponds to the centre of the circular domain. The parameter values used are given in Table 7.1.

The initial conditions for hyphae, tips, internal substrate and siderophores corresponds to the initial plug of mycelium placed on the Petri dish at  $(-M, 0)$  of radius  $R$ . Following earlier work, the initial conditions are therefore taken to be

$$\begin{aligned}\frac{\rho(x, 0)}{\rho_0} &= \frac{n(x, 0)}{n_0} = \frac{s_i(x, 0)}{s_{i0}} = \frac{C(x, 0)}{C_0} = \frac{1 - \tanh(\phi(r - R))}{2} \\ \rho'(x, 0) &= 0, \quad \frac{s_e(x, 0)}{s_{e0}} = \frac{1 - \tanh(\phi x)}{2} \\ \frac{I(x, 0)}{I_0} &= \frac{T(x, 0)}{T_0} = \frac{1 + \tanh(\phi x)}{2}\end{aligned}\tag{7.3}$$

where  $\phi$  is a scalar constant and  $r = \sqrt{(x + M)^2 + y^2}$  denotes the distance from the “inoculation” site. We set  $M = 0.2$  corresponding to the centre of each plug of mycelium and  $R = 0.2$  corresponding to the radius of the fungal inoculum throughout. The initial iron and toxic compound concentrations are proportional to  $\frac{1}{2}(1 + \tanh(\phi x))$ , which is mostly on the right hand side of the Petri dish and the external substrate concentration is proportional to  $\frac{1}{2}(1 - \tanh(\phi x))$  mostly on the left hand side of the Petri dish (schematic representation is shown in Figure 7.4). Note that the domain has the same dimensions as used in the Fomina et al.

(2000) experiments in Chapter 6.

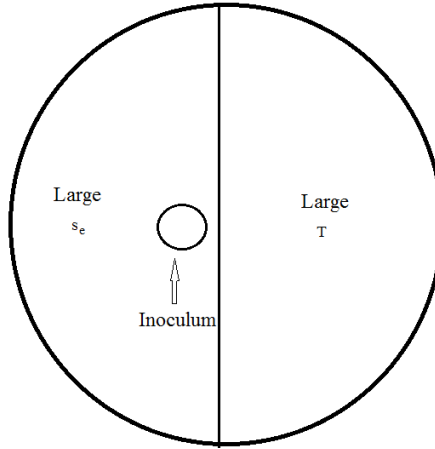


**Figure 7.4:** *Initial configuration used for the simulations.*

The model equations (7.1) were solved in COMSOL with the initial data in equation (7.3), parameter values from Table 7.1 and zero flux boundary conditions. A common problem with numerical software is a computational error resulting from a division by zero in the Jacobian matrix. To avoid such errors we incorporated an  $\epsilon$  term in certain absolute value expressions to avoid divisions by zero and set it the value  $\epsilon = 10^{-16}$  (smaller and larger values were considered in a small number of test cases but did not influence the results obtained). This is a standard approach designed to bypass numerical problems related to the precision of the computer used. Typical results are shown in Figure 7.5.

| Initial Parameters | Rescaled Value | Dimensions              | Description                              |
|--------------------|----------------|-------------------------|--|
| $v$                | 0.5            | $L^5T^{-1}N^{-1}$       | Directed tip velocity                    |
| $g_0$              | 1              | $MN^{-1}T^{-1}$         | Siderophore production rate              |
| $d_\rho$           | 0.2            | $T^{-1}$                | Hyphal inactivation rate                 |
| $d_i$              | 0              | $T^{-1}$                | Inactive hyphae loss rate                |
| $\alpha$           | $10^4$         | $LT^{-1}N^{-1}$         | Branching rate                           |
| $\beta$            | $10^4$         | $LT^{-1}$               | Anastomosis rate                         |
| $c_1$              | 900            | $L^3T^{-1}N^{-1}$       | Uptake rate of external substrate        |
| $c_2$              | 1              | $NL^{-1}$               | Growth cost                              |
| $c_3$              | $10^3$         | $L^3T^{-1}N^{-1}$       | Uptake of external substrate             |
| $c_4$              | $10^{-8}$      | $L^{-1}$                | Active translocation cost                |
| $c_5$              | $10^{-7}$      | $NM^{-1}$               | Siderophore secretion cost               |
| $D_n$              | 0.1            | $L^4T^{-1}N^{-1}$       | Tip diffusion coefficient                |
| $D_i$              | 10             | $L^3T^{-1}$             | Internal substrate diffusion coefficient |
| $D_a$              | 10             | $L^5T^{-1}$             | Active translocation constant            |
| $D_e$              | $10^{-4}$      | $L^2T^{-1}$             | External substrate diffusion coefficient |
| $D_C$              | 0.3            | $L^2T^{-1}$             | Diffusion coefficient of siderophores    |
| $D_I$              | $10^{-5}$      | $L^2T^{-1}$             | Diffusion coefficient of iron            |
| $D_T$              | $10^{-7}$      | $L^2T^{-1}$             | Toxic substance diffusion coefficient    |
| $\kappa$           | 2              | $L^6T^{-1}N^{-1}M^{-1}$ | Repellor strength coefficient            |
| $\phi$             | 20             | -                       | Scalar constant of initial data          |
| $r_1$              | $10^2$         | $L$                     | Reaction (loss) rate of Siderophores     |
| $r_2$              | $10^2$         | $L$                     | Reaction (loss) rate of iron             |
| $\rho_0$           | 0.1            | $L^{-1}$                | Initial active hyphal density            |
| $n_0$              | 0.1            | $L^{-2}$                | Initial tip density                      |
| $s_{i0}$           | 0.4            | $NL^{-2}$               | Initial internal substrate density       |
| $s_{e0}$           | 0.6            | $NL^{-2}$               | Initial external substrate density       |
| $C_0$              | 0.4            | $ML^{-2}$               | Initial siderophore density              |
| $I_0$              | 0.4            | $ML^{-2}$               | Initial iron density                     |
| $T_0$              | 2              | $ML^{-2}$               | Initial toxic compound density           |

**Table 7.1:** *The initial data and parameter values used to solve model equations (7.1). The parameter values used for fungal growth are from the calibrated experiments reported in Boswell et al. (2003a). The values for iron, siderophore and toxic compound have been assumed based on known similar calibrated processes.*

The hyphal biomass and tip density accumulate on the periphery of the toxicity zone (Figure 7.5). This is expected since the modelled toxicity restricts growth of hyphal biomass in the right hand region. As nutrients are present across the border, the hyphal biomass can be seen to grow parallel to the  $y$ -axis in this region. This is the typical behaviour seen in experiments, (see Figures 7.2 and 7.3). However, some hyphal tips penetrate the toxic region (Figure 7.5). This feature arises as the tip flux comprises a number of components and the “desire” of tips to avoid increased toxicity regions is cancelled out by their straight line growth habit coupled with diffusion. The presence of internal substrate is observed



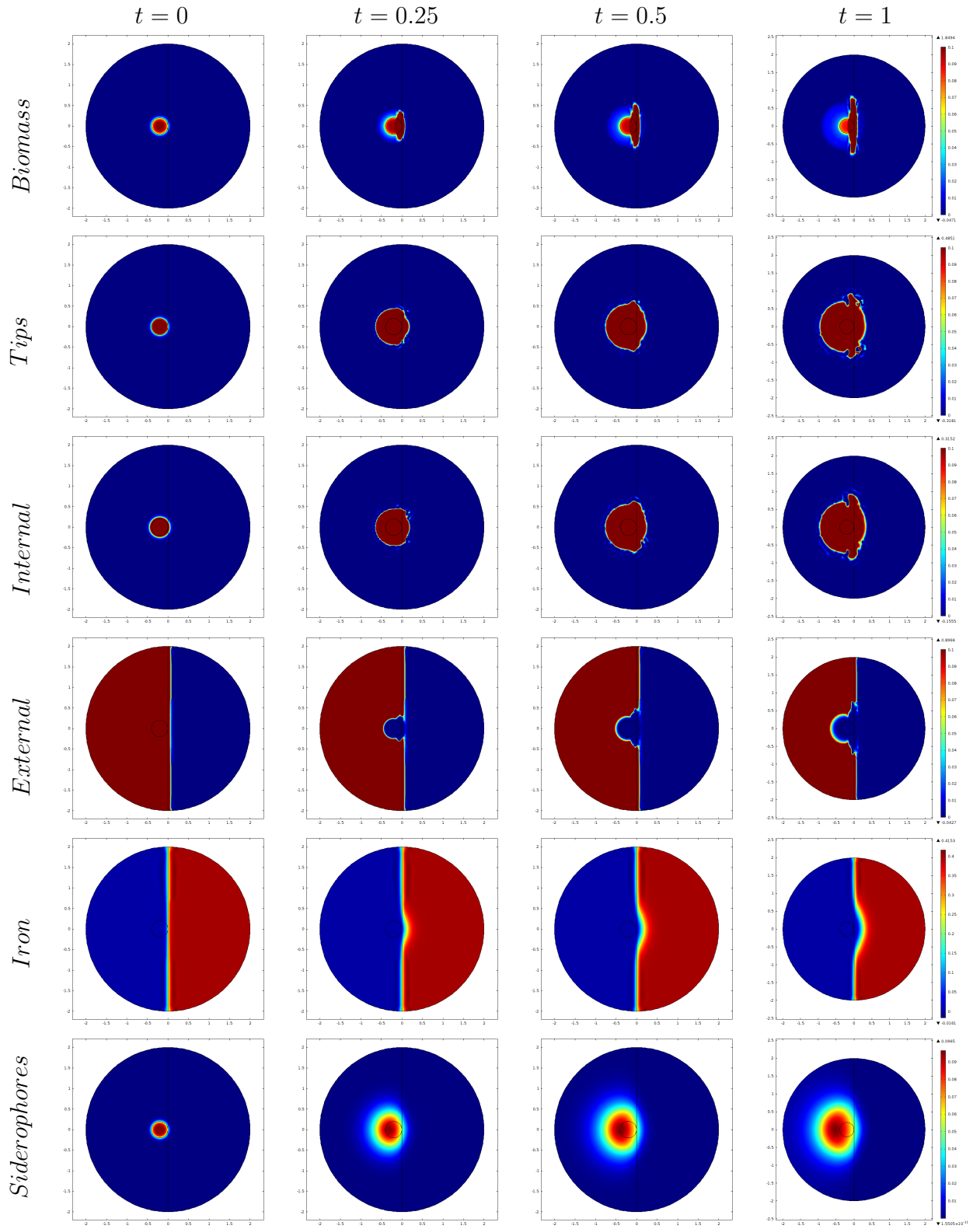


**Figure 7.5:** 2d representation of the solutions to equations (7.1) with initial data (7.3) and parameter values from Table 7.1 on a “fine” mesh grid size in COMSOL are presented. The total hyphal biomass ( $\rho + \rho'$ ), tip density ( $n$ ), internal substrate ( $s_i$ ), external substrate densities ( $s_e$ ), the iron ( $I$  on the right half domain) and siderophore concentrations ( $C$ ) are shown at times stated above. [For a movie of these plots please see external folder labelled: Comsol - Movie\_files - Fig-7.5]

throughout the domain and the resultant uptake of the external substrate.

An important observation from Figure 7.5 is the depletion of unbound iron due to the interaction with siderophores. A pseudo semi-circular region centred around the inoculation site can be seen to form, indicating the loss of iron and the presence of siderophores, consistent with experimental observations (Figures 7.2 and 7.3). Indeed, a “bulge” can also be seen to form on the periphery of the interaction zone that depicts the loss of iron. Also shown are regions where siderophores have not bound with iron. Siderophores seem to be present where there is a high presence of hyphal biomass. The proliferation of siderophore and the uptake of iron is shown in Figure 7.6 where the contours of siderophores are plotted. The depiction of siderophores in Figure 7.5, is in accordance to experimental observations (see, for example, Figures 7.2 and 7.3).

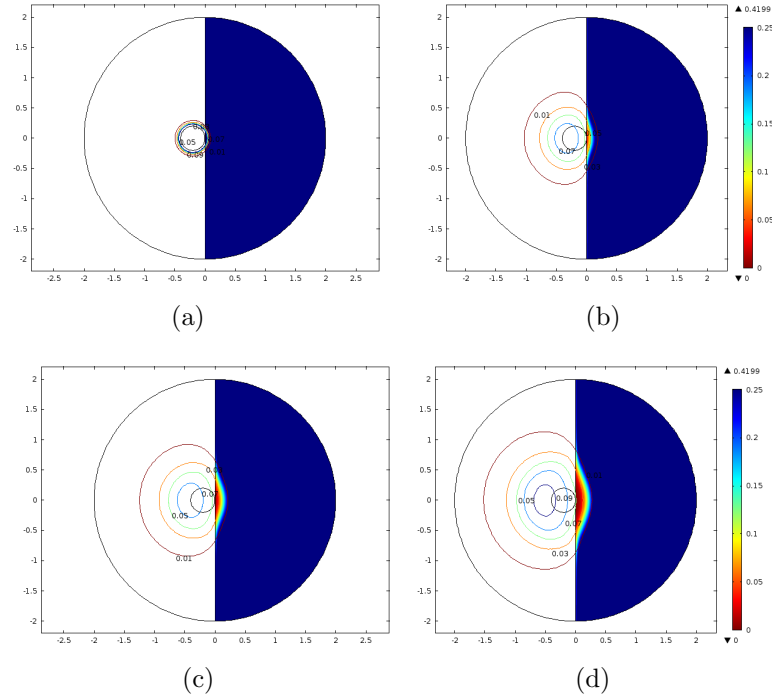


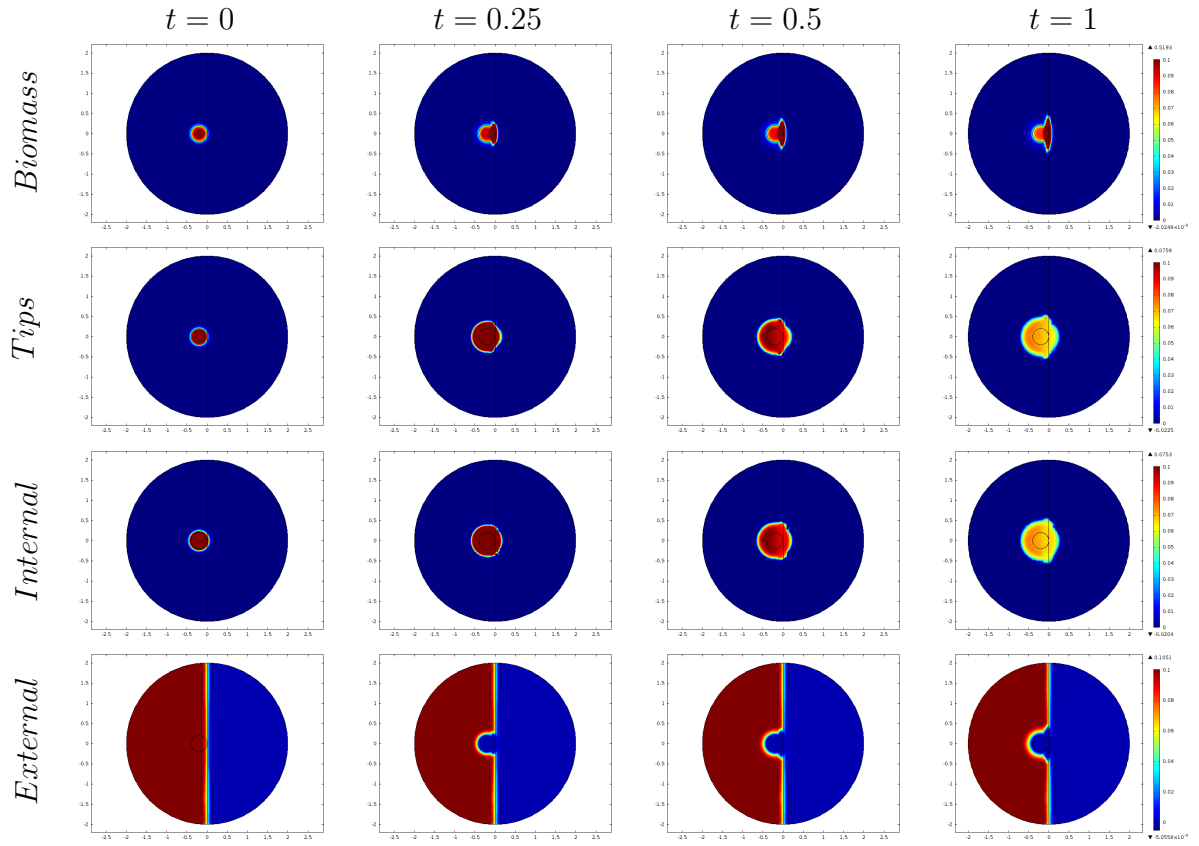
**Figure 7.6:** *The distribution of iron  $I$  (blue) and siderophores  $C$  (orange contours) of equations (7.1) solved with initial data (7.3) and parameter values from Table 7.1 is shown at times (a)  $t = 0$ , (b)  $t = 0.25$ , (c)  $t = 0.50$  and (d)  $t = 1$  respectively. [For a movie of these plots please see external folder labelled: Comsol - Movie\_files - Fig\_7.6]*

The numerical simulations in this current section corresponds to a species of fungi that have high repulsion against the toxicity present in the agar com-

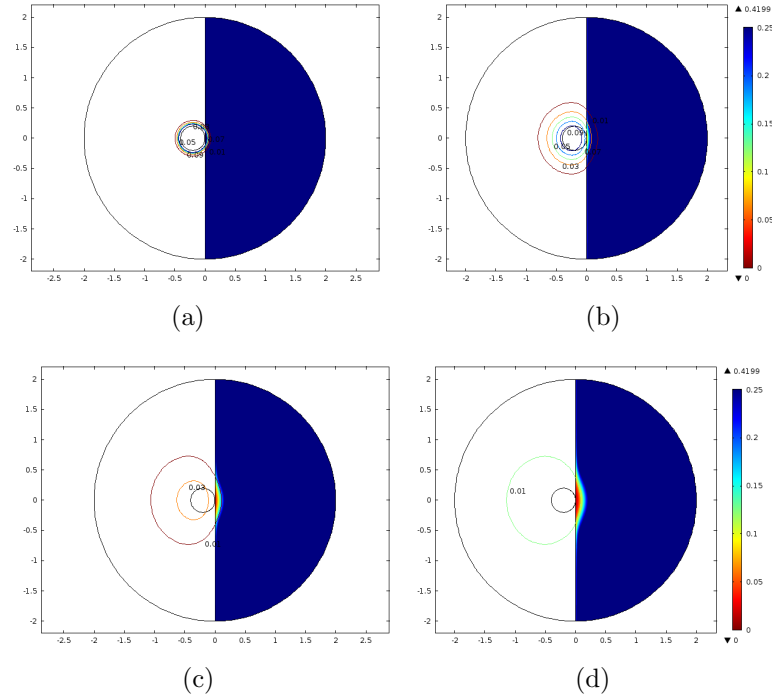
plex. The advantages of our mathematical model (7.1) is that it has the ability to fully explore alternative scenarios. Some of these possible cases include observing the siderophore behaviour with changes in the external nutrient, iron concentration, internal substrate and initial siderophore concentration. A subset of these scenarios will be explored via simulation in following sections.

### 7.2.2 Variations in the external substrate

We will simulate the behaviour of our model equations (7.1) with initial data specified in equation (7.3), using parameter values specified in Table 7.1 but varying only the maximum initial external substrate concentration ( $s_{e0}$ ). Specifically investigated are cases corresponding to, first, a reduced nutrient concentration (Figure 7.7 with  $s_{e0} = 0.1$ , compared to the default value of  $s_{e0} = 0.6$ ) and, second, an increased nutrient concentration ( $s_{e0} = 1$ ). When  $s_{e0} = 0.1$ , it can be seen in Figure 7.7 that the area covered by the model biomass has reduced due to the low quantity of substrate present in the domain compared to the default parameter case (Figure 7.5).



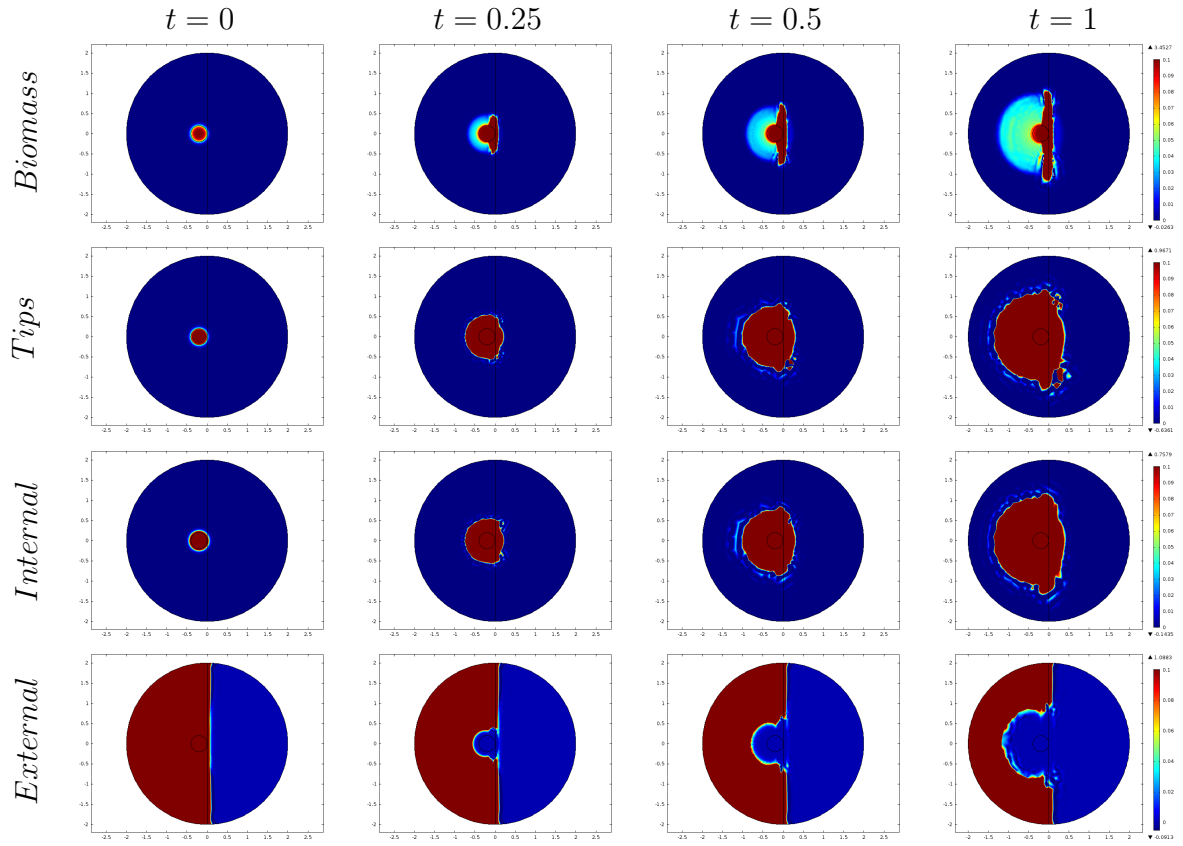
**Figure 7.7:** 2d representation of the solutions to equations (7.1) with initial data (7.3) and parameter values from Table 7.1 on a “normal” mesh grid size in COMSOL are presented. The total hyphal biomass ( $\rho + \rho'$ ), tip density ( $n$ ), internal substrate ( $s_i$ ) and external substrate densities ( $s_{e0} = 0.1$ ) are shown at times stated above. [For a movie of these plots please see external folder labelled: *Comsol - Movie\_files - Fig.7.7*]



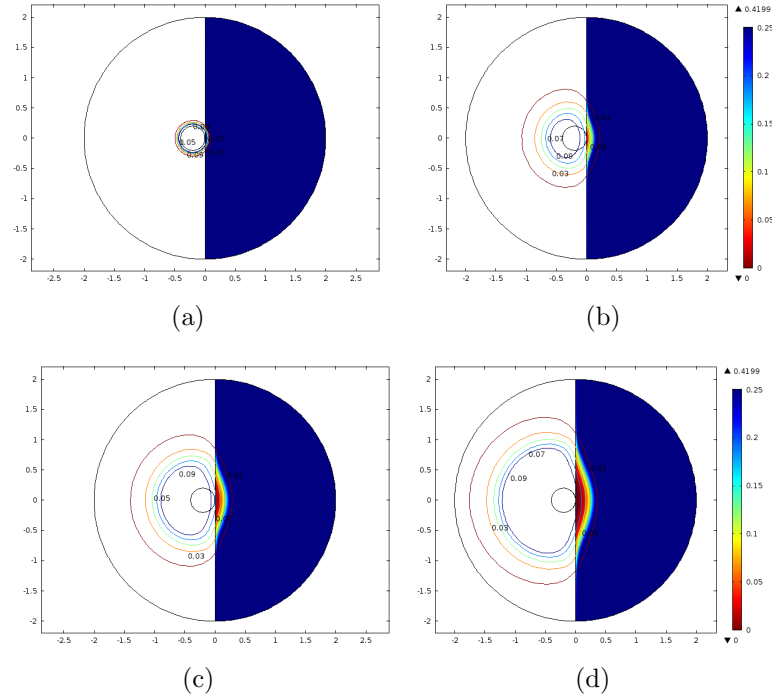
**Figure 7.8:** *The distribution of iron I (blue) and siderophores C (orange contours) under the influence of nutrient depleted substrate ( $s_{e0} = 0.1$ ) when equations (7.1) solved with initial data (7.3) and parameter values from Table 7.1 is shown at times (a)  $t = 0$ , (b)  $t = 0.1$ , (c)  $t = 0.50$  and (d)  $t = 1$  respectively. [For a movie of these plots please see external folder labelled: Comsol - Movie\_files - Fig.7.8]*

Figure 7.8 shows the distribution of siderophore populations and a small region where the iron have bonded with the siderophores. This distribution is significantly less than that observed when the default value for  $s_{e0}$  was used (Figure 7.6). Also, notice the contour levels on the left hand side are depleting with time. This is due to less external substrate in the domain, resulting in lower internal substrates and thus lower siderophore release.

Conversely when the external substrate concentration was increased (Figure 7.9) the model biomass extends over a greater area and is more dense than the default parameter case (Figure 7.5). Furthermore, Figure 7.10 shows a greater amount of siderophores present in the iron domain and thus a greater uptake of iron has arisen.



**Figure 7.9:** 2d representation of the solutions to equations (7.1) with initial data (7.3) and parameter values from Table 7.1 on a “normal” mesh grid size in COMSOL are presented. The total hyphal biomass ( $\rho + \rho'$ ), tip density ( $n$ ), internal substrate ( $s_i$ ) and external substrate densities ( $s_{e0} = 1$ ) are shown at times stated above. [For a movie of these plots please see external folder labelled: *Comsol - Movie\_files - Fig.7.9*]



**Figure 7.10:** *The distribution of iron I (blue) and siderophores C (orange contours) under the influence of nutrient-rich substrate ( $s_{e0} = 1$ ) when equations (7.1) is solved with initial data (7.3) and parameter values from Table 7.1 is shown at times (a)  $t = 0$ , (b)  $t = 0.25$ , (c)  $t = 0.50$  and (d)  $t = 1$  respectively. [For a movie of these plots please see external folder labelled: Comsol - Movie\_files - Fig\_7.10]*

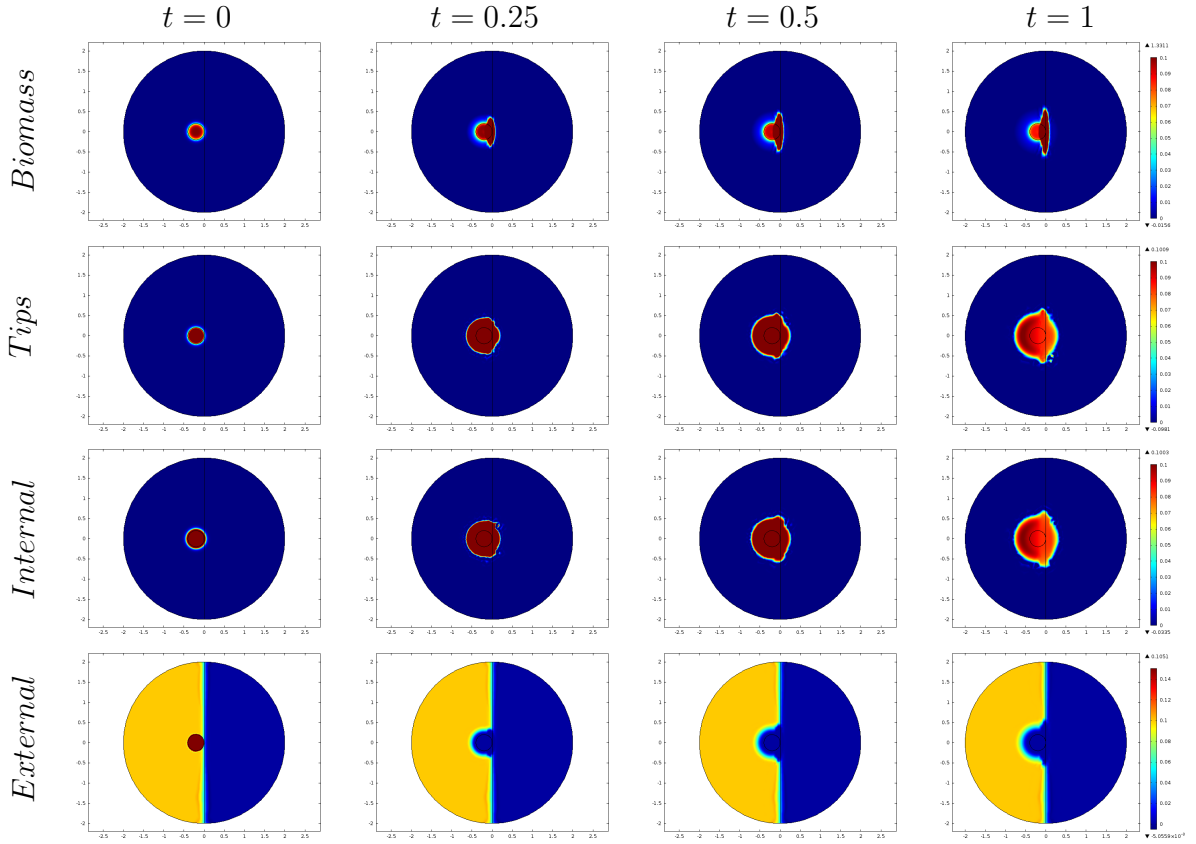
### 7.2.3 Non-uniform nutrient distribution

The focus of this section will be simulating the behaviour of fungi placed onto a nutrient rich region of the Petri dish. The nutrient preparation is an important aspect of controlled experiments (Schwyn and Neilands, 1987). We will explore how our system behaves in such situations by considering a simple case where the initial inoculum is placed on a single nutrient rich region of the Petri dish representing the instance when external nutrients from the culture used to form the inoculum is also transplanted. This will be depicted via changing the initial amount of external resource present on the Petri dish where the fungal inoculum is placed. We use the following initial data to denote the external substrate where

the inoculum is placed

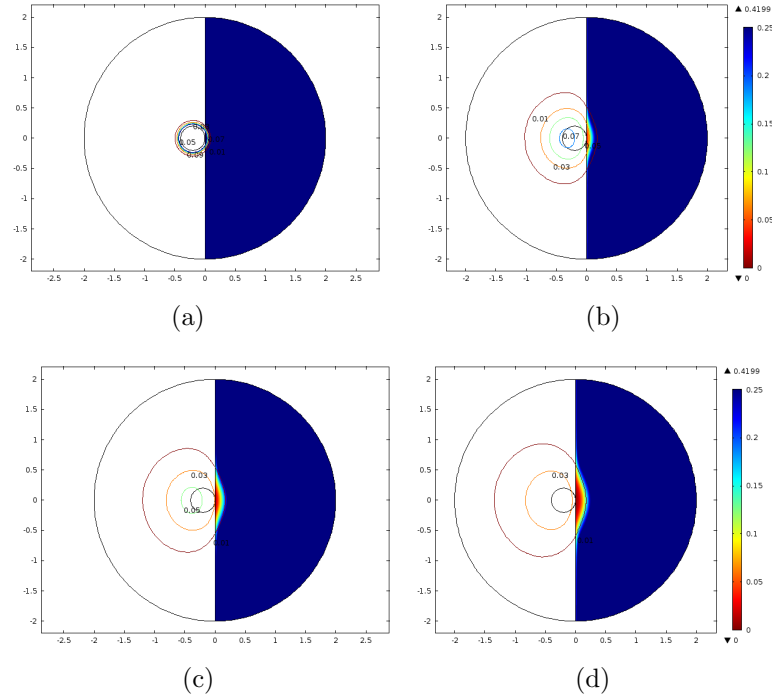
$$s_e(x, y, 0) = \begin{cases} s_{e0} \frac{(1 - \tanh(\phi x))}{2}, & \text{if } r > R, \\ \hat{s}_{e0} \frac{(1 - \tanh(\phi(r - R)))}{2}, & \text{if } r < R, \end{cases} \quad (7.4)$$

where  $r = \sqrt{(x + M)^2 + y^2}$ , where  $M = R = 0.2$  and  $\hat{s}_{e0}$  represents the maximum initial external substrate inside the inoculum region.  $s_{e0}$  still denotes the maximum initial substrate concentration outside of inoculum. Thus, setting  $\hat{s}_{e0} = 1$  and  $s_{e0} = 0.1$  and keeping all other parameters the same (Table 7.1), we obtain the results shown in Figure 7.11.



**Figure 7.11:** 2d representation of the solutions to equations (7.1) with initial data (7.3), (7.4) and parameter values from Table 7.1 except  $\hat{s}_{e0} = 1$  and  $s_{e0} = 0.1$  on a “normal” mesh grid size in COMSOL are presented. The total hyphal biomass ( $\rho + \rho'$ ), tip density ( $n$ ), internal substrate ( $s_i$ ) and external substrate densities ( $s_{e0}$ ) are shown at times stated above. [For a movie of these plots please see external folder labelled: Comsol - Movie\_files - Fig-7.11]





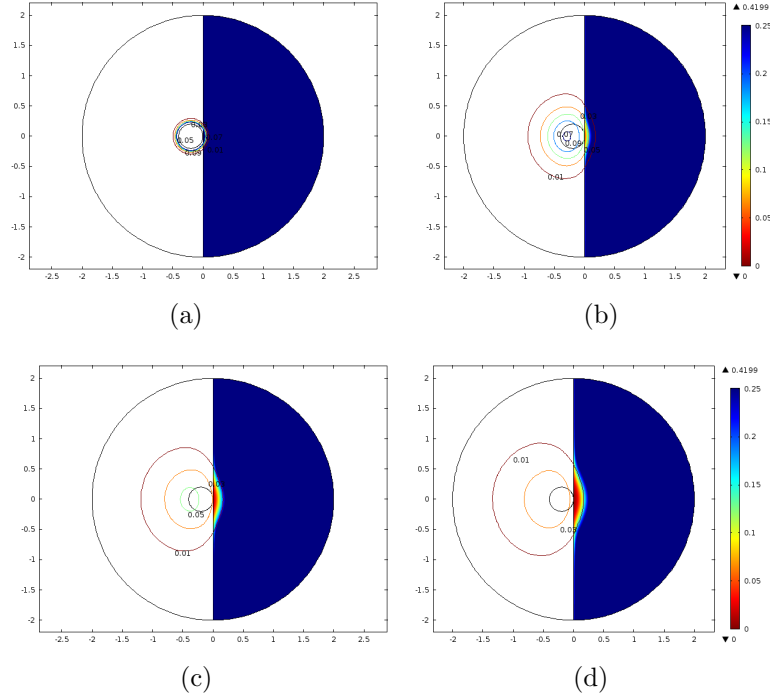
**Figure 7.12:** *The distribution of iron I (blue) and siderophores C (orange contours) under the influence of varying substrate ( $\hat{s}_{e0} = 1$  and  $s_{e0} = 0.1$ ) of equations (7.1) when solved with initial data (7.3), (7.4) and parameter values from Table 7.1 is shown at times (a)  $t = 0$ , (b)  $t = 0.25$ , (c)  $t = 0.50$  and (d)  $t = 1$  respectively. [For a movie of these plots please see external folder labelled: Comsol - Movie\_files - Fig-7.12]*

Figure 7.11 show that the biomass has covered only a small area of the Petri dish due to the low quantity of substrate present in the domain ( $s_{e0} = 0.1$ ) resulting in a lower uptake of iron and a reduction of siderophores produced, similar to the behaviour observed in Figure 7.7. In Figure 7.12, the presence of siderophores in the iron domain is much less than in Figure 7.8 but significantly more than in Figure 7.6 due to discrepancy in the initial nutrient concentration available to the fungi.

#### 7.2.4 Dependence on initial internal substrate

An interesting feature of our model is the initial internal substrate. In formulating the model we assumed the production of siderophores are determined by the amount of internal substrate within the mycelium. If a species of fungi is cultivated on a nutrient rich Petri dish from which an inoculum is taken and placed on the

Petri dish containing the iron, where the nutrient concentration is low minimal then the inoculum will have a greater quantity of internal substrate, hence it should be able to produce siderophores more rapidly. The corresponding model equations were solved as described above but with  $s_{i0} = 1$ . The results are very similar to that of Figure 7.7, therefore only the iron and siderophore contour plot is shown in Figure 7.13.



**Figure 7.13:** The distribution of iron  $I$  (blue) and siderophores  $C$  (orange) with high initial internal substrate ( $s_{i0} = 1$ ) in a low nutrient environment ( $s_{e0} = 0.1$ ) of equations (7.1) when solved with initial data (7.3), (7.4) and parameter values from Table 7.1 is shown at times (a)  $t = 0$ , (b)  $t = 0.25$ , (c)  $t = 0.50$  and (d)  $t = 1$  respectively. [For a movie of these plots please see external folder labelled: *Comsol - Movie\_files - Fig-7.13*]

It is interesting to observe from Figure 7.13 that siderophores are able to bind with a large quantity of iron. Comparing Figure 7.13 to Figure 7.8, it can be seen that more iron is taken up due to the greater initial internal substrate present. This is a significant observation because fungal species of interest are usually prepared on a separate Petri dish. A small region of the grown fungal mycelium is then sampled and placed on to the partitioned Petri dish on a new nutrient source. If the nutrient agar is not well mixed or a reduced concentration

of nutrient is used, the initial internal substrate can provide the initial burst of energy required for the fungi to look for an energy source or acquire essential minerals (i.e. iron).

The analysis in this section also demonstrates the role of the inoculum, namely the outcome can be influenced by which region of the mycelium a sample has been acquired since internal nutrients vary throughout the fungal colony.

### 7.2.5 Varying iron concentration

In this section we will explore the effects of increasing the iron concentration (from  $I_0 = 0.4$  to  $I_0 = 1$ ) on the right hand side of the domain.

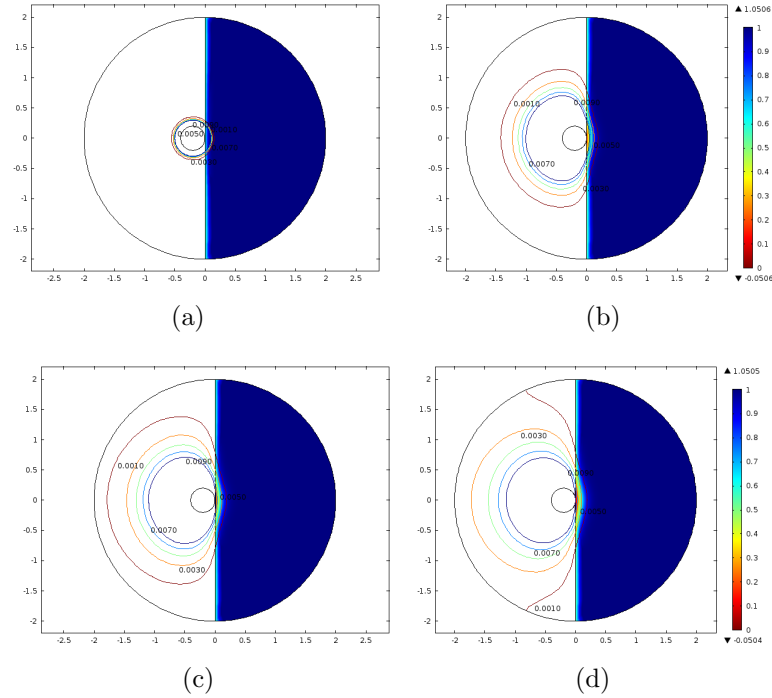


**Figure 7.14:** *Equations (7.1) is solved with with initial data (7.3), (7.4) and parameter values from Table 7.1. The distribution of iron  $I$  (blue) and siderophores  $C$  (orange contours) under the influence of a high iron concentration ( $I_0 = 1$ ) on the right hand side of the domain is shown at times (a)  $t = 0$ , (b)  $t = 0.25$ , (c)  $t = 0.50$  and (d)  $t = 1$  respectively. [For a movie of these plots please see external folder labelled: Comsol - Movie\_files - Fig.7.14]*

Figure 7.14 shows the penetration of siderophore into the iron domain exhibiting large concentrations of iron resulting in the uptake of iron having solved

the model equations as before.

Some experimental observations (Machuca and Milagres, 2003; Srivastava et al., 2013) have explored the impact of mixing different iron concentrations when preparing the agar (nutrient substrate) to see how it effects siderophore detection. We can explore various scenarios such as increasing the iron content on the left hand side of the Petri dish or have a continual addition of iron onto the inoculum to observe the impact on iron uptake. For simplicity we will explore the effects of a uniform distribution of iron across the Petri dish. Thus the corresponding initial data becomes  $I(x, y, 0) = I_0$  where  $I_0$  is a constant and all other parameters and initial data are unchanged (e.g. equation (7.3) and Table 7.1).

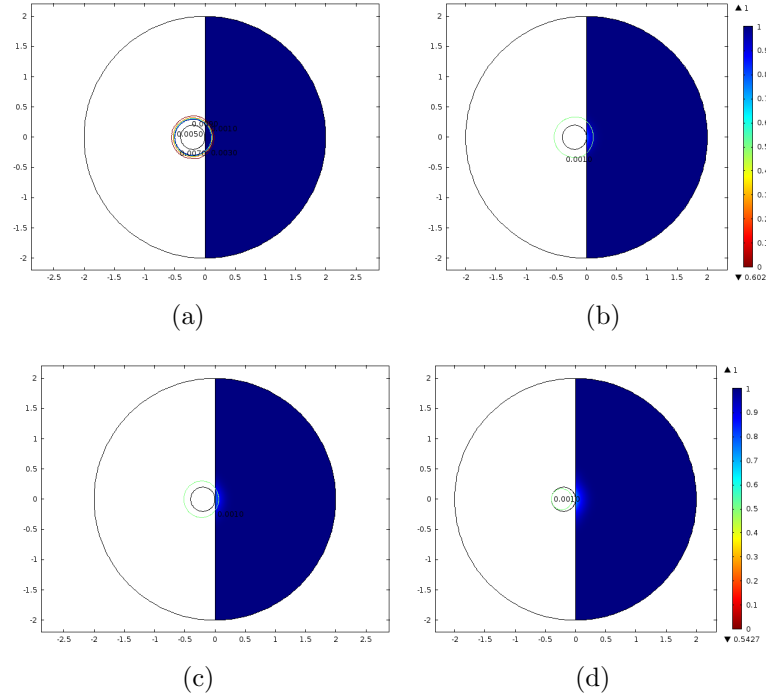


**Figure 7.15:** Equations (7.1) are solved with initial data (7.3), (7.4) and parameter values from Table 7.1. The distribution of iron  $I$  (blue) and siderophores  $C$  (orange contours) under the influence of high iron concentration across the domain ( $I(x, y, 0) = 1$ ) is shown at times (a)  $t = 0$ , (b)  $t = 0.25$ , (c)  $t = 0.50$  and (d)  $t = 1$  respectively. [For a movie of these plots please see external folder labelled: Comsol - Movie\_files - Fig-7.15]

Although the iron is distributed across the entire domain, Figure 7.15 depicts the iron concentration only on the right hand side of the domain. Thus comparing Figure 7.15 to Figure 7.14 it can be seen that less iron is taken up from

the right hand side of the domain. This is in correspondence with the experimental findings of Srivastava et al. (2013) and others where it was found that the higher the quantity of iron present in the domain containing the fungal inoculum, the less siderophores binded with the iron on the right hand side of the Petri dish. This behaviour is more prominent in the one dimensional cross sectional plot shown in Figure 7.16.

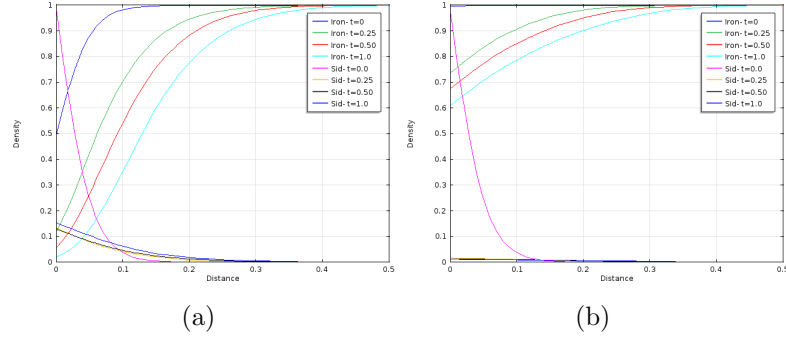


**Figure 7.16:** A cross section representation of iron  $I$  (right hand side of each plot) and siderophores  $C$  (left hand side of each plot). (a) Depicts the behaviour of siderophores when the initial iron concentration is large ( $I(x, y, 0) = 1$ ) is on the right hand side of the Petri dish only, (b) depicts the behaviour of siderophores when the initial iron concentration is large everywhere. Shown at times indicated. [For a movie of these plots please see external folder labelled: *Comsol - Movie\_files - Fig-7.16*]

## 7.3 Conclusion

The research on siderophore production and function in fungi is still in its adolescence. There are many new species of siderophores being detected and new information on their behaviour is being observed. Due to some fungi having the ability to uptake toxic substances from polluted landscapes in a safe and cost effective manner, the use of fungi in the area of bio-remediation has gained popularity over the past few decades. The intricate functionality of fungi in these fields has been well studied but only recently have the discovery and importance of siderophores come to light. However, mathematical research has been limited in the study of siderophores analysis.

The mathematical modelling in this chapter could shed some light onto studies involving siderophore and iron interactions. Often laboratory experiments

involving fungal interactions with iron require many replicates to be carried out to verify experimental results and observe the behaviours of different strains under varying conditions. This is often rewarded with insufficient outcomes forcing the experiments to be reproduced.

The model we have proposed in equation (7.1) is a continuous model that captures the entire process; the growth of fungi, uptake of nutrients, release of siderophores and interaction with iron. We solved the model equations numerically and simulated results resembling experimental observations (see Figures 7.5 - 7.16). Furthermore the model was explored under various conditions and the results obtained conformed to that observed in experiments (i.e. Milagres et al., 1999; Srivastava et al., 2013).

In Section 7.2.1 our model equations simulated experimental studies of Milagres et al. (1999), using partitioned Petri dishes. We explored the impact on growth of fungi and the detection of siderophores. It was found that external substrate impacted on the growth of the biomass and thus ultimately iron uptake. It maybe tempting to falsely conclude that in low nutrient environments fungi produce less siderophores. Aliasghar zad et al. (2009) found that in an extremely low micro-nutrient (such as Fe, Zn, Cu and Mn) environment, *Arbuscular mycorrhizal* fungi (AMF) secreted more siderophores, whereas regularly dosing the AMF with a commercial ‘nutrient solution’ reduced siderophore production. This does not nullify our result but rather it is in correspondence with our findings of increasing the iron concentration in the left hand domain (Figure 7.16). A possible explanation for less siderophore being detected in a low substrate domain is due to the biomass having less energy to produce siderophore, thus less siderophore are able to reach the iron domain.

The model explored a case of non-uniform external substrate distribution. It is our hypothesis that if the nutrient in the inoculum domain is not uniformly mixed, then it could have a negative impact on the detection of siderophores. Our model also investigated an interesting case related to varying internal substrate. In laboratory experiments fungi are grown on a separate Petri dish with its own source of growth medium. Once grown, a section is cut and put onto a fresh nutrient source region of the iron containing Petri dish. If the inoculum was taken from a region of the fungal colony where there is likely to be a high concentration of internal substrate present and placed onto the Petri dish with low external substrate, then a greater detection of siderophores is predicted (Figure 7.13). This

result may assist a researcher to determine which region the sample inoculum is taken from (i.e. the outer edges of the fungal colony may contain lower internal substrate).

The numerical simulations provided elements of a travelling wave solution that are most easily illustrated by viewing model siderophore and iron densities along the  $y = 0$  cross section of the domain (see Figure 7.17).

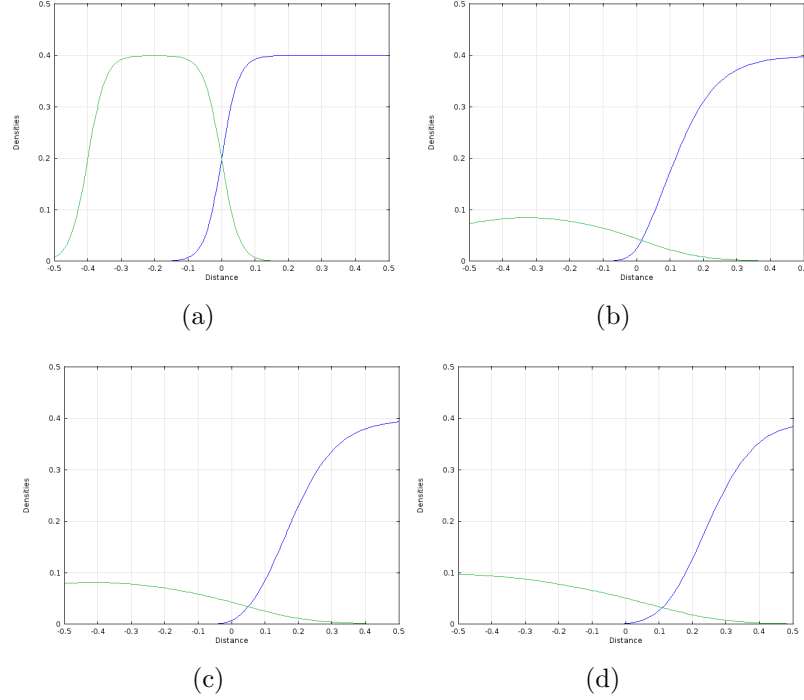


**Figure 7.17:** Equations (7.1) are solved with initial data (7.3) and parameter values from Table 7.1. The distribution of iron  $I$  (blue) and siderophores  $C$  (green) from Figure 7.5 along  $y = 0$  is shown at times (a)  $t = 0$ , (b)  $t = 0.25$ , (c)  $t = 0.50$  and (d)  $t = 1$  respectively. [For a movie of these plots please see external folder labelled: Comsol - Movie\_files - Fig-7.17]

From Figure 7.17, the siderophores clearly diffuse and interact with the iron causing the iron density to decrease and the resultant distributions to propagate to the right. Hence there is a resemblance of a travelling wave coinciding with the movement of siderophores and iron. The main reaction region occurs at the interaction zone which is of great importance as this can tell us how quickly the siderophores are bonding with the iron. We will investigate this phenomenon in Chapter 8 by considering a simpler set of model equations and attempt to understand the existence and key properties of this travelling wave solution.

# Chapter 8

## Modelling Siderophore-Iron Interactions: An Analytical Approach

The previous chapter investigated the production and spread of siderophores from a fungal biomass into a domain containing iron. It was seen (Figure 7.17) that the interface between the siderophore population and the unbound iron distribution appeared to exhibit characteristics of a travelling wave solution. Indeed this has been seen in experiments (e.g. Milagres et al., 1999). In this chapter a number of simplified mathematical models will be developed and analysed to more fully understand this dynamic. The initial focus will be on the siderophore population and iron density while the siderophore-iron complexes will be introduced later. In all instances, only movement in a single spatial variable will be considered.

### 8.1 Analysis of siderophore-iron interaction

To understand the travelling wave-like phenomena relating to the distributions of siderophores and iron seen in the previous chapter, e.g. Figure 7.17, we construct a simplified mathematical model. The equations for siderophores and iron from (7.1) are

$$\begin{aligned}\frac{\partial C}{\partial t} &= D_C \nabla^2 C + g(s_i) - r_1 C I, \\ \frac{\partial I}{\partial t} &= D_I \nabla^2 I - r_2 C I,\end{aligned}\tag{8.1}$$



where  $r_1$  and  $r_2$  denote reaction constants associated with the loss of siderophores and free iron that have bonded to form siderophore-iron complexes and  $g(s_i)$  represents the production of siderophores. As the siderophores are only produced by the fungal mycelium and a single siderophore-iron complex forms from a single siderophore and a single iron molecule  $r_1 = r_2$  and so equation (8.1) can be simplified to give

$$\begin{aligned}\frac{\partial C}{\partial t} &= D_C \nabla^2 C - rCI, \\ \frac{\partial I}{\partial t} &= D_I \nabla^2 I - rCI,\end{aligned}\tag{8.2}$$

where the production of new siderophores is captured by using suitable boundary conditions at  $x = 0$  when solved over the semi-infinite domain  $(0, \infty)$ . The semi-infinite boundary conditions are

$$\begin{aligned}C &= C_0 \text{ at } x = 0 \text{ \& } C \rightarrow 0 \text{ as } x \rightarrow \infty \\ I &\rightarrow I_0 \text{ as } x \rightarrow \infty \text{ \& } I = 0 \text{ at } x = 0.\end{aligned}\tag{8.3}$$

Thus for simplicity the fungal biomass is effectively assumed constant and restricted to the region where  $x < 0$  and we only focus on the siderophore and iron populations where  $x > 0$ . Recall earlier chapters, and indeed multiple other investigations, (e.g. Edelstein, 1982; Davidson, 1998; Boswell et al., 2003a) demonstrated that the fungal biomass can advance as a travelling wave with constant velocity. Hence the  $x$ -axis can be regarded as a slowly moving frame of reference where the  $x$  coordinate denotes the distance from the leading edge of the model biomass. Alternatively, the biomass can be regarded as being stationary, representing the instance at the boundary of a “polluted” region. Equation (8.2) is a well known system of equations which has been studied extensively (e.g. Gálfi and Rácz, 1988; Koza, 1996) on infinite domains. Here we consider investigating the simplified model equations on a semi-infinite domain by first seeking self-similar solutions, then progressing onto small time asymptotic behaviour and large time asymptotic approximations.

### 8.1.1 Self similar solutions

We consider model equations (8.2) representing the diffusion of siderophores from a static fungal biomass into a semi-infinite region containing unbound iron with initial data depicted schematically in Figure 8.1 over  $(0, \infty)$  and is broadly similar to that presented in Figure 7.17 obtained from the more complete set of equations (7.1). Here,  $C_0$  and  $I_0$  represent initial values of the siderophore and iron densities respectively.

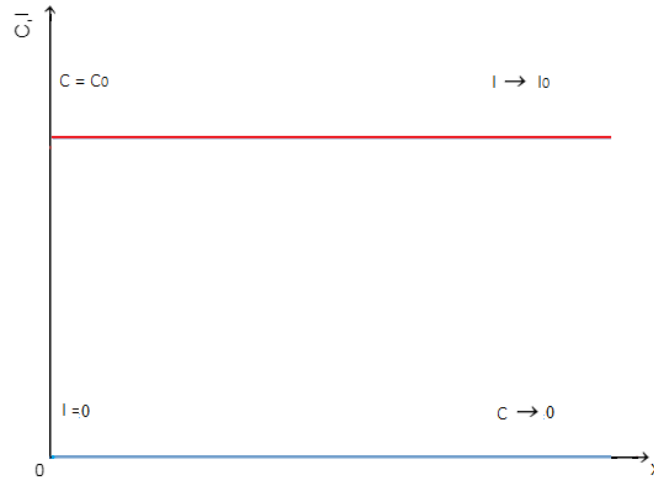


**Figure 8.1:** A schematic drawing of the profiles of  $C$  (blue, initially taking the value of zero everywhere except at  $x = 0$ ) and  $I$  (red, initially taking the value  $I_0 > 0$  everywhere except at  $x = 0$ ) at time  $t = 0$ .

In the previous simulations of the extended model equations we saw that the siderophores and iron profiles shifted to the right over time (Figure 7.17) once the reaction has occurred. In the absence of a chemical reaction equation (8.2) reduces to

$$\begin{aligned}\frac{\partial \bar{c}}{\partial t} &= D_{\bar{c}} \frac{\partial^2 \bar{c}}{\partial x^2}, \\ \frac{\partial \bar{i}}{\partial t} &= D_{\bar{i}} \frac{\partial^2 \bar{i}}{\partial x^2}.\end{aligned}\tag{8.4}$$

Thus the strategy now adopted is to consider the solution of (8.4) but with appropriate boundary conditions. To solve the system of equations in (8.4), we seek a self similar solution to reduce the system with two variables ( $t$  and  $x$ ) to a system involving a single variable. Therefore to non-dimensionalise the first

equation in (8.4) we introduce  $x = \vartheta X$ ,  $t = \varsigma T$  and  $C = \Gamma \bar{c}$  so that

$$\frac{\Gamma}{\varsigma} \frac{\partial C}{\partial T} = \frac{\Gamma}{\vartheta^2} D_{\bar{c}} \frac{\partial^2 C}{\partial X^2}. \quad (8.5)$$

From equation (8.5) we obtain  $\varsigma = \vartheta^2$  and so we have the similarity coordinate

$$\eta = \frac{x}{2\sqrt{t}}. \quad (8.6)$$

Hence using  $\eta$ , equation (8.4) becomes,

$$-2\eta \frac{d\bar{c}}{d\eta} = D_{\bar{c}} \frac{d^2 \bar{c}}{d\eta^2}. \quad (8.7)$$

Equation (8.7) can easily be solved using the substitution  $\omega = \frac{d\bar{c}}{d\eta}$ . Thus, integrating twice yields

$$\bar{c} = \int_0^\eta K e^{-\frac{z^2}{D_{\bar{c}}}} dz + \bar{K}, \quad (8.8)$$

where  $K$  and  $\bar{K}$  are constants. Using the substitution  $u = \frac{z}{\sqrt{D_{\bar{c}}}}$  we get

$$\bar{c} = K \sqrt{D_{\bar{c}}} \int_0^{\frac{\eta}{\sqrt{D_{\bar{c}}}}} e^{-u^2} du + \bar{K}. \quad (8.9)$$

Therefore using the error function  $\text{erf}(\phi) = \frac{2}{\sqrt{\pi}} \int_0^\phi e^{-u^2} du$  we obtain the following solutions (a similar approach can be taken for  $\bar{i}$ ),

$$\begin{aligned} \bar{c} &= P_{\bar{c}} \text{erf}\left(\frac{\eta}{\sqrt{D_{\bar{c}}}}\right) + Q_{\bar{c}}, \\ \bar{i} &= P_{\bar{i}} \text{erf}\left(\frac{\eta}{\sqrt{D_{\bar{i}}}}\right) + Q_{\bar{i}}, \end{aligned} \quad (8.10)$$

where  $P_{\bar{c}}$ ,  $P_{\bar{i}}$ ,  $Q_{\bar{c}}$  and  $Q_{\bar{i}}$  are constants. We now evaluate the constants for two distinct cases corresponding to small and large times. For small time approximations, it has been assumed no reaction between the siderophores and iron has taken place. For large time it is assumed the reaction only takes place inside a narrow reaction zone.

### 8.1.2 Small time asymptotic limit

For small times, the leading order equations in (8.2) are in fact given by (8.4) whose solutions are given by (8.10). Using the boundary conditions from equation (8.3), we obtain

$$\begin{aligned}\bar{c} &= C_0 \left( 1 - \operatorname{erf} \left( \frac{\eta}{\sqrt{D_{\bar{c}}}} \right) \right), \\ \bar{i} &= I_0 \operatorname{erf} \left( \frac{\eta}{\sqrt{D_{\bar{i}}}} \right).\end{aligned}\tag{8.11}$$

Suppose  $x_m$  denotes the position of the reaction front. This is defined to be the location where the reaction rate  $r\bar{c}\bar{i}$  is maximum, i.e. where  $(r\bar{c}\bar{i})_\eta = 0$ . Using the above relationship, there is a particular value of  $\eta$  say, where  $x_m = 2\bar{\alpha}\sqrt{t}$ . Hence by substituting  $\eta = \bar{\alpha}$  into  $(r\bar{c}\bar{i})_\eta = 0$  we find the position where the maximum reaction rate between siderophores and iron takes place corresponding to the root of

$$0 = \frac{2C_0 \left( 1 - \operatorname{erf} \left( \frac{\bar{\alpha}}{\sqrt{D_{\bar{c}}}} \right) \right) I_0 e^{-\frac{\bar{\alpha}^2}{D_{\bar{i}}}}}{\sqrt{\pi D_{\bar{i}}}} - \frac{2C_0 e^{-\frac{\bar{\alpha}^2}{D_{\bar{c}}}} I_0 \operatorname{erf} \left( \frac{\bar{\alpha}}{\sqrt{D_{\bar{i}}}} \right)}{\sqrt{\pi D_{\bar{c}}}}.\tag{8.12}$$

After some algebraic manipulation, equation (8.12) yields the following which is satisfied at the reaction front

$$e^{\frac{\bar{\alpha}^2}{D_{\bar{c}}}} \operatorname{erfc} \left( \frac{\bar{\alpha}}{\sqrt{D_{\bar{c}}}} \right) = \sqrt{\frac{D_{\bar{i}}}{D_{\bar{c}}}} e^{\frac{\bar{\alpha}^2}{D_{\bar{i}}}} \operatorname{erf} \left( \frac{\bar{\alpha}}{\sqrt{D_{\bar{i}}}} \right)\tag{8.13}$$

where  $\operatorname{erfc}(\cdot)$  is the complementary error function. The value of  $\bar{\alpha}$  satisfying equation (8.13) allows us to calculate the position of the reaction front. While (8.13) can be solved numerically, depending on the values of  $D_{\bar{c}}$  and  $D_{\bar{i}}$ , certain analytical approximations can be obtained. Three cases have been identified and are described. For notational convenience we use  $\bar{\beta} = \frac{\bar{\alpha}}{\sqrt{D_{\bar{c}}}}$  and  $\bar{\gamma} = \sqrt{\frac{D_{\bar{c}}}{D_{\bar{i}}}}$  and therefore equation (8.13) becomes

$$e^{\bar{\beta}^2 \bar{\gamma}^2} \operatorname{erf}(\bar{\beta} \bar{\gamma}) = \bar{\gamma} e^{\bar{\beta}^2} \operatorname{erfc}(\bar{\beta}).\tag{8.14}$$

Therefore  $\bar{\beta}$  is a function of  $\bar{\gamma}$  (i.e.  $\bar{\beta} = \bar{\beta}(\bar{\gamma})$ ).

### Case 1

Consider  $\bar{\gamma} \rightarrow \infty$  and we suppose that  $\bar{\beta} \rightarrow 0$ , but  $\bar{\beta}\bar{\gamma} \rightarrow \infty$ . We can see that

$$\begin{aligned} \text{as } \bar{\beta} \rightarrow 0, \quad e^{\bar{\beta}^2} &\rightarrow 1, \quad \text{erfc}(\bar{\beta}) \rightarrow 1, \\ \text{as } \bar{\beta}\bar{\gamma} \rightarrow \infty, \quad \text{erf}(\bar{\beta}\bar{\gamma}) &\rightarrow 1. \end{aligned}$$

Therefore equation (8.14) becomes

$$e^{\bar{\beta}^2\bar{\gamma}^2} = \bar{\gamma}. \quad (8.15)$$

Hence from equation (8.15) we get

$$\bar{\beta} = \pm \frac{1}{\bar{\gamma}} \sqrt{\ln(\bar{\gamma})}. \quad (8.16)$$

We take the positive root because in a semi-infinite domain only  $\bar{\beta} > 0$  is appropriate since  $\bar{\alpha} > 0$ . Therefore from equation (8.16) we can see that as  $\bar{\gamma} \rightarrow \infty \implies \bar{\beta}\bar{\alpha} \rightarrow \infty$  and  $\bar{\beta} \rightarrow 0$ .

### Case 2

Consider  $\bar{\gamma} \rightarrow 0$  and we suppose that  $\bar{\beta} \rightarrow \text{a constant}$ , then  $\bar{\beta}\bar{\gamma} \rightarrow 0$ . We know that  $\text{erf}(x) = \frac{2}{\sqrt{\pi}} \int_0^x e^{-t^2} dt$  and  $\lim_{x \rightarrow 0} \text{erf}(x) = \frac{2x}{\sqrt{\pi}}$ . Hence, we see that

$$\text{as } \bar{\beta}\bar{\gamma} \rightarrow 0, \quad e^{\bar{\beta}^2\bar{\gamma}^2} \rightarrow 1, \quad \text{erf}(\bar{\beta}\bar{\gamma}) \rightarrow \frac{2\bar{\beta}\bar{\gamma}}{\sqrt{\pi}}.$$

Then equation (8.14) becomes

$$\frac{2\bar{\beta}}{\sqrt{\pi}} = e^{\bar{\beta}^2} \text{erfc}(\bar{\beta}). \quad (8.17)$$

Hence numerically solving equation (8.17) we find that  $\bar{\beta} = 0.531597$ .

### Case 3

We now consider the case when the diffusion coefficient for the siderophores and iron are equal  $\bar{\gamma} = 1$  (i.e.  $D_{\bar{c}} = D_{\bar{i}} = D$ ). Hence, equation (8.14) becomes

$$\text{erf}(\bar{\beta}) = \text{erfc}(\bar{\beta}).$$

Using  $\operatorname{erfc}(x) = 1 - \operatorname{erf}(x)$  yields

$$2 \operatorname{erf}(\bar{\beta}) = 1, \quad \implies \bar{\beta} = \operatorname{erf}^{-1}\left(\frac{1}{2}\right).$$

Hence

$$\bar{\beta} = 0.476936. \quad (8.18)$$

A schematic representation of all the valid cases from the analysis above is depicted in Figure 8.2.

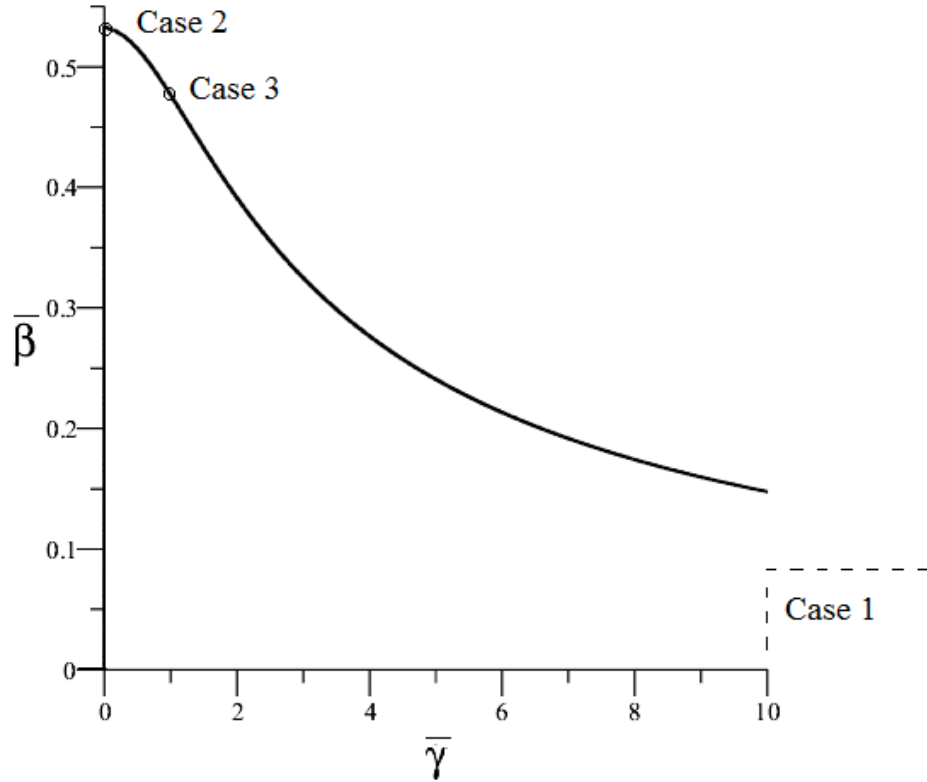


**Figure 8.2:** *A schematic summary of the 3 cases for small time asymptotic solutions with  $\bar{\beta}$  obtained from equation (8.14).*

Numerical solutions of  $\bar{\alpha}$  obtained from equation (8.13) compare favourably to the above approximations (see Table 8.1).

|               |               | Parameters                        |                                    |                                    | Approximation ( $\bar{\alpha}$ ) | Cases |
|---------------|---------------|-----------------------------------|------------------------------------|------------------------------------|----------------------------------|-------|
| $D_{\bar{c}}$ | $D_{\bar{i}}$ | Numerical $\bar{\beta}$<br>(8.14) | Numerical $\bar{\gamma}$<br>(8.14) | Numerical $\bar{\alpha}$<br>(8.13) |                                  |       |
| $10^{-1}$     | $10^{-7}$     | 0.002628                          | 1000                               | 0.000831                           | 0.000831                         | 1     |
| $10^{-2}$     | $10^{-6}$     | 0.002141                          | 100                                | 0.002141                           | 0.002141                         | 1     |
| $10^{-6}$     | $10^{-2}$     | 0.531590                          | 0.01                               | 0.000532                           | 0.000532                         | 2     |
| $10^{-7}$     | $10^{-1}$     | 0.531597                          | 0.001                              | 0.000168                           | 0.000168                         | 2     |
| 1             | 1             | 0.476936                          | 1                                  | 0.476936                           | 0.476936                         | 3     |

**Table 8.1:** *Equations for small time asymptotic solution (8.13) are solved for  $\bar{\alpha}$  numerically for various parameter values.*

Our model in equation (7.1) is based on experimental settings involving Petri dishes where the siderophore detection is in solid medium (recall the iron complex is solidified and then cut in half). This protocol suggests iron has a higher viscosity than the siderophores i.e.  $D_{\bar{c}} \gg D_{\bar{i}}$ . Hence case 1 is most applicable to our requirements. However, some studies involving siderophore detection are carried out in liquid medium in tubes (Machuca and Milagres, 2003; Bholay et al., 2012; Gamit and Tank, 2014). This involves the microorganisms under inspection being mixed into the solution containing the CAS agar (iron complex) where the colour change is observed (from blue to yellow typically) due to siderophores binding with iron. For this setting, the iron will have a lower viscosity than the Petri dish protocol and thus case 2 approximation for  $\bar{\alpha}$  will be appropriate. Clearly this case is not relevant for our application. Case 3 could possibly arise where the diffusivity for both the iron and siderophore are known to be similar.

Therefore the result obtained above indicates where the maximum rate of reaction between the siderophores and iron takes place at small times. We can obtain some information regarding the velocity of the reaction front from equation (8.13). As  $x_m = 2\bar{\alpha}\sqrt{t}$  corresponds to position, we can easily obtain the velocity of the position of maximal reaction rate for small times to be given by  $x'_m = \frac{\bar{\alpha}}{\sqrt{t}}$ . The acceleration can also be found from  $x''_m = -\frac{\bar{\alpha}}{2\sqrt{t^3}}$ , which tells us the position of the maximum reaction rate is slowing down with time. Unfortunately, it is not easy to continue the small time asymptotic expansion, although such an approach was applied by Trevelyan (2009) in an infinite domain.

### 8.1.3 Large time asymptotic limit

In Chapter 7 (Figure 7.17) a one-dimensional plot of siderophores and iron were depicted and a travelling wave at the reaction front was observed. In the previous section we investigated the small-time asymptotic behaviour of the siderophore and iron reaction front. In this section we search for a solution to equation (8.2) at large times. We can find a solution by separating the system around the reaction zone into regions as shown in Figure 8.3. Since diffusion is the only mechanism for the movement, we suppose  $x_f = 2\bar{\alpha}\sqrt{t}$  where well-known results on the spread of material via diffusion in a single spatial dimension have been exploited and  $\bar{\alpha}$  is a constant to be determined.

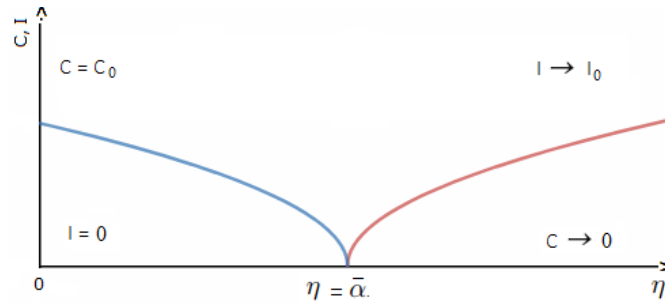


**Figure 8.3:** *Schematic drawing of the siderophore  $C$  (blue) and iron  $I$  (red) profiles around  $\eta = \bar{\alpha}$ .*

In classical studies the model equations (8.2) have been studied in an infinite domain and a solution can be found in the literature (e.g. Danckwerts, 1950; Gálfi and Rácz, 1988; Koza, 1996). However, our focus is on a semi-infinite domain where no results are known to exist. To perform the analysis attention is focused on the reaction zone close to  $\eta = \bar{\alpha}$  and applying suitable boundary conditions on the total flux coming into the reaction zone from both sides so we can determine a solution for the reaction front position. Also notice that the iron and siderophore complex concentrations tends to zero (i.e.  $CI \rightarrow 0$ ) outside the reaction zone. Thus there are three regions: that to the left of the reaction front where the iron is depleted, the reaction front itself around  $\eta = \bar{\alpha}$ , and the region to the right of the reaction front where there are no siderophores. Away from the reaction front either  $C$  or  $I$  is zero and hence in those two regions equation (8.2) simplifies to those in (8.10). The long time behaviour seen in the numerical results in Figure 7.17 (also see movie file Fig7.17-1d\_sid\_iron\_long\_time.avi) suggest the following



boundary conditions for the left and right most regions

$$\begin{aligned} \text{LHS: } C = C_0 \text{ at } \eta = 0 \text{ \& Reaction front: } C = 0 \text{ at } \eta = \bar{\alpha}, \\ \text{RHS: } I \rightarrow I_0 \text{ as } \eta \rightarrow \infty \text{ \& Reaction front: } I = 0 \text{ at } \eta = \bar{\alpha}. \end{aligned} \quad (8.19)$$

Using the general solution given in equation (8.10) and by applying the above boundary conditions we obtain the particular solution

$$\begin{aligned} \bar{c} = C_0 \left[ 1 - \frac{\text{erf}\left(\frac{\eta}{\sqrt{D_{\bar{c}}}}\right)}{\text{erf}\left(\frac{\bar{\alpha}}{\sqrt{D_{\bar{c}}}}\right)} \right] \text{ and } \bar{i} = 0 \quad \text{for } \eta < \bar{\alpha}, \\ \bar{i} = I_0 \left[ 1 - \frac{\text{erfc}\left(\frac{\eta}{\sqrt{D_{\bar{i}}}}\right)}{\text{erfc}\left(\frac{\bar{\alpha}}{\sqrt{D_{\bar{i}}}}\right)} \right] \text{ and } \bar{c} = 0 \quad \text{for } \eta > \bar{\alpha}. \end{aligned} \quad (8.20)$$

To find  $\bar{\alpha}$  we balance the flux at the reaction zone denoted by  $x_f = 2\bar{\alpha}\sqrt{t}$ . By assuming continual low concentrations of  $I$  and  $C$ , we are assuming the overall flux of the material at  $x_f$  is zero, i.e. the flux coming into the region ( $\eta = \bar{\alpha}$ ) is given by

$$D_{\bar{c}}\bar{c}_{\eta} + D_{\bar{i}}\bar{i}_{\eta} = 0. \quad (8.21)$$

Therefore using (8.20), it follows that at  $\eta = \bar{\alpha}$

$$e^{\frac{\bar{\alpha}^2}{D_{\bar{i}}}} \text{erfc}\left(\frac{\bar{\alpha}}{\sqrt{D_{\bar{i}}}}\right) = \sqrt{\frac{D_{\bar{i}}}{D_{\bar{c}}}} \frac{I_0}{C_0} e^{\frac{\bar{\alpha}^2}{D_{\bar{c}}}} \text{erf}\left(\frac{\bar{\alpha}}{\sqrt{D_{\bar{c}}}}\right). \quad (8.22)$$

In equation (8.22), there are four parameters,  $D_{\bar{c}}$ ,  $D_{\bar{i}}$ ,  $C_0$  and  $I_0$ , and it is possible to solve this equation numerically to calculate  $\bar{\alpha}$ . However, analytical approximations can be constructed under certain situations. Five important cases are described below

### Case 1

Suppose,

$$\bar{\alpha} \ll \sqrt{D_{\bar{c}}}, \sqrt{D_{\bar{i}}}. \quad (8.23)$$

Using (8.23) we can see that

$$\begin{aligned} \text{as } \frac{\bar{\alpha}}{\sqrt{D_i}} \rightarrow 0, \quad e^{\frac{\bar{\alpha}^2}{D_i}} \rightarrow 1, \quad \operatorname{erfc}\left(\frac{\bar{\alpha}}{\sqrt{D_i}}\right) &\rightarrow 1 - \frac{2\bar{\alpha}}{\sqrt{\pi D_i}}, \\ \text{as } \frac{\bar{\alpha}}{\sqrt{D_c}} \rightarrow 0, \quad e^{\frac{\bar{\alpha}^2}{D_c}} \rightarrow 1, \quad \operatorname{erf}\left(\frac{\bar{\alpha}}{\sqrt{D_c}}\right) &\rightarrow \frac{2\bar{\alpha}}{\sqrt{\pi D_c}}. \end{aligned}$$

Therefore equation (8.22) becomes

$$1 - \frac{2\bar{\alpha}}{\sqrt{\pi D_i}} \approx \sqrt{\frac{D_i}{D_c}} \frac{I_0}{C_0} \frac{2\bar{\alpha}}{\sqrt{\pi D_c}}. \quad (8.24)$$

We can rearrange equation (8.24) to get the approximation

$$\bar{\alpha} \rightarrow \frac{\sqrt{\pi D_i} C_0 D_c}{2(C_0 D_c + I_0 D_i)}. \quad (8.25)$$

For the above approximation to be valid we need  $\frac{\bar{\alpha}}{\sqrt{D_i}} \rightarrow 0$ . Hence from equation (8.25) we obtain

$$\frac{\bar{\alpha}}{\sqrt{D_i}} = \frac{\sqrt{\pi} C_0 D_c}{2(C_0 D_c + I_0 D_i)} \rightarrow 0, \quad \text{i.e.} \quad \frac{C_0 D_c}{C_0 D_c + I_0 D_i} \rightarrow 0.$$

Alternatively this means

$$\frac{C_0 D_c + I_0 D_i}{C_0 D_c} \rightarrow \infty$$

and therefore

$$\frac{I_0 D_i}{C_0 D_c} \rightarrow \infty \quad \implies \quad \frac{D_i}{D_c} \gg \frac{C_0}{I_0}. \quad (8.26)$$

We also need  $\frac{\bar{\alpha}}{\sqrt{D_c}} \rightarrow 0$ . In a similar way for (8.25) we obtain

$$\frac{\bar{\alpha}}{\sqrt{D_c}} = \frac{\sqrt{\pi D_c D_i} C_0}{2(C_0 D_c + I_0 D_i)} \rightarrow 0,$$

i.e.

$$\frac{C_0 D_c + I_0 D_i}{\sqrt{D_c D_i} C_0} \rightarrow \infty$$

and so

$$1 + \frac{I_0 D_i}{C_0 D_c} \rightarrow \infty.$$

Thus

$$\frac{D_{\bar{i}}}{D_{\bar{c}}} \rightarrow 0 \quad \text{or} \quad \frac{I_0 D_{\bar{i}}}{C_0 D_{\bar{c}}} \gg \sqrt{\frac{D_{\bar{i}}}{D_{\bar{c}}}},$$

i.e.

$$D_{\bar{c}} \gg D_{\bar{i}} \quad \text{or} \quad \frac{D_{\bar{i}}}{D_{\bar{c}}} \gg \left( \frac{C_0}{I_0} \right)^2. \quad (8.27)$$

Therefore in order for the approximation of  $\bar{\alpha}$  in equation (8.25) to be valid, we can see from equations (8.26) and (8.27) that the following conditions must be satisfied;

$$1 \gg \frac{D_{\bar{i}}}{D_{\bar{c}}} \gg \frac{C_0}{I_0} \quad (8.28)$$

or

$$\frac{D_{\bar{i}}}{D_{\bar{c}}} \gg \max \left( \left( \frac{C_0}{I_0} \right)^2, \frac{C_0}{I_0} \right). \quad (8.29)$$

## Case 2

Suppose,

$$\bar{\alpha} \gg \sqrt{D_{\bar{c}}}, \quad \sqrt{D_{\bar{i}}}. \quad (8.30)$$

Using (8.30) we can see that

$$\begin{aligned} \text{as } \frac{\bar{\alpha}}{\sqrt{D_{\bar{c}}}} \rightarrow \infty, \quad \text{erf} \left( \frac{\bar{\alpha}}{\sqrt{D_{\bar{c}}}} \right) &\rightarrow 1, \\ \text{as } \frac{\bar{\alpha}}{\sqrt{D_{\bar{i}}}} \rightarrow \infty, \quad \text{erfc} \left( \frac{\bar{\alpha}}{\sqrt{D_{\bar{i}}}} \right) &\rightarrow \frac{e^{-\frac{\bar{\alpha}^2}{D_{\bar{i}}}}}{\sqrt{\pi}} \frac{\sqrt{D_{\bar{i}}}}{\bar{\alpha}}. \end{aligned}$$

Then equation (8.22) becomes

$$e^{\frac{\bar{\alpha}^2}{D_{\bar{i}}}} \left( \frac{e^{-\frac{\bar{\alpha}^2}{D_{\bar{i}}}}}{\sqrt{\pi}} \frac{\sqrt{D_{\bar{i}}}}{\bar{\alpha}} \right) = \sqrt{\frac{D_{\bar{i}}}{D_{\bar{c}}}} \frac{I_0}{C_0} e^{\frac{\bar{\alpha}^2}{D_{\bar{c}}}}. \quad (8.31)$$

We can simplify equation (8.31) to get

$$\frac{2C_0^2}{\pi I_0^2} = \frac{2\bar{\alpha}^2 e^{\frac{2\bar{\alpha}^2}{D_{\bar{c}}}}}{D_{\bar{c}}}. \quad (8.32)$$

Let  $y = \frac{2\bar{\alpha}^2}{D_{\bar{e}}}$ , then from equation (8.32)

$$\frac{2C_0^2}{\pi I_0^2} = ye^y$$

and so

$$y = W\left(\frac{2C_0^2}{\pi I_0^2}\right) \quad (8.33)$$

where  $W$  is the Lambert W function. Hence, from equation (8.33) we obtain

$$\bar{\alpha} \rightarrow \sqrt{\frac{D_{\bar{e}}}{2} W\left(\frac{2C_0^2}{\pi I_0^2}\right)}. \quad (8.34)$$

In order for (8.34) to be a valid approximation we need  $\frac{\bar{\alpha}}{\sqrt{D_{\bar{e}}}} \rightarrow \infty$ . Hence from equation (8.34) we obtain

$$\frac{\bar{\alpha}}{\sqrt{D_{\bar{e}}}} = \sqrt{\frac{1}{2} W\left(\frac{2C_0^2}{\pi I_0^2}\right)} \rightarrow \infty,$$

i.e.

$$\frac{2C_0^2}{\pi I_0^2} \rightarrow \infty. \quad (8.35)$$

We also need  $\frac{\bar{\alpha}}{\sqrt{D_{\bar{i}}}} \rightarrow \infty$ . Hence from equation (8.34) we obtain

$$\frac{\bar{\alpha}}{\sqrt{D_{\bar{i}}}} = \sqrt{\frac{D_{\bar{e}}}{2D_{\bar{i}}} W\left(\frac{2C_0^2}{\pi I_0^2}\right)} \rightarrow \infty. \quad (8.36)$$

Therefore in order for the approximation of  $\bar{\alpha}$  in equation (8.34) to be valid, we can see from equations (8.35) and (8.36) that the following conditions must be satisfied:

$$C_0 \gg I_0 \text{ and } \frac{D_{\bar{e}}}{D_{\bar{i}}} = \Omega(1), \quad (8.37)$$

where  $\frac{D_{\bar{e}}}{D_{\bar{i}}}$  is asymptotically greater than or equal to order 1.

### Case 3

Here we consider equal diffusion coefficients, (i.e.  $D_i = D_c = D$ ). Hence equation (8.22) becomes

$$e^{\frac{\bar{\alpha}^2}{D}} \operatorname{erfc}\left(\frac{\bar{\alpha}}{\sqrt{D}}\right) = \frac{I_0}{C_0} e^{\frac{\bar{\alpha}^2}{D}} \operatorname{erf}\left(\frac{\bar{\alpha}}{\sqrt{D}}\right). \quad (8.38)$$

Using the identity  $\operatorname{erfc}(x) = 1 - \operatorname{erf}(x)$ , equation (8.38) becomes

$$1 - \operatorname{erf}\left(\frac{\bar{\alpha}}{\sqrt{D}}\right) = \frac{I_0}{C_0} \operatorname{erf}\left(\frac{\bar{\alpha}}{\sqrt{D}}\right) \implies \operatorname{erf}\left(\frac{\bar{\alpha}}{\sqrt{D}}\right) = \frac{C_0}{I_0 + C_0}.$$

Hence,

$$\bar{\alpha} = \sqrt{D} \operatorname{erf}^{-1}\left(\frac{C_0}{I_0 + C_0}\right). \quad (8.39)$$

### Case 4

Here we suppose

$$\frac{\bar{\alpha}}{\sqrt{D_c}} \rightarrow 0 \text{ and } \frac{\bar{\alpha}}{\sqrt{D_i}} \rightarrow \infty. \quad (8.40)$$

Using (8.40) we can see that

$$\begin{aligned} \text{as } \frac{\bar{\alpha}}{\sqrt{D_i}} \rightarrow \infty, \quad \operatorname{erfc}\left(\frac{\bar{\alpha}}{\sqrt{D_i}}\right) &\rightarrow \frac{e^{-\frac{\bar{\alpha}^2}{D_i}}}{\sqrt{\pi}} \frac{\sqrt{D_i}}{\bar{\alpha}}, \\ \text{as } \frac{\bar{\alpha}}{\sqrt{D_c}} \rightarrow 0, \quad e^{\frac{\bar{\alpha}^2}{D_c}} &\rightarrow 1, \quad \operatorname{erf}\left(\frac{\bar{\alpha}}{\sqrt{D_c}}\right) \rightarrow \frac{2\bar{\alpha}}{\sqrt{\pi D_c}}. \end{aligned}$$

Therefore equation (8.22) becomes

$$e^{\frac{\bar{\alpha}^2}{D_i}} \left( \frac{e^{-\frac{\bar{\alpha}^2}{D_i}}}{\sqrt{\pi}} \frac{\sqrt{D_i}}{\bar{\alpha}} \right) = \sqrt{\frac{D_i}{D_c}} \frac{I_0}{C_0} \frac{2\bar{\alpha}}{\sqrt{\pi D_c}}. \quad (8.41)$$

We can simplify equation (8.41) to get

$$\bar{\alpha} \rightarrow \sqrt{\frac{D_c C_0}{2I_0}}. \quad (8.42)$$

In order for (8.42) to be a valid approximation, the conditions in (8.40) need to hold. Thus we need  $\frac{\bar{\alpha}}{\sqrt{D_{\bar{c}}}} \rightarrow 0$ . Hence from equation (8.42) we obtain

$$\begin{aligned} \frac{\bar{\alpha}}{\sqrt{D_{\bar{c}}}} &= \sqrt{\frac{C_0}{2I_0}} \rightarrow 0, \\ \frac{C_0}{I_0} &\rightarrow 0. \end{aligned} \quad (8.43)$$

We also need from (8.40)  $\frac{\bar{\alpha}}{\sqrt{D_{\bar{i}}}} \rightarrow \infty$ . Hence from equation (8.42) we obtain

$$\frac{\bar{\alpha}}{\sqrt{D_{\bar{i}}}} = \sqrt{\frac{C_0 D_{\bar{c}}}{2I_0 D_{\bar{i}}}} \rightarrow \infty,$$

i.e.

$$\frac{C_0 D_{\bar{c}}}{I_0 D_{\bar{i}}} \rightarrow \infty. \quad (8.44)$$

Therefore in order for the approximation of  $\bar{\alpha}$  in equation (8.42) to be valid, the following conditions must be satisfied;

$$\frac{D_{\bar{c}}}{D_{\bar{i}}} \gg \frac{I_0}{C_0} \gg 1. \quad (8.45)$$

### Case 5

Finally we consider the case where

$$\frac{\bar{\alpha}}{\sqrt{D_{\bar{c}}}} \rightarrow \infty \text{ and } \frac{\bar{\alpha}}{\sqrt{D_{\bar{i}}}} \rightarrow 0. \quad (8.46)$$

Using (8.46) we can see that

$$\begin{aligned} \text{as } \frac{\bar{\alpha}}{\sqrt{D_{\bar{c}}}} &\rightarrow \infty, \quad \text{erf}\left(\frac{\bar{\alpha}}{\sqrt{D_{\bar{c}}}}\right) \rightarrow 1, \\ \text{as } \frac{\bar{\alpha}}{\sqrt{D_{\bar{i}}}} &\rightarrow 0, \quad e^{\frac{\bar{\alpha}^2}{D_{\bar{i}}}} \rightarrow 1, \quad \text{erfc}\left(\frac{\bar{\alpha}}{\sqrt{D_{\bar{i}}}}\right) \rightarrow 1. \end{aligned}$$

Then equation (8.22) becomes

$$1 = \sqrt{\frac{D_{\bar{i}}}{D_{\bar{c}}}} \frac{I_0}{C_0} e^{\frac{\bar{\alpha}^2}{D_{\bar{c}}}}. \quad (8.47)$$

We can simplify equation (8.47) to get

$$\bar{\alpha} \rightarrow \sqrt{\frac{D_{\bar{c}}}{2} \ln \left( \frac{D_{\bar{c}} C_0^2}{D_{\bar{i}} I_0^2} \right)}. \quad (8.48)$$

In order for (8.48) to be a valid approximation, conditions (8.46) must hold. Therefore we need  $\frac{\bar{\alpha}}{\sqrt{D_{\bar{c}}}} \rightarrow \infty$ . Hence from equation (8.48) we obtain

$$\frac{\bar{\alpha}}{\sqrt{D_{\bar{c}}}} = \sqrt{\frac{1}{2} \ln \left( \frac{D_{\bar{c}} C_0^2}{D_{\bar{i}} I_0^2} \right)} \rightarrow \infty,$$

i.e.

$$\frac{D_{\bar{c}} C_0^2}{D_{\bar{i}} I_0^2} \rightarrow \infty. \quad (8.49)$$

Also from (8.46) we need  $\frac{\bar{\alpha}}{\sqrt{D_{\bar{i}}}} \rightarrow 0$ . Hence from equation (8.48) we obtain

$$\frac{\bar{\alpha}}{\sqrt{D_{\bar{i}}}} = \sqrt{\frac{D_{\bar{c}}}{2D_{\bar{i}}} \ln \left( \frac{D_{\bar{c}} C_0^2}{D_{\bar{i}} I_0^2} \right)} \rightarrow 0,$$

i.e.

$$\frac{D_{\bar{c}}}{D_{\bar{i}}} \rightarrow 0, \quad (8.50)$$

since in (8.49) we require  $\frac{D_{\bar{c}} C_0^2}{D_{\bar{i}} I_0^2} \rightarrow \infty$ . Therefore in order for the approximation of  $\bar{\alpha}$  in equation (8.48) to be valid, the following conditions are to be satisfied

$$1 \gg \frac{D_{\bar{c}}}{D_{\bar{i}}} \gg \frac{I_0^2}{C_0^2}. \quad (8.51)$$

A schematic representation of the approximations of  $\bar{\alpha}$  in terms of  $\frac{D_{\bar{c}}}{D_{\bar{i}}}$  against  $\frac{I_0}{C_0}$  for the five cases identified above is shown in Figure 8.4.

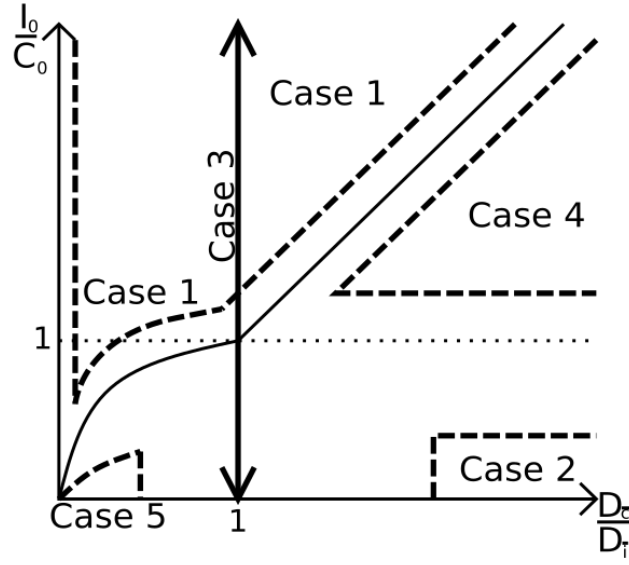


**Figure 8.4:** A schematic summary of all cases when large time asymptotic solutions for  $\bar{\alpha}$  obtained from equation (8.22) are valid.

There is excellent agreement between numerical solutions of equation (8.22) and the approximations for  $\bar{\alpha}$ , the position where the maximum reaction between the siderophores and iron occurs, constructed above (Table 8.2).

| Parameters    |               |           |           |                                 |                              |       |
|---------------|---------------|-----------|-----------|---------------------------------|------------------------------|-------|
| $D_{\bar{c}}$ | $D_{\bar{i}}$ | $C_0$     | $I_0$     | Numerical $\bar{\alpha}$ (8.22) | Approximation $\bar{\alpha}$ | Cases |
| $10^{-2}$     | $10^{-8}$     | $10^{-7}$ | 20        | $4.409175 \times 10^{-7}$       | $4.409089 \times 10^{-7}$    | 1     |
| $10^{-2}$     | $10^{-8}$     | 20        | $10^{-7}$ | $4.137789 \times 10^{-1}$       | $4.137789 \times 10^{-1}$    | 2     |
| 1             | 1             | $10^{-2}$ | $10^{-4}$ | 1.823818                        | 1.823818                     | 3     |
| $10^{-2}$     | $10^{-8}$     | $10^{-7}$ | $10^{-4}$ | $2.223458 \times 10^{-3}$       | $2.223607 \times 10^{-3}$    | 4     |
| $10^{-8}$     | $10^{-2}$     | $10^{-2}$ | $10^{-7}$ | $2.145964 \times 10^{-4}$       | $2.145966 \times 10^{-4}$    | 5     |

**Table 8.2:** Equations for large time asymptotic solution (8.22) were solved for  $\bar{\alpha}$  numerically for varying parameter values and compared to analytical approximations.

The simulations obtained from the numerical solution showed there was a shift to the left and a drop in densities between the siderophores and iron, which can be seen in Figure in 7.17. Furthermore, the initial distribution had a “large reaction zone” (i.e. a large region in which both the iron and siderophore concentration were non-zero). Hence the above analysis may not be suitable for



the initial movement. Additionally the small time analysis failed to provide insight into individual wave properties such as the initial velocity and acceleration. Thus an alternative approach is required for such analysis. We will utilise the Laplace decomposition method used in earlier chapters.

## 8.2 Laplace decomposition method on wave speed approximation

In the analysis carried out so far we have not been able to identify the immediate impact on the individual motion of the siderophore and iron profiles for the simulations in the previous chapter. The self similar analysis in the previous section provided some insight into the approximate position where the reaction occurs under some specified boundary conditions. Our small time asymptotic solution allowed us to describe the position of the reaction front  $x_f$ , but was not used to determine the individual motion for the siderophore and iron populations. Thus an alternative method is sought.

In Chapter 3 the Laplace decomposition method (LDM) was successfully used to construct formulae to determine the initial kinetic characteristics for any system of PDEs for small times. Using this technique we can obtain an analytical formula for the velocity and acceleration of siderophores and iron for small times in the current setting. This transient phase is often imperceptible in experiments as it is not easy to determine due to the magnitudes of the elements involved but is possible to obtain using our mathematical techniques. The LDM also provides a semi analytical form of the spatial and temporal evolution of the siderophore and iron populations.

We apply the LDM to equation (8.2) with initial conditions,

$$\begin{aligned} C(x, 0) &= \check{C}_0 \left( \frac{1 - \tanh(\theta x)}{2} \right), \\ I(x, 0) &= \check{I}_0 \left( \frac{1 + \tanh(\phi x)}{2} \right), \end{aligned} \tag{8.52}$$

where  $\check{C}_0$  and  $\check{I}_0$  are constants.  $\theta$  and  $\phi$  are constants used to control the gradients of the profiles for the siderophore and iron respectively, which are similar to the initial data in Chapter 7 although the domain is now infinite. As previously, we

seek a series solution of the form

$$\begin{aligned} C(x, t) &= \bar{C}_0 + \bar{C}_1 t + \bar{C}_2 t^2 + \dots \\ I(x, t) &= \bar{I}_0 + \bar{I}_1 t + \bar{I}_2 t^2 + \dots \end{aligned}$$

The system of equations (8.1) with  $g(s_i) = 0$  and initial conditions (8.52) is solved using the Laplace decomposition method of which the first few terms are

$$\begin{aligned} C(x, t) &= \check{C}_0 \left( \frac{1 - \tanh(\theta x)}{2} \right) + \frac{\check{C}_0}{4} \left[ -4D_C \tanh(\theta x)^3 \theta^2 \right. \\ &\quad \left. + (4\theta^2 D_C + r\check{I}_0(1 + \tanh(\phi x))) \tanh(\theta x) \right. \\ &\quad \left. - r\check{I}_0(1 + \tanh(\phi x)) \right] t + \dots \\ I(x, t) &= \check{I}_0 \left( \frac{1 + \tanh(\phi x)}{2} \right) + \frac{\check{I}_0}{4} \left[ 4D_I \tanh(\phi x)^3 \phi^2 \right. \\ &\quad \left. + (-4\phi^2 D_I + r\check{C}_0(-1 + \tanh(\theta x))) \tanh(\phi x) \right. \\ &\quad \left. + r\check{C}_0(-1 + \tanh(\theta x)) \right] t + \dots \end{aligned}$$

and an illustrative example is shown in Figure 8.5.

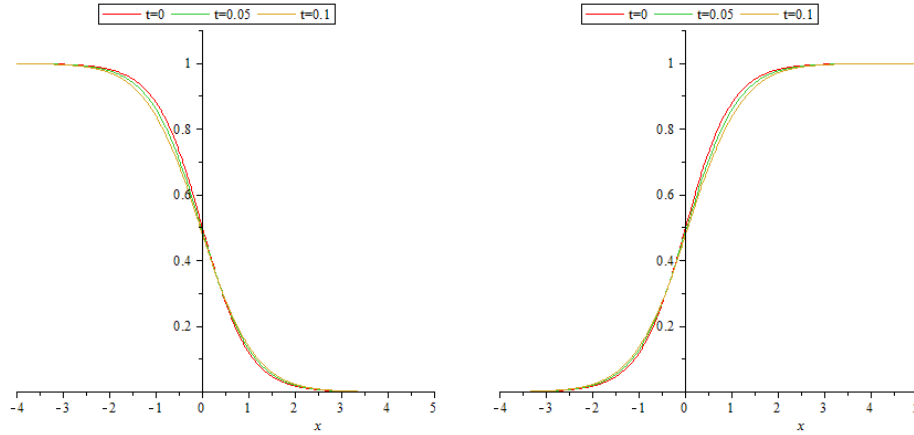


**Figure 8.5:** Plot of siderophore and iron concentration with 3 terms generated with LDM using parameters  $D_C = D_I = \check{C}_0 = \check{I}_0 = r = \phi = \theta = 1$  shown at times  $t = 0, 0.05$  and  $0.1$ .

Using the same techniques as described previously the initial velocities of

the siderophores and iron populations at  $x = 0$  are given by

$$\text{Velocity of Siderophore} = -\frac{\bar{C}_1}{\bar{C}'_0} = \frac{-r\check{I}_0}{2\theta}, \quad (8.53)$$

$$\text{Velocity of Iron} = -\frac{\bar{I}_1}{\bar{I}'_0} = \frac{r\check{C}_0}{2\phi}, \quad (8.54)$$

while the initial accelerations are given by

$$\begin{aligned} \text{Acceleration of Siderophore} &= \frac{2\bar{C}'_0\bar{C}'_1\bar{C}_1 - 2\bar{C}_2(\bar{C}'_0)^2 - (\bar{C}_1)^2\bar{C}''_0}{(\bar{C}'_0)^3}, \\ &= \frac{r\check{I}_0(2r\check{I}_0\phi + \check{C}_0r\theta + 4D_C\phi\theta^2 - 8D_C\theta^3 - r\check{I}_0\theta)}{4\theta^2}, \end{aligned} \quad (8.55)$$

$$\begin{aligned} \text{Acceleration of Iron} &= \frac{2\bar{I}'_0\bar{I}'_1\bar{I}_1 - 2\bar{I}_2(\bar{I}'_0)^2 - (\bar{I}_1)^2\bar{I}''_0}{(\bar{I}'_0)^3}, \\ &= \frac{-r\check{C}_0(2r\check{C}_0\theta + \check{I}_0r\phi + 4D_I\theta\phi^2 - 8D_I\phi^3 - r\check{C}_0\phi)}{4\phi^2}. \end{aligned} \quad (8.56)$$

Tables 8.3 and 8.4 compare the velocity and acceleration formulae in equations (8.53), (8.55), (8.54) and (8.56), for various parameter values to numerical approximations obtained by numerically solving equations (8.2) using Matlab.

| Parameters |       |     |       |       |          |        | Wave front velocity |              |             |            | Wave front acceleration |                 |              |
|------------|-------|-----|-------|-------|----------|--------|---------------------|--------------|-------------|------------|-------------------------|-----------------|--------------|
| $D_C$      | $D_I$ | $r$ | $C_0$ | $I_0$ | $\theta$ | $\phi$ | Equation (8.53)     | $t = 0.0001$ | $t = 0.001$ | $t = 0.01$ | $t = 0.1$               | Equation (8.55) | $t = 0.0001$ |
| 1          | 1     | 1   | 1     | 1     | 1        | 1      | -0.500              | -0.500       | -0.500      | -0.500     | -0.530                  | -0.50           | -0.50        |
| 2          | 1     | 1   | 1     | 1     | 1        | 2      | -0.500              | -0.500       | -0.500      | -0.500     | -0.490                  | 1.00            | 0.99         |
| 0.3        | 0.1   | 1   | 0.4   | 0.4   | 1        | 1      | -0.200              | -0.200       | -0.200      | -0.200     | -0.203                  | -0.04           | -0.04        |
| 0.3        | 0.01  | 1   | 0.4   | 0.4   | 1        | 2      | -0.200              | -0.200       | -0.200      | -0.199     | -0.188                  | 0.16            | 0.16         |

**Table 8.3:** Equations in (8.2) were solved numerically and the velocities and accelerations of the leading edge of the wave fronts starting at  $x = 0$  were calculated at the times indicated. The initial velocity and acceleration of the leading edge for the siderophore concentration profile obtained analytically from equations (8.53) and (8.55) are shown for comparison.

The approximations using the velocity and acceleration formulae compare favourably to the numerical approximations. From Tables 8.3 and 8.4 it can be seen that the approximations become less accurate as time increases.

The primary observation is that the respective velocities of the siderophore and iron populations have opposite signs at the first moment of interaction. This signifies the loss of siderophores and iron as they are binding to form a siderophore-iron complex. Thus, the results in this section are consistent with the COMSOL

| Parameters |       |     |       |       |          |        |                 | Wave front velocity |             |            |           | Wave front acceleration |              |
|------------|-------|-----|-------|-------|----------|--------|-----------------|---------------------|-------------|------------|-----------|-------------------------|--------------|
| $D_C$      | $D_I$ | $r$ | $C_0$ | $I_0$ | $\theta$ | $\phi$ | Equation (8.54) | $t = 0.0001$        | $t = 0.001$ | $t = 0.01$ | $t = 0.1$ | Equation (8.56)         | $t = 0.0001$ |
| 1          | 1     | 1   | 1     | 1     | 1        | 1      | 0.500           | 0.500               | 0.500       | 0.500      | 0.530     | 0.500                   | 0.502        |
| 2          | 1     | 1   | 1     | 1     | 1        | 2      | 0.250           | 0.250               | 0.250       | 0.270      | 0.270     | 2.875                   | 2.875        |
| 0.3        | 0.1   | 1   | 0.4   | 0.4   | 1        | 1      | 0.200           | 0.200               | 0.200       | 0.200      | 0.196     | -0.040                  | -0.040       |
| 0.3        | 0.01  | 1   | 0.4   | 0.4   | 1        | 2      | 0.100           | 0.100               | 0.100       | 0.100      | 0.099     | -0.008                  | -0.008       |

**Table 8.4:** *Equations in (8.2) were solved numerically and the velocities and accelerations of the leading edge of the wave fronts starting at  $x = 0$  were calculated at the times indicated. The initial velocity and acceleration of the leading edge for the iron concentration obtained analytically from equations (8.54) and (8.56) are shown for comparison.*

simulations and provides a semi-analytical approach to capturing the behaviour of initial impact upon contact between the iron and siderophore densities. The results provided using the LDM approach is only valid for the particular initial data chosen and will vary for different initial conditions.

## 8.3 Siderophore-iron complex

In the previous sections, attention was focused only on the populations of unbounded siderophores and iron molecules while the population of the siderophore-iron complex itself was neglected. Since such entities have eluded physical observations in experiments, in this final section on siderophore dynamics we construct and solve model equations representing the dynamics of both siderophores and siderophore-iron complexes. In particular, we will consider the case where a fungal biomass is separated from an infinite and static supply of iron by a constant distance  $L$  and siderophores released by the biomass diffuse to the iron whereupon they form complexes and diffuse back to the biomass. This is broadly similar to the situation encountered by an expanding biomass where the biomass and iron distributions are advancing and retreating respectively in a linear fashion separated by a constant distance. A similar approach was undertaken in Leventhal et al. (2016), except the siderophore-iron complexes were only considered as arising from a single bacterial cell.

### 8.3.1 Siderophore distribution

We have seen in previous sections that once the siderophores are released by the fungus, their motion is governed by diffusion. Therefore siderophore concentra-

tion, denoted by  $C$ , can be represented using the diffusion equation

$$\frac{\partial C}{\partial t} = D_c \frac{\partial^2 C}{\partial x^2} \quad (8.57)$$

on  $(0, L)$ . As before, the production (and loss) of siderophores will be accounted for through suitable boundary conditions.

To solve equation (8.57) we need to define the initial and boundary conditions. We assume there are initially no siderophores and therefore  $C(x, 0) = 0$ . We also assume that siderophores are released by the biomass at a constant rate  $k$ . Thus if the biomass is confined to the region  $x < 0$ , and the unbound iron to  $x > L$ , the release of siderophores from the biomass corresponds to the boundary condition  $D_c C_x(0, t) = -k$ . When the siderophores reach the iron at  $x = L$ , they are assumed to immediately form siderophore-iron complexes and hence there is a secondary boundary condition  $C(L, t) = 0$ . Thus, we have inhomogeneous boundary conditions and the problem is specified as

$$\begin{aligned} C_t &= D_c C_{xx} & \text{for } 0 < x < L, & t > 0 \\ IC : C(x, 0) &= 0, & \text{for } 0 \leq x \leq L \\ BCs : D_c C_x(0, t) &= -k, & \text{for } t > 0 \\ C(L, t) &= 0, & \text{for } t > 0. \end{aligned} \quad (8.58)$$

We can solve (8.58) by constructing the solution  $C(x, t)$  in terms of the steady state solution and a time dependent solution, i.e.  $C(x, t) = C_s(x) + \hat{C}(x, t)$ , where  $C_s$  denotes the steady state solution.

The equilibrium solution  $C_s(x)$ , must satisfy

$$\begin{aligned} 0 &= D_c C_s'' & \text{for } 0 < x < L \\ BCs : D_c C_s'(0) &= -k \text{ and } C_s(L) = 0, \end{aligned} \quad (8.59)$$

where primes denote differentiation with respect to  $x$ . Integrating twice and applying the boundary conditions gives

$$C_s(x) = -\frac{kx}{D_c} + \frac{kL}{D_c}. \quad (8.60)$$

To find  $\hat{C}(x, t)$  it is necessary to solve (8.58) which with  $C(x, t) = C_s(x) + \hat{C}(x, t)$

gives

$$\begin{aligned}
\frac{\partial C_s}{\partial t} + \frac{\partial \hat{C}}{\partial t} &= D_c \left( \frac{\partial^2 C_s}{\partial x^2} + \frac{\partial^2 \hat{C}}{\partial x^2} \right) && \text{for } 0 < x < L, \quad t > 0 \\
IC : C_s(x) + \hat{C}(x, 0) &= 0, && \text{for } 0 \leq x \leq L \\
BCs : C_s(L) + \hat{C}(L, t) &= 0, && \text{for } t > 0 \\
D_c C'_s(0) + D_c \hat{C}'(0, t) &= -k, && \text{for } t > 0.
\end{aligned} \tag{8.61}$$

Given the solution  $C_s(x)$  constructed above, (8.61) simplifies to the following

$$\begin{aligned}
\hat{C}_t &= D_c \hat{C}_{xx} && \text{for } 0 < x < L, \quad t > 0 \\
IC : \hat{C}(x, 0) &= -C_s(x), && \text{for } 0 \leq x \leq L \\
BCs : \hat{C}(L, t) &= 0, && \text{for } t > 0 \\
D_c \hat{C}'(0, t) &= 0, && \text{for } t > 0.
\end{aligned} \tag{8.62}$$

Notice that the BCs are now homogeneous. Equation (8.62) is solved using the method of separation of variables. Assume  $\hat{C}(x, t)$  can be separated to a product of two functions,

$$\hat{C}(x, t) = X(x)T(t).$$

Thus using separation of variables, a basic solution to equation (8.62) is

$$\hat{C}_n(x, t) = \left( A_n \cos(\sqrt{\lambda_n}x) + B_n \sin(\sqrt{\lambda_n}x) \right) e^{-D_c \lambda_n t} \tag{8.63}$$

where  $A_n, B_n$  are constants and

$$\lambda_n = \left( \frac{(2n+1)\pi}{2L} \right)^2. \tag{8.64}$$

Using the boundary conditions in (8.62), it follows  $B_n = 0$  and hence the particular solution

$$\hat{C}(x, t) = \sum_{n=0}^{\infty} A_n e^{-D_c \lambda_n t} \cos(\sqrt{\lambda_n}x). \tag{8.65}$$

To find  $A_n$  we need to utilise the Fourier series. We know that the steady state solution is  $C_s(x) = -\frac{kx}{D_c} + \frac{kL}{D_c}$  and initially there are no siderophores present, i.e.

$C(x, 0) = 0$ . Therefore at  $t = 0$  equation (8.65) becomes

$$\frac{kx}{D_c} - \frac{kL}{D_c} = \sum_{n=0}^{\infty} A_n \cos(\sqrt{\lambda_n}x). \quad (8.66)$$

Using the Fourier series,  $A_n$  is given by

$$A_n = \frac{2k}{LD_c} \int_0^L (x - L) \cos(\sqrt{\lambda_n}x) dx. \quad (8.67)$$

Applying integration by parts to equation (8.67) we obtain

$$A_n = -\frac{2k}{D_c L \lambda_n}. \quad (8.68)$$

Substituting equation (8.68) into (8.65) yields

$$\hat{C}(x, t) = -\sum_{n=0}^{\infty} \frac{2k}{D_c L \lambda_n} e^{-D_c \lambda_n t} \cos(\sqrt{\lambda_n}x),$$

or more usefully

$$\hat{C}(x, t) = -\sum_{n=0}^{\infty} \frac{8kL}{D_c (2n+1)^2 \pi^2} e^{-D_c \left(\frac{(2n+1)\pi}{2L}\right)^2 t} \cos\left(\frac{(2n+1)\pi}{2L}x\right). \quad (8.69)$$

Hence, the solution to the PDE in equation (8.58) is

$$C(x, t) = -\frac{kx}{D_c} + \frac{Lk}{D_c} - \sum_{n=0}^{\infty} \frac{8kL}{D_c (2n+1)^2 \pi^2} e^{-D_c \left(\frac{(2n+1)\pi}{2L}\right)^2 t} \cos\left(\frac{(2n+1)\pi}{2L}x\right). \quad (8.70)$$

### 8.3.2 Siderophore-iron complex distribution

We now focus on the siderophore-iron complex. The siderophore-iron complex only exists when iron binds with siderophores and then the complex's motion is determined by diffusion alone. Therefore we can model the siderophore-iron complex also using the diffusion equation

$$\frac{\partial V}{\partial t} = D_v \frac{\partial^2 V}{\partial x^2}, \quad (8.71)$$

on  $(0, L)$  where  $V$  denotes the siderophore-iron complex concentration. To solve equation (8.71) we need to define appropriate initial and boundary conditions. We assume there are initially no siderophore-iron complexes, i.e.  $V(x, 0) = 0$ . For positive times at  $x = 0$  it is assumed the complex is immediately absorbed by the fungal biomass and hence  $V(0, t) = 0$ . The complex is formed at the boundary  $x = L$  when the iron and siderophore combine and therefore the flux of the complex leaving must balance with the flux of the siderophore arriving, i.e.  $D_v V_x(L, t) = -D_c C_x(L, t)$ . Thus, we seek  $V$  to satisfy the inhomogeneous boundary problem

$$\begin{aligned}
V_t &= D_v V_{xx} & \text{for } 0 < x < L, & & t > 0 \\
IC : & V(x, 0) = 0, & & \text{for } 0 \leq x \leq L \\
BCs : & D_v V_x(L, t) = -D_c C_x(L, t), & \text{for } t > 0 \\
& V(0, t) = 0, & \text{for } t > 0.
\end{aligned} \tag{8.72}$$

As seen previously, due to the inhomogeneous boundary conditions the solution for the PDE in equation (8.72) will be of the form  $V(x, t) = V_s(x) + \bar{V}(x, t) + \hat{V}(x, t)$  where  $\bar{V}$  and  $\hat{V}$  are carefully chosen with regards to the boundary conditions and further  $\hat{V}$  satisfies initial data, while  $V_s$  represents the final steady state solution.

The solution  $V(x, t) = V_s(x) + \bar{V}(x, t) + \hat{V}(x, t)$  must satisfy the equation and initial/boundary conditions in (8.72) i.e.

$$\begin{aligned}
\frac{\partial}{\partial t}(V_s(x) + \bar{V}(x, t) + \hat{V}(x, t)) &= D_v \frac{\partial^2}{\partial x^2}(V_s(x) + \bar{V}(x, t) + \hat{V}(x, t)), & \text{for } 0 < x < L \\
IC : V_s(x) + \bar{V}(x, 0) + \hat{V}(x, 0) &= 0, & \text{for } 0 \leq x \leq L \\
BCs : D_v(V'_s(L) + \bar{V}'(L, t) + \hat{V}'(L, t)) &= -D_c C'_s(L) - D_c \hat{C}'(L, t) & \text{for } t > 0 \\
V_s(0) + \bar{V}(0, t) + \hat{V}(0, t) &= 0 & \text{for } t > 0
\end{aligned} \tag{8.73}$$

where primes denotes differentiation with respect to  $x$ . To find the equilibrium solution of the complex from (8.73),  $V_s$  must satisfy

$$\begin{aligned}
0 &= D_v V''_s & \text{for } 0 < x < L \\
BCs : & D_v V'_s(L) = -D_c C'_s(L) \\
& V_s(0) = 0.
\end{aligned} \tag{8.74}$$



Since  $C'_s = -\frac{k}{D_c}$  from the solution of (8.60), integrating (8.74) twice and applying the boundary conditions gives

$$V_s(x) = \frac{kx}{D_v}. \quad (8.75)$$

Now suppose  $\bar{V}(x, t)$  satisfies

$$\begin{aligned} \bar{V}_t &= D_v \bar{V}_{xx} && \text{for } 0 < x < L \\ BCs : \quad \bar{V}_x(L, t) &= -\frac{D_c}{D_v} \hat{C}_x(L, t) = -\sum_{n=0}^{\infty} \frac{2k(-1)^n}{D_v L \sqrt{\lambda_n}} e^{-D_c \lambda_n t} && \text{for } t > 0 \\ \bar{V}(0, t) &= 0, && \text{for } t > 0. \end{aligned} \quad (8.76)$$

Notice from (8.69), since  $-\frac{D_c}{D_v} \hat{C}_x(L, t) = -\sum_{n=0}^{\infty} \frac{2k(-1)^n}{D_v L \sqrt{\lambda_n}} e^{-D_c \lambda_n t}$  we seek a solution of the form  $\bar{V} = f_n(x) e^{-D_c \lambda_n t}$ . From equation (8.76) we obtain

$$f_n(x) = \bar{A}_n \sin \left( \sqrt{\frac{D_c \lambda_n}{D_v}} x \right) + \bar{B}_n \cos \left( \sqrt{\frac{D_c \lambda_n}{D_v}} x \right) \quad (8.77)$$

where  $\bar{A}_n$  and  $\bar{B}_n$  are constants. Thus using the boundary conditions for  $\bar{V}(x, t)$  from (8.76) it follows  $\bar{B}_n = 0$  and

$$\bar{A}_n = \frac{-2k(-1)^n}{\sqrt{D_c D_v} \lambda_n L \cos \left( \sqrt{\frac{D_c \lambda_n}{D_v}} L \right)} \quad (8.78)$$

resulting in

$$\bar{V}(x, t) = \sum_{n=0}^{\infty} \bar{A}_n \sin \left( \sqrt{\frac{D_c \lambda_n}{D_v}} x \right) e^{-D_c \lambda_n t}. \quad (8.79)$$

To determine  $\hat{V}(x, t)$  it remains to solve

$$\begin{aligned} \hat{V}_t &= D_v \hat{V}_{xx}, && \text{for } 0 < x < L \\ IC : \quad \hat{V}(x, 0) &= -V_s(x) - \bar{V}(x, 0), && \text{for } 0 \leq x \leq L \\ BCs : \quad \hat{V}_x(L, t) &= 0 && \text{for } t > 0 \\ \hat{V}(0, t) &= 0 && \text{for } t > 0. \end{aligned} \quad (8.80)$$

Notice that the boundary conditions are homogeneous hence we solve this using the method of separation of variables. Assume  $\hat{V}(x, t)$  can be separated to a

product of two functions of the form seen previously. Hence using separation of variables with the boundary conditions in (8.80) we obtain

$$\hat{V}(x, t) = \sum_{m=0}^{\infty} \hat{B}_m e^{-D_v \lambda_m t} \sin(\sqrt{\lambda_m} x) \quad (8.81)$$

where  $\lambda_m$  takes the same form as stated in (8.64). To find  $\hat{B}_m$  we need to utilise the Fourier series. Recall,  $V(x, t) = V_s(x) + \bar{V}(x, t) + \hat{V}(x, t)$  and using the initial conditions from equation (8.80) we get  $\hat{V}(x, 0) = -V_s(x) - \bar{V}(x, 0)$ . We know that the steady state solution is  $V_s(x) = \frac{kx}{D_v}$  and  $\bar{V}_n(x, t) = \sum_{n=0}^{\infty} \bar{A}_n \sin\left(\sqrt{\frac{D_c \lambda_n}{D_v}} x\right) e^{-D_c \lambda_n t}$  therefore at  $t = 0$  equation (8.80) becomes

$$\sum_{m=0}^{\infty} \hat{B}_m \sin(\sqrt{\lambda_m} x) = -\frac{kx}{D_v} - \sum_{n=0}^{\infty} \bar{A}_n \sin\left(\sqrt{\frac{D_c \lambda_n}{D_v}} x\right). \quad (8.82)$$

Using the Fourier series, the constants  $\hat{B}_m$  are given by

$$\hat{B}_m = \frac{2}{L} \int_0^L \left[ -\frac{kx}{D_v} - \sum_{n=0}^{\infty} \bar{A}_n \sin\left(\sqrt{\frac{D_c \lambda_n}{D_v}} x\right) \right] \sin(\sqrt{\lambda_m} x) dx \quad (8.83)$$

which can be more conveniently written as

$$\begin{aligned} \hat{B}_m = & \underbrace{-\frac{2k}{D_v L} \int_0^L x \sin(\sqrt{\lambda_m} x) dx}_{I_1} \\ & \underbrace{-\frac{2}{L} \int_0^L \sum_{n=0}^{\infty} \bar{A}_n \sin\left(\sqrt{\frac{D_c \lambda_n}{D_v}} x\right) \sin(\sqrt{\lambda_m} x) dx}_{I_2} \end{aligned} \quad (8.84)$$

where  $I_1$  and  $I_2$  are used to denote the two integrals. Applying integration by parts to  $I_1$ , noting that  $\cos(\sqrt{\lambda_m} L) = 0$  and  $\sin(\sqrt{\lambda_m} L) = \sin(\frac{(2m+1)\pi}{2}) = (-1)^m$ , yields

$$I_1 = -\frac{2k(-1)^m}{D_v L \lambda_m}. \quad (8.85)$$

To determine  $I_2$  we utilise the compound angle formulae  $\cos(A-B) - \cos(A+B) = 2 \sin(A) \sin(B)$  and  $\sin(A+B) = \sin(A) \cos(B) + \cos(B) \sin(A)$  and the above

identities to get

$$I_2 = \frac{2(-1)^m \sqrt{D_c D_v}}{L} \sum_{n=0}^{\infty} \bar{A}_n \frac{\sqrt{\lambda_n}}{D_c \lambda_n - D_v \lambda_m} \cos \left( \sqrt{\frac{D_c \lambda_n}{D_v}} L \right), \quad (8.86)$$

provided  $D_c \lambda_n \neq D_v \lambda_m$ . From equations (8.85) and (8.86) we therefore deduce

$$\hat{B}_m = -\frac{2k(-1)^m}{D_v L \lambda_m} + \frac{2(-1)^m \sqrt{D_c D_v}}{L} \sum_{n=0}^{\infty} \bar{A}_n \frac{\sqrt{\lambda_n}}{D_c \lambda_n - D_v \lambda_m} \cos \left( \sqrt{\frac{D_c \lambda_n}{D_v}} L \right). \quad (8.87)$$

Thus from equation (8.81),  $\hat{V}$  is given by

$$\hat{V}(x, t) = \sum_{m=0}^{\infty} \hat{B}_m \sin(\sqrt{\lambda_m} x) e^{-D_v \lambda_m t} \quad \text{provided } D_c \lambda_n - D_v \lambda_m \neq 0. \quad (8.88)$$

It was stated earlier that the solution to equation (8.72) is of the form  $V(x, t) = V_s(x) + \bar{V}(x, t) + \hat{V}(x, t)$ . Thus the siderophore-iron complex population is given by

$$V(x, t) = \frac{kx}{D_v} + \sum_{n=0}^{\infty} \bar{A}_n \sin \left( \sqrt{\frac{D_c \lambda_n}{D_v}} x \right) e^{-D_c \lambda_n t} + \sum_{m=0}^{\infty} \hat{B}_m \sin(\sqrt{\lambda_m} x) e^{-D_v \lambda_m t}, \quad (8.89)$$

where  $\bar{A}_n$  and  $\hat{B}_m$  are given in (8.78) and (8.87) respectively. Notice the solution is valid so long as  $\frac{D_c}{D_v} \neq \frac{\lambda_m}{\lambda_n}$  or equivalently  $\frac{D_c}{D_v} \neq \left( \frac{2m+1}{2n+1} \right)^2 \forall n, m$ . Typical solutions from equations (8.70) and (8.89) are shown in Figure 8.6 for different times where  $D_c$  and  $D_v$  have been selected so that  $\frac{D_c}{D_v}$  is not a square of a quotient of odd numbers (for an animation please see file Fig-8.6.gif).

We notice a small lag before the complex approaches its steady state from Figure 8.6. This is due to the fact that no complex can exist without some interaction with the siderophores. Hence the siderophore-iron complexes start being produced when the flux of siderophores is sufficiently high at the boundary  $x = L$ . We can estimate this time lag by supposing that complexes can only be detected when their production first exceeds a critical value  $\Phi$ . Hence if  $t = t_c$  when

$$-D_c C_x(L, t) = \Phi, \quad (8.90)$$

then using equation (8.70) we get

$$\Phi = k - \sum_{n=0}^{\infty} \frac{2k(-1)^n}{L\sqrt{\lambda_n}} e^{-D_c\lambda_n t_c}. \quad (8.91)$$

As equation (8.91) represents the first instance where the siderophores are detectible, to get a good approximation we keep the first term of the series i.e.  $n = 0$  only. Thus, since  $\lambda_0 = \left(\frac{\pi}{2L}\right)^2$  equation (8.91) becomes

$$\Phi \approx k - \frac{4k}{\pi} e^{\frac{-D_c\pi^2 t_c}{4L^2}} \quad (8.92)$$

and with some further algebraic manipulation

$$t_c \approx \frac{4L^2}{D_c\pi^2} \ln \left( \frac{4k}{(k - \Phi)\pi} \right). \quad (8.93)$$

Therefore the time when the siderophore-iron complexes are first detected is given by equation (8.93). Its dependence on domain size  $L$ , siderophore production rate  $k$  and diffusion coefficient  $D_c$  match intuitive expectations. Equation (8.93) can be simplified further provided  $k \gg \Phi$  (i.e. the amount of complex on the right cannot exceed the flux of siderophores arriving from the left) resulting in

$$t_c \approx \frac{4L^2}{D_c\pi^2} \ln \left( \frac{4}{\pi} \right). \quad (8.94)$$

which is essentially a transit time for a diffusive process (Edelstein-Keshet, 2005).

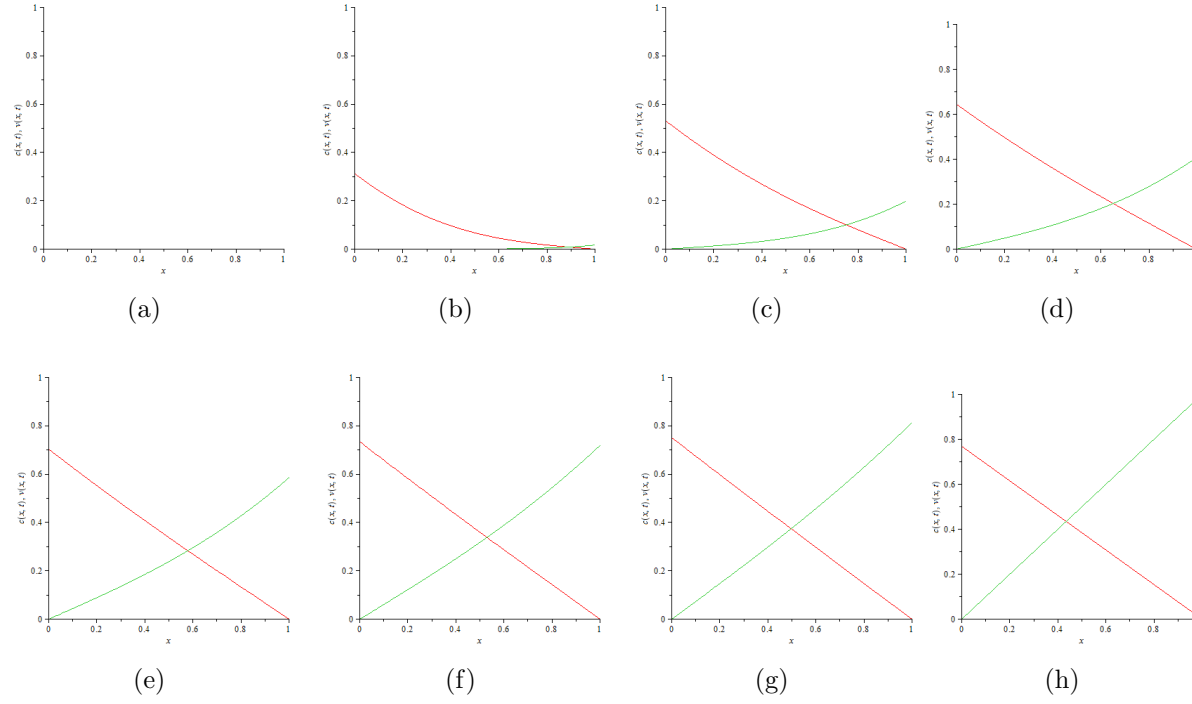


**Figure 8.6:** Solutions of equations (8.58) and (8.72) from equations (8.70) and (8.89) using parameter values  $k = 0.1$ ,  $D_c = 0.13$ ,  $D_v = 0.1$ ,  $L = 1$  and truncating the series at 100 terms. Siderophores are represented by the curve on the left hand side and the siderophore-iron complex is on the right hand side shown at times (a)  $t=0$ , (b)  $t=0.1$ , (c)  $t=0.3$ , (d)  $t=0.5$ , (e)  $t=0.7$ , (f)  $t=0.9$ , (g)  $t=1.1$  and (h)  $t=50$ . [For a movie of these plots please see external folder labelled: Comsol - Movie\_files - Fig8.6.gif]

### 8.3.3 Equal diffusion of siderophore and siderophore-iron complex

The solution constructed above required that  $D_c$  was not a quotient of odd square multiples of  $D_v$ . In particular, this meant that the solution was not valid if  $D_c$  and  $D_v$  were equal. While there are good biological reasons as to why  $D_c \neq D_v$  (e.g. due to different molecular weights between the siderophores and their complexes), it is nonetheless possible to construct the mathematical solution. A valid solution for  $V(x, t)$  that satisfies the case where  $D_c = D_v = D$  can be constructed by seeking  $\bar{V} = (f(x) + h(x) t) e^{-D\lambda_n t}$ . All previous BCs are the same, thus

$$\begin{aligned} \bar{V}_t &= D\bar{V}_{xx} \quad \text{for } 0 < x < L \\ BCs: \quad \bar{V}_x(L, t) &= -\hat{C}_x(L, t) = -\sum_{n=0}^{\infty} \frac{2k(-1)^n}{DL\sqrt{\lambda_n}} e^{-D\lambda_n t} \quad \text{for } t > 0 \\ \bar{V}(0, t) &= 0, \quad \text{for } t > 0, \end{aligned} \quad (8.95)$$

where once again  $-\hat{C}_x(L, t) = -\sum_{n=0}^{\infty} \frac{2k(-1)^n}{DL\sqrt{\lambda_n}} e^{-D\lambda_n t}$ . From equation (8.95) we obtain the following two equations

$$\begin{aligned} h_{xx}(x) + \lambda_n h(x) &= 0 \\ f_{xx}(x) + \lambda_n f(x) &= \frac{h(x)}{D}. \end{aligned} \quad (8.96)$$

Solving the homogeneous ODE from equation (8.96) we obtain

$$h(x) = K_1 \sin\left(\sqrt{\lambda_n} x\right) + K_2 \cos\left(\sqrt{\lambda_n} x\right), \quad (8.97)$$

where  $K_1$  and  $K_2$  are constants. Using the left hand side boundary conditions (i.e.  $\bar{V}(0, t) = 0$ ) for  $\bar{V}(x, t)$  from (8.95), it follows  $K_2 = 0$  and hence

$$h(x) = K_1 \sin\left(\sqrt{\lambda_n} x\right). \quad (8.98)$$

From the non-homogenous ODE in equation (8.96), the particular integral for  $f(x)$  can be determined to be of the form

$$f(x) = \bar{K}_1 x \sin\left(\sqrt{\lambda_n} x\right) + \bar{K}_2 x \cos\left(\sqrt{\lambda_n} x\right), \quad (8.99)$$

where  $\bar{K}_1$  and  $\bar{K}_2$  are constants. Using equation (8.97) and (8.99) after applying some simplification we obtain

$$\sqrt{\lambda_n} \left( 2\bar{K}_1 \cos \left( \sqrt{\lambda_n} x \right) - 2\bar{K}_2 \sin \left( \sqrt{\lambda_n} x \right) \right) = \frac{h(x)}{D}. \quad (8.100)$$

Comparing coefficients in equation (8.100) with (8.98) gives

$$K_1 = -2\bar{K}_2 \left( D\sqrt{\lambda_n} \right) \text{ and } \bar{K}_1 = 0. \quad (8.101)$$

Evaluating  $\bar{V}_x(L, t)$  at the right hand side boundary  $\bar{V}_x(L, t) = -\hat{C}_x(L, t)$  we obtain

$$f_x(L) + h_x(L) t = \frac{-2k(-1)^n}{DL\sqrt{\lambda_n}}. \quad (8.102)$$

Using equations (8.98), (8.99) and (8.101) we get

$$\bar{K}_2 = \frac{2k}{D\lambda_n L^2} \implies K_1 = \frac{-4k}{\sqrt{\lambda_n} L^2}. \quad (8.103)$$

Therefore using equations (8.103)

$$\begin{aligned} f(x) &= \frac{2k}{D\lambda_n L^2} x \cos \left( \sqrt{\lambda_n} x \right), \\ h(x) &= \frac{-4k}{\sqrt{\lambda_n} L^2} \sin \left( \sqrt{\lambda_n} x \right), \end{aligned} \quad (8.104)$$

and finally from equation (8.104) we obtain

$$\bar{V}(x, t) = \sum_{n=0}^{\infty} \frac{2k}{L^2} \left( \frac{x}{D\lambda_n} \cos(\sqrt{\lambda_n} x) - \frac{2t}{\sqrt{\lambda_n}} \sin(\sqrt{\lambda_n} x) \right) e^{-D\lambda_n t}. \quad (8.105)$$

Thus,

$$\hat{V}(x, t) = \sum_{m=0}^{\infty} \tilde{B}_m \sin(\sqrt{\lambda_m} x) e^{-D\lambda_m t}. \quad (8.106)$$

Recall  $V(x, t) = V_s(x) + \bar{V}(x, t) + \hat{V}(x, t)$ . Using the same initial conditions used in equation (8.80), we get  $\hat{V}(x, 0) = -V_s(x) - \bar{V}(x, 0)$ . We know that the steady state solution is still the same, i.e.  $V_s(x) = \frac{kx}{D}$ , and we determined  $\bar{V}(x, t)$  in

equation (8.105). Therefore at  $t = 0$  equation (8.81) now becomes

$$\sum_{m=0}^{\infty} \tilde{B}_m \sin(\sqrt{\lambda_m} x) = -\frac{kx}{D} - \sum_{n=0}^{\infty} \frac{2k}{L^2} \left( \frac{x}{D\lambda_n} \cos(\sqrt{\lambda_n} x) \right). \quad (8.107)$$

Using the Fourier series,  $\tilde{B}_m$  is given by

$$\tilde{B}_m = \frac{2}{L} \int_0^L \left[ -\frac{kx}{D} - \sum_{n=0}^{\infty} \frac{2k}{DL^2\lambda_n} x \cos(\sqrt{\lambda_n} x) \right] \sin(\sqrt{\lambda_m} x) dx, \quad (8.108)$$

$$= \underbrace{-\frac{2k}{DL} \int_0^L x \sin(\sqrt{\lambda_m} x) dx}_{\check{I}_1} - \underbrace{\sum_{n=0}^{\infty} \frac{4k}{D\lambda_n L^3} \int_0^L x \cos(\sqrt{\lambda_n} x) \sin(\sqrt{\lambda_m} x) dx}_{\check{I}_2} \quad (8.109)$$

where  $\check{I}_1$  and  $\check{I}_2$  are used to denote the two integrals. Applying integration by parts to  $\check{I}_1$  we obtain

$$\check{I}_1 = -\frac{2k(-1)^m}{D\lambda_m L}. \quad (8.110)$$

To determine  $\check{I}_2$  we need to utilise the same identities as before and after significant algebraic manipulation we obtain

$$\check{I}_2 = - \sum_{n=0, n \neq m}^{\infty} \frac{2k(-1)^m}{D\lambda_n L^3} \left( \frac{2L(-1)^n \sqrt{\lambda_n}}{\lambda_n - \lambda_m} \right) - \frac{k}{D\sqrt{\lambda_m^3} L^2}, \quad (8.111)$$

where the last term comes from the case when  $n = m$ . Adding the term from equation (8.110) and (8.111) together and substituting into equation (8.108), results in

$$\tilde{B}_m = -\frac{2k(-1)^m}{D\lambda_m L} - \sum_{n=0, n \neq m}^{\infty} \frac{4k(-1)^{m+n}}{D\sqrt{\lambda_n} L^2} \left( \frac{1}{\lambda_n - \lambda_m} \right) - \frac{k}{D\sqrt{\lambda_m^3} L^2}. \quad (8.112)$$



The complete solution for  $V(x, t)$  in the case where  $D_c = D_v = D$  is therefore given by

$$\begin{aligned}
V(x, t) = & \frac{kx}{D} + \frac{2k}{L^2} \sum_{n=0}^{\infty} \left[ \left( \frac{x}{D\lambda_n} \cos(\sqrt{\lambda_n} x) - \frac{2t}{\sqrt{\lambda_n}} \sin(\sqrt{\lambda_n} x) \right) e^{-D\lambda_n t} \right] \\
& - \frac{k}{DL^2} \sum_{m=0}^{\infty} \left[ \frac{2L(-1)^m}{\lambda_m} + \sum_{n=0, n \neq m}^{\infty} \frac{4(-1)^{m+n}}{\sqrt{\lambda_n}} \left( \frac{1}{\lambda_n - \lambda_m} \right) \right. \\
& \left. + \frac{1}{\sqrt{\lambda_m^3}} \right] \sin(\sqrt{\lambda_m} x) e^{-D\lambda_m t}.
\end{aligned} \tag{8.113}$$

Typical solutions from equations (8.70) and (8.113) with  $D_c = D_v$  are shown in Figure 8.7 for different times (for an animation please see file Fig\_8.7.gif). Notice the solution characteristics are similar to the previous case.

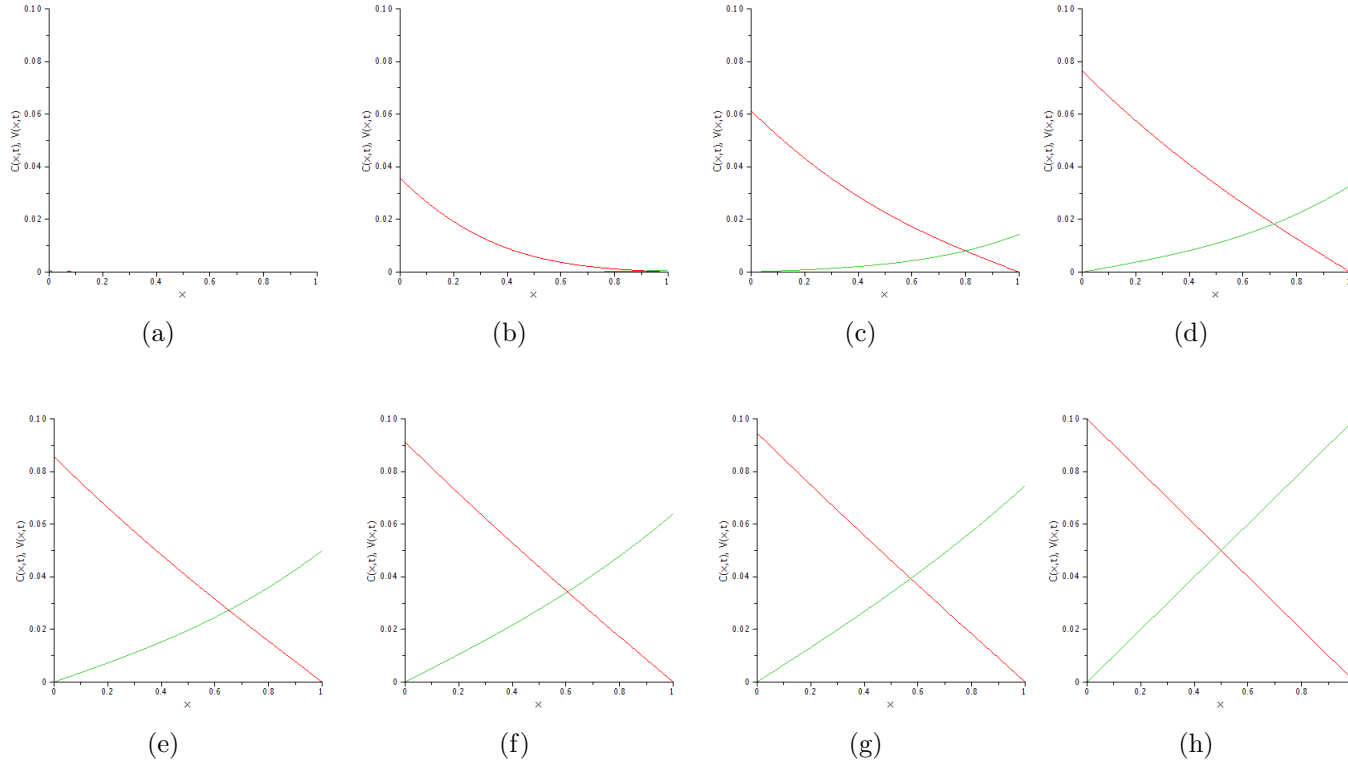


**Figure 8.7:** *Solutions of equations (8.58) and (8.72) from equations (8.70) and (8.113) using parameter values  $k = 0.1$ ,  $D = 1$ ,  $L = 1$  and truncating the series at 20 terms ( $n = m = 20$ ). Siderophores are represented by the curve on the left hand side and the siderophore-iron complex is on the right hand side shown at times (a)  $t=0$ , (b)  $t=0.1$ , (c)  $t=0.3$ , (d)  $t=0.5$ , (e)  $t=0.7$ , (f)  $t=0.9$ , (g)  $t=1.1$  and (h)  $t=10$ . [For a movie of these plots please see external folder labelled: Comsol - Movie\_files - Fig8.7.gif]*

## 8.4 Conclusion

The models seen in this chapter were simplified to consider small and large time asymptotic approximations on the interactions between siderophores and iron. This investigation culminated in well-formed analytical results. However, the small time asymptotic solution didn't easily reveal the behaviour upon immediate contact between the siderophore and iron, due to the initial conditions used. This required us to use another technique, the Laplace decomposition method, introduced in earlier chapters.

Our analysis suggests that, in the first instance, when the siderophores and iron interact, they both initially retreat and then proliferate forward as time progresses once a “stable” distribution has been formed. This process happens in the transient phase of the experiment and it is unlikely to be visually detectable due to the size of siderophores and time scales involved. However, our mathematical model not only captured this behaviour, but using our analysis we were also able to quantify it and furthermore it supports numerical results.

New analytical results were also obtained when the siderophore-iron complex was modelled. In experiments it has been shown that siderophores diffuse and can only be detected once they bind with and remove iron mixed within a chemical substance (CAS agar), thus it is the absence of iron that is usually apparent. In laboratory experiments conforming to the methods used by Milagres et al. (1999), the siderophores are not immediately detectable due to the partitioning of the Petri dish, but once some siderophores have chelated the iron, the production of the complexes can be detected via a colour change (i.e. turning from a blue colour to orange/yellow). Using our proposed model (i.e. equation (8.93)), it has been possible to approximate the length of time before the complex is initially formed. Equations (8.70) and (8.89) will be of benefit to researchers provided they can determine the diffusion coefficient for the siderophore  $D_c$  and the siderophore-iron complex  $D_v$ .

Mathematical models involving siderophores are still scarce, especially in the field of fungal studies, but there are a handful of papers involving bacteria (i.e. Eberi and Collinson, 2009; Leventhal et al., 2016, 2019, and references within) that resemble models similar to our simplified model (e.g. equations (8.2)). Siderophores are typically depicted as a single entity in these studies and lack the transition from a microscopic study to a macroscopic one. The investigations described here not only provide a comprehensive model for the growth of

the microorganism density (i.e. fungi) but also capture its intricate behaviours in response to changes in its vicinity. Thus, the models developed here may allow for quantitative and qualitative predictions to be made on actual experimental studies.

# Chapter 9

## Conclusion

### 9.1 Concluding remarks

Fungi are tremendously important to human society and their importance is likely to increase. In recent times there are great concerns in seeking alternative sustenance due to overpopulation and steady decline in livestock cultivation which has been the primary food source among the greater population. Indeed, currently in human populations there has been a rise in the rates of vegetarianism and veganism since most of (if not all) the nutritional requirements for a healthy well-being and lifestyle can be obtained from fungi. Furthermore, climate change causing a rise in sea levels will reduce the amount of agricultural farmland. Moreover, a significant proportion of land is barren and not suitable for agricultural purposes due to toxins in the polluted landscapes. To add further negativity to an already overwhelming problem, pathogenic fungi are continually having a negative impact on yield resulting in huge losses in agriculture. The work carried out in this thesis have provided potential methods and analysis to better understand the intricacies of fungal interactions in a scientifically sound manner that is crucial to the applications addressing these issues.

Edelstein-Keshet's work on single species laid the foundation to representing fungal densities using a continuous modelling approach. Although Edelstein-Keshet's work has been well studied, results were constructed which, to the author's knowledge, have not been obtained in previous investigations.

Exploring the four primary phenotypes devised by Edelstein (1982), a general analytical solution was determined for the YWD phenotype and using a specific form of initial conditions, particular analytical solutions were obtained

for the FHD and FXD phenotypes. Due to their coupled nature, the primary approach in solving these system of PDEs are via numerical methods, however an analytical solution is more advantageous than numerical results, e.g. is less computationally intensive and more accurate. Using the Laplace decomposition method, we also successfully constructed a semi-analytical approach to solving systems of partial differential equations that resulted in some novel results. Our investigation demonstrated that the Laplace decomposition method provides good approximations on the position of an invading wave front. However, the technique undeniably has some limitations; in particular the approximate series solution appears to only be valid for a small region in the space - time plane regardless of the number of terms generated in the series. Despite the potential lack of overall convergence of the generated series, we observed an interesting phenomena occurring in our system of equations for the fungal YWD phenotype. Using a number of terms from the semi-analytical solution, the position of the leading wave did not appear to be affected by the spurious oscillations behind it (due to non convergence of the series) and seemed to be in perfect alignment with the closed form solution for large times. Due to the nature of the system of equations used to model fungal phenotypes, there are strong similarities in the structure of all such model equations. Hence, despite the lack of any known general analytical solutions for the other phenotypes, we expect the methodology used for the YWD phenotype to gain crucial information regarding the wave properties of other phenotypes.

Utilising the decomposition method further, we provided formulae that are in excellent agreement with numerical results in approximating the initial kinematic properties of the leading edge of any system of PDEs provided the gradient is not zero (i.e.  $u_x \neq 0$ ). The methods developed to determine the initial velocity and acceleration can also be extended further to include initial jerk, snap, crackle and pop. One main drawback of relying on numerical solutions is that parameter values have to be calibrated in advance and it is therefore often difficult to isolate the influence of one parameter on the system. Numerical solutions are also useful in determining asymptotic behaviour for large times but often fail to provide any information around its initial state. Hence using the velocity and acceleration equations proposed, we can predict the initial development of a system. This information is of relevance to researchers concerned with determining the initial speed of a complex system of equations and is not limited to the models

of fungi explored in this thesis.

Fungal application in biotechnology, and in particular bioremediation and biological control, both share a common feature; that is fungal interactions of some kind, e.g. with other fungi or with pollutants in the terrestrial landscape. Interspecies fungal competition is inevitable in heterogeneous environments where fungi combat other fungi via two primary means: releasing volatile organic compounds or through consuming a rival's nutrient source. The investigation carried out in this body of work has primarily focused on how nutrient availability can influence the outcome of fungal interactions by altering the rate at which they degrade a rival's hyphae and hyphal tips. In particular, the mathematical model predicted the circumstances under which pairwise competition would result in the displacement of one species by another, the intermingling (or coexistence) of multiple species and the emergence of deadlock where a stalemate is reached.

In experiments involving mycelial networks, the majority of the variables cannot be controlled but can be measured experimentally, e.g. the speed of tip growth, branching and the death rate of a fungal network hyphae. One variable that can be controlled, however, is the nutrient concentration. We have provided a simple yet powerful description of how nutrient concentrations can influence interactions between different fungal species. Through phase-space analysis, the existence of travelling wave solutions in the model equations were demonstrated which essentially can be regarded as comparing the production of new biomass material through hyphal tip branching and extension to that lost through degradation via either natural means or competition. Furthermore, bounds on the travelling wave speed were also obtained in certain cases. Our modelling has shown that hyphal degradation plays an important role in pairwise fungal competition; it significantly reduces the region of the parameter space where intermingling (or coexistence) can arise and extends the regions corresponding to displacement and therefore provides a further competitive advantage to a fungus. Due to the structure of the model equations the analysis is not limited to fungal species but can also be applied to a whole suite of predator-prey type systems, reaction-diffusion-advection type systems and others.

A key limitation of the modelling approach in Chapter 4 relates to the reduction of the biomass expansion to a single spatial dimension. In experimental configurations, and indeed often in the terrestrial environments, growth is essentially planar and hence there may be inherent differences in the biomass

structures produced in such settings. Thus an appropriate model capable of capturing these behaviours was obtained via expanding the one-dimensional models to a two-dimensional setting in Chapter 5. The key difference between one and two dimensional models is that a one dimensional model describes qualitative and quantitative outcome of a system along a single axis e.g. growth/no growth, whereas a two dimensional model more fully illustrates the qualitative outcome that may alter the quantitative predictions of a one dimensional model e.g. the growth of one fungus around another mycelium or pollutant which quantifiably changes the rate of the interactions.

Boswell et al. (2002) engineered an elegant two-dimensional model that captured the growth of *Rhizoctonia solani* and found it to be in excellent agreement with calibrated experimental data. The devised model consisted of mixed hyperbolic-parabolic type equations. We used this model as the basis of our investigation and extended it further to capture complex fungal interactions in two-dimensional domains.

The primary observation obtained from the analysis was that the variation of resources accessible to fungal species has a significant influence on the outcome of competition. The model equations formulated were used to investigate various scenarios involving resource distributions namely, the outcome of competition with distinct resources, perpetual availability of distinct resources, resource availability at time intervals, distinct resources spread across the domain and a single resource on a unified domain. The prevailing findings of the analysis was that access to greater concentration of resources is sufficient to gain advantage in fungal interactions. Fungi are abundantly used in the field of agriculture, bioremediation and bio-technology. Thus the techniques and the analysis seen in Chapter 5 can provide benefits to the respective fields. Primarily, by determining the critical nutrient concentrations required to obtain a sought after outcome will provide greater control over the desired outcome.

Fungi are known to be extremely versatile. Certain species of fungi are known to grow extremely well in harsh conditions and even in polluted landscapes. To capture some basic functionality we extended Boswell's model to simulate the experimental work of Fomina et al. (2000, 2003) involving fungal behaviour in toxic domains in Chapter 6. We tested various cases from these papers and successfully replicated some observations with the aid of numerical simulations. With our model we simulated several observations within the space of a few minutes



and provided useful insights about the biology otherwise not obvious from experimental observations alone. One such case is the formation of biomass on the toxic domain, a phenomenon which until now has been unexplained. We hypothesised that a patch may contain localised higher nutrient concentrations due to non-uniform mixing of the nutrients allowing the hyphae to colonise. Another aspect explored using the model was the impact of inoculating biomass on a substrate rich domain to observe how it reacts with adverse conditions. It was shown that provided the biomass had access to significant amounts of resources in its immediate vicinity, it is better able to react to and even penetrate polluted regions (i.e. more “energy” is available to overcome the effects of the toxicity). This aspect was not explored in Fomina et al. (2000, 2003).

In Chapter 7 we explored an area still in its infancy in terms of mathematical research as a whole but especially in the field of fungal studies; that is the study of siderophores. The model we have proposed is a continuous model that captures the entire process; the growth of fungi, uptake of nutrients, release of siderophores and interaction with iron. Furthermore the model was explored under various conditions and the results obtained conformed to that seen in experiments.

Typically, laboratory experiments involving fungal interactions with iron require many replicates to verify experimental results and observe the behaviours of different strains under varying conditions. This is often rewarded with insufficient outcomes forcing the experiments to be reproduced. Additionally it is our hypotheses that if the nutrient in the inoculum domain is not uniformly mixed, then it could have a negative impact on the distribution of siderophores. The release of siderophores cannot yet be measured in a quantitative real-time manner, however, our model has made predictions of this. What can currently be measured is the uptake of iron from a growth medium, a feature that has successfully been included in the mathematical model presented. The investigations described here not only provide a comprehensive model for the growth of the microorganism density (i.e. fungi) but also capture its intricate behaviours in response to changes in its vicinity.

The analysis carried out in Chapter 8 focussed on siderophores and iron interactions. As the siderophores are only produced by the fungal mycelium and assuming siderophore-iron complexes are part of each component, we can simplify the model equations from Chapter 7. In accordance to the experimental observa-

tion it was reasonable to explore the equations on a semi-infinite domain. Thus investigating the simplified set of equations by first seeking self-similar solutions, then progressing onto small time asymptotic and large time asymptotic approximations resulted in closed form expressions involving the diffusion coefficients and initial parameters giving approximations that were in excellent agreement with numerical results.

However, despite the elegance of the solutions obtained from the small time and large time asymptotic approximations, the first moment of interaction between the siderophores and iron would be difficult to capture. Thus applying the techniques developed in Chapter 3, it was seen that the respective velocities of siderophores and iron have interchanging signs. This implies that initially the siderophore and iron profiles move in opposite directions to each other, which signifies the loss of siderophores and iron as they are binding to form a siderophore-iron complex, at rates that depend on the binding rates and diffusion coefficients of the iron and siderophore populations. These results were consistent with the COMSOL simulations in Chapter 7 and provided a semi-analytical approach to capturing the behaviour of initial impact upon contact between the iron and siderophore densities.

Furthermore, in the latter section of Chapter 8, focus was on the siderophore-iron complex from which we successfully produced elegant analytical solutions that captured the biological phenomena of siderophores diffusion before and after their interaction with iron. There was a lag observed between the release of siderophores and the time when complexes were formed. We determined a formula that can estimate this time lag by supposing that complexes can only be detected when their production first exceeds a critical value. Using our proposed models researchers may determine the length of time before the complex is initially formed. Also our models will be of immense benefit to researchers provided they can determine the diffusion coefficients for the siderophore and the siderophore-iron complex. Thus, the model developed may allow for quantitative and qualitative predictions to be made on experimental studies.

## 9.2 Future work

In this section some possible avenues for future exploration are considered.

It would be interesting to investigate the convergence of the Laplace de-

composition method as a function of space and time in regards to the single species model explored in this thesis and other phenotypes explored by Edelstein (1982). A starting point would be to visit the work of Cherruault (1990) for inspiration and then use the approach suggested by Ray (2014) which has shown promising results proving the existence and uniqueness of a series solution produced via decomposition methods.

The work developed in Chapters 4 and Chapter 5 laid the foundation that can extend the principles and concepts to more complex systems involving the effects of temperature and water on the outcome of pairwise competition. Furthermore, including more than a single type of branching and anastomosis or a combination of branching patterns would be an interesting avenue to explore. Also, inter-specific competition between fungi displaying different morphologies, could result in interesting outcomes having significant biotechnological applications.

The analysis in Chapter 5 can be extended further to investigate interactions between multiple species on the same domain with different morphologies. The analysis carried out in this thesis assumed the tip and hyphal degradation by a rival species was the same: varying these parameters may lead to a greater understanding of the outcome of fungal competition. The parameter values utilised can be refined and determined for different species using techniques used in artificial intelligence and machine learning, e.g. neural network, classifications, such that for a specific fungal species, a suitable set of parameters are suggested that are inline with experimental studies. There are large databases that contain data on various fungal species hence an interesting study could be carried out.

The work in Chapter 6 can potentially be extended to include quorum sensing in to the model, which can easily be achievable with the current model. Quorum sensing in fungi is an area which has still not really been explored thoroughly (but see Turrá et al., 2016) and thus exploring this field using the models in Chapter 6 could provide some novel and intriguing results.

The models formulated in Chapter 7 needs to be compared to real life models, thus natural future work would entail calibrating the models to experimental observations. Due to the ample literature available, this task can in principle be achieved. Another interesting avenue to explore is to adapt the model suggested here to simulate siderophore detection on a non partitioned domain mimicking experimental work of Bertrand et al. (2010). Furthermore, the model can be

revisited to incorporate an “on/off” feature to release siderophores only when critical levels of iron are experienced within the mycelium to incorporate further realism to the model. There are fungal species that evolve without the ability to produce siderophores; however they can absorb siderophore-iron complexes from the heterogeneous environment. This feature would be fascinating to explore investigating fungal competition. The uptake of siderophore-iron complex was not included in this body of work, thus future work could also incorporate this feature into the models. Additionally, the work in Chapter 8 can be extended via considering a moving boundary to represent a continuous influx of siderophores. A suggested starting point for an interested researcher would be to explore the work of Danckwerts (1950).

All in all, despite the novel models, techniques and results contributed to the field of fungal analysis provided in this thesis, the research has not been fully exhausted. Many fascinating and intellectually stimulating questions have been proposed that pave the way for future researchers to find inspiration from and thus extend the current work further.

The work presented in this thesis contributes to a growing body of knowledge in modelling interactions involving fungi, especially under different environmental settings. Some of the proposed predictions remain as open problems for experimental verification and validation.

# Bibliography

- K. Abbaoui and Y. Cherruault. Convergence of Adomian's method applied to differential equations. *Computers & Mathematics with Applications*, 28(5):103–109, 1994a.
- K. Abbaoui and Y. Cherruault. Convergence of Adomian's method applied to nonlinear equations. *Mathematical and Computer Modelling*, 20(9):69–73, 1994b.
- A. Abdelrazec and D. Pelinovsky. Convergence of the Adomian decomposition method for initial-value problems. *Numerical Methods for Partial Differential Equations*, 27(4):749–766, 2011.
- A. H. M. Abdelrazec. Adomian decomposition method: Convergence analysis and numerical approximation. Master's thesis, McMaster University, School of Graduate studies, 2008.
- G. Adomian. A new approach to the heat equationan application of the decomposition method. *Journal of Mathematical Analysis and Applications*, 113(1):202–209, 1986.
- G. Adomian. A review of the decomposition method in applied mathematics. *Journal of Mathematical Analysis and Applications*, 135(2):501–544, 1988.
- G. Adomian. A review of the decomposition method and some recent results for nonlinear equations. *Computers & Mathematics with Applications*, 21(5):101–127, 1991a.
- G. Adomian. Solving frontier problems modelled by nonlinear partial differential equations. *Computers & Mathematics with Applications*, 22(8):91–94, 1991b.
- G. Adomian. *Solving Frontier Problems of Physics: The Decomposition Method (Fundamental Theories of Physics)*. Springer, 1994.

- G. Adomian and R. Rach. Light scattering in crystals. *Journal of Applied Physics*, 56:2592–2594, 1984.
- G. Adomian and R. Rach. Polynomial nonlinearities in differential equations. *Journal of Mathematical Analysis and Applications*, 109:90–95, 1985a.
- G. Adomian and R. Rach. Nonlinear plasma response. *Journal of Mathematical Analysis and Applications*, 111:114–118, 1985b.
- G. Adomian and R. Rach. Nonlinear differential equations with negative power nonlinearities. *Journal of Mathematical Analysis and Applications*, 112:497–501, 1985c.
- G. Adomian and R. Rach. Solution of nonlinear ordinary and partial differential equations of physics. *Journal of Mathematical and Physical Sciences*, 25(5-6): 703–718, 1991.
- E. Y. Agadjanov. Numerical solution of Duffing equation by the Laplace decomposition algorithm. *Application of Mathematics and Computing*, 177:572–580, 2006.
- E. Ahmed and S. J. M. Holmström. Siderophores in environmental research: roles and applications. *Microbial Biotechnology*, 7(3):196–208, 2014.
- W. Al-Hayani. Solving nth-order integro-differential equations using the combined Laplace transform-Adomian decomposition method. *Applied Mathematics*, 4: 882–886, 2013.
- A. H. S. Al-Taie. *Continuum Models for Fungal Growth*. PhD thesis, University of Dundee, 2011.
- N. Aliasgharzad, E. Shirmohamadi, and S. Oustan. Siderophore production by *Mychorrhizal sorghum* roots under micronutrient deficient condition. *Soil & Environment*, 28(2):119–123, 2009.
- L. J. S. Allen. *An Introduction to Mathematical Biology*. Pearson Education Ltd., 2007.
- M. Y. Andrews, C. M. Santelli, and O. W. Duckworth. Digital image quantification of siderophores on agar plates. *Data in Brief*, 6:890–898, 2016a.

- M. Y. Andrews, C. M. Santelli, and O. W. Duckworth. Layer plate cas assay for the quantitation of siderophore production and determination of exudation patterns for fungi. *Journal of Microbiological Methods*, 121:41–43, 2016b.
- G. Antonissen, A. Martel, F. Pasmans, R. Ducatelle, E. Verbrugghe, V. Vandebroucke, S. Li, F. Haesebrouck, F. V. Immerseel, and S. Croubels. The impact of *Fusarium* mycotoxins on human and animal host susceptibility to infectious diseases. *Toxins(Basel)*, 6(2):430–452, 2014.
- V. B. Asio. The role of mycorrhiza in the mineral nutrition of plants. Website, 29 August 2010. URL <http://soil-environment.blogspot.co.uk/2010/08/role-of-mycorrhiza-in-mineral-nutrition.html>.
- P. Baldrian. Interaction of heavy metals with white-rot fungi. *Enzyme and Microbial Technology*, 32:78–91, 2003.
- W. Balmant, M. H. Sugai-Guerios, J. H. Coradin, N. Krieger, A. F. Junior, and D. A. Mitchell. A model for growth of a single fungal hypha based on well-mixed tanks in series: “Simulation” of nutrient and vesicle transport in aerial reproductive hyphae. *PLoS One*, 10(3):1–22, 2015.
- S. Bartnicki-Garcia, D. D. Bartnicki, G. Gierz, R. Lopez-Franco, and C. E. Bracker. Evidence that Spitzenkörper behavior determines the shape of a fungal hypha: A test of the hyphoid model. *Experimental Mycology*, 19(2):153–159, 1995.
- B. S. Barua, A. Suzuki, and P. N. D. Hoang. Effects of different nitrogen sources on interactions between ammonia fungi and non-ammonia fungi. *Mycology:An International Journal on Fungal Biology*, 3(1):36–53, 2012.
- E. Bayer and G. McIntyre. Biodegradable, fungus-grown foam could replace styrofoam, July 2011. URL <http://designtoimprovelife.dk/mycobondstyrofoampolymer/>.
- E. Bayer and G. McIntyre. Ecovative, 2014. URL <http://www.ecovative.com/>.
- J. L. Beard. Why iron deficiency is important in infant development. *Journal of Nutrition*, 138:2534–2536, 2008.

- J. P. Bellenger, T. Wichard, A. B. Kustka, and A. M. L. Kraepiel. Uptake of molybdenum and vanadium by a nitrogen-fixing soil bacterium using siderophores. *Nature Geoscience*, 1:243–246, 2008.
- J. W. Bennett and M. Klich. Mycotoxins. *Clinical Microbiology Reviews*, 16(3): 497–516, 2003.
- S. Bertrand, J-P. Bouchara, M-C. Venier, P. Richomme, O. Duval, and G. Larcher. N $\alpha$ -methyl coprogen b, a potential marker of the airway colonization by *Scedosporium apiospermum* in patients with cystic fibrosis. *Medical mycology: official publication of the International Society for Human and Animal Mycology (Med Mycol)*, 48(Suppl. 1):S98–S107, 06 2010.
- A. D. Bholay, P. U. Jadhav, B. V. Borkhataria, and V. D. Mayuri. Fluorescent pseudomonads as plant growth promoting rhizobacteria and their siderophore-genesis. *IOSR Journal of Pharmacy and Biological Sciences*, 3(1):27–32, 2012.
- J. Biazar, E. Babolian, and R. Islam. Solution of the system of ordinary differential equations by Adomian decomposition method. *Applied Mathematics and Computation*, 147:713–719, 2004.
- M. Blackwell. The fungi:1, 2, 3 ... 5.1 million species. *American Journal of Botany*, 98(3):426–438, 2011.
- L. Boddy. Saprotrophic cord-forming fungi: warfare strategies and other ecological aspects. *Mycological Research*, 97:641–655, 1993.
- L. Boddy. Interspecific combative interactions between wood-decaying basidiomycetes. *FEMS Microbiology Ecology*, 31(3):185–194, 2000.
- L. Boddy, J. Wood, E. Redman, J. Hynes, and M. D. Fricker. Fungal network response to grazing. *Fungal Genetics and Biology*, 47:522–530, 2010.
- A. Bogumił, L. S. Paszt, A. Lisek, P. Trzciński, and A. Harbuzov. Identification of new *Trichoderma* strains with antagonistic activity against *Botrytis cinerea*. *Polish Society for Horticultural Science. Folia Horticulturae*, 25(2): 123–132, 2013.
- G. P. Boswell. Modelling mycelial networks in structured environments. *Mycological Research*, 112:1015–1025, 2008.



- G. P. Boswell. Modelling combat strategies in fungal mycelia. *Journal of Theoretical Biology*, 304:226–234, 2012.
- G. P. Boswell and I. Carver. A lattice-free model of translocation-induced outgrowth in fungal mycelia. *IAENG International Journal of Applied Mathematics*, 38(4):173–179, 2008.
- G. P. Boswell and F. A. Davidson. Modelling hyphal networks. *Fungal Biology Reviews*, 26:30–38, 2012.
- G. P. Boswell, H. Jacobs, F. A. Davidson, G. M. Gadd, and K. Ritz. Functional consequences of nutrient translocation in mycelial fungi. *Journal of Theoretical Biology*, 217:459–477, 2002.
- G. P. Boswell, H. Jacobs, F. A. Davidson, G. M. Gadd, and K. Ritz. Growth and function of fungal mycelia in heterogeneous environments. *Bulletin of Mathematical Biology*, 65:447–477, 2003a.
- G. P. Boswell, H. Jacobs, F. A. Davidson, G. M. Gadd, and K. Ritz. A positive numerical scheme applied to a mixed-type 1D partial differential equation model for fungal growth. *Applied Mathematics and Computation*, 138:321–340, 2003b.
- G. P. Boswell, H. Jacobs, K. Ritz, G. Gadd, and F. A. Davidson. The development of fungal networks in complex environments. *Bulletin of Mathematical Biology*, 69:605–634, 2007.
- H. Boukhalfa, J. Lack, S. D. Reilly, L. Herman, and M. P. Neu. Siderophore production and facilitated uptake of iron and plutonium in *P. putida*. *AIP Conference Proceedings*, 673:343–344, 2003.
- C. M. Brasier. *Phytophthora cinnamomi* and oak decline in southern Europe. Environment constraints including climate change. *Anales des Sciences Forestières*, 53(2-3):347–358, 1996.
- A. Braud, F. Hoegy, K. Jezequel, T. Lebeau, and I. J. Schalk. New insights into the metal specificity of the *Pseudomonas aeruginosa* pyoverdine-iron uptake pathway. *Environmental Microbiology*, 11(5):1079–1091, 2009.
- M. Brundrett. Mycorrhizal associations and other means of nutrition of vascular plants: Understanding the global diversity of host plants by resolving conflicting

- information and developing reliable means of diagnosis. *Plant and Soil*, 320: 37–77, 2009.
- H. Brunswik. *Untersuchungen uber Geschlechts- und Kernverhaltnisse bei der Hymenomycetengattung Coprinus. [Studies on gender and core conditions in the genus in Hymenomycetengattung Coprinus]*. K. Goebel. eds Gustav Fisher, 1924.
- A. H. R. Buller. *Researches on Fungi*. Longmans Green, London, 1931.
- K. E. Bushley, R. Raja, P. Jaiswal, J. S. Cumbie, M. Nonogaki, A. E. Boyd, C. A. Owensby, B. J. Knaus, J. Elser, D. Miller, Y. Di, K. L. McPhail, and J. W. Spatafora. The genome of *Tolypocladium inflatum*: Evolution, organization, and expression of the cyclosporin biosynthetic gene cluster. *PLOS Genetic*, 9(6):1–20, 2013. doi: DOI:10.1371/journal.pgen.1003496.
- R. J. W. Byrde and H. J. Willetts. *The Brown Rot Fungi of Fruit: Their Biology and Control*. Pergamon, 1977.
- A. Cabaj and A. Kosakowska. Iron-dependent growth of and siderophore production by two heterotrophic bacteria isolated from brackish water of the southern baltic sea. *Microbiological Research*, 164:570–577, 2009.
- M. J. Carlile, S. C. Watkinson, and G. W. Gooday. *The Fungi*. Academic Press, 2nd edition, 2001.
- C. Cheng, E. J. O’Brien, D. McCloskey, J. Utrilla, C. Olson, R. A. LaCroix, T. E. Sandberg, A. M. Feist, B. O. Palsson, and Z. A. King. Laboratory evolution reveals a two-dimensional rate-yield tradeoff in microbial metabolism. *PloS Computational Biology*, 15(6):1–14, 2019.
- Y. Cherruault. Convergence of Adomian’s method. *Mathematical and Computer Modelling*, 14:83–86, 1990.
- M. J. A. Choudhury, P. M. J. Trevelyan, and G. P. Boswell. Determining the kinematic properties of an advancing front using a decomposition method. *IAENG International Journal of Applied Mathematics*, 46(4):578–584, 2016.
- M. J. A. Choudhury, P. M. J. Trevelyan, and G. P. Boswell. A mathematical model of nutrient influence on fungal competition. *Journal of Theoretical Biology*, 438: 9–20, 2018.

- C. Chyu, T. F. Hsieh, and Y. C. Chang. *Rhizoctonia Species: Taxonomy, Molecular Biology, Ecology, Pathology and Disease Control*. Springer Netherlands, 1996.
- D. Cohen. Computer simulation of biological pattern generation processes. *Nature*, 216:246–248, 1967.
- P. J. Cotty, L. Antilla, and P. J. Wakelyn. *Biological control: a global perspective*. CAB International, Oxfordshire, UK, 2007.
- E. Czembor, L. Stępień, and A. Waśkiewicz. Effects of environmental factors on *Fusarium* species and associated mycotoxins in maize grain grown in Poland. *PLOS ONE*, 10(7):1–18, 2015.
- P. V. Danckwerts. Unsteady-state diffusion or heat conduction with moving boundary. *Transactions of the Faraday Society*, 46:701–712, 1950.
- F. A. Davidson. Modelling qualitative response of fungal mycelia to heterogeneous environments. *Journal of Theoretical Biology*, 195:281–292, 1998.
- F. A. Davidson, B. D. Sleeman, A. D. M. Rayner, J. W. Crawford, and K. Ritz. Context-dependent macroscopic patterns in growing and interacting mycelial networks. *Proceedings of the Royal Society of London B Biological Sciences*, 263(1372):873–880, 1996.
- M. Dehghan and M. Tatari. The use of Adomian decomposition method for solving problems in calculus of variations. *Mathematical Problems in Engineering*, doi:org/10.1155/MPE/2006/65379, 2006.
- J. W. Dorner, R. J. Cole, W. J. Connick, D. J. Daigle, M. R. McGuire, and B. S. Shasha. Evaluation of biological control formulations to reduce aflatoxin contamination in peanuts. *Biological Control*, 26(3):318–324, 2003.
- V. Duarte. Macieira (*malus domestica* borkh): bitter rot. online, October 2004. URL [http://www.ufrgs.br/agrofitossan/galeria/tipos.asp?id\\_nome=7](http://www.ufrgs.br/agrofitossan/galeria/tipos.asp?id_nome=7).
- J. P. Dudley and M. H. Woodford. Bioweapons, biodiversity, and ecocide: Potential effects of biological weapons on biological diversity: Bioweapon disease outbreaks could cause the extinction of endangered wildlife species, the erosion of genetic diversity in domesticated plants and animals, the destruction

- of traditional human livelihoods, and the extirpation of indigenous cultures. *Bioscience*, 52(7):583–592, 2002.
- H. J. Eberi and S. Collinson. A modeling and simulation study of siderophore mediated antagonism in dual-species biofilms. *Theoretical Biology and Medical Modelling*, 6(30):1–16, 2009.
- L. Edelstein. The propagation of fungal colonies: A model for tissue growth. *Journal of Theoretical Biology*, 98:679–701, 1982.
- L. Edelstein and B. Ermentrout. Models for branching networks in two dimensions. *SIAM Journal on Applied Mathematics*, 49(4):1136–1157, 1989.
- L. Edelstein and L. A. Segel. Growth and metabolism in mycelial fungi. *Journal of Theoretical Biology*, 104:187–210, 1983.
- L. Edelstein-Keshet. *Mathematical Models in Biology*. Society for Industrial and Applied Mathematics, 2005.
- B. J. O. Efiuvweuwere and M. Chynyere. The microbiology and deterioration of soft drinks subjected to two different marketing. *Global Journal of Pure and Applied Sciences*, 7(1):43–48, 2001.
- M. Eisendle, M. Schrettl, C. Kragl, D. Müller, P. Illmer, and H. Haas. The intracellular siderophore ferriicrocin is involved in iron storage, oxidative-stress resistance, germination, and sexual development in *Aspergillus nidulans*. *Eukaryotic Cell*, 5(10):1596–1603, 2006.
- I. L. El-Kalla. Error analysis of Adomian series solution to a class of nonlinear differential equations. *Applied Mathematics E-Notes*, 7:214–221, 2007.
- S. N. Elgazery. Numerical solution for the Falkner-Skan equation. *Chaos, Solitons and Fractals*, 35:738–746, 2008.
- J. A. Evans, C. A. Eyre, H. J. Rogers, L. Boddy, and C. T. Müller. Changes in volatile production during interspecific interactions between four wood rotting fungi growing in artificial media. *Fungal Ecology*, 1:57–68, 2008.
- J. Fadaei. Application of Laplace: Adomian decomposition method on linear and nonlinear system of pdes. *Applied Mathematical Sciences*, 27:1307–1315, 2011.

- R. E. Falconer, J. L. Bown, N. A. White, and J. W. Crawford. Biomass recycling and the origin of phenotype in fungal mycelia. *Proceedings of the Royal Society of London B Biological Sciences*, 272(1573):1727–1734, 2005.
- R. E. Falconer, J. L. Bown, N. A. White, and J. W. Crawford. Modelling interactions in fungi. *Journal of the Royal Society Interface*, 5:603–615, 2008.
- R. E. Falconer, J. L. Bown, E. McAdam, P. Perez-Reche, A. T. Sampson, J. Van Der. Bulcke, and N. A. White. Modelling fungal colonies and communities: challenges and opportunities. *IMA Fungus*, 1(2):155–159, 2010.
- R. E. Falconer, J. L. Bown, N. A. White, and J. W. Crawford. Linking fungal individuals to community scale patterns. *Fungal Ecology*, 4:76–82, 2011.
- R. E. Falconer, G. Battaia, S. Schmidt, P. Baveye, C. Chenu, and W. Otten. Microscale heterogeneity explains experimental variability and non-linearity in soil organic matter mineralisation. *PLOS ONE*, 10(5):1–12, 2015.
- A. Flores-Maltos, L. V. Rodriguez-Duran, J. Renovato, J. C. Contreras, R. Rodriguez, and C. N. Aguilar. Catalytical properties of free and immobilized *Aspergillus niger* Tannase. *Enzyme Research*, doi:org/10.4061/2011/768183, 2011.
- M. Fomina, K. Ritz, and G. M. Gadd. Negative fungal chemotropism to toxic metals. *FEMS Microbiology Letters*, 193:207–211, 2000.
- M. Fomina, K. Ritz, and G. M. Gadd. Nutritional influence on the ability of fungal mycelia to penetrate toxic metal-containing domains. *Mycological Research, British Mycological Society*, 107 (7):861–871, 2003.
- G. M. Gadd. Interactions of fungi with toxic metals. *New Phytologist*, 124:25–60, 1993.
- G. M. Gadd. Metals, mineral and microbes: geomicrobiology and bioremediation. *Microbiology*, 156(Pt 3):609–643, 2010.
- L. Gálfi and A. Rácz. Properties of the reaction front in an  $A+B \rightarrow C$  type reaction-diffusion process. *Physical Review A*, 38(6):3151–3154, 1988.

- D. A. Gamit and S. K. Tank. Effect of siderophore producing microorganism on plant growth of *Cajanus cajan* (pigeon pea). *International Journal of Research in Pure and Applied Microbiology*, 4(1):20–27, 2014.
- S. K. Ghosh, S. Pal, and N. Chakraborty. The qualitative and quantitative assay of siderophore production by some microorganism and effects of different media on its production. *International Journal of Chemical Science*, 13(4):1621–1629, 2015.
- M. Giovannetti, P. Fortuna, A. S. Citernes, S. Morini, and M. P. Nuti. The occurrence of anastomosis formation and nuclear exchange in intact arbuscular mycorrhizal networks. *New Phytologist*, 151:717–724, 2001.
- F. Giráldez and M. A. Herrero. *Mathematics, Developmental Biology and Tumor Growth*. American Mathematical Society, 2009.
- M. Girbardt. Die ultrastruktur der apikalregion von pilzhypen [The ultra-structure of the apical region of fungal hyphae]. *Protoplasma*, 67:413–441, 1969.
- N. L. Glass, D. J. Jacobson, and P. K. Shiu. The genetics of hyphal fusion and vegetative incompatibility in filamentous ascomycete fungi. *Annual Review of Genetics*, 34:165–186, 2000.
- N. L. Glass, C. Rasmussen, M. G. Roca, and N. D. Read. Hyphal homing, fusion and mycelial interconnectedness. *Trends in Microbiology*, 12(3):135–141, 2004.
- G. A. Gledson, M. D. Martins, P. L. Cláudio, and G. J. Salvador. A solution of nonlinear equation for the gravity wave spectra from Adomian decomposition method: a first approach. *Revista Brasileira de Meteorologia*, 28:357–363, 2013. ISSN 0102-7786.
- G. W. Gooday. The dynamics of hyphal growth. *Mycological Research*, 99:385–394, 1995.
- A. Goyal, R. Sanghi, A. K. Misra, and J. B. Shukla. A modeling study on the role of fungi in removing inorganic pollutants. *Mathematical Biosciences*, 244(2):116–124, 2013.
- C. M. Gruhn, A. V. Gruhn, and O. K. Miller. *Boletiniellus merulioides* alters root morphology of *Pinus densiflora* without mycorrhizal formation. *Mycologia*, 84:528–533, 1992.

- M. Gupta and S. Shrivastava. Mycoremediation: A management tool for removal of pollutants from environment. *Indian Journal of Applied Research*, 4(8):289–291, 2014.
- H. Haas. Fungal siderophore metabolism with a focus on *Aspergillus fumigatus*. *Natural Product Reports*, 31:1266–1276, 2014.
- J. B. Hagen. Five kingdoms, more or less: Robert Whittaker and the broad classification of organisms. *BioScience Oxford Journals*, 62(1):67–74, 2012.
- J. M. Halley, H. N. Comins, J. H. Lawton, and M. P. Hassell. Competition, succession and pattern in fungal communities: towards a cellular automata model. *Oikos*, 70:435–442, 1994.
- S. D. Harris. Branching of fungal hyphae: regulation, mechanisms and comparison with other branching systems. *Mycologia*, 100(6):823–832, 2008.
- L. Heaton, B. Obara, V. Grau, N. Jones, T. Nakagaki, L. Boddy, and M. Fricker. Analysis of fungal networks. *Fungal Biology Reviews*, 26:12–29, 2012.
- M. A. Helal and M. S. Mehanna. The tanh method and Adomian decomposition method for solving the foam drainage equation. *Applied Mathematics and Computation*, 190:599–609, 2007.
- D. V-D. Helm and G. Winkelmann. *Hydroxamates and polycarboxylates as iron transport agents (siderophores) in fungi*. In *Metal Ions in Fungi* (G. Winkelmann & D. Winge, eds). Marcel Dekker, 1994.
- T. Hillen and H. G. Othmer. The diffusion limit of transport equations derived from velocity jump processes. *SIAM Journal on Applied Mathematics*, 61:751–775, 2000.
- J. Hiscox, G. Clarkson, M. Savoury, G. Powell, I. Savva, M. Lloyd, J. Shipcott, A. Choimes, X. A. Cumbriu, and L. Boddy. Effects of pre-colonisation and temperature on interspecific fungal interactions in wood. *Fungal Ecology*, 21: 32–42, 2016.
- L. Ho-Man, W. Zhen-Wen, Y. Zhi-Hong, Y. Kin-Lam, P. Xiao-Ling, and C. Kwai-Chung. Interactions between *Arbuscular Mycorrhizae* and plants in phytoremediation of metal-contaminated soils. *Pedosphere*, 23 (5):549–563, 2013.

- P. H. F. Hobbelen, N. D. Paveley, and F. van den Bosch. The emergence of resistance to fungicides. *PLoS ONE*, 9(3):1–14, 2014.
- R. F. Hogervorst, M. A. J. Dijkhuis, M. A. van der Schaar, M. P. Berg, and H. A. Verhoef. Indications for the tracking of elevated nitrogen levels through the fungal route in a soil food web. *Environmental Pollution*, 126:257–266, 2003.
- S. Hopkins. *A Hybrid Mathematical Model of Fungal Mycelia: Tropisms, Polarised Growth and Application to Colony Competition*. PhD thesis, University of Glamorgan, 2011.
- S. Hopkins and G. P. Boswell. Mycelial response to spatiotemporal nutrient heterogeneity: a velocity-jump mathematical model. *Fungal Ecology*, 5:124–136, 2012.
- T. Horio and B. R. Oakley. The role of microtubules in rapid hyphal tip growth of *Aspergillus nidulans*. *Molecular Biology of the Cell*, 16(2):918–926, 2005.
- M. Hussain and M. Khan. Modified Laplace decomposition method. *Applied Mathematical Sciences*, 4(36):1769–1783, 2010.
- J. Hynes, T. C. Müller, T. H. Jones, and L. Boddy. Changes in volatile production during the course of fungal mycelial interactions between *Hypholoma fasciculare* and *Resinicium bicolor*. *Journal of Chemical Ecology*, 33(1):43–57, 2007.
- A. V. Ibarra-Medina, R. Ferrera-Cerrato, A. Alarcon, M. E. Lara-Hernandez, and J. M. Valdez-Carrasco. Isolation and screening of *Trichoderma* strains antagonistic to *Sclerotinia sclerotiorum* and *Sclerotinia minor*. *Mexican Journal of Mycology*, 31:53–63, 2010.
- F. B. Iluyemi and M. M. Hanafi. Mycelial growth interactions and mannan-degrading enzyme activities from fungal mixed cultures grown on palm kernel cake. *African Journal of Biotechnology*, 8(10):2283–2288, 2009.
- P. Indiragandhi, R. Anandham, M. Madhaiyan, G-H. Kim, and T. Sa. Cross-utilization and expression of outer membrane receptor proteins for siderophore uptake by Diamondback moth *Plutella xylostella* (Lepidoptera : Plutellidae) gut bacteria. *FEMS Microbiology Letters*, 289:27–33, 2008.



- S. L. Jackson and I. B. Heath. Roles of calcium ions in hyphal tip growth. *Microbiological Reviews*, 57:367–382, 1993.
- H. Jacobs, G. P. Boswell, K. Ritz, F. A. Davidson, and G. M. Gadd. Solubilization of calcium phosphate as a consequence of carbon translocation by *Rhizoctonia solani*. *FEMS Microbiology Ecology*, 40:65–71, 2002.
- L. Johnson. Iron and siderophores in fungal-host interactions. *Mycological Research*, 112:170–183, 2008.
- M. J. Keeling and P. Rohani. *Modelling infectious diseases in human and animals*. Princeton University Press, 2008.
- P. Kennedy. Ectomycorrhizal fungi and interspecific competition: species interactions, community structure, coexistence mechanism, and future research directions. *New Phytologist*, 187:895–910, 2010.
- Y. Keskin and G. Oturan. Reduced differential transform method for partial differential equations. *International Journal of Nonlinear Sciences and Numerical Simulation*, 10(6):741–749, 2009.
- Y. Keskin and G. Oturan. Reduced differential transform method for solving linear and nonlinear wave equations. *Iranian Journal of Science & Technology, Transaction A*, 34(A2):113 – 122, 2010.
- M. Khan, M. Hussain, H. Jafari, and Y. Khan. Application of Laplace decomposition method to solve nonlinear coupled partial differential equations. *World Applied Sciences Journal*, 9(Special Issue of Applied Math):13–19, 2010.
- S. A. Khuri. A Laplace decomposition algorithm applied to class of nonlinear differential equations. *Journal of Applied Mathematics*, 1(4):141–155, 2001.
- S. A. Khuri. A new approach to Bratus problem. *Applied Mathematics and Computation*, 147(1):131–136, 2004.
- M. Koutb and E. H. Ali. Potential of *Epicoccum purpurascens* strain 5615 aumc as a biocontrol agent of *Pythium irregulare* root rot in three leguminous plants. *Mycobiology*, 38(4):286–294, 2010.

- Z. Koza. The long-time behavior of initially separated  $A + B \rightarrow 0$  reaction-diffusion systems with arbitrary diffusion constants. *Journal of Statistical Physics*, 85(1-2):179–191, 1996.
- S. M. Kraemer, A. Butler, P. Borer, and J. Cervini-Silva. Siderophores and the dissolution of iron-bearing minerals in marine systems. *Reviews in Mineralogy and Geochemistry*, 59(1):53–84, 2005.
- E. Kurniati, N. Arfarita, T. Imati, T. Higuchi, A. Kanno, K. Yamamoto, and M. Sekine. Potential bioremediation of mercury-contaminated substrate using filamentous fungi isolated from forest soil. *Journal of Environmental Sciences*, 26:1223–1231, 2014.
- S. H. Lee, M. D. Fricker, and M. A. Porter. Mesoscale analyses of fungal networks as an approach for quantifying phenotypic traits. *Journal of Complex Networks*, 5:145–159, 2017.
- G. E. Leventhal, M. Ackermann, and K. Schiessl. Benefits of siderophore release lie in mediating diffusion limitation at low iron solubility. *bioRxiv*, doi:org/10.1101/093948, 2016. URL <https://www.biorxiv.org/content/10.1101/093948v1>.
- G. E. Leventhal, M. Ackermann, and K. Schiessl. Why microbes secrete molecules to modify their environment: The case of iron-chelating siderophores. *Journal of the Royal Society Interface*, 16(150):1–25, 2019.
- D. A. Lipson. The complex relationship between microbial growth rate and yield and its implications for ecosystem processes. *Frontiers in Microbiology*, 6:615, 2015.
- J. Lockwood, M. P. Marchetti, and M. F. Hoopes. *Invasive Ecology (2ed)*. John Wiley & Sons, 2013.
- A. J. De Lucca. Harmful fungi in both agriculture and medicine. *Revista Iberoamericana de Micologia*, 24(1):3–13, 2007.
- S. U. Luk, T.K. Lee, J. Liu, D. T. Lee, Y. T. Chiu, S. Ma, I. O. Ng, Y. C. Wong, F. L. Chan, and M. T. Ling. Chemopreventive effect of psp through targeting of prostate cancer stem cell-like population. *PLoS One*, 6(5):1–9, 2011.

- A. Machuca and A. M. F. Milagres. Use of CAS-agar plate modified to study the effect of different variables on the siderophore production by *Aspergillus*. *Letters in Applied Microbiology*, 36:177–181, 2003.
- J. Manjunathan, N. Subbulakshmi, R. Shanmugapriya, and V. Kaviyarasan. Proximate and mineral composition of four edible mushroom species from South India. *International Journal of Biodiversity and Conservation*, 3(8):386–388, 2011.
- A. Manteca, D. Claessen, C. Lopez-Iglesias, and J. Sanchez. Aerial hyphae in surface cultures of *Streptomyces lividans* and *Streptomyces coelicolor* originate from viable segments surviving an early programmed cell death event. *FEMS Microbiology Letters*, 274(1):118–125, 2007.
- B. Marçais, O. Caël, and C. Delatour. Interaction between root rot basidiomycetes and phytophthora species on pendunculate oak. *Plant Pathology*, 60:296–303, 2011.
- H. Marschner. *Mineral nutrition of higher plants*. Academic Press, 1995.
- T. J. McLoughlin, J. P. Quinn, A. Bettermann, and R. Bookland. *Pseudomonas cepacia* suppression of sunflower wilt fungus and role of antifungal compounds in controlling the disease. *Applied Environmental Microbiology*, 58(5):1760–1763, 1992.
- R. Meher and S. K. Meher. Analytical treatment and convergence of the Adomian decomposition method for instability phenomena arising during oil recovery process. *International Journal of Engineering Mathematics*, doi:org/10.1155/2013/752561, 2013.
- H. L. Mehl and P. J. Cotty. Nutrient environments influence competition among *Aspergillus flavus* genotypes. *Applied and Environmental Microbiology*, 79(5):1473–1480, 2013.
- A. Meskauskas, M. D. Fricker, and D. Moore. Simulating colonial growth of fungi with the neighbour-sensing model of hyphal growth. *Mycological Research*, 108(11):1241–1256, 2004a.

- A. Meskauskas, L. J. McNulty, and D. Moore. Concerted regulation of all hyphal tips generates fungal fruit body structures: experiments with computer visualizations produced by a new mathematical model of hyphal growth. *Mycological Research*, 108(4):341–353, 2004b.
- M. Miethke and M. A. Marahiel. Siderophore-based iron acquisition and pathogen control. *Microbiology and Molecular Biology Reviews*, 71(3):413–451, 2007.
- A. M. F. Milagres, A. Machuca, and D. Napoleão. Detection of siderophore production from several fungi and bacteria by a modification of chrome azurol s (cas) agar plate assay. *Journal of Microbiological Methods*, 37:1–6, 1999.
- M. A. Mohamed and M. S. Torky. Numerical solution of nonlinear system of partial differential equations by the Laplace decomposition method and the Padé approximation. *American Journal of Computational Mathematics*, 3:175–184, 2013.
- G. F. Morley, J. A. Sayer, S. C. Wilkinson, M. M. Gharieb, and G. M. Gadd. *Fungal sequestration, mobilization and transformation of metals and metalloids*. Cambridge University Press, 1996.
- A. Morón-Ríos, S. Gómez-Cornelio, B. O. Ortega-Morales, S. D. Rosa-Garcia, L. P. Partida-Martínez, P. Quintana, J. A. Alayón-Gamboa, and S. Cappello-Garcia. Interactions between abundant fungal species influence the fungal community assemblage on limestone. *PLOS ONE*, 12:1–20, 2017.
- J. B. Neilands. Siderophores: structure and function of microbial iron transport compounds. *The Journal of Biological Chemistry*, 270(45):26723–26726, 1995.
- N. Ngarhasta, B. Some, K. Abbaoui, and Y. Cherruault. New numerical study of Adomian method applied to a diffusion model. *Kybernetes*, 31(1):61–75, 2002.
- R. Niehus, A. Picot, N. M. Oliveira, S. Mitri, and K. R. Foster. The evolution of siderophore production as a competitive trait. *Evolution: International Journal of Organic Evolution*, 71(6):1443–1455, 2017.
- L. Nissen. A survey of mitosporic fungi. FungalBlog, October 2012. URL <http://ldnissen30269.blogspot.co.uk/2012/10/lab-6.html>.

- H. Oberegger, M. Schoeser, I. Zadra, B. Abt, and H. Haas. SREA is involved in regulation of siderophore biosynthesis, utilization and uptake in *Aspergillus nidulans*. *Molecular Microbiology*, 41(5):1077–1089, 2001.
- B. L. O’Brien, J. L. Parrent, J. A. Jackson, J. M. Moncalvo, and R. Vilgalys. Fungal community analysis by large-scale sequencing of environmental samples. *Applied and Environmental Microbiology*, 71:5544–5550, 2005.
- S. V. Olishkevskya and N. N. Zhdanova. Chemotropism of soil filamentous fungi towards copper ions. *Russian Journal Translation: Mycology and Phytopathology*, 43(1):58–67, 2009.
- L. A. Olsen, E. R. Choffnes, D. A. Relman, and L. Pray. *Fungal Diseases: An Emerging Threat to Human, Animal, and Plant Health: Workshop Summary*. National Academies Press, 2011. Forum on Microbial Threats and Board on Global Health and Institute of Medicine.
- Microbiology Online. Observing fungi in a petri dish. Website. URL <http://www.microbiologyonline.org.uk/teachers/observing-microbes/observing-fungi-in-a-petri-dish>.
- J. F. Peberdy. Protein secretion in filamentous fungi trying to understand a highly productive black box. *Trend in Biotechnology*, 12:50–57, 1994.
- S. Perez-Miranda, N. Cabirol, R. George-Tellez, L. S. Zamudio-Rivera, and F. J. Fernandez. O-CAS, a fast and universal method for siderophore detection. *Journal of Microbiological Methods*, 70(1):127–131, 2007.
- C. Persson, S. Olsson, and H. Jansson. Growth of *Arthrobotrys superba* from a birch wood resource base into soil determined by radioactive tracing. *FEMS*, 31(1):47–51, 2000.
- C. C. Philpott, S. Leidgens, and A. G. Frey. Metabolic remodeling in iron-deficient fungi. *Biochimica et Biophysica Acta (BBA) - Molecular Cell Research*, 1823(9): 1509–1520, 2012.
- M. J. Plank and M. J. Simpson. Models of collective cell behaviour with crowding effects: comparing lattice-based and lattice-free approaches. *Journal of the Royal Society Interface*, 9(76):2983–2996, 2012.

- M. J. Plank and B. D. Sleeman. Lattice and non-lattice models of tumour angiogenesis. *Bulletin of Mathematical Biology*, 66:1785–1819, 2004.
- J. I. Prosser and A. P. J. Trinci. A model for hyphal growth and branching. *Journal of General Microbiology*, 111:153–164, 1979.
- I. E. De La Providencia, F. A. De Souza, F. Fernandez, N. S. Delmas, and S. Declerck. Arbuscular mycorrhizal fungi reveal distinct patterns of anastomosis formation and hyphal healing mechanisms between different phylogenetic groups. *New Phytologist*, 165(1):261–271, 2005.
- R. Rach. A new definition of the Adomian polynomials. *Kybernetes*, 37:910–955, 2008.
- R. Ramachandran and J. J. Gnanados. Mycoremediation for the treatment of dye containing effluents. *International Journal of Computing Algorithm*, 2:286–293, 2013.
- C. Ratledge and L. G. Dover. Iron metabolism in pathogenic bacteria. *Annual Review of Microbiology*, 54:881–941, 2000.
- S. Saha Ray. New approach for general convergence of the Adomian decomposition method. *World Applied Sciences Journal*, 32(11):2264–2268, 2014.
- N. D. Read, A. B. Goryachev, and A. Lichius. The mechanistic basis of self-fusion between conidial anastomosis tubes during fungal colony initiation. *Fungal Biology Reviews*, 26:1–11, 2012.
- J. C. Renshaw, G. D. Robson, A. P. J. Trinci, M. G. Wiebe, F. R. Livens, D. Collison, and R. J. Taylor. Fungal siderophores: structures, functions and applications. *Mycological Research*, 106(10):1123–1142, 2002.
- C. G. Reynaga-Pena, G. Gierz, and S. Bartnicki-Garcia. Analysis of the role of the Spitzenkörper in fungal morphogenesis by computer simulation of apical branching in *Aspergillus niger*. *Proceedings of the National Academy of Sciences of the United States of America*, 94:9096–9101, 1997.
- K. Ritz. Growth response of some soil fungi to spatially heterogeneous nutrients. *FEMS Microbiology Ecology*, 1:269–280, 1995.

- M. G. Roca, L. C. Davide, M. D. Mendes-Costa, and A. Wheals. Conidial anastomosis tubes in *Colletotrichum*. *Fungal Genetics and Biology*, 40(2):138–145, 2003.
- T. D. Rotheray, T. H. Jones, M. Fricker, and L. Boddy. Grazing alters network architecture during interspecific mycelial interactions. *Fungal Ecology*, 1:124–132, 2008.
- T. D. Rotheray, M. Chancellor, T. H. Jones, and L. Boddy. Grazing by collembola affects the outcome of interspecific mycelial interactions of cord-forming basidiomycetes. *Fungal Ecology*, 4(1):1–14, 2010.
- F. J. Ryan, G. W. Beadle, and E. L. Tatum. The tube method of measuring the growth rate of neurospora. *American Journal of Botany*, 30:784–799, 1943.
- M. Safari and M. Danesh. Application of Adomian’s decomposition method for the analytical solution of space fractional diffusion equation. *Advances in Pure Mathematics*, 1:345–350, 2011.
- H. M. Safuan, I. N. Towers, Z. Javanoski, and H. S. Sidhu. On travelling wave solutions of the diffusive Leslie-Gower model. *Applied Mathematics and Computation*, 274:362–371, 2016.
- M. Saha, S. Sarkar, B. Sarkar, B. K. Sharma, S. Bhattacharjee, and P. Tribedi. Microbial siderophores and their potential applications: a review. *Environmental Science and Pollution Research International*, 23(5):3984–3999, 2016.
- G. S. Saharan and N. Mehta. *Sclerotinia Diseases of Crop Plants: Biology, Ecology and Disease Management*. Springer Netherlands, 2008.
- B-I. Sang, K. Hori, and H. Unno. A mathematical description for the fungal degradation process of biodegradable plastics. *Mathematics and Computers in Simulation*, 65:147–155, 2004.
- S. M. Sanzani, M. Reverberi, and R. Geisen. Mycotoxins in harvested fruits and vegetables: Insights in producing fungi, biological role, conducive conditions, and tools to manage postharvest contamination. *Postharvest Biology and Technology*, 122:95–105, 2016.

- B. Sasirekha and S. Srividya. Siderophore production by *Pseudomonas aeruginosa* FP6, a biocontrol strain for *Rhizoctonia solani* and *Colletotrichum gloeosporioides* causing diseases in chilli. *Agriculture and Natural Resources*, 50:250–256, 2016.
- H. P. Schmitz, A. Kaufmann, M. Kohli, P. P. Laissue, and P. Philippsen. From function to shape: A novel role of a formin in morphogenesis of the fungus *Ashbya gossypii*. *Molecular Biology*, 17:130–145, 2006.
- K. H. Schütte. Translocation in fungi. *New Phytologist*, 55:164–182, 1956.
- B. Schwyn and J. B. Neilands. Universal chemical assay for the detection and determination of siderophores. *Analytical Biochemistry*, 160(1):47–56, 1987.
- M. A. Selosse, F. Richard, H. Xinhua, and S. W. Simard. Mycorrhizal networks: des liaisons dangereuses? [Mycorrhizal networks: the dangerous liaisons?]. *Trends in Ecology and Evolution*, 21(11):621–628, 2006.
- F. Sempere and M. P. Santamarina. Study of the interactions between *Penicillium Oxalicum Currie & Thom* and *Alternaria alternata* (Fr.) Keissler. *Brazilian Journal of Microbiology*, 41(3):700–706, 2010.
- G. S. Shephard. Risk assessment of aflatoxins in food in Africa. *Food additives & contaminants. Part A, Chemistry, analysis, control, exposure & risk assessment*, 25(10):1246–1256, 2008.
- S. E. Smith and D. J. Read. *Mycorrhizal Symbiosis (2ed)*. Academic Press, 1997.
- M. P. Srivastava, R. Tiwari, and N. Sharma. Effect of different cultural variables on siderophores produced by *Trichoderma spp*. *International Journal of Advanced Research*, 1(8):1–6, 2013.
- P. K. Srivastava, A. Vaish, S. Dwivedi, D. Chakrabarty, N. Singh, and R. D. Tripathi. Biological removal of arsenic pollution by soil fungi. *Science of the Total Environment*, 409:2430–2442, 2011.
- P. Stamets. What is the Stamets p value system? Website, 6 March 2010. URL <http://www.fungi.com/blog/items/what-is-the-stamets-p-value-system.html>.



- P. Stamets. Fungi perfecti. Website, December 2014. URL <http://www.fungi.com/blog/items/the-petroleum-problem.html>.
- G. Steinberg. Hyphal growth: a tale of motors, lipids, and the Spitzenkörper. *Eukaryotic Cell*, 6:351–360, 2007.
- M. Tataria, M. Dehghan, and M. Razzaghi. Application of the Adomian decomposition method for the Fokker-Planck equation. *Mathematical and Computer Modelling*, 45:639–650, 2007.
- D. L. Taylor, I. C. Herriott, K. E. Stone, J. W. McFarland, M. G. Booth, and M. B. Leigh. Structure and resilience of fungal communities in Alaskan boreal forest soils. *Canadian Journal of Forest Research*, 40:1288–1301, 2010.
- M. Tlalka, M. Fricker, and S. Watkinson. Imaging of long-distance  $\alpha$ -aminoisobutyric acid translocation dynamics during resource capture by *Serpula lacrymans*. *Applied and Environmental Microbiology*, 74:2700–2708, 2008.
- C. J. Torkelson, E. Sweet, M. R. Martzen, M. Sasagawa, C. A. Wenner, J. Gay, A. Putiri, and L. J. Standish. Phase 1 clinical trial of *Trametes versicolor* in women with breast cancer. *International Scholarly Research Network*, doi:org/10.5402/2012/251632, 2012.
- P. M. J. Trevelyan. Analytical small-time asymptotic properties of  $A+B \rightarrow C$  fronts. *Physical Review E: Statistical, Nonlinear, and Soft Matter Physics*, 80(4):046118, 2009.
- D. Turrá, D. Nordzieke, S. Vitale, M. El-Ghalid, and A. Di Pietro. Hyphal chemotropism in fungal pathogenicity. *Seminars in Cell & Developmental Biology*, 57:69–75, 2016.
- J. Utermark and P. Karlovsky. Role of Zearalenone Lactonase in protection of *Gliocladium roseum* from fungitoxic effects of the mycotoxin Zearalenone. *Applied and Environmental Microbiology*, 73(2):637–642, 2007.
- L. Váchová, Michal Čáp, and Z. Palková. Yeast colonies: A model for studies of aging, environmental adaptation, and longevity. *Oxidative Medicine and Cellular Longevity*, doi:org/10.1155/2012/601836, 2012.

- K. R. Vankudoth, A. Boda, G. Sivadevuni, and M. R. Solipuram. Effect of indigenous fungi on ochratoxin a produced by two species of penicillium. *Animal Nutrition*, 2(3):225–228, 2016.
- V. C. Verma, S. K. Singh, and S. Prakash. Bio-control and plant growth promotion potential of siderophore producing endophytic streptomyces from *Azadirachta indica* A. Juss. *Journal of Basic Microbiology*, 51:550–556, 2011.
- A. M. Wazwaz. The modified decomposition method and Padé approximants for a boundary layer equation in unbounded domain. *Applied Mathematics and Computation*, 177(2):737–744, 2006.
- R. H. Whittaker. On the broad classification of organisms. *Quarterly Review*, 34(3):210–226, 1959.
- R. H. Whittaker. New concepts of kingdoms of organisms. *Science*, 163:150–160, 1969.
- R. H. Whittaker and L. Margulis. Protist classification and the kingdoms of organisms. *BioSystems*, 10:3–18, 1978.
- G. Winkelmann. Structural and stereochemical aspects of iron transport in fungi. *Biotechnology Advances*, 8:207–231, 1991.
- G. Winkelmann. Microbial siderophores-mediated transport. *Biochemical Society Transactions*, 30:691–695, 2002.
- F. Wu and P. Khlangwiset. Evaluating the technical feasibility of aflatoxins risk reduction strategies in Africa. *Food additives & contaminants. Part A, Chemistry, analysis, control, exposure & risk assessment*, 27(5):658–676, 2010.
- H. Yang, R. King, U. Reichu, and E. D. Giles. Mathematical model for apical growth, septation, and branching of mycelial microorganisms. *Biotechnology and Bioengineering*, 39(1):49–58, 1992.
- M. E. Zain. Impact of mycotoxins on humans and animals. *Journal of Saudi Chemical Society*, 15(2):129–144, 2011.
- M. B. Zimmermann and R. F. Hurrell. Nutritional iron deficiency. *Lancet*, 370:511–520, 2007.